
**Cenozoic tectonic deformation, thermochronology and exhumation of
the Diancang Shan metamorphic massif along Ailao Shan-Red River
shear zone, southeastern Tibet, China**

Dissertation
zur Erlangung des Doktorgrades
der Mathematisch-Naturwissenschaftlichen Fakultäten
der Georg-August-Universität zu Göttingen

vorgelegt von

Shuyun Cao

aus Hunan, China

Göttingen 2010

D 7

Referent: Prof. Dr. Bent T. Hansen

Geowissenschaftliches Zentrum der Georg-August Universität Göttingen, Germany

Korreferent: Dr. Bernd Leiss

Geowissenschaftliches Zentrum der Georg-August Universität Göttingen, Germany

Korreferent: Prof. Dr. Franz Neubauer

Department Geography and Geology, University of Salzburg, Austria

Tag der mündlichen Prüfung: November 3th, 2010

Real knowledge, like everything else of value, is not to be obtained easily, it must be worked for, studied for, thought for and more than all, must be prayed for.

----Thomas Arnold

In memory of my deep beloved father.

*Thanks to my family and the countless good souls everywhere,
who believed in me, encouraged me and helped me,
for their love, care and support,
so that this thesis could become reality one day*

.....

Don't part with your illusions.

*When they are gone you may still exist,
but you have ceased to live.*

----Mark Twain

Acknowledgements

That the dissertation can be successfully completed and appear here owes to so many people. However, it is impossible to express my sincere gratefulness to everyone. In case his or her name is missing here, I apologize for any oversights, but I would like to express my sincere thanks and my gratefulness to all of you for any kind of help you granted me so that I finally could hand in this piece of work as my PhD thesis.

I would like to thank the members of my PhD committee, Dr. Bernd Leiss, Professor Dr. Werner F. Kuhs and Professor Dr. Bent Hansen, Dr. Axel Vollbrecht who enabled me to pursue my research in Goettingen University. Specially, I would like to give my grateful thanks to my advisor, Dr. Bernd Leiss, for his constant supervision of my work, for guiding and introducing me to the X-ray texture geometer, for supporting my research and for allowing me a certain freedom to pursue my interests and my projectives, for his inspiring and challenging me in our discussions. I would like to thank him for his personal attention and the freedom I enjoyed during my stay in Goettingen. I also owe my deep gratitude to Professor Dr. Werner F. Kuhs for providing me a pleasant and friendly working environment and for his kind attention and help during my PhD studies.

The major part of my PhD projects was only possible with the collaboration, help and support of many people. Specially, it is my honor to express my deep gratitude to Professor Dr. Junlai Liu, who led me to enter the gate of structural geology, microstructural geology and texture analysis, and walked with me on the way of my work. He was not required to help me, but offered me a hand. Without his suggestions, encouragement and support, enlightened discussions and sharing of ideas, the dissertation would not be written well at the moment. Furthermore, I would like to express my heartfell gratitude to Professor Dr. Franz Neubauer for giving me the opportunity to carry out the Ar/Ar measurement in his laboratory, for a fruitful cooperation and for very useful discussions about the Ar/Ar dating results. I would also like to thank Dr. Johann Genser for his kind help by the acquisition and calculation of the Ar/Ar data and deep thanks to his wife who gave her kind help for my staying in Salzburg.

I am grateful to Dr. Axel Vollbrecht for his patience, personal and scientific advice, for inspirational discussions and help. We, together with very friendly Dr. Klaus Wemmer and other colleagues of the Departments of Structural Geology and Isotope Geology at Goettingen, have had a nice time during the field work in Sweden and during my stay in Goettingen. Although, in order to focus on one main topic to discuss the geology questions, I did not put the Sweden work in this thesis, I really thank every body who organized and granted the chance for me to be with

you for the field work. Many thanks go to Dr. Klaus Wemmer who collected nice big samples for me and give me a lot of other help. I also want to acknowledge Mrs. Marie-France Hesse, Mrs. Brigitte Hinz and Mrs. Offerle Karin for their help concerning administrative matters. And also my thanks to Dr. Jens M. Walter, Dr. Steffi Burchardt, Dr. Nadine Friese, Dr. Micheal Krumbholz for their friendly support.

I am also grateful to the people of the crystallography department, who have been very nice to me, and been supportive whenever I needed help. Specially, I wish to offer my sincere thankfulness to Mr. Klaus Haepe. I have been very lucky to always get his friendly and kind help on many things. I could't thank him enough for his endless patience in sharing my happiness, sadness or even crying. Mr. Klaus Haepe often acted like a kind father.

The publications included in this thesis greatly benefited from the thoughtful, critical and constructive reviews by Prof. Dr. Tom Blenkinsop, Dr. Manuel Díaz Azpiroz, Dr. Sergio Llana-Fúnez, Dr. Josep Poblet, Prof. Dr. Liu Zhenhong, Dr. Inna Safonova, Prof. Dr. M. Santosh, Prof. Juhn Liou, Prof. John Craddock. Prof. Michel Fraure, Prof. Lorence G. Collins, Dr. Zhang Jian, Prof. Yang Jinhui, Prof. W. Gary Emst, Dr. Inna Safonova, Dr. Zhang Yanbin, Ms. Isabella Merschdorf and several anonymous reviewers. Their constructive comments definitely improved the quality of the papers. I am also greatly indebted to many teachers in the past and present, starting from school education till the completion of the studies.

One person who is unfortunately no longer able to celebrate the completion of my PhD. thesis with me. This is my beloved father who passed away too early. He was the very first one to encourage me to step forward to work towards my PhD. He was always so proud of me and had been looking forward to the day when I finally finish my PhD. Wherever he is now, this thesis is dedicated to him and I hope he is pround of my success and very happy. Thank you, my father, I really miss you.

I am greatly thankful to all my family members. I would also have not reached this point without the support from my mother, maternal uncle, brother and sisters. I want to give my deep thanks to them for encouraging me and for the understanding of my long education, when I had only very little time to be with them during my whole study and work until now.

Special thanks also to Liu Renyi, for his motivation and support, his understanding and patience in these years for my study. He was always there for guarding my back and made my dream of a PhD come true in the end.

Finally, the financial support from the China Government Schlorship project is gratefully acknowledged.

Summary

Chapter 1 This thesis outlines the Cenozoic tectonic evolution of a critically important area within the India-Eurasian collision zone, i.e. the Diancang Shan (DCS) metamorphic massif along the Ailao Shan-Red River (ASRR) shear zone situated to the southeast of the Tibetan plateau. Detailed macro- and microstructural, and textural studies, and metamorphic analysis of the highly sheared rocks in the shear zone help elucidating the tectono-thermal history of the shear zone. Thermochronology and structural analysis of the granitic intrusions are applied to constrain the timing and duration of the ductile shearing and exhumation of the high-grade metamorphic and mylonitic rocks. The regional tectonic implications of the Ailao Shan-Red River shear zone are discussed on the basis of structural and thermochronological studies.

Chapter 2 describes the results of a detailed study of the micro- and submicro-structures and textural styles of the typical mylonitic amphibolite rocks from the Diancang Shan high-grade metamorphic complex. Various micro- and submicro-structures are developed in the amphibole mylonitic rocks. Deformed porphyroclasts of amphibole and fine-grained matrix of amphibole, plagioclase and quartz are the main constituents of the amphibolitic mylonites. Different mineral phases in the rocks show distinct deformation characteristics. Microstructural analysis and P/T estimation suggest that the amphibole grains in the mylonitic rocks are deformed and dynamically recrystallized at amphibolite facies. In the mylonitic amphibolites, there are two types of amphibole porphyroclasts, i.e. type I “hard” and type II “soft” porphyroclasts. They have their [001] crystallographic orientations subnormal and subparallel to the stretching lineation of the rocks, respectively. The two types of porphyroclasts show distinct deformation microstructures and sub-microstructures formed by various deformation mechanisms, which contribute in different ways to the generation of the fine-grained matrix. Shape preferred orientation analysis, misorientation analysis of the two types of porphyroclasts and new fine grains around them further prove the generation of the fine grains in matrix from the type II porphyroclasts. The type I “hard” porphyroclasts are deformed mainly by mechanical rotation, work hardening and intragranular microfracturing. In contrast, the deformation of the type II “soft” porphyroclasts is mainly attributed to crystalline plasticity, i.e. twinning, dislocation creep and dynamic recrystallization. During the deformation of the type II porphyroclasts, the (100) [001] slip system plays a dominant role during deformation and grain size reduction of amphibole. Twinning along the active (100) slip system, in combination with dislocation creep (gliding and climbing) governs the nucleation of subgrains and formation of dynamically recrystallized fine grains, a process here named *Twinning Nucleation Recrystallization*.

Chapter 3 outlines the results for macro- and micro-structures and textures of mylonites in the Diancang Shan metamorphic complex. High-temperature mylonites derived from either granitic rocks or amphibolitic rocks constitute the main part of the shear zone in the high-grade metamorphic complex. The detailed macro- and microstructural correlation of these samples can establish the structural evolution of the mylonitic metamorphic complex. Macroscopic fold patterns and microstructural features characterize the high-temperature flow of rocks. Optical microscopy and transmission electron microscope (TEM) analysis reveals the dominance of high-temperature recovery and recrystallization of quartz, feldspar and amphibole. Amphibole texture analyses give clues to the importance of (100) [001] slip systems during dynamic recrystallization. P-T calculations reveal pressure and temperature conditions of shearing at lower amphibolite facies. All the observations suggest that the deformation microstructures and textures are attributed to high-temperature deformation and dynamic recrystallizations due to left-lateral shearing along the Ailao Shan-Red River shear zone.

Our SHRIMP-II U-Pb dating of zircons from a synkinematic monzogranite, as discussed in Chapter 4, give an age of 30.88 Ma. The porphyritic synkinematic monzogranitic intrusion displays the above-mentioned high-temperature deformation microstructures and textures, which constrains the lower limit of timing of initiation of the left-lateral shearing at early Oligocene. This has allowed the reevaluation of tectonic models that link Oligocene-Miocene left-lateral movement of Ailao Shan-Red River to the opening of the South China Sea.

Chapter 4 presents the integrated study of the timing of plutonic intrusions and shearing in the wall rocks using optical microscope (deformation microstructures), EBSD (textures of amphibolite, quartz and feldspar) and SHRIMP-II zircon U-Pb dating in the Diancang Shan massif. Meso- and microstructural and textural analysis reveals intensive plastic deformation of feldspar, quartz and amphibole under amphibolite facies, which consistently document a left-lateral shearing. The porphyritic monzogranite mylonite along the shear zone possesses evidences where the granite experienced a sequential and progressive process from crystallization during magma emplacement, through submagmatic flow to solid-state plastic deformation. It is suggested that the early-kinematical pluton subsequently experienced strong left-lateral strike-slip shearing. The development of complex textures in quartz and feldspar from the granitic mylonites may have recorded a successive variation of deformation conditions during progressive shearing. They are coherent with solid-state high-temperature ductile deformation during regional left-lateral shearing. Relatively low-temperature modification of the

quartz c-axis orientations can be related to an exhumation and cooling event of the Diancang Shan massif during a later event. All the magmatic zircons in the monzogranitic mylonites give U-Pb ages of ca. 31 Ma for the crystallization of the granite. This age provides therefore the lower limit of the left-lateral shearing along the Ailao Shan-Red River shear zone at the Diancang Shan high-grade metamorphic massif.

Chapter 5 documents post-kinematic granitic plutonism in the Diancang Shan metamorphic massif. Combined LA-ICP-MS dating of magmatic zircons and structural and microstructural evidence allow us to constrain the timing relationships between emplacement of the granitic intrusions and left-lateral strike-slip shearing in the Diancang Shan massif. From the analyses, we reasonably suggest that the age of ca. 24 Ma represent an upper timing for the termination of the ductile left-lateral strike-slip shearing, and the youngest age of ca. 21 Ma is inferred to date the final phase of regional ductile deformation and left-lateral shearing at least in the Diancang Shan massif. Thus the main left-lateral ductile shearing occurred between 27 and 21 Ma at high-temperature conditions (amphibolite facies) and terminated at about 21 Ma at relatively lower-temperatures. During or after the emplacement of the youngest dikes at ca. 21 Ma, brittle deformation occurred, resulting in the rapid cooling and exhumation of the Diancang Shan massif to a shallow crustal level.

Chapter 6 further focuses on Eocene-Miocene tectono-magmatic evolution of the Diancang Shan massif mainly based on our structural analysis and new SHRIMP-II and LA-ICP-MS zircon U/Pb isotopic dating results from the different granitic rocks. The combined structural and geochronological results revealed a succession of magmatic intrusion and crystallization events related to shearing in the Diancang Shan massif. All the samples record three stage of successive kinematic evolution of the shear zone from Eocene to Miocene ages between ca. 34 and 20 Ma. The emplacement of the pre-kinematic alkaline magmas appears to have been accompanied by development of Eocene to Oligocene rifted sedimentary basins. We also propose that the emplacement of pre-kinematic plutons occurred during late Eocene to Oligocene (ca. 34-31 Ma) possibly related to the high-alkali magmatism activity in response to the post-collisional extension. The recognition of shearing microstructures and metamorphic assemblages in the syn-kinematic granitic intrusions in the Diancang Shan imply a transition from magmatic through submagmatic to solid-state plastic deformation during the emplacement of the plutons. To document this transition is an important issue to prove that the solid-state plastic deformation occurred at high-temperature conditions, given that the plutonic process within the strike-slip

shear zone system is synkinematic. Final stages of progressive shearing can be constrained by the youngest-phase of magmatism by zircon crystallization age related to brittle shearing continued ca. 21 Ma. Zircon U/Pb geochronological results suggest that the continental left-lateral ductile shearing of the ASRR shear zone initiated after ca. 31 Ma, culminated during the main periods between ca. 27 and 24 Ma at high-temperature metamorphic conditions and slowed at ca. 21 Ma at relative low-temperature conditions.

Chapter 7 Exhumation of the high-grade rocks in the Diancang Shan metamorphic massif from deep to shallow crustal levels is evidenced by the temporal transition from amphibolite facies shearing and mylonitization, through greenschist facies retrograde ductile-brittle faulting, and brittle faulting at and near the surface. New $^{40}\text{Ar}/^{39}\text{Ar}$ ages of amphibole, muscovite, biotite, and K-feldspar from mostly mylonitic rocks help constrain the kinematic and thermal evolution of the massif during the exhumation since Oligocene. The thermochronologic studies reveal at least three stages of exhumation and cooling from late Oligocene to Pliocene, e.g. 28–13 Ma, 13–5 Ma and 5–0 Ma. The initiation of the unroofing history of the Diancang Shan massif was resulted from ductile left-lateral shearing along the ASRR since late Oligocene. An onset diachronous and subsequent even cooling and exhumation characterizes the early thermal history of the massif. Exhumation may have stopped due to the cessation of the left-lateral shearing at ca. 21 Ma, continued cooling lasted to relatively low temperature conditions until 9 to 6 Ma. The second stage of cooling started from 13 Ma and lasted to the recent active faulting. The diversity of cooling rates at its early stage from 13 to 6 Ma suggests differences in exhumation rates at various localities. Ductile to brittle shearing along the eastern flank retrograde normal shear zone is the best explanation for the exhumation during this stage. The inhomogeneous cooling and exhumation of the lower plate of the normal fault zone is possibly resulted from the tilting of the lower plate block or differential exhumation of slabs in the lower plate. A final stage cooling and exhumation of the DCS massif since 6 to 4 Ma is recognized when extending and plotting the higher temperature cooling paths to a lower temperature at about 16°C of the present day average surface temperature. It is therefore suggested that diachronous cooling and exhumation continuously spans to the surface. The tectonic exhumation of the DCS massif consists a part of the tectono-thermal evolution and diachronous exhumation of the metamorphic complexes broadly since 36 Ma in a fan-shaped area bounded by the Red River fault zone and Sagaing fault zone in SE Asia. Extrusion-induced strike-slip shearing and rotation-resulted normal faulting played important roles in the diachronous cooling and exhumation of the DCS massif and other metamorphic complexes in SE Asia.

List of publications: comulated for this thesis

Paper 1 Orientation-related deformation mechanisms of naturally deformed amphibole in amphibolite mylonites from the Diancang Shan, SW, Yunnan, China

Shuyun Cao, Junlai Liu, Bernd Leiss, 2010. (Journal of Structural Geology 32, 606-622)

Paper 2 Deformation microstructures and textures, and regional tectonic significance of high-temperature shearing of the Diancang Shan Complex, Yunnan, China

Shuyun Cao, Junlai Liu, Bernd Leiss, 2009. (Trabajos de Geología Journal 29, 147-155)

Paper 3 Initiation of left-lateral deformation along the Ailao Shan-Red River shear zone: new microstructural, textural and geochronological constraints from the Diancang Shan metamorphic massif, SW Yunnan, China

Shuyun Cao, Junlai Liu, Bernd Leiss, Axel Vollbrecht, Johann Genser, Franze Neubauer, Chunqiang Zhao, 2011. (International Geology Review. DOI: 10.1080/00206814.2010.543789.)

Paper 4 New zircon U-Pb geochronology from the post-kinematic granitic plutons in the Diancang Shan metamorphic massif along the Ailao Shan-Red River shear zone and its geological implications

Shuyun Cao, Junlai Liu, Bernd Leiss, Chunqiang Zhao, 2010. (Acta Geologica Sinica 84, 801-840)

Paper 5 Oligo-Miocene shearing along the Ailao Shan-Red River shear zone: constraints from structural analysis and zircon U-Pb geochronology of magmatic rocks in the Diancang Shan massif, SE Tibet, China.

Shuyun Cao, Junlai Liu, Bernd Leiss, Franz Neubauer, Johann Genser, Chunqiang Zhao, 2011. (Gondwana Research 19, 975-993. DOI: 10.1016/j.gr.2010.10.006.)

Paper 6 Exhumation of the Diancang Shan metamorphic complex along the Ailao Shan-Red River belt, southwestern Yunnan, China: Evidence from $^{40}\text{Ar}/^{39}\text{Ar}$ thermochronology

Shuyun Cao, Franz Neubauer, Junlai Liu, Johann Genser, Bernd Leiss, 2011. (Journal of Asian Earth Science, doi:10.1016/j.jseaes.2011.04.017)

Table of contents

Cenozoic tectonic deformation, thermochronology and exhumation of the Diancang Shan metamorphic massif along Ailao Shan-Red River shear zone, southeastern Tibet, China	I
D 7 II	
Acknowledgements	I
Summary	III
List of publications: comulated for this thesis	VII
Table of contents	VIII
List of figures and tables	XII
1. Introduction and tectonic framework	1
1.1 Motivation	1
1.2 Cenozoic tectonic activity, magmatism and timing of shearing along the ASRR shear zone	3
1.3 Metamorphic complexes and exhumation	6
1.4 Summary of the thesis	7
1.5 References	9
2. Orientation-related deformation mechanisms of naturally deformed amphibole in amphibolite mylonites from the Diancang Shan, SW Yunnan, China	16
Abstract	16
2.1 Introduction	17
2.2 Geological setting and structural analysis	18
2.3 Methods of fabric analyses	21
2.4 Microstructural and submicrostructural observations	22
2.4.1 Amphibolite mylonites and two types of porphyroclasts-optical microstructures	22
2.4.2 Optical grain size and aspect ratio analysis	25
2.4.3 Submicrostructural characterization - TEM observation	27
2.5 Textures -EBSD analysis	30
2.5.1 LPO data	30
2.5.2 Misorientation	33
2.6 Mineral chemistry analysis of amphibole-plagioclase and P-T estimation	36
2.7 Discussion	39
2.7.1 "Soft" - "hard" behavior of amphibole porphyroclasts	39
2.7.2 Twinning, subgrain nucleation and dynamic recrystallization	41
2.7.3 Role of secondary phases: quartz and plagioclase	43
2.8 Conclusions	44
Acknowledgements	45
References	45
3. Deformation microstructures, textures and regional tectonic significance of high-temperature shearing of the Diancang Shan Complex, Yunnan, China	51
Abstract	51
3.1 Introduction	51
3.2 Techniques	52

3.3 Results	54
3.3.1 Macro-and micro-structures of mylonites from high grade metamorphic complex	54
3.3.2 Texture analysis of amphibole in amphibolitic mylonites	59
3.3.3 Estimation and calculation of pressure and temperature during deformation	59
3.4 Discussions and Conclusions	59
3.4.1 Indication of high-temperature deformation	59
3.4.2 Significance of high-temperature shearing	60
Acknowledgement	60
References	61
4. Initiation of left-lateral deformation along the Ailao Shan-Red River shear zone: new geochronological, microstructural and textural constraints from the Diancang Shan metamorphic massif, SW Yunnan, China	62
Aabstract	62
4.1 Introduction	63
4.2 Geological setting and structural geology	66
4.3 Samples and techniques	69
4.3.1 Sample descriptions	69
4.3.2 Analytical methods	70
4.4. Microstructures	72
4.4.1 Microstructures for late magmatic crystallization in the early kinematic monzogranite	72
4.4.2 Plastic deformation of main mineral phases	73
4.5. Textures–EBSD analysis	76
4.5.1 Quartz texture	76
4.5.2 Amphibole texture	78
4.5.3 Feldspar Texture	79
4.6 Thermochemistry results	80
4.7 Discussion	82
4.7.1 Early-kinematic plutonism: magmatic crystallization	82
4.7.2 Solid-state plastic deformation	84
4.7.3 Timing of initiation of left-lateral shearing in the Diancang Shan massif	86
4.8 Conclusions	86
Acknowledgements	87
References	87
5. Zircon U-Pb geochronology from the post-kinematic granitic plutons in the Diancang Shan metamorphic massif along the Ailao Shan-Red River shear zone and its geological implications	100
Abstract	100
5.1 Introduction	100
5.2 Geological Setting	102
5.3 High-temperature Ductile Deformation of Mylonites from the High-grade Metamorphic Belt	106
5.4 Relationships between the Post-kinematic Intrusions and Deformation	108
5.4.1 Mesoscopic deformation within the syn- and post-kinematic granitic dikes and veins	108
5.4.2 Microfabrics in the thin sections	108
5.5 Zircons and U-Pb LA-ICP-MS Data	109
5.5.1 Analytical techniques	109
5.5.2 Zircon and geochronology results	111

5.6 Discussion	112
5.6.1 The timing of termination and duration of ductile strike-slip shearing	112
5.6.2 Implications for the exhumation of the high-grade metamorphic complex	113
5.7 Conclusions	115
Acknowledgements	115
References	115
6. Oligo-Miocene shearing along the Ailao Shan-Red River shear zone: constraints from structural analysis and zircon U/Pb geochronology of magmatic rocks in the Diancang Shan massif, SE Tibet, China	123
Abstract	123
6.1 Introduction	123
6.2. Geological setting and macro-structural analysis	127
6.3. Analytical techniques	130
6.3.1 Optical microscopy	130
6.3.2 U/Pb zircon dating	130
6.4. Petrology, microfabrics and geochronology	133
6.4.1. Pre-kinematic plutons	133
6.4.2 Syn-kinematic plutons	141
6.4.3 Post-kinematic intrusions	144
6.5. Discussion	147
6.5.1 U/Pb ages and the timing of shearing along the ASRR shear zone	147
6.5.2 Exhumation and magmatism during transpression/transension in the high-grade metamorphic massif	150
6.5.3 Regional tectonic implications	152
6.6. Conclusions	154
Acknowledgements	154
References	155
7. Exhumation of the Diancang Shan metamorphic complex along the Ailao Shan-Red River belt, southwestern Yunnan, China: evidence from $^{40}\text{Ar}/^{39}\text{Ar}$ thermochronology	168
Abstract	168
7.1 Introduction	169
7.2 Geological setting	171
7.2.1 Deformation structures and microfabrics in sheared high-grade metamorphic rocks	173
7.2.2 Low-grade retrograde zone	176
7.2.3 Cenozoic brittle faults, fault-bounded basin and sediments	178
7.3. Analytical techniques and sample descriptions	179
7.3.1 Analytical techniques	179
7.3.2 Sample descriptions	180
7.4. Results	186
7.4.1 Amphibole (T_c ca. 550°C)	188
7.4.2 White mica (T_c ca. 425 °C)	189
7.4.3 Biotite (T_c ca. 300 °C)	189
7.4.4 K-feldspar (T_c ca. 250 °C)	190
7.5 Discussion	194
7.5.1 Cooling paths and age compilations	194
7.5.2 Cooling history of the metamorphic rocks and tectonic deformation	196
7.5.3 Regional tectonic implications	202
7.6. Conclusions	203

Acknowledgements	209
References	209
8. Summary and outlook	217
8.1 Macro- and microstructures, textures and deformation mechanisms	217
8.2 Timing of left-lateral shearing along the Ailao Shan-Red River shear	218
8.3 Eocene-Miocene tectono-magmatic evolution in the Ailao Shan-Red River shear zone	219
8.4 Cooling history and exhumation of the high-grade metamorphic complexes	220
8.5 Concluding remarks and future work	221
Curriculum vitae	223

List of figures and tables

Chapter 1

Fig. 1. 1 Tectonic sketch map of Southeast Asia	5
--	---

Chapter 2

Fig. 2. 1 Tectonic setting and structural outline of Diancang Shan area	20
Fig. 2. 2 Mesoscopic structures of ductile sheared amphibolites from the central high strain shear zone	23
Fig. 2. 3 Microstructures in amphibolite mylonites and ultramylonites.....	24
Fig. 2. 4 Diagram showing the relationship between the amphibole aspect ratios and the orientation of long axes of the grains	27
Fig. 2. 5 Submicrostructures of amphibole grains from mylonitic rocks.....	28
Fig. 2. 6 Deformation submicrostructures in quartz and plagioclase grains.	29
Fig. 2. 7 EBSD fabric data of amphiboles from the mylonitic and ultramylonitic amphibolites	32
Fig. 2. 8 Misorientation angle frequency distributions of amphiboles.....	34
Fig. 2. 9 EBSD inverse pole figure.....	36
Fig. 2. 10 Mineral chemistry of amphibole grains in the amphibolite mylonites	38
Fig. 2. 11 Schematic diagram showing the dynamic recrystallization of amphibole by twinning nucleation recrystallization.....	42
Table 2. 1 Grain size and aspect ratio	26
Table 2. 2 Mineral chemistry analyses of amphibole and P-T estimation/calculation.....	37

Chapter 3

Fig. 3. 1 Tectonic setting and structural outline of Diancang Shan area	53
Fig. 3. 2 Macroscopic structural evidences of high-temperature ductile deformation, observed in high grade metamorphic rocks in Diancang Shan.....	54
Fig. 3. 3 Microscopic high-temperature deformation characteristics of high grade metamorphic rocks in Diancang Shan.....	56
Fig. 3. 4 Amphibole textures of recrystallized matrix grains of amphibolitic mylonite obtained by EBSD analysis.....	57
Fig. 3. 5 Submicrostructural characteristics in amphibole and quartz from high grade metamorphic rocks (TEM).	58

Chapter 4

Fig. 4. 1	Tectonic sketch map of major tectonic features of Southeast Asia	65
Fig. 4. 2	Structural outline of the Diancang Shan area	68
Fig. 4. 3	Geological section across the Diancang Shan massif and macroscopic structural evidence of ductile deformation in high-grade metamorphic rocks in the Diancang Shan	69
Fig. 4. 4	Macro- and microstructures of dated granitic mylonites from Diancang Shan	73
Fig. 4. 5	Microscopic high-temperature plastic deformation characteristics of main minerals	75
Fig. 4. 6	Quartz c-and a-axes textures were measured in eight samples collected from mylonitic monzogranite	77
Fig. 4. 7	Amphibole textures measured from amphibolitic mylonite	79
Fig. 4. 8	Feldspar textures were measured from two mylonitic monzogranite	80
Fig. 4. 9	Cathodoluminescence images of representative zircons, sites of analyzed spots, U/Pb Concordia diagram and weighted average age diagram	81
Table 4. 1	Summary of SHRIMP U-Pb zircon results	99

Chapter 5

Fig. 5. 1	Tectonic sketch map of Southeast Asia	103
Fig. 5. 2	Geological map of the Diancang Shan area	105
Fig. 5. 3	Microscopic high-temperature plastic deformation characteristics of mylonites from the high-grade metamorphic belt	107
Fig. 5. 4	Meso-structural relationships between post-kinematic rocks and their wall rocks ..	110
Table 5. 1	Zircon U-Pb LA-ICP-MS analytical data of the post-kinematic intrusions in the Diancang Shan metamorphic massif	122

Chapter 6

Fig. 6. 1	Tectonic sketch of Southeast Asia	126
Fig. 6. 2	Structural outline of the Diancang Shan area.....	130
Fig. 6. 3	Meso-structural relationships between granitic rocks and their wall rocks.....	134
Fig. 6. 4	Sketch maps of diagnostic features of pre-, syn- and post-kinematic granites in strike slip fault zones.....	135
Fig. 6. 5	Deformation microstructures of intrusions.....	137
Fig. 6. 6	Cathodoluminescence (CL) images of representative zircons	140
Fig. 6. 7	U/Pb SHRIMP-II and LA-ICP-MS concordia diagrams and weighted average age diagrams.....	147

Table 6. 1 Zircon U/Pb SHRIMP-II analytical data	164
Table 6. 2 Zircon U/Pb LA-ICP-MS analytical data	165

Chapter 7

Fig. 7. 1 Tectonic sketch map of Southeast Asia	172
Fig. 7. 2 Structural outline of the Diancang Shan massif	175
Fig. 7. 3 Meso- and micro-structures of high-grade metamorphic rocks from the central part of the DCS massif	175
Fig. 7. 4 Meso- and micro-structures from the retrograde metamorphic belt along the eastern flank of the DCS massif	178
Fig. 7. 5 Sample locations and Ar/Ar ages of this study	181
Fig. 7. 6 Microstructures of the dated samples from the DCS massif	184
Fig. 7. 7 $^{40}\text{Ar}/^{39}\text{Ar}$ data for amphibole	187
Fig. 7. 8 $^{40}\text{Ar}/^{39}\text{Ar}$ data for white mica	190
Fig. 7. 9 $^{40}\text{Ar}/^{39}\text{Ar}$ data for biotite	192
Fig. 7. 10 $^{40}\text{Ar}/^{39}\text{Ar}$ data for K-feldspar	193
Fig. 7. 11 Time-integrated cooling rates of Diancang Shan massif.....	198
Fig. 7. 12 <i>Tentative models for three stages of exhumation of the Diancang Shan metamorphic complex.....</i>	201
<i>Table 7. 1 ^{40}Ar-^{39}Ar step heating data for amphibole, muscovite, biotite and K-feldspar of the Diancang Shan massif</i>	205
<i>Table 7.2. Summary of thermochronologic data of the samples from the DCS massif.....</i>	198

1 Introduction and tectonic framework

1.1 Motivation

The current most spectacular tectonic activity in Asia is widely cited as the consequence of continental collision between the Indian and Eurasian plates since the early Eocene (e.g. Molnar and Tapponnier, 1975; Tapponnier et al., 1982). Crustal thickening/thinning, plateau development, magmatism and large-scale strike-slip faulting extend well beyond the Himalaya and the Tibetan plateau, deep into the southeast of the Asian continent (e.g. Molnar and Tapponnier, 1975; Tapponnier et al., 1982, 1986; Chung et al., 1997, 1998, 2005) (Fig. 1.1). Various models and hypotheses have been proposed to explain the kinematic and tectonic processes associated with the formation of the Tibetan plateau and plate-scale deformation in Southeast Asia (e.g. England and McKenzie, 1988; Tapponnier et al., 1982, 1993; Peltzer and Saucier, 1996; Wang and Burchfiel, 1997; Jolivet et al., 2001). Indicated by paleomagnetic data the area is dominated by southeastward displacement and rotation of the Indochina Block as a consequence of the extrusion of the blocks from the India-Asia collision zone along major fault zones, e.g. the Gaoligong and Sagaing shear zones in the west, and the Ailao Shan-Red River (ASRR) shear zone in the east (e.g. Tapponnier et al., 1977, 1982, 1986; Huang and Opdyke, 1993; Yang and Besse, 1993, 1995; Chung et al., 1997, 1998; Wang et al., 1998, 2000; Sato et al., 1999; Burchfiel and Wang, 2003; Tanaka et al., 2008) (Fig. 1.1). Deep-crustal high-grade metamorphic rocks are exposed within or immediately adjacent to the continental strike-slip fault systems in SE Asia in a fan-shaped area, which is bounded by the fault zones (e.g. Liu et al., 2007). Deformation and exhumation of the metamorphic massifs in the collisional and post-collisional zones involving orogen-parallel extension and strike-slip faulting in SE Asia have been documented (e.g. Tapponnier et al., 1990; Tran et al., 1998; Jolivet et al., 1999; Wang et al., 2000; Maluski, et al., 2001). It is shown that the strike-slip shear zones are the key structures in the reconstruction of the relative movement of crustal blocks where non-coaxial/coaxial deformation produces large-scale displacement during the Cenozoic geodynamic evolution of SE Asia (e.g. Tapponnier et al., 1990; Houseman and England, 1993; Leloup et al., 1995; Passchier and Coelho, 2006). Shearing along the ASRR shear zone is assumed to have led to over 500 km southeastward displacement of the Indochina block (e.g. Huang, 1960; Tapponnier et al., 1986, 1990; Leloup et al., 1995; Chung et al., 1997; Searle, 2006) relative to the Yangtze-South China block, and is accompanied by the opening of the South China Sea (e.g. Pelzer et al., 1988; Tapponnier et al., 1990; Harrison et al., 1992, 1996; Leloup et al., 1995; Fyhn et al., 2009).

Combined tectonic and geomorphologic studies have yielded valuable insights into the Southeast Asian tectonics. Specially, research spanning more than twenty years have provided a wealth of information on the structural and thermal evolution, geometries of the ASRR shear zone and Red River fault (e.g. Harrison et al., 1992; Schärer et al., 1990, 1994; Leloup and Kienast 1993; Leloup et al., 1995, 2001a, b; Harrison et al. 1996; Chung et al., 1997; Wang et al., 1998b, 2000; Zhang and Schärer 1999; Morley et al., 2000; Sun et al., 2003; Schoenbohm et al., 2004; Liu et al., 2006; Yeh et al., 2008; Zhang et al., 2009). One particularly important topic of interests is the deformation and thermochronological signature of left-lateral shearing, with the aim of constraining the timing and rate of shearing, cooling history and exhumation process of the metamorphic massifs along the ASRR belt (e.g. Schärer et al., 1994; Zhang and Schärer, 1999; Sassier et al., 2009, Cao et al., 2010b, c). Recent geophysical studies have provided further evidence of the deep structure of the ASRR fault (e.g. Zhang et al., 2009). Although there is a general recognition that the major strike-slip faults clearly play a key role in the Cenozoic development of the Indian-Eurasian plate collision, controversy still exists over the metamorphism and deformation, timing of initiation and the duration of strike-slip shearing, the thermal history, the processes and mechanisms of exhumation of the high-grade metamorphic rocks and their tectonic implications. Therefore, detailed knowledges of structural, sub- and microstructural and textural analysis of the deformed rocks, constraining the ages of shearing along crustal-scale faults by dating the emplacements of plutons and thermochronology of the metamorphic and deformed rocks are the fundamental tools for resolution of these viewpoints and also for the understanding of the accommodation of the tectonic plates during continental collision and post-collisional evolution.

The following chapters of this thesis formulate a new comprehensive, integrated history of tectonic development of the ASRR shear zone region, based on new structural, microstructural, textural and thermochronology and quantitative P-T analysis of the highly sheared high grade metamorphic and plutonic rocks in the DCS massif. Results are interpreted in the context of main questions related to the nature of continental deformation along the ASRR shear zone. These include: 1) the main deformation characteristics of meso- and microstructures, textures, the deformation mechanisms and deformation conditions of the high-grade mylonitic rocks in the shear zone; 2) the relative timing between deformation, metamorphism and magmatism; and 3) the cooling history and uplift/exhumation processes and mechanisms (P-T-t-D path). This study, seeking to have detailed and quantitative analysis, not only allow us to precisely establish the age framework of Cenozoic deformation and magmatic activities in the DCS massif, but can be used to better constrain the timing and duration of ASRR shearing and build the P-T-t-D path

of evolution. The data presented could also allow us to improve the current geodynamic models for the tectonic significance of magmatism and exhumation of the massifs along the ASZZ shear zone, in particular of the Indian-Eurasian plate interaction during the collisional and post-collisional stages in Southeast Asia.

1.2 Cenozoic tectonic activity, magmatism and timing of shearing along the ASRR shear zone

A crucially important Cenozoic tectonic belt in the Southeast Asia is the NW-trending Ailao Shan-Red River (ASRR) left-lateral strike-slip shear zone extending over a length of 1000 km. The ASRR shear zone represents the eastern boundary of Indochina plate and has been long recognized as one of the main geological discontinuities of Southeast Asia (e.g. Tapponnier et al., 1982, 1986; Wang et al., 1997). It records a complex structural evolution in which the kinematics of the deformation vary both spatially and temporally and plays important roles in accommodating the southeastward extrusion of the Indochina block during Indian-Eurasian plate collision and post-collisional evolution (e.g. Tapponnier et al., 1982, 1986, 1990; Zhong et al., 1990). The ASRR metamorphic belt comprises four narrow high-grade metamorphic massifs, e.g. the Xuelong Shan (XLS), Diancang Shan (DCS), Ailao Shan (ALS) massifs in China and Day Nui Con Voi (DNCV) massif in Vietnam. These massifs are exposed between Paleozoic to Mesozoic cover rocks and are bounded in many places by Neogene-Quaternary basins (e.g. Bureau of Geology and Mineral Resources of Yunnan, 1983, 1991). They present good cases telling that strike-slip and normal faults are related to exhumation of the metamorphic complexes during the Indian and Eurasian plate interactions (e.g. Tapponnier et al., 1982, 1986; Leloup et al., 1995).

The Cenozoic tectonothermal episode is composed of two periods of strike-slip motion that are generally considered to be most influential in the geological evolution of the ASRR. One is the large-scale left-lateral strike-slip of over 500 km southeastward displacement. The ductile shearing is considered to be the results of the southeastward extrusion of the Indochina block since Miocene (e.g. Huang, 1960; Tapponnier et al., 1986, 1990; Chung et al., 1997; Searle, 2006). Numerous shear criteria indicate that the high-grade metamorphic rocks have undergone intense left-lateral ductile shearing (e.g. Tapponnier et al., 1986, 1990; Leloup et al., 1993, 1995; Jolivet et al., 2001; Leloup et al., 2001b; Liu et al., 2007; Anczkiewicz et al., 2007). The major left-lateral strike-slip displacement is suggested to be responsible for exhumation of the high-grade metamorphic complexes (e.g. Anczkiewicz et al., 2007). Current geomorphologic and

geodetic data indicate that the Red River fault is a right-lateral strike-slip fault zone (e.g. Allen et al., 1984; Burchfiel and Wang, 2003). Recently some workers suggested that the strike-slip motion changed from sinistral to dextral with a normal component during the late Miocene, and some new GPS measurements across the ASRR concluded that the ASRR is currently inactive (e.g. Jolivet et al., 2001). Thermochronological studies conducted in the region of the ASRR shear zone have focused on these metamorphic complexes and tectonic-magmatic signatures with the aim of constraining the timing and amount of displacement, rate of movement along the shear zones and exhumation processes (e.g. Schärer et al., 1990, 1994; Harrison et al., 1992; Leloup and Kienast, 1993; Zhang and Schärer 1999; Gilley et al., 2003, Cao et al., 2010b, c).

It is still an important issue for the understanding of the development of the shearing complexes and processes of crustal deformation to understand the relative timing of metamorphism, magmatism and deformation. Generally, the deformed granitic rocks are spatially and temporally associated with orogeny and active deformation. In particular, tectonomagmatic relationships along the crustal-scale strike-slip shear zones can be demonstrated from detailed comparison of structures and fabrics developed within tectonic plutons with their mylonitic host rocks (e.g. Paterson et al., 1998; Rosenberg, 2004). Hence, it is becoming increasingly clear that detailed studies of the structures, microstructures and textures and precise dating of magmatic crystallization can be used to better constrain the timing of regional tectonic events (e.g. Miller and Paterson, 1994). However, using plutons to construct the orogenic deformation history requires very careful multidisciplinary studies and specially a rather careful definition for pre-, syn- or post-tectonic emplacement and their deformation characteristics and conditions (e.g. Paterson, 1989; Searle, 2006; Cao et al., 2010c). Therefore, we invoke an extensive database of the precise determination of the deformation ages of the Diancanshan tectonites which have great implications on constraining the timing of the ductile shear zones developed in the Diancang Shan region, and therefore further re-evaluating the tectonic essence and exhumation of the Diancang Shan and discuss its significance on the tectonic evolution of the ASRR.

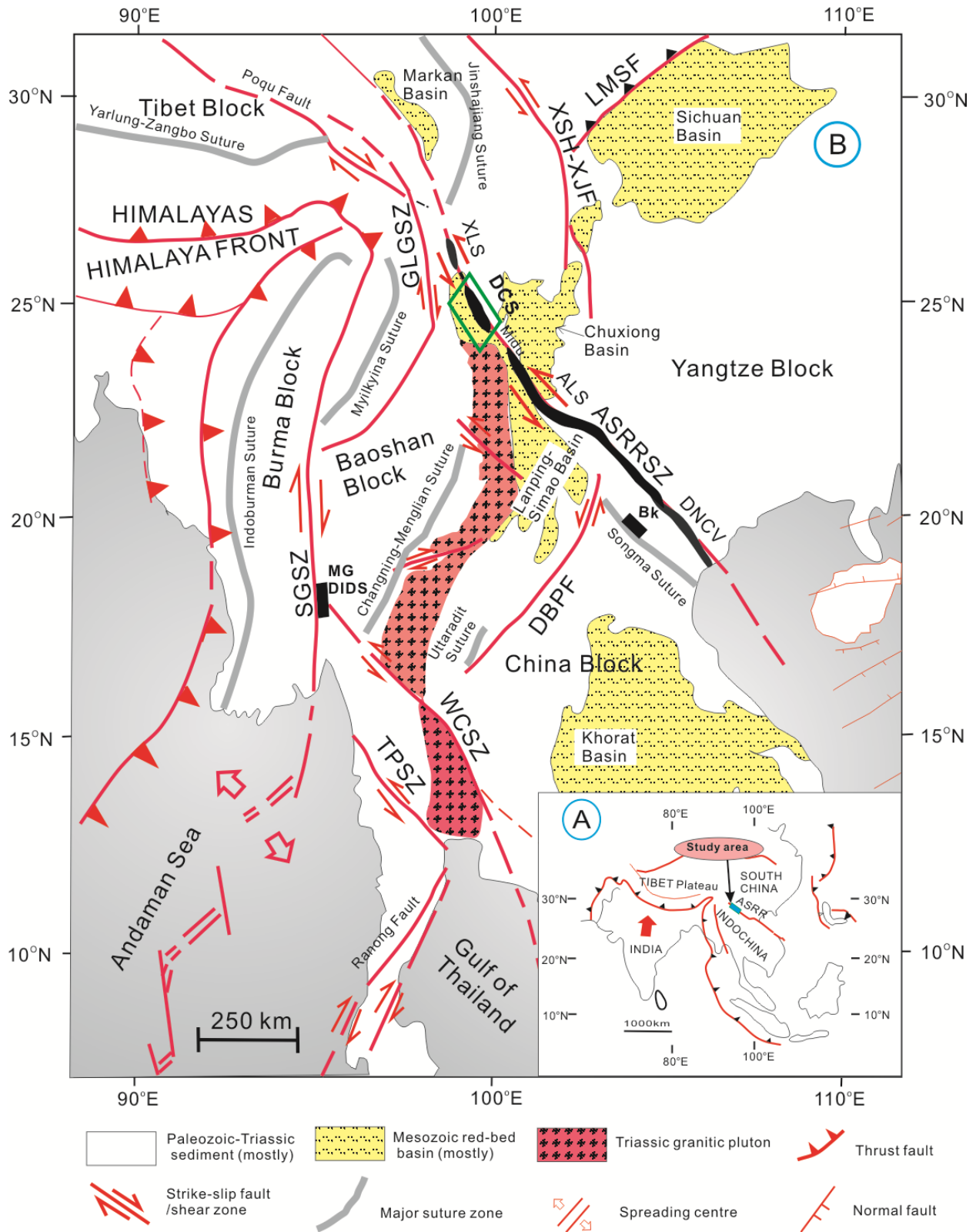


Fig. 1. 1 Tectonic sketch map of Southeast Asia (modified after Tapponnier et al. (1986), Leloup et al. (1995) and Morley (2007)). A) Geologic sketch of the tectonic extrusion of the Indochina block in relation of the Indian-Eurasian continental collision. B) Major sutures and shear zones/faults in Southeast Asia. GLGSZ = Gaoligong shear zone; SGSZ = Sagaing shear zone; TPSZ = Three Pagoda shear zone; WCSZ = Wang Chao shear zone; LMSF= Longmen Shan Fault; XSH-XJF = Xianshuihe-Xiaojiang Faults; DBPF = Dien Bien Phu

Fault; ASRRSZ = Ailao Shan-Red River shear zone; XLS = Xuelong Shan metamorphic massif; DCS = Diancang Shan metamorphic massif; ALS = Ailao Shan metamorphic massif; DNCV = Day Nui Con Voi metamorphic massif; BK=Bu Khang complex; MG=Mogok gneiss dome; DIDS= Doi-Inthanon-Doi-Suthep metamorphic complex

1.3 Metamorphic complexes and exhumation

The high-grade metamorphic complexes or metamorphic core complexes e.g. the Bu Khang dome and Day Nui Con Voi complex in Vietnam, the Mogo metamorphic complex in Burma, the Maoping metamorphic core complex in Thailand and Ailao Shan-Red River (ASRR) metamorphic complex belt in Yunnan, China (e.g. Tapponnier et al., 1990; Tran, et al., 1998; Tran et al., 1998; Jolivet, et al., 1999; Maluski, et al., 2001, Wang et al., 2000) are exposed in a fan-shaped area in Southeast Asia. Late orogenic extensional tectonics (Cenozoic) associated with ductile strike-slip faulting and syntectonic leucogranite emplacement occurred diachronously throughout the complexes. Four narrow NW-SE oriented high-grade metamorphic massifs are exposed along the ASRR shear zone. The massifs are bounded in many places by Mesozoic and Cenozoic basins, e.g. the Mesozoic Lanping Basin to the west of ASRR, the Cenozoic to recent Erhai Lake basin to the eastern of DCS massif (e.g. Bureau of Geology and Mineral Resources of Yunnan, 1983). The ASRR metamorphic belt with average elevations between 2000–3000 m is situated at the southeastern Tibetan Plateau. In the DCS massif, the average elevation of the “relict landscapes” (e.g. Clark, 2003), are generally between 4000–3500 m from south to north, the southern section is ca. 4000 m, the middle section ca. 3700 m and the northern section ca. 3500 m (Luo Pingshan). The highest mountain peak is the Malong Feng (4122 m). In the Red River region, “relict landscapes” are generally between 2000 and 2500 m, except for in the northwest Ailao Shan range, where the average elevation is close to 3000 m.

Exhumation is a generic term describing the return of once deep-seated metamorphic rocks to the Earth’s surface or responsible for unroofing of the deep-seated rocks to the surface (e.g. Ring et al., 1999). Generally, exhumation is explained by the operation of several main processes: extension and thinning, normal faulting, channel flow, strike-slip faulting and erosion (e.g. Ring et al., 1999). These processes are important for refining the cooling and exhumation history of high-grade metamorphic rocks, which is a relatively fast geological process, not only for the exhumation and disturbance within the crust that they cause, but also for their influence on the formation of orogenic topography and the contribution to production of synorogenic sediments.

However, what are the mechanisms for the exhumation of high-grade metamorphic rocks within the fan-shaped area in Southeast Asia? Several models have been put forward to explain

the exhumation process and mechanisms of these high-grade metamorphic complexes. Most early hypotheses assumed that the exhumation of the high-grade metamorphic complexes in SE Asia was related to the Cenozoic left-lateral strike-slip shearing during the extrusion of Indochina block (e.g. Tapponnier et al., 1982, 1990; Leloup et al., 2001b). For example, most authors suggested that the ASRR left-lateral strike-slip shearing was a long-lasting event accompanied by the exhumation along the shear zone, started at least ca. 35 Ma ago and lasted until ca. 17 Ma (e.g. Schärer et al., 1990, 1994; Harrison et al., 1992; Leloup et al., 1993a, 1995; Zhang and Schärer, 1999; Gilley et al., 2003). Exhumation of the shear zone rocks has been variously responded to the transtension resulting in opening of the South China Sea (e.g. Briais et al., 1993; Leloup et al., 1995; Harrison et al., 1996; Leloup et al., 2001), to the contemporaneous regional shortening and tranpression (e.g. Wang and Burchfiel, 1997; Schoenbohm et al., 2004), or to both synchronous or nonsynchronous tranpression and transtension (e.g. Leloup and Kienast, 1993; Leloup et al., 1995). Extension and exhumation in the Tibet orogen and in SE Asian orogenic belts are attributed to postorogenic collapse of overthickened crust following Inda-Asian collision (e.g. Chung et al., 1998, 2005). The intraplate extension of deformation is suggested to be also an important process during and after collision, which caused sudden uplift, regional extension, evidenced by the late Paleogene (40-30 Ma) high potassic alkaline magmatic rocks in western Yunnan and eastern Tibet (Chung et al., 1997, 1998; Wang et al., 1998). The mountains to basins are the consequence of “extensional collapse”, a process occurring after convective lithospheric thinning that, in many cases, has changed continental collision zones. These magmatic activities suggest a diachronous uplift history for the Tibetan plateau and the SE Asia (Chung et al., 1998). Recently, viscous models suggested a weak lower-crustal channel flow, which resulted in crustal thickening and long wave-length uplift of the southeastern margin of the Tibetan plateau (e.g. Clark and Royden, 2000).

The relationship between metamorphism, deformation and granitic magmatism within the metamorphic complex bears information on the processes in the well-exposed complexes, e.g. relative components of crustal thickening/thinning, the rate and nature of cooling, and the exhumation mechanisms.

1.4 Summary of the thesis

In general, the chapters of this thesis progress chronologically through the tectonic evolution of the ASRR region, with emphasis on the DCS complex. These observations documented in the thesis represent an overall outline of a comprehensive history of the development of the ASRR

shear zone and the associated high-grade metamorphic belt in the context of the major topics discussed in the preceding sections. High-temperature mylonites derived from either granitic or amphibolitic rocks constitute the main part of the shear zones. Structural, microstructural, sub-microstructural and textural analysis of sheared high-grade metamorphic rocks reveal that deformation occurred at amphibolite facies metamorphic conditions. Intense plastic deformation of feldspar, quartz and amphibole under such conditions consistently document left-lateral shearing along the ASRR shear zone. The c-axes directions of quartz are coherent with solid-state deformation at high (under amphibolite facies) to low-temperature deformation conditions. The development of complex c-axes directions in quartz from the granitic mylonites may have recorded a successive variation of deformation conditions during progressive shearing in the DCS massif. The relatively low-temperature modification of the quartz c-axis textures can be related to three main stages of exhumation and cooling of the DCS high-grade metamorphic massif. Sheared amphibolite mylonites are characterized by porphyroclastic microstructures and the ultramylonites are highly lineated with alternating amphibole- and quartzofeldspathic domains. Amphibole and plagioclase grains are intensively deformed with obvious grain size reduction, but quartz grains are recrystallized dominantly by grain growth. Initial crystallographic orientations of amphibole grains from the host rocks have strong effects on the behavior of the grains during deformation. Twinning nucleation recrystallization (TNR) is one of the most important processes that operate during dynamic recrystallization of amphibole.

We presented new evidence and further insights into the Cenozoic tectono-magmatic evolution of the ASRR shear zone. Structural and microstructural analysis of the plutonic intrusions in the DCS reveals the existence of different types of granitic plutonic intrusions spatially confined to the shear zone and temporally related to the left-lateral shearing along the ASRR shear zone in DCS massif. The combined structural and geochronological results of SHRIMP-II and LA-ICP-MS zircon U-Pb isotopic dating have revealed a succession of magmatic intrusions related to Oligocene to Miocene shearing in the DCS massif. It is suggested from the study that the left-lateral ductile shearing along the ASRR shear zone initiated after ca. 31 Ma, culminating during the main periods between ca. 27 and 24 Ma at high-temperature metamorphic conditions and at ca. 21 Ma at relative lower temperature conditions. Deep-crustal level high-grade metamorphic rocks were exposed within or immediately adjacent to the continental strike-slip fault systems in SE Asia in a fan-shaped area, which is bounded by the ASRR fault to the east and the Sagaing fault to the west. We also present new $^{40}\text{Ar}/^{39}\text{Ar}$ age data of amphibole, muscovite, biotite and K-feldspar collected from granitic rocks, amphibolitic rocks and mica schists from the Diancang Shan (DCS) metamorphic massif. These data, coupled with

U-Pb zircon ages from the pre-, syn- and post-kinematic granites and structural investigations further constrain the timing of regional deformation as well as the cooling history and exhumation processes of the high-grade metamorphic complex in DCS. The data show that there are three stages of dominant cooling and exhumation of the DCS massif. The early stage of the thermochronological evolution of the DCS massif started with an onset diachronous from >27 to 23 Ma, but subsequent homogeneous cooling and exhumation. The latter two stages are shown to be diachronous throughout the whole period of evolution from 13 to 0 Ma. At a regional scale, the tectonic exhumation of the DCS massif comprises a part of the tectono-thermal evolution and diachronous exhumation of the metamorphic complexes broadly since 36 Ma in a fan-shaped area bounded by the Red River fault zone and Sagaing fault zone in SE Asia. Extrusion-induced strike-slip shearing and rotation-resulted normal faulting played important roles in the diachronous cooling and exhumation of the metamorphic complexes in SE Asia.

This thesis integrates these observations with existing structural, geomorphic and thermochronologic data to outline the Cenozoic tectonic the thermal evolution of the ASRR shear zone and provide new insights into a complete and well-dated succession of tectonic events of the ASRR metamorphic belt. Each of the body chapters of this thesis is written for a separate publication. As such, there is some unavoidable overlap among the papers.

1.5 References

- Allen, C.R., Gillespie, A.R., Han, Y., Sieh, K.E., Zhang, B., Zhu, C., 1984. Red River and associated faults, Yunnan province, China: Quaternary geology, slip rates, and seismic hazard, *Geological Society of American Bulletin*, 95, 686–700.
- Anczkiewicz, R., Viola, G., Muntener, O., Thirlwall, M.F., Villa, I.M., Quong, N.Q., 2007. Structure and shearing conditions in the DayNuiCon Voi massif: Implications for the evolution of the Red River shear zone in northern Vietnam. *Tectonics*, 26, TC2002, doi:10.1029/2006TC001972.
- Briais, A., Patriat, P., Tapponnier, P., 1993. Updated interpretation of magnetic anomalies and seafloor spreading stages in the South China Sea: implications for the Tertiary tectonics of Southeast Asia. *Journal of Geophysical Research*, 98, 6299–6328.
- Burchfiel, B.C., Wang, E.C., 2003. Northwest-trending, middle Cenozoic, left-lateral faults in southern Yunnan, China, and their tectonic significance. *Journal of Structural Geology*, 25, 781–792.

- Bureau of Geology and Mineral Resources of Yunnan, 1983. Geological map of Yunnan, Kunming, China.
- Bureau of Geology and Mineral Resources of Yunan, 1991. Geological map of Yunnan, Kunming, China.
- Cao, S.Y., Liu, J.L., Leiss, B., 2010a. Orientation-related deformation mechanisms of naturally deformed amphibole in amphibolite mylonites from the Diancang Shan, SW Yunnan, China. *Journal of Structural Geology*, 32, 606–622.
- Cao, S.Y., Liu, J.L., Leiss, B., Neubauer, F., Genser, J., Zhao, C.Q., 2010b. Oligo-Miocene shearing along the Ailao Shan-Red River shear zone: constraints from structural analysis and zircon U-Pb geochronology of magmatic rocks in the Diancang Shan massif, SE Tibet, China. *Gondwana Research*. DOI: 10.1016/j.gr.2010.10.006.
- Cao, S.Y., Liu, J.L., Leiss, B., Vollbrecht, A., Neubauer, F., Genser, J., Zhao, C.Q., 2010c. Initiation of left-lateral deformation along the Ailao Shan-Red River shear zone: new microstructural, textural and geochronological constraints from the Diancang Shan metamorphic massif, SW Yunnan, China. *International Geology Review*. DOI: 10.1080/00206814.2010.543789.
- Chung, S.L., Lee, T.Y., Lo, C.H. Wang, P.L. Chen, C.Y., Yem, N.T., Hoa, T.T., Wu, G.Y., 1997. Intraplate extension prior to continental extrusion along the Ailao Shan Red River shear zone. *Geology*, 25, 311–314.
- Chung, S.L., Lo, C.H., Lee, T.Y, Zhang, Y. Q., Xie, Y.W., Li, X.H., Wang, K.L., Wang, P. L., 1998. Diachronous uplift of the Tibetan plateau starting from 40 Myr age. *Nature*, 394, 769–773.
- Chung, A.L., Chu, M.F., Zhang, Y.Q., Xie, Y.W., Lo, C.H., Lee, T.Y., Lan, C.Y., Zhang, X.H., Zhang, Q., Wang, Y.Z., 2005. Tibetan tectonic evolution inferred from spatial and temporal variations in post-collisional magmatism. *Earth-Science Reviews*, 68, 173–196.
- Clark, M.K, Royden, L.H., 2000. Topographic ooze: Building the eastern margin of Tibet by lower crustal flow. *Geology*, 28, 703–706.
- Clark, M.K., 2003. Late Cenozoic uplift of southeatern Tibet (PhD thesis): Massachusetts Institute of Techmology, 226p.
- England, P.C., Houseman, G.A., 1988. The mechanics of the Tibetan Plateau. *Philosophical Transactions of the Royal Society of London*, A 326, 301–320.
- England, P.C., Molnar, P., 1990. Surface uplift of rocks, and exhumation of rocks. *Geology*, 18, 1173–1177.

- Fyhn, M.B.W., Boldreel, L.O., Nielsen, L.H., 2009. Geological development of the Central and South Vietnamese margin: Implications for the establishment of the South China Sea, Indochinese escape tectonics and Cenozoic volcanism. *Tectonophysics*, 478, 184–214.
- Gilley, L.D., Harrison, T.M., Leloup, P.H., Ryerson, F.J., Lovera, O.M., Wang, J.H., 2003. Direct dating of left-lateral deformation along the Red River shear zone, China and Vietnam. *Journal of Geophysical Research*, 108, doi:10.1029/2001 JB001726.
- Harrison, T.M., Chen, W.J, Leloup, P.H., 1992. An early Miocene transition in deformation regime within the Red River fault zone, Yunnan, and its significance for Indo-Asian tectonics. *Journal of Geophysical Research*, 97(B5), 7159–7182.
- Harrison, T.M, Leloup, P.H., Ryerson, F.J., Tapponnier, P., Lacassin, R., Chen, W.J., 1996. Diachronous initiation of transtension along the Ailao Shan-Red River Shear zone, Yunnan and Vietnam. In: Harrison, T.M., Yin, A. (Eds.). *The Tectonics of Asia*. Cambridge University Press, New York, pp. 208–226.
- Houseman, G., England, P., 1993. Crustal thickening versus lateral expulsion in the Indian-Asian continental collision. *Journal of Geophysics Research*, 98, 12233–12249.
- Huang, T.K., 1960. Characteristics of the structure of China: Preliminary conclusions. *Scientica Sinica*, 9(4), 492–544.
- Huang, K., Opdykea, N.D., 1993. Paleomagnetic results from Cretaceous and Jurassic rocks of South and Southwest Yunnan: evidence for large clockwise rotations in the Indochina and Shan-Thai-Malay terranes. *Earth and Planetary Science Letters*, 117, 507–524.
- Jolivet L., Maluski H., Beyssac O., Goffé B., Lepvrier C., Phan Truong T., Nguyen Van V., 1999. Oligocene-Miocene Bu Khang extensional gneiss dome in Vietnam: Geodynamic implications. *Geology*, 27, 67–70.
- Jolivet, L., Beyssac, O., Goffé, B., Avigad, D., Lepvrier, C., Maluski, H., Thang, T.T., 2001. Oligo–Miocene midcrustal subhorizontal shear zone in Indochina, *Tectonics*, 20, 46–57.
- Leloup, P.H., Harrison, T.M., Ryerson, F.J., Chen, W.J., Li, Q., 1993. Structural, petrological and thermal evolution of a Tertiary Ductile strike-slip shear zone, Diancang Shan, Yunnan. *Journal of Geophysical Research*, 98, 6715–6743.
- Leloup, P.H., Kienast, J.R., 1993. High-temperature metamorphism in a major strike-slip shear zone: the Ailao Shan–Red River, People’s Republic of China. *Earth and Planetary Science Letters*, 118, 213–234.
- Leloup, P.H., Lacassin, R., Tapponnier, P., Schärer, U. Zhong, D.L., Liu, X.H., Zhang, L.S., Ji, S.C., Phan, T.T., 1995. The Ailao Shan-Red River shear zone (Yunnan, China), Tertiary transform boundary of Indochina. *Tectonophysics*, 251, 3–84.

- Leloup, P.H., Lacassin, R., Tapponnier, P., Harrison, T.M., 2001a. Comment on “Onset timing of left-lateral movement along the Ailao Shan–Red River shear zone: $^{40}\text{Ar}/^{39}\text{Ar}$ dating constraint from the Nam Dinh area, northeastern Vietnam” by Wang et al., 2000, *Journal of Asian Earth Sciences*, 18, 281–292. *Journal of Asian Earth Sciences*, 20, 95–99.
- Leloup, P.H., Arnaud, N., Lacassin, R., Kienast, J.R., Harrison, T.M., Phan Trong, T.T., Replumaz, A., Tapponnier, P., 2001b. New constraints on the structure, thermochronology, and timing of the Ailao Shan–Red River shear zone, SE Asia, *Journal of Geophysical Research*, 106, 6683–6732.
- Liu, J.L., Song, Z.J., Cao, S. Y., Zhai, Y.F., Wang A.J., Gao, L., Xiu, Q.Y., Cao, D.H., 2006. The dynamic setting and processes of tectonic and magmatic evolution of the oblique collision zone between Indian and Eurasian plates: exemplified by the tectonic evolution of the Three River region, eastern Tibet. *Acta Petrologica Sinica*, 22, 775–786.
- Liu, J.L., Cao, S.Y., Zhai, Y.F., Song, Z.J. Wang, A.J., Xiu, Q.Y., Gao, L., Guan, Y., 2007. Rotation of Crustal Blocks as an Explanation of Oligo–Miocene Extension in Southeastern Tibet–Evidenced by the Diancangshan and Nearby Metamorphic Core Complexes. *Earth Science Frontiers*, 14, 40–48.
- Maluski, H., Lepvrier, C., Jolivet, L., Carter, A., Roques, D., Beyssac, O., Tang, T.T., Thang, N.D., Avigad, D., 2001. Ar–Ar and fission-track ages in the Song massif: Early Triassic and Cenozoic tectonics in northern Vietnam. *Journal of Asian Earth Science*, 19, 233–248.
- Miller, R.B, Paterson, S.R., 1994. The transition from magmatic to high-temperature solid-state deformation: implications from the Mount Stuart batholiths, Washington. *Journal of Structural Geology*, 16(6), 853–865.
- Molnar, P. and Tapponnier, P., 1975. Cenozoic tectonics of Asia: Effects of a continental collision. *Science*, 189, 419–426.
- Morley, C.K., 2002. A tectonic model for the Tertiary evolution of strike-slip faults and rift basins in SE Asia. *Tectonophysics*, 347, 189–215
- Passchier, C.W., Trouw, R.A.J., 2005. *Microtectonics*. P56. Springer-Verlag, Berlin.
- Paterson, S.R., Vernon, R.H., Tobisch, O.T., 1989. A review of criteria for the identification of magmatic and tectonic foliations in granitoids. *Journal of Structural Geology*, 11, 349–363.
- Paterson, S.R., Fowler, T.K., Schmidt, K.L., Yoshinobu, A.S., Yuan, E.S., Miller, R.B., 1998. Interpreting magmatic fabric patterns in plutons. *Lithos*, 44, 53–82.
- Peltzer, G., Tapponnier, P., 1988. Formation and evolution of strike-slip faults, rifts, and basins during the India–Asia collision: an experimental approach. *Journal of Geophysical Research*, 93(15), 85–117.

- Peltzer, G., Saucier, F., 1996. Formation and evolution of strike-slip faults, rifts and basins during India-Asia collision: An experimental approach. *Journal of Geophysical Research*, 93, 15085–15117.
- Ring, U., Brandon, M.T., 1999. Ductile deformation and mass loss in the Franciscan subduction complex: implications for exhumation processes in accretionary wedges. In: Ring, U., Brandon, M.T., Lister, G.S., Willett, S.D. (EDS) *Exhumation processes: Normal faulting, ductile flow and erosion*. Geological Society, London, Special Publications, 154, 55–86.
- Rosenberg, C.L., 2004. Shear zones and magma ascent: A model based on a review of the Tertiary magmatism in the Alps. *Tectonics*, 23(3), 1–21.
- Sassier, C., Leloup, P.H., Rubatto, D., Galland, O., Yue, Y., Lin, D., 2009. Direct measurement of strain rates in ductile shear zones: A new method based on syntectonic dikes. *Journal of Geophysical Research-Solid Earth*, 114, 1–32.
- Sato, K., Liu, Y.Y., Zhu, Z.C., Yang, Z.Y., Otofujii, Y.I., 1999. Paleomagnetic study of middle Cretaceous rocks from Yunlong, western Yunnan, China: evidence of southward displacement of Indochina. *Earth and Planetary Science Letters*, 165, 1–15.
- Schärer, U., Tapponnier, P., Lacassin, R., Leloup, P.H., Dalai, Z., Ji, S.C., 1990. Intraplate tectonics in Asia: a precise age for large-scale Miocene movement along the Ailao Shan-Red River shear zone, China. *Earth and Planetary Science Letters*, 97, 65–77.
- Schärer, U., Zhang, L.S., Tapponnier, P., 1994. Duration of strike-slip movements in large shear zones: The Red River belt, China. *Earth and Planetary Science Letters*, 126, 379–397.
- Schoenbohm, L.M., Whipple, K.X., Burchfiel, B.C., Chen, L., 2004. Geomorphic constraints on surface uplift, exhumation and plateau growth in the Red River region, Yunnan Province, China, *Geological Society of American Bulletin*, 116(7), 895–909.
- Searle, M., 2006. Role of the Red River Shear zone, Yunnan and Vietnam, in the continental extrusion of SE Asia. *Journal of the Geological Society, London*, 163, 1025–1036.
- Sun, Z., Zhong, Z.H., Zhou, D., Qiu, X.L., Wu, S.M., 2003. Deformation mechanism of Red River fault zone during Cenozoic and experimental evidences related to Yinggehai basin formation. *Journal of Tropical Oceanography*, 22(2), 1–9.
- Tanaka, K., Mu C, Sato, K., Takemoto, K., Miura, D., Liu, Y., Zaman, H., Yang, Z., Yokoyama, M., Iwamoto, H., Uno, K., Otofujii, Y., 2008. Tectonic deformation around the eastern Himalayan syntaxis: constraints from the Cretaceous palaeomagnetic data of the Shan-Thai Block. *Geophysical Journal International*, 175, 713–728.
- Tapponnier, P., Molnar, P., 1977. Active faulting and tectonics of China, *Journal of Geophysical Research*, 82, 2905–2930.

- Tapponnier, P., Peltzer, G., Armijo, R., Le Dain, A.Y., Cobbold, P., 1982. Propagating extrusion tectonic in Asia: new insights from simple experiments with plasticine. *Geology*, 10, 611–616.
- Tapponnier, P., Peltzer, G., Armijo, R., 1986. On the mechanics of the collision between India and Asia. In: Coward, M.P., Ries, A.C. (Eds.), *Collision Tectonics*. Geological Society of London Special Publication, 19, 115–157.
- Tapponnier, P., Lacassin, R., Leloup, P.H., Schärer, U., Zhong, D.L., Liu, X.H., Ji, S.C., Zhang, L.S., Zhong, J.Y., 1990. The Ailao Shan/Red River metamorphic belt: Tertiary left-lateral shear between Indochina and South China. *Nature*, 343, 431–437.
- Tran, N.N., Mitsuhiro, T., Tetsumaru, I., 1998. P–T–t paths and post-metamorphic exhumation of the Day Nui Con Voi shear zone in Vietnam. *Tectonophysics*, 290, 299–318.
- Wang, E., Burchfiel, B.C., 1997. Interpretation of Cenozoic tectonics in the right-lateral accommodation zone between the Ailao Shan shear zone and the eastern Himalayan syntaxis. *International Geology Review*, 39, 191–219.
- Wang, P.L., Lan, C.Y., Yem, N.T., Lo, C.H., Lee, T.Y., Chung, S.L., 1998. Thermochronological evidence for the movement of the Ailao Shan-Red River shear zone: a perspective from Vietnam. *Geology*, 26, 887–890.
- Wang, P.L., Lo, C.H., Chung, S.L., Lee, T.Y., Lan, C.Y., Thang, T.V., 2000. Onset timing of left-lateral movement along the Ailao Shan-Red River shear zone: $^{40}\text{Ar}/^{39}\text{Ar}$ dating constraint from the Nam Dinh area, northeastern Vietnam. *Journal of Asian Earth Science*, 18, 281–292.
- Yang, Z., Besse, J., 1993. Paleomagnetic study of Permian and Mesozoic sedimentary rocks from northern Thailand supports the extrusion model for Indochina. *Earth and Planetary Science Letters*, 117, 525–552.
- Yang, Z., Besse, J., Suteetorn, V., Bassoulet, J.P., Fontaine, H., Buffetaut, E., 1995. Lower-Middle Jurassic paleomagnetic data from the Mae Sot area (Thailand), Paleogeographic evolution and deformation history of Southeastern Asia. *Earth and Planetary Science Letters*, 136, 325–341.
- Yeh, M.W., Lee, T.Y., Lo, C.H., Chung, S.L., Lan, C.Y., Anh, T.T., 2008. Structural evolution of the Day Nui Con Voi metamorphic complex: Implications on the development of the Red River Shear Zone, Northern Vietnam. *Journal of Structural Geology*, 30(12), 1540–1553.
- Zhang, L.S., Schärer, U., 1999. Age and origin of magmatism along the Cenozoic Red River shear belt. *China. Contributions to Mineralogy and Petrology*, 134, 67–85.

- Zhang, X., Wang, Y.H., 2009. Crustal and upper mantle velocity structure in Yunnan, Southwest China. *Tectonophysics*, 471, 171-185.
- Zhong, D.L., Tapponnier, P., Wu, H.W., Zhang, L.S., Ji, S.C., Zhong, J.Y., Liu, X.H., Schaerer, U., Lacassiu, R., Leloup, P., 1990. Large-Scale Strike-Slip-Fault the Major Structure of Intracontinental Deformation after Collision. *Chinese Science Bulletin*, 35(4), 304–309.

This chapter has been published as: Shuyun Cao, Junlai Liu, Bernd Leiss, 2010. Orientation-related deformation mechanisms of naturally deformed amphibole in amphibolite mylonites from the Diancang Shan, SW Yunnan, China. Journal of Structural Geology 32, 606-622.

2 Orientation-related deformation mechanisms of naturally deformed amphibole in amphibolite mylonites from the Diancang Shan, SW Yunnan, China

Abstract

Sheared amphibolite rocks from Diancang Shan high-grade metamorphic complex along the Ailao Shan-Red River shear zone, southwestern Yunnan, China, show typical mylonitic microstructures. The mylonites are characterized by porphyroclastic microstructures and the ultramylonites are highly lineated with alternating amphibole- and quartzofeldspathic domains. Microstructural analysis and P/T estimation suggest that the amphibole grains in the mylonitic rocks are deformed and dynamically recrystallized at amphibolite facies.

In the mylonitic amphibolites, there are two types of amphibole porphyroclasts, i.e. type I “hard” and type II “soft” porphyroclasts. They have their [001] crystallographic orientations subnormal and subparallel to the stretching lineation of the rocks, respectively. The two types of porphyroclasts show distinct deformation microstructures and sub-microstructures formed by various deformation mechanisms, which contribute in different ways to the generation of the fine-grained matrix. Shape preferred orientation analysis, misorientation analysis of the two types of porphyroclasts and new fine grains around them further prove the generation of the fine grains in matrix from the type II porphyroclasts. The type I “hard” porphyroclasts are deformed mainly by mechanical rotation, work hardening and intragranular microfracturing. In contrast, the deformation of the type II “soft” porphyroclasts is mainly attributed to crystalline plasticity, i.e. twinning, dislocation creep and dynamic recrystallization. During the deformation of the type II porphyroclasts, the (100) [001] slip system plays a dominant role during deformation and grain size reduction of amphibole. Twinning along the active (100) slip system, in combination with dislocation creep (gliding and climbing) governs the nucleation of subgrains and formation of dynamically recrystallized fine grains, a process here named *Twinning Nucleation Recrystallization*.

2.1 Introduction

Amphibole is one of the most important components in middle to lower crustal rocks. The deformation behavior of amphibole provides important clues to the understanding of mechanical, rheological and physical properties of the crust (e.g. Drury and Ural, 1990; Stünitz, 1993; Barruol and Kern, 1996; Berger and Stünitz, 1996; De Meer et al., 2002; Kitamura, 2006; Díaz Azpiroz et al., 2007; Tatham et al., 2008). Amphibole typically shows brittle to ductile behavior under a wide range of deformation P-T conditions, as revealed by studies on naturally and experimentally deformed amphiboles (e.g. Rooney et al., 1970, 1975; Biermann, 1981; Hacker and Christie, 1990; Berger and Stünitz, 1996; Díaz Azpiroz et al., 2007).

Early studies on deformation of amphibole have focused on slip systems and deformation twinning in experimentally and naturally deformed amphibole crystals. The main slip systems determined in amphibole are (100) [001], (010) [001] and (hk0) [001] (e.g. Rooney et al., 1970, 1975; Dollinger and Blacic, 1975; Skrotzki, 1992; Jiang and Skrotzki, 1996). Experimental studies reveal that deformation twins are commonly (101) and rarely (100) (e.g. Rooney et al., 1970, 1975; Buck, 1970; Hacker and Christie, 1990). In naturally deformed amphibole, however, (100) twinning (e.g. Dollinger and Blacic, 1975; Biermann, 1981; Biermann and Van Roermund, 1983; Kenkmann, 2000; Imon et al., 2002) predominates over (101) and other twinning systems (e.g. Morrison-Smith, 1976; Allison and La Tour, 1977; Cumbest et al., 1989; Hacker and Christie, 1990). Observations on naturally deformed amphiboles have also revealed variations of deformation mechanisms at different P-T conditions (e.g. Allison and La Tour, 1977; Nyman et al., 1992; Babai and La Tour, 1994; Leiss et al., 2002; Imon et al., 2002, 2004; Díaz Azpiroz et al., 2007). It is generally accepted that amphibole is deformed by brittle processes and concomitant breakdown reactions under greenschist facies (e.g. Brodie and Rutter, 1985) or even at amphibolite facies (Lafrance and Vernon, 1993), e.g. by microfracturing (e.g. along (110) cleavage plane, Allison and La Tour, 1977; Nyman et al., 1992) or mass transfer (Brodie and Rutter, 1985; Stünitz, 1993; Shelley, 1994; Imon et al., 2002, 2004). Dominance of dislocation activity, subgrain formation and dynamic recrystallization may occur at higher temperature and pressure conditions (Biermann and Van Roermund, 1983; Cumbest et al., 1989; Skrotzki, 1992), although it is inferred that amphibole generally does not deform significantly by intracrystalline plasticity below 650-700 °C in the presence of fluid (Berger and Stünitz, 1996).

In polyphases rocks, mineral phases (e.g. plagioclase) mostly behave in different ways during deformation. It is found that at approximately 700 °C and up to 900 MPa deformation of amphibole grains in monophase layers is characterized by crystal plasticity, but in the two-phase mixtures by granular flow (Kruse and Stünitz, 1999). Therefore, the formation of deformation

microstructures and variation of deformation mechanisms of the polyphase rocks may be attributed to the leading role of chemical disequilibrium. Detailed studies on amphibole deformation at low-pressure conditions suggest that dissolution-precipitation creep and cataclastic flow, rigid body rotation within a weaker plagioclase matrix, and subgrain rotation recrystallization may explain the deformation and dynamic recrystallization at different conditions (Díaz Azpiroz et al., 2007). The texture types of amphibole and plagioclase in the polyphase rocks mostly result from varying deformation modes of the different mineral phases (Leiss et al., 2002).

From the above discussions, there still exist significant disagreements on the deformation behavior of amphibole under different conditions. It appears that the high temperature deformation of amphibole is a complex process and the dominant deformation mechanisms are still unclear. The present study on amphibolite mylonites collected from Diancang Shan, SW Yunnan, China, provides new results for and constraints on the deformation and dynamic recrystallization of amphibole at amphibolite facies conditions, by applying OM (Optical Microscope), TEM (transmission electron microscope), EPMA (electron probe microanalysis) and EBSD (electron backscattered diffraction) techniques. Microstructural, submicrostructural and LPO (lattice preferred orientation) texture studies reveal that the amphibolite mylonites and ultramylonites developed from amphibolite rocks by progressive shearing. Different mineral phases in the rocks show distinct deformation characteristics. Amphibole and plagioclase grains are intensely deformed with obvious grain size reduction, but quartz grains are recrystallized dominantly by grain growth. Initial crystallographic orientations of amphibole grains from the host rocks have strong effects on the behavior of the grains during deformation. Most fine grains are generated by combined twinning and dislocation creep of parent amphibole grains with specific preferred crystallographic and shape orientations. Twinning along (100), in combination with dislocation creep (gliding and climbing) governs the nucleation of subgrains and formation of dynamically recrystallized fine amphibole grains.

2.2 Geological setting and structural analysis

Large scale left-lateral strike-slip shearing along the Ailao Shan-Red River shear zone in SW China plays important roles in accommodating the southeastward extrusion of the Indochina block during Indian-Eurasian collision (e.g. Zhong et al., 1990; Lacassin et al., 1993; Leloup et al., 1993, 1995; Burchfiel and Wang, 2003; Schärer et al., 1994). Over 500 km of southeastward displacement of the Indochina block relative to the Yangtze-South China block occurred along

the shear zone (e.g. Leloup et al., 2001; Liu et al., 2006; Morley, 2007) (2.1a).

Several blocks of middle to lower crustal metamorphic rocks are exposed along the Ailao Shan-Red River shear zone. They appear as lens-shaped bodies and are fault-bounded from non-metamorphic Paleozoic to Cenozoic rocks to the east and weakly deformed Paleozoic and Mesozoic meta-sedimentary rocks to the west. The Diancang Shan metamorphic complex is a typical such block, which is composed of three structural units, i.e. the central high strain shear zone, the western low-grade metamorphic volcanic-sedimentary sequence in the Lanping basin, and the eastern superimposed retrograde metamorphic belt (Liu et al., 2008) (2.1b).

Proterozoic metamorphic rocks, including amphibolites, amphibole-plagioclase gneisses, sillimanite schists and marbles (e.g. Sha, 1998; Sha et al., 2002), and plutonic intrusions of various ages are highly mylonitized during left-lateral shearing and are widely exposed in the central high strain shear zone. High temperature (amphibolites facies) assemblages preserved in these mylonites include: almandine, staurolite, kyanite and sillimanite in schists; tremolite, diopside, olivine, calcite and dolomite in marbles; and amphibole, garnet and plagioclase in amphibolites. Mesoscopic structures for high temperature shearing prevail in the central high strain shear zone. Complex and sheath folds formed by ductile flow are frequently observed in sheared schists and granitic mylonites. A remarkable feature of the mylonites (both metamorphic and granitic-derived) is their extremely strong stretching lineation fabrics, in contrast to poorly developed mylonitic foliation, thus forming L and L-S tectonites. When present, mylonitic foliation strikes NNW-SSE. Stretching lineation is subhorizontal or plunge gently either to the NNW or to the SSE (2.1c).

Retrograde metamorphism overprinted the high temperature metamorphic belt along the eastern flank of the Diancang Shan range and is possibly related to exhumation of the Diancang Shan high-grade metamorphic complex in a later event (or metamorphic core complex, Liu et al., 2007). Early high temperature mylonites are sheared at greenschist facies in this zone, resulting in low temperature mineral assemblages and fabrics in chloritic mylonites. Mafic minerals (e.g. amphibole and biotite) are chloritized, quartz grains are deformed by crystal plasticity, and plagioclase grains deform mainly by fracturing, forming domino and similar microstructures. Some granitic plutons are sheared into L-S tectonites instead of L and L-S tectonites. S-C fabrics are formed with S-planes defined by flattened grain aggregates of quartz and plagioclase and C-plane by chlorite grains. Striae, mostly defined by growth of fibrous chlorite grains, are widely distributed in the easternmost part of this belt. On the other hand,

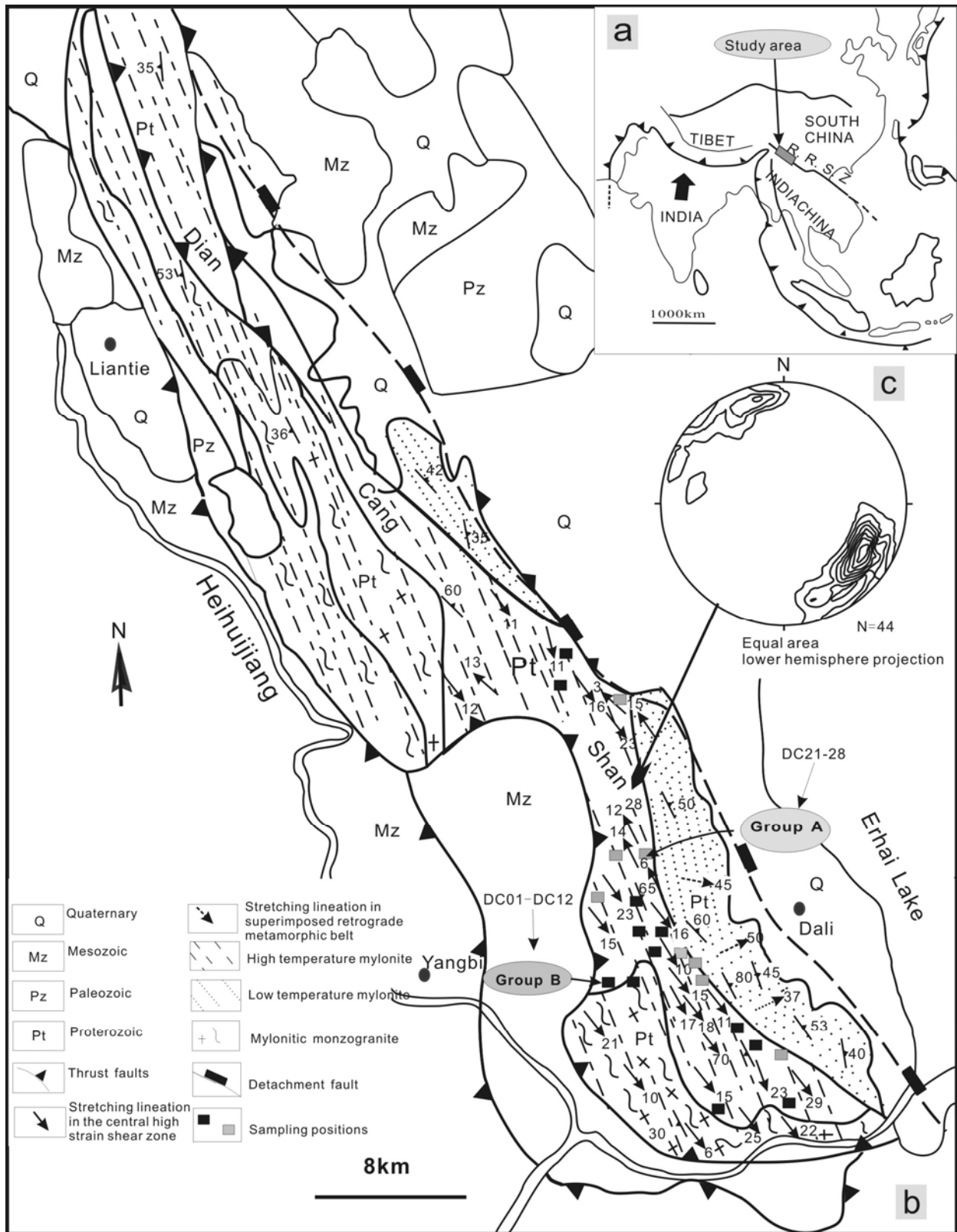


Fig. 2.1 Tectonic setting and structural outline of Diancang Shan area. a. regional tectonic framework of Southeast Asia. b. simplified geological map of Diancang Shan area. Group A (grey squares) comprises amphibolite mylonites and Group B (black squares) amphibolite ultramylonites. c. equal area projection of stretching lineation from high temperature mylonites. Lower hemisphere projection. R.R.S.Z= Ailao Shan-Red River Shear Zone.

mylonitic foliation from the superimposed retrograde metamorphic belt has similar attitudes to those from the central high strain shear zone, striking NW-SE and dipping to the E, but the stretching lineation shows high plunge angle angles (70°-90°).

U-Pb dating of monazite and xenotime from synkinematic granite dikes in the high temperature mylonites and ⁴⁰Ar-³⁹Ar dating of amphibole, biotite and muscovite suggest ductile shearing along the Ailao Shan-Red River shear zone before 22-24 Ma and cooling during exhumation of the high-grade rocks between 23 Ma and 7 Ma (e.g. Schärer et al., 1994). It is generally accepted that Cenozoic strike-slip shearing along the Ailao Shan-Red River shear zone is the main process for the occurrence of structural and microstructural assemblages in high-grade metamorphic rocks. Exhumation of the high-grade metamorphic rocks is possibly due to detachment faulting along the eastern flank of the Diancang Shan in late Cenozoic (Liu et al., 2007).

2.3 Methods of fabric analyses

Optical microstructural observations and measurements were primarily conducted on thin sections of amphibole mylonite and ultramylonite samples. All samples were cut parallel to the kinematic XZ section, i.e. parallel to the stretching lineation and, where visible, normal to the weak foliation. Some samples were also cut parallel to the YZ section (normal to the stretching lineation and the weak foliation). XZ sections of selected samples were used to accomplish EBSD texture analyses. LPO data of amphibole were acquired with a Hitachi S-3400N-II scanning electron microscope with a tungsten filament mounted with an EBSD detector. An acceleration voltage of 20 kV applied with a beam current of 3 nA and a working distance of 20 mm resulted in 0.1 µm of spatial resolution and 0.5° of angular resolution. EBSP (electron backscatter pattern) analyses were completed using the HKL CHANNEL5 software package. LPO measurements were done using point scan and mapping modes. Point scan mode was applied to acquire EBSP data from amphibole porphyroclasts and fine grains around them in amphibole mylonites, and mapping mode with automated beam scanning was used to work on fine amphibole grains in ultramylonite

TEM (Hitachi H-8100) observations at 20-30 kV voltages were applied to reveal the sub-microstructural features, including dislocation and twin sub-microstructures of the mylonitic rocks. EDS (Energy Dispersive Spectrometry, using an Oxford INCA Energy 350) attached on both TEM and SEM is the major technique identifying mineral phases and determining variation of mineral components during TEM/SEM/EBSD analysis. Quantitative amphibole mineral

chemistry analysis was performed by EDS on a Shimadzu EPMA-1600 electron microprobe. The probe current was 3 nA and the accelerating voltage was 15 kV. The analyses were performed on polished, carbon-coated thin sections.

2.4 Microstructural and submicrostructural observations

2.4.1 Amphibolite mylonites and two types of porphyroclasts-optical microstructures

Two groups of samples of amphibolite mylonite and ultramylonite from the central high strain shear zone in the Diancang Shan range (Figs. 2.1b and 2.2) are observed, which show different characteristics. Mylonite samples (Nos. DC21-28) (Fig. 2.2a) have about 15-20% relic porphyroclasts of amphiboles (Fig. 2.3a-e). As the most fundamental structural characteristics of the amphibolite mylonites, the strong stretching lineation and weak foliation (i.e. L or L > S fabrics) lead to alternating quartzofeldspathic and amphibole domains in sections are parallel to the L fabrics. Coarse amphibole grains mostly occur in amphibole-rich domains, while fine amphibole grains occur in quartzofeldspathic domains. Elongated coarse amphibole grains, laminated biotite grains, lens-shaped plagioclase and quartz aggregates constitute the foliation and lineation. The porphyroclasts embedded in a fine-grained matrix are the most prominent characteristics of the amphibolite mylonites, although they constitute only a minor portion of the sample volume in both the mylonites to ultramylonites. Ultramylonite samples (Nos. DC01-12) (Fig. 2.2b) are characterized by very few (<5%) relic amphibole porphyroclasts. Amphibole, plagioclase and biotite grains occur as extremely fine grains. Quartz forms ribbons with a thickness 160-200 μm (Fig. 2.3f). They are homogeneous in microstructures and grain size distribution throughout the samples.

There are two distinct types of amphibole porphyroclasts (type I “hard” and type II “soft”) in the mylonitic amphibolites. They are different in their [001]-axes orientations relative to the stretching lineation:

1) Type I porphyroclasts have their crystallographic [001]-axes orientation lying in the mylonitic foliation and normal or subnormal to the stretching lineation (Fig. 2.3b). They are generally rounded or subrounded in shape in thin sections parallel to XZ and typically show (110) and (110) cleavage planes forming angles of 56° . Some grains show cleavage pairs with smaller angles suggesting [001]-axes are not always exactly perpendicular to the lineation. Type I porphyroclasts behave as “hard” porphyroclasts (e.g. Burg et al., 1986). They are fractured or have tangled dislocations (as shown in the next section), with rare evidence for intragranular

plastic deformation. Such grains often have sharp boundaries and generally do not show any transition into fine grains in the matrix. Short irregular and randomly oriented intragranular fractures are only observed in some of the type I porphyroclasts. In the adjacent matrix grains, e.g. amphibole, quartz or feldspar, there is no indication of deformation related to the fracturing. Some of the fractures are cleavage fractures formed along cleavage planes, but others are not related to the crystallographic features. The former generally have long extensions or are through-going features in the entire amphibole grains. The latter are, however, generally short open cracks. They often disappear in the grains and are sometimes offset by the cleavage fractures (Fig. 2.3b).

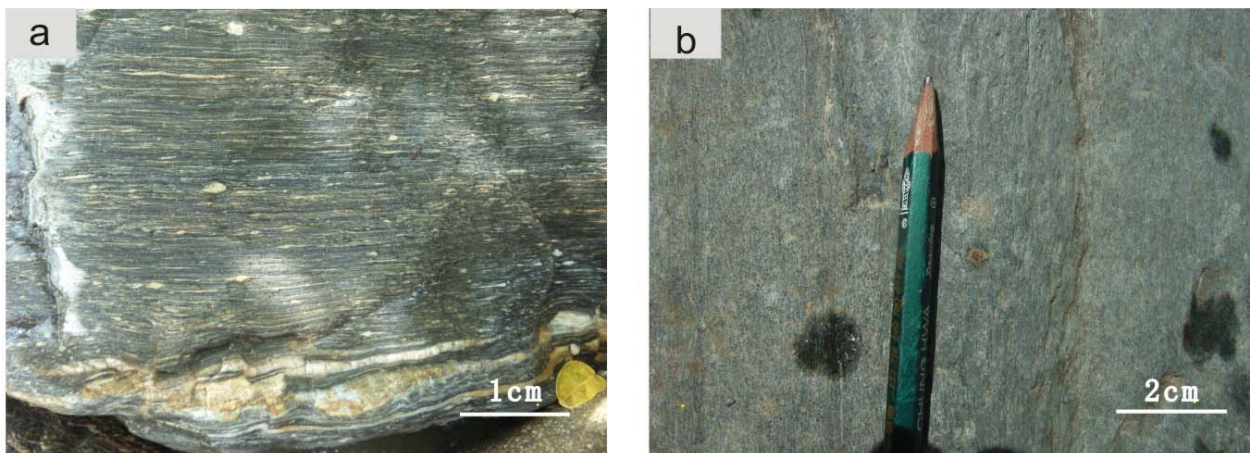


Fig. 2.2 Mesoscopic structures of ductile sheared amphibolites from the central high strain shear zone. a. strongly developed lineation of an amphibolite mylonite (L-fabric); b. amphibolite ultramylonite with strong stretching lineation.

2) Type II porphyroclasts have their [001]-axes orientation parallel or sub-parallel to the stretching lineation (Fig. 2.3c and d). They are either augen, lens or fish-shaped. A group of parallel cleavages along (110) orientation are common in the porphyroclasts. σ and ϕ tails are possibly formed in porphyroclasts in a stable position during general flow and δ tails are possibly around permanently rotated porphyroclasts (Passchier and Trouw, 2005; Fig. 2.3d). Abundant evidences for crystal plastic deformation are observed in the porphyroclasts. Undulatory or inhomogeneous extinction occurs in most of the porphyroclasts, more abundant in the cores than in the marginal zones. Microtwins are not easily detectable optically due to their micron scale in width. With ion-thinned ultrathin sections, twins are sometimes observed. They show diffuse characteristics and are thin lamellae parallel to the [001]-axes of the host grains. Their boundaries are straight and sharp. Core-mantle structures are formed due to the

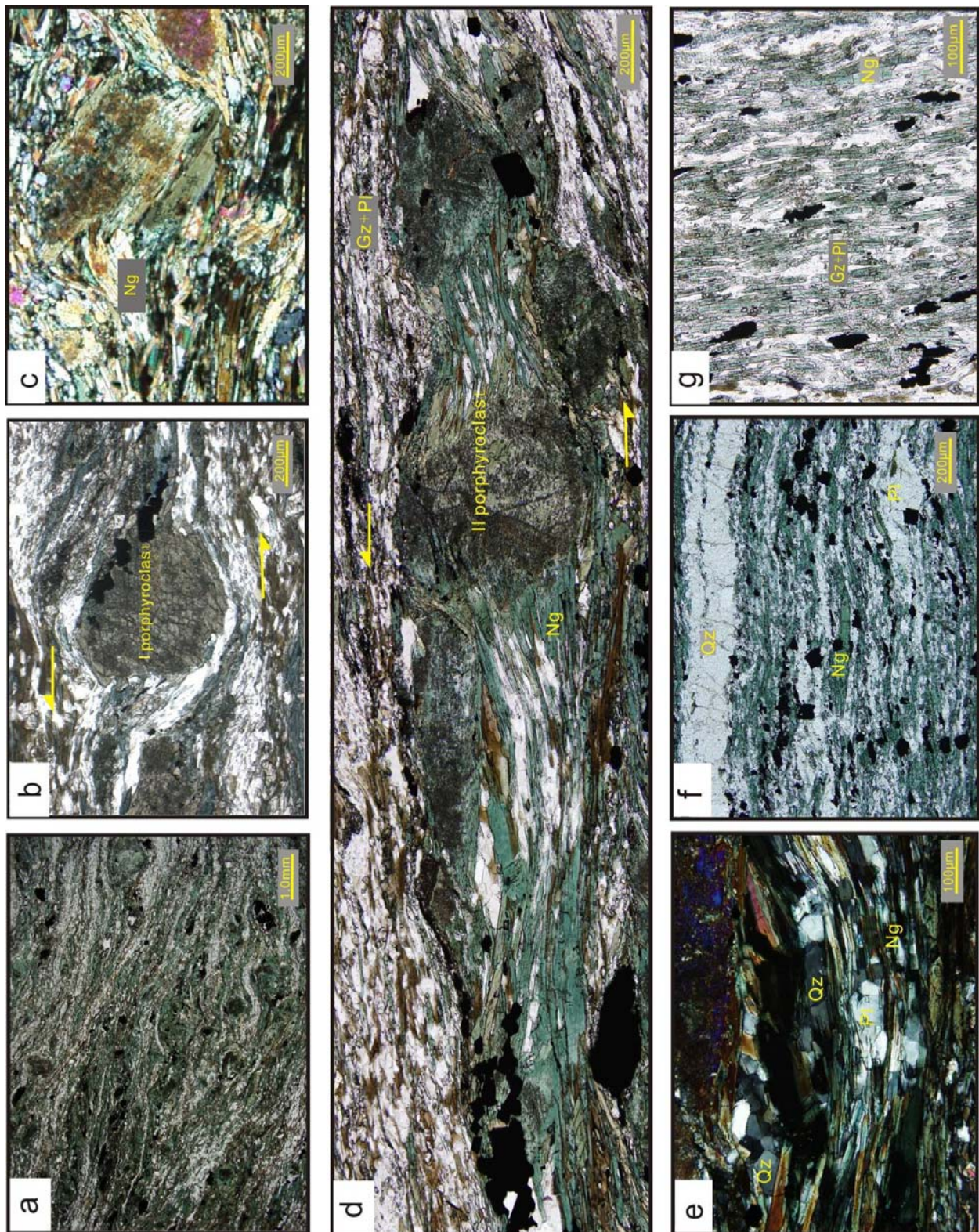


Fig. 2.3 Microstructures in amphibolite mylonites and ultramylonites. a. laminated and banded structures by alternating quartzofeldspathic and amphibole domains; b. type I porphyroclasts of amphibole with [001]-axes normal to the stretching lineation; c. new fine grains formed by subgrains being separated from the host grain of amphibole; d. typical type II porphyroclasts of amphibole with [001]-axes parallel to shearing direction; e. triple junctions of quartz grains, and quartz and plagioclase grains are in lens-shaped or banded distribution; f. and g. new fine grains of amphibole in ultramylonite have strong shape preferred dimensional and

crystallographic orientations parallel to stretching lineation. Ng- new fine grains; QZ- quartz grains; Pl- plagioclase grains. Arrows- stretching lineation or shearing direction. a, b, c and e- cross-polarization; d, f and g- parallel polarization.

occurrence of subgrains with different shapes. Subgrains surrounding type II porphyroclasts are mostly equant in shape. Occasionally lamellar subgrains are in the transition between deformed cores and fine grains in the matrix. An obvious difference of the type II from the type I porphyroclasts is the gradual transition from the type II porphyroclasts into fine grains in the matrix. On both sides of the porphyroclasts, some fine grains are connected with them (Fig. 2.3c and d). The observation suggests that type II porphyroclasts are easily deformed by crystalline plasticity. They behave as “soft” porphyroclasts during shearing and contribute to the generation of fine grains in the matrix.

The main volume (more than 75%) of amphibolite mylonites consists of fine-grained matrix. Fine grains surrounding type I porphyroclasts are randomly oriented and do not show obvious shape and crystallographic preferred orientations. Some fine grains, however, have transitional relations with type II porphyroclast grains (e.g. fine grains are obviously distributed between ϕ -shaped grains, Fig. 2.3d). They are generally aligned in the [001]-axes direction of the porphyroclasts. Fine amphibole grains in the mylonites are characterized by the following features (Fig. 2.3f and g): a) they are generally single crystals; b) grains are acicular or columnar-shaped; c) they are homogeneously distributed and have strong shape preferred orientations, forming L-fabrics of the mylonites; d) normal to the long axes of the grains there is a group of intragranular fractures; e) fine grains in the ultramylonites rarely show obvious evidences of intragranular plastic deformation, although undulatory extinction can be occasionally observed.

2.4.2 Optical grain size and aspect ratio analysis

The brief microfabric description about the grain sizes and shape preferred orientations (SPOs) is presented in Table 2.1 and Fig. 2.4. The long axis (A) and short axes (B) of the two types of porphyroclasts and fine grains in matrix were measured on XZ sections separately. The grain sizes $[(A+B)/2]$ and aspect ratios ($R=A/B$) are calculated using the measurements. The detailed procedure for measurement and calculation is after by Díaz Aspiroz and Fernández (2003).

The type I porphyroclasts have grain sizes ranging between 200 μm and 500 μm , while the type II porphyroclasts have a wider range of grain size variation (e.g. from 200 μm to 1.5 mm) than the type I porphyroclasts. The fine-grained amphiboles of the matrix are mostly ranging

from 100 to 200 μm (Table 2.1). The aspect ratios of grains are closely related to the types of grains, varying from 1 to 2 for type I porphyroclasts, 2 to 5 for type II porphyroclasts and 5 to 20 for fine grains in the matrix, respectively. Two important factors may contribute to the variations in grain sizes and aspect ratios of the two types of porphyroclasts. Initial differences in their crystallographic orientations are of the first order. Mechanical rotation of the type I porphyroclasts resulted in the equant shapes in sections normal to [001]-axis. Progressive shearing of type II porphyroclasts may have contributed to the elongated grains with a large grain sizes and high aspect ratios. The small grain sizes and high aspect ratios of the fine grains in the matrix, however, are possibly related to the mechanisms of generation of the fine grains, as discussed in the following context.

The SPOs of amphibole grains are shown by their long-axis orientations with respect to the foliation direction (ϕ), and aspect ratios (R). The long axis orientation of each amphibole grain was measured as the angle (ϕ , anticlockwise positive) from the foliation trace in the XZ section to the direction of the long axis (Fig. 2.4). In the R- ϕ diagram, different types of grains cluster in different ranges. The ϕ values of the type II porphyroclasts are mostly in the range from -30 to $+45^\circ$, and those of the fine-grained grains cluster between -30 and $+30^\circ$. They have some overlaps, but the latter are more concentrated around the $\phi=0^\circ$ axis. The similarity of the R- ϕ values of the type II porphyroclasts and fine grains in the matrix are interpreted by the deviation of the fine grains from the porphyroclasts. Their difference may be attributed to progressive rotation of the new fine grains towards a specific orientation, e.g. the direction of the kinematic lineation after separation from their parent grains. The distribution pattern of the type I porphyroclasts is, however, more randomly in the range from 30 to 90° (minus or plus). Such a random variation is possibly due to the effect of mechanical rotation, instead of plastic deformation, of the type I porphyroclasts.

Table 2. 1 grain size and aspect ratio data from mylonitic and ultramylonitic amphibolite samples

Type	Type I porphyroclasts	Type II porphyroclasts	Fin-grained amphibole
Amphibole grain-size	200-500 μm	200 μm -1.5mm	100-200 μm
Amphibole aspect ratio	1-2	2-5	5-20

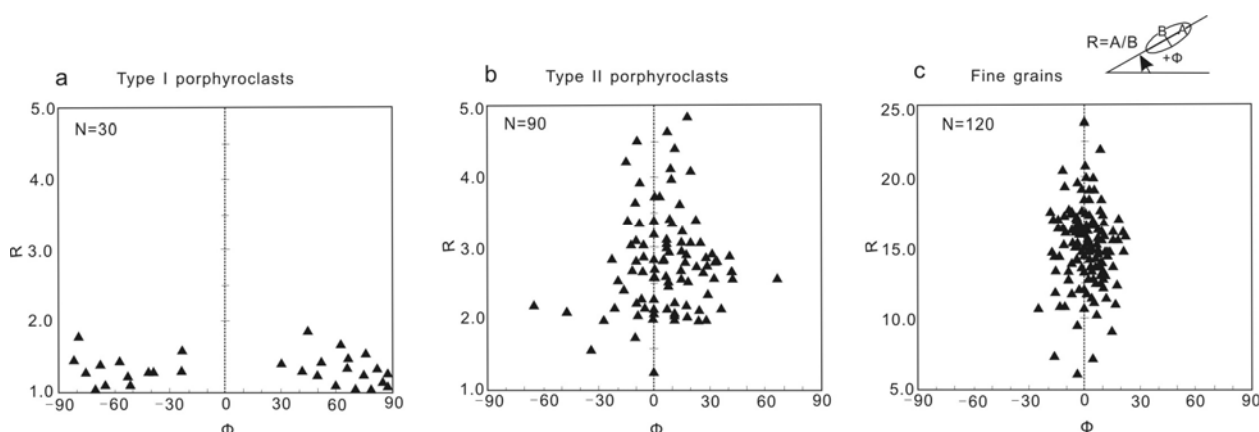


Fig. 2.4 Diagram showing the relationship between the amphibole aspect ratios (R) and the orientation of long axes of the grains with respect to the foliation direction (ϕ) in the XZ section a. type I porphyroclasts; b. type II porphyroclasts; c. fine grains from matrix. (ϕ) is positive when measured anticlockwise from the foliation trace.

2.4.3 Submicrostructural characterization - TEM observation

TEM analysis of the two groups of samples reveals the existence of various types of dislocation submicrostructures in amphibole (from both deformed porphyroclasts and recrystallized grains) (Fig. 2.5), quartz and plagioclase grains (Fig. 2.6). There are free dislocations, dislocation dipoles, dislocation arrays, dislocation walls, subgrains formed by dislocation walls and twin boundaries, and tangled dislocations.

The type I porphyroclasts are hardened grains characterized by dominant tangled dislocations in the core and also in the marginal zones (Fig. 2.5a). They are highly entangled without obvious variation from grain to grain or within a porphyroclast. In some of the grains, different types of free dislocations are present also. Most are dipoles and few are straight free dislocations. They are probably new dislocations formed during progressive deformation. Thin deformation twins are rare and have very small lengths when occurring. Furthermore, the type I porphyroclasts generally have straight and regular grain boundaries. They are not mantled and there are no transition zones (i.e. subgrains) between the porphyroclasts and fine-grained matrix.

In type II porphyroclasts free dislocations (Fig. 2.5b-d) are common and are generally short lines (0.20-0.33 μm). Most of the free dislocations are not aligned to specific crystallographic orientations. Free dislocations occur in the cores of the deformed type II porphyroclasts, in the subgrains developed from the mantle of the porphyroclasts, and in

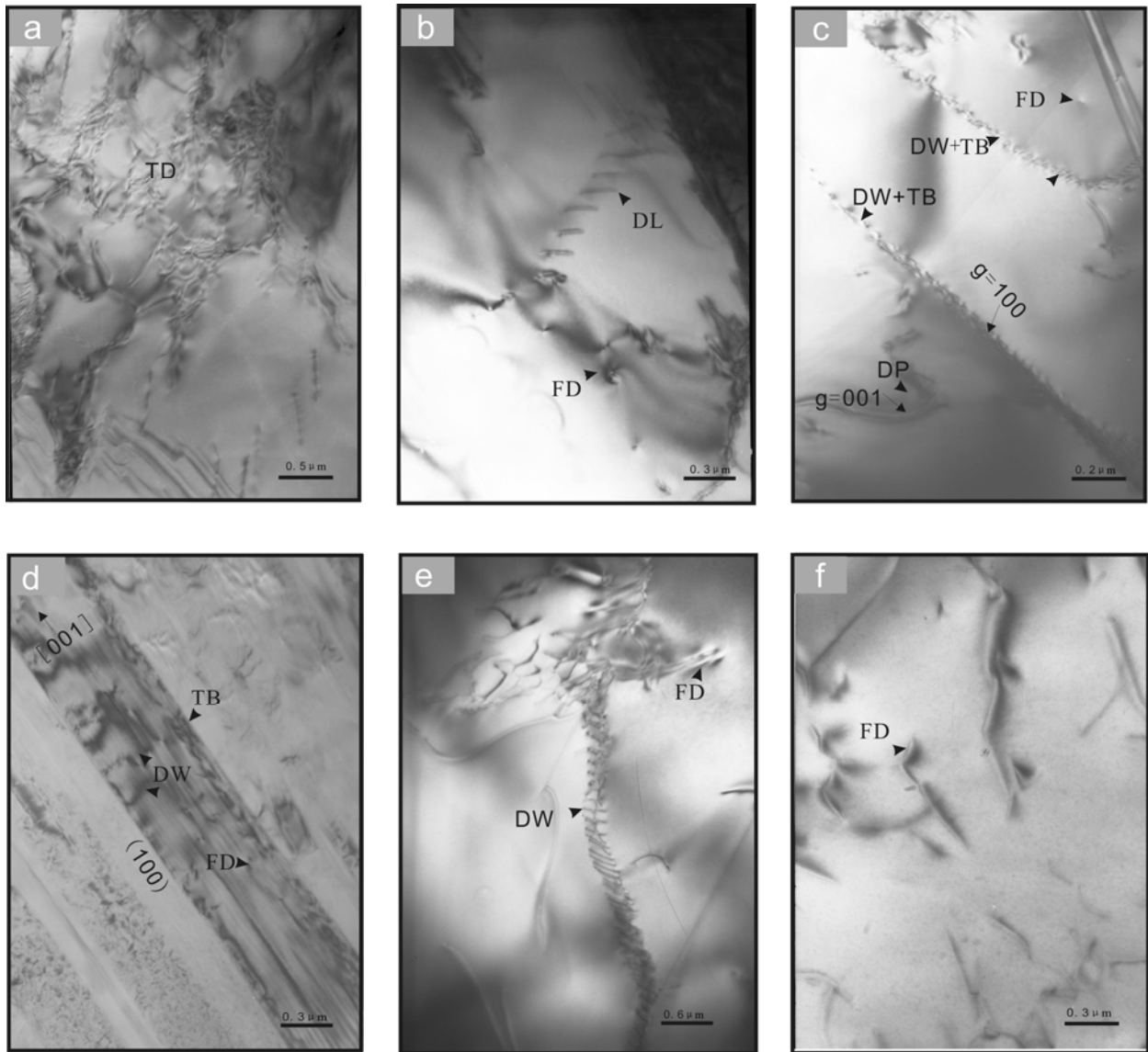


Fig. 2.5 Submicrostructures of amphibole grains from mylonitic rocks. a. tangled dislocations from the core of a type I amphibole porphyroclast; b. free dislocations and regular dislocation arrays; c. dislocation dipoles, dislocation walls and free dislocations; d. regular twin boundaries, dislocations in twins and twinned hosts, and dislocation walls perpendicular to twin boundaries; e. a dislocation wall; f. fine amphibole grains containing a few free dislocations; b-e taken from margins of type II amphibole porphyroclasts; FD- free dislocation; DL- dislocation array; DP- dislocation dipole; TD- tangled dislocation; DW- dislocation wall. TB- twin boundary.

some fine grains around the porphyroclasts. Those in the cores and in the subgrains are often curved, forming dislocation dipoles bulging in the direction of dislocation climb, and in most cases curving to the (001) dislocation walls (Fig. 2.5c). Free dislocations are self-organized into dislocation arrays (Fig. 5b) or dislocation walls (Fig. 2.5c), generally along (001) and (100) planes (Fig. 5c and d), implying the softened characteristic of the type II porphyroclasts. Twin boundaries often constituted by well-organized dislocations (Fig. 2.5c and d), suggest that they

form a special type of dislocation walls. However, they differ from the other type of dislocation walls in that they are parallel arrays of dislocations that bound dislocation free domains (e.g. twins and twin hosts). Such domains are straight and narrow lamellae of micron scale in width and they are oriented parallel to specific crystallographic orientations (e.g. (100)). A very few subgrains formed by dislocation walls in different orientations, resulting in irregular or polygonal shapes. Most subgrains, however, are configured by combinations of dislocation walls and twin boundaries (Fig. 2.5c and d), and generally show acicular to columnar shapes (Fig. 2.3f and g). They are the dominant type of subgrains, possibly due to the ease of twinning at the prevailing conditions.

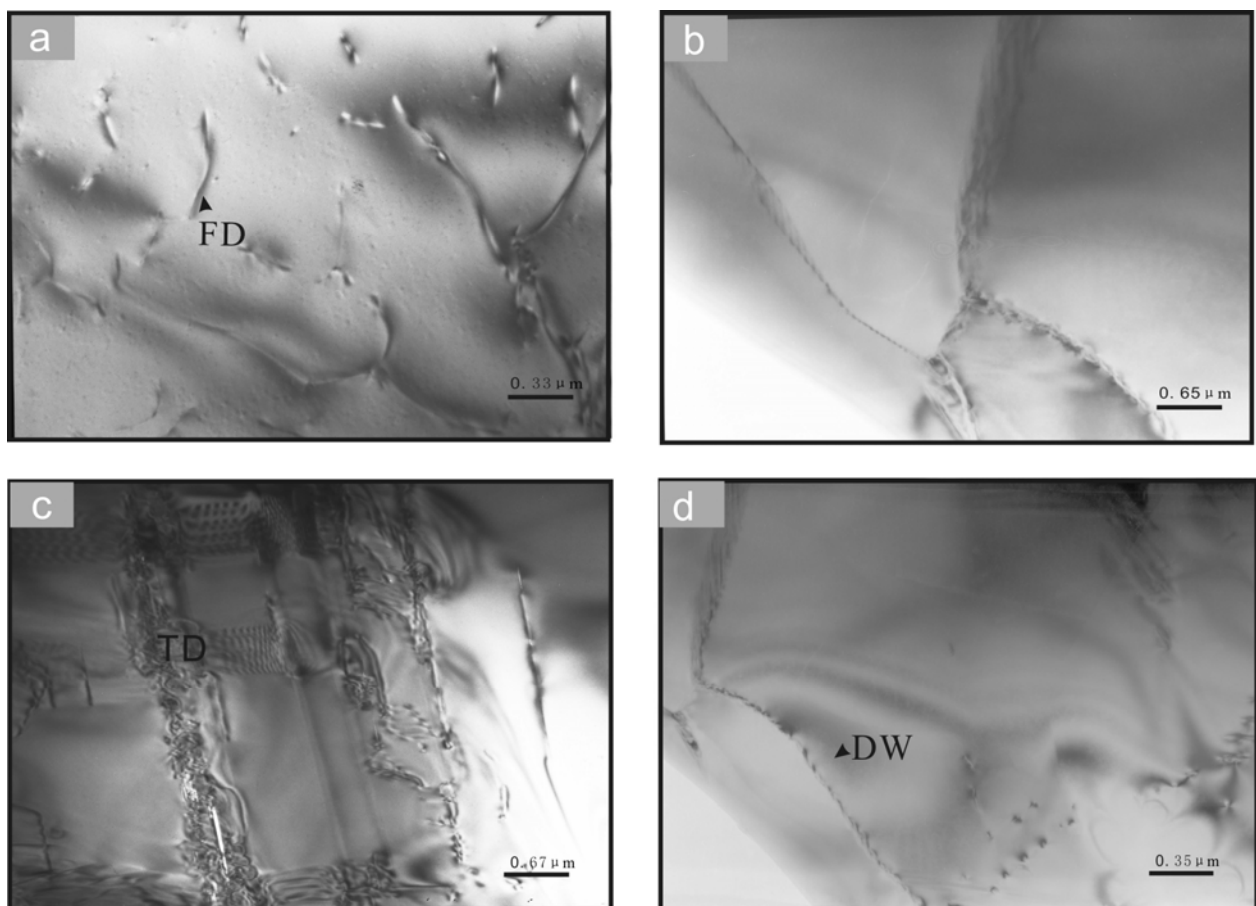


Fig. 2.6 Deformation submicrostructures in quartz and plagioclase grains from amphibolite mylonitic rocks. a. very few free dislocations in quartz; b. dislocation networks or subgrains in a deformed quartz grain; c. tangled dislocations in the core of a porphyroclastic plagioclase; d. dislocation walls and a few free dislocations in deformed plagioclase grains. FD- free dislocation; TD- tangled dislocation; DW- dislocation wall.

Fine amphibole grains in the matrix of the mylonitic rocks are extremely elongated and characterized by high aspect ratios, as also shown by the optical measurements. The grains

contain very few free dislocations (Fig. 2.5f), probably resulting from strain accumulation during progressive deformation. Most fine grains have straight grain boundaries parallel to crystallographic [001]-axes orientation of the amphibole crystal. They are acicular or columnar shapes defined by and parallel to the configuration of twins.

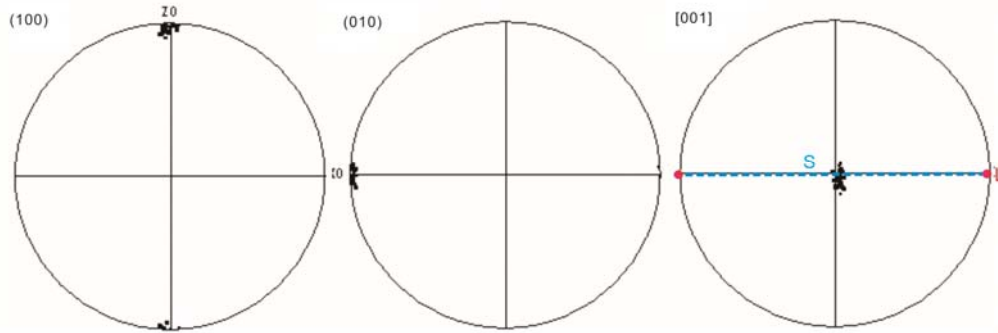
The dislocation density calculation reveals great variations for the different types of grains. A significant decrease in the density is detected from the “hard-worked” type I porphyroclasts, to “softened” type II porphyroclasts and to dynamically recrystallized new fine grains, e.g. the dislocation densities are approximately $3 \times 10^8 \text{ cm}^{-2}$ in the type I porphyroclasts, about $5 \times 10^8 \text{ cm}^{-2}$ in the mantle of type II porphyroclasts, and about $2 \times 10^3 \text{ cm}^{-2}$ in the fine-grained amphibole grains in the matrix. Although the small size of the regions for dislocation calculation is associated with the heterogeneity of the dislocation distribution in plastically deformed materials, and may lead to the ρ -values that are not representative, or are inconsistent with the plastic behaviors of the materials, the general tendency of dislocation density variation in the different types of grains is in good correlation with the optical microscopy and TEM observations.

2.5 Textures -EBSD analysis

2.5.1 LPO data

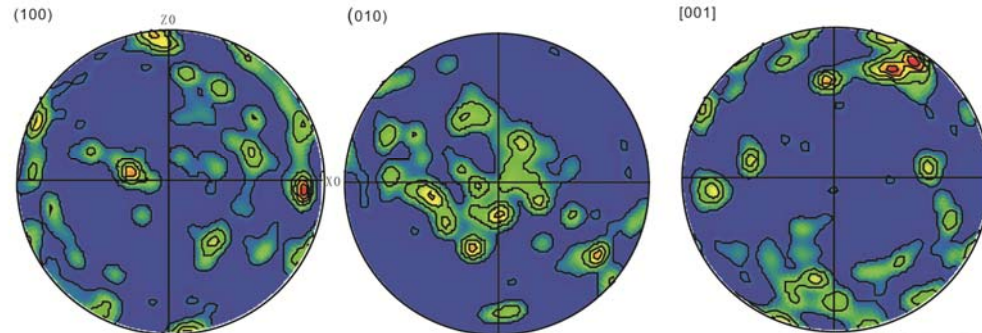
Fig. 2.7 give some of the typical EBSD pole figures of type I porphyroclasts, fine matrix grains around the type I porphyroclasts, type II porphyroclasts, fine grains around type II porphyroclasts and fine grains from the matrix in ultramylonites. Fig. 2.7a gives 39 measured orientations of typical type I porphyroclast. The porphyroclast is oriented with [001]-axes parallel to Y. The (100)- plane is parallel to XY and normal to Z of the sample. In Fig. 2.7b the orientation pattern of fine grains around the above type I porphyroclast reveals the diversity of (100), (010) and [001]-directions of these grains. They have relatively random misorientations from the porphyroclast varying from low angles to about 90° . Such orientation patterns imply that there is no progressive transition from the type I “hard” porphyroclasts to fine grains around them and the orientation of the fine grains may have been disturbed due to the rotation of the porphyroclast.

a Type I porphyroblast



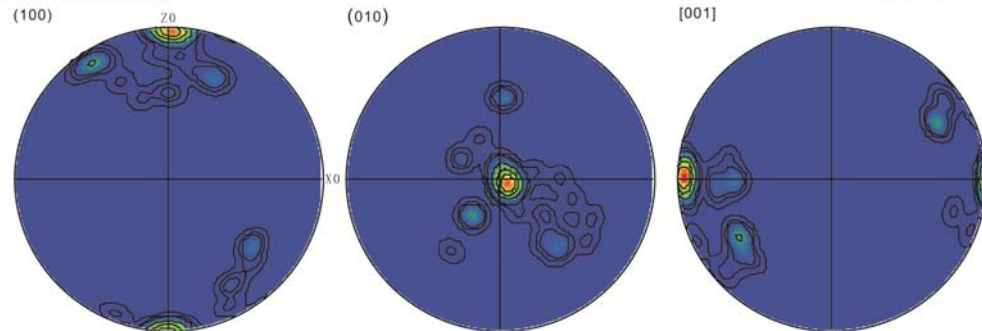
39 data points

b Fine grains around type I porphyroblast



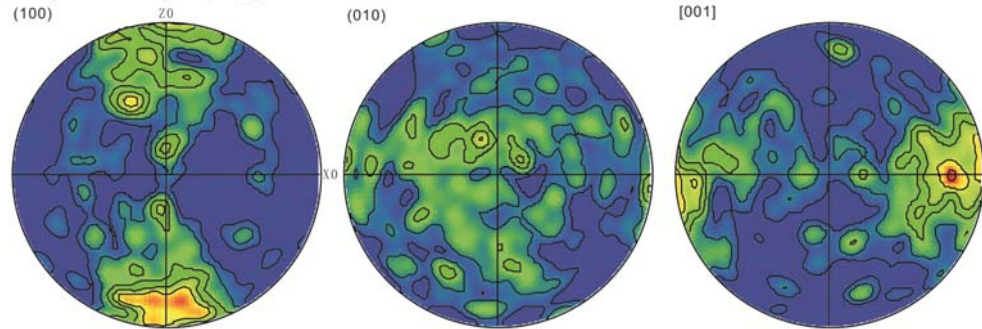
159 data points
Max=10

c Type II porphyroclasts



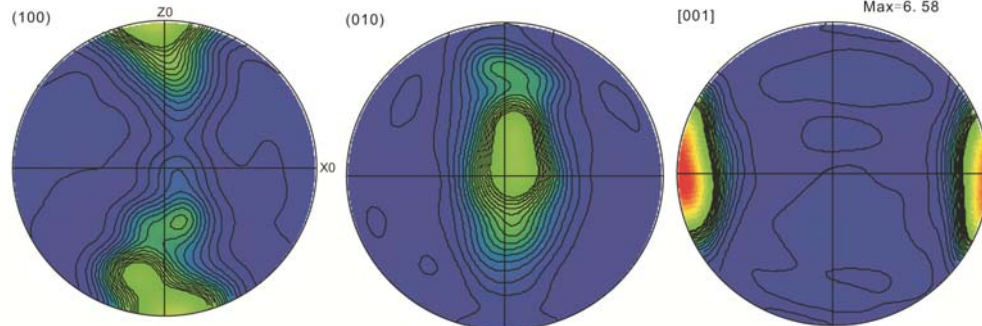
120 data points
Max=80.12

d Fine grains around Type II porphyroclasts



597 data points
Max=6.58

e Fine grains



21897 data points
Max=18.95

Fig. 2.7 EBSD fabric data of amphiboles from the mylonitic and ultramylonitic amphibolites. a. orientation of a type I porphyroclast; b. fabrics of a type I porphyroclast and fine grains around it. c. fabrics of type II porphyroclasts. d. fabrics of fine grains around the type II porphyroclasts; e. fabrics of fine grains from matrix of ultramylonites. Foliation is XY- broken line and lineation is X direction in this plane. Equal area and lower hemisphere projection, couture lines are multiples of random distribution.

[001]-axes and (100)-planes of the type II porphyroclasts dominantly form maxima lying in the X and XY orientations, respectively (Fig. 2.7c). Fine grains around the type II porphyroclasts have slight variations in their LPOs (Fig. 2.7d). Some of the secondary [001] and (100) maxima have angles up to 26° from those of the porphyroclasts, possibly reflect misorientation at the σ -, δ - or ϕ -shaped tails of these porphyroclasts. The majority, however, are overlapping and are transiting into the orientations of the porphyroclasts, suggesting that most of the fine matrix grains take the orientations of the orientations of their precursor type II porphyroclasts. Similar patterns exist for many of the type II porphyroclasts. The similarity of LPO patterns of the type II porphyroclasts with the fine grains around them (Fig. 2.7c, and d) imply that most of the new fine grains surrounding type II porphyroclasts are derived from the type II porphyroclasts and they finally become stabilized in the direction of the stretching lineation (or the shearing direction).

Mapping of fine matrix amphibole grains from samples of mylonitic and ultramylonitic amphibolites give similar LPO patterns to those of the type II porphyroclasts and fine grains around them (Fig. 2.7 c-e). The orientation patterns are simple and are characterized by strong maxima of [001]-axis in the X direction and of (100) in the Z direction of the samples. Correspondingly (010) forms a maximum in the Y direction. Such similarity in LPO patterns of the different types of grains provides further information for the origin of matrix grains from the "soft" oriented porphyroclasts. There is a slight dispersion of (100) and (010) of matrix grains towards a girdle parallel to the YZ-plane. Such a complication of the orientation patterns is possibly due to perturbation of grain orientations by foliation inflexion or owing to perturbation by any type of porphyroclasts. It may also suggest that (1) there is a minor slight rotation of some fine grains around their [001]-axes once they become independent from their parental porphyroclasts or (2) the fine grains are formed from a secondary population of parental porphyroclasts oriented also with their [001]-axes parallel to X but with a different (100) and (010) orientation, considering the well documented slip system ((010) as the slip plane) in naturally and experimentally deformed amphiboles (Díaz Azpiroz et al., 2007, and references therein on page 641).

2.5.2 Misorientation

The crystallographic misorientation between two crystals can be described by the misorientation angle distribution (MAD) or by rotation axis (e.g. Randle, 1993; Lloyd et al., 1997; Fliervoet et al., 1999). Our misorientation analyses are based on the measurements of crystallographic orientations by the EBSD. Because the data acquisition of porphyroclasts and the fine grains around porphyroclasts was by point scan mode, these data allow us to have uncorrelated misorientation calculating their associated misorientation from the randomly selected grain pairs that are not necessarily in physical contact (Fliervoet et al., 1999). This approach is similar to the method of factorial misorientation analysis described by Lloyd et al. (1997).

The misorientations of fine grains around type I and II porphyroclasts, and fine grain matrix show obvious differences. In the uncorrelated MAD of a type I porphyroclast and fine grains around it (Fig. 2.8b), there is a major peak at 5 to 15 ° in coincidence with the data from the porphyroclast (Fig. 2.8a). The fine grains around the type I porphyroclast, however, show random distribution of misorientation angles, from 15 to 170°, implying that they do not have close relationship in view of crystallographic orientation (Fig. 2.8b). The MADs of the type II porphyroclasts are different from those of type I porphyroclasts. Three peaks of 0-10°, 25-65 ° and 105-165 ° misorientation angles may represent parent grains in different orientations (Fig. 2.8c). The MADs of fine grains around the type II porphyroclasts and in the matrix of ultramylonites, however, have obvious similarities (Fig. 2.8d and e). Missing low angle misorientations are different from the MADs of both the type I and type II porphyroclasts. However, they show some overlaps with those of the type II porphyroclasts. The differences and similarities of MADs of different types of grains support the idea that the matrix grains are genetically related to the fine grains around the type II porphyroclasts, and therefore to the porphyroclasts. In contrast, the type I porphyroclasts are not related to any of the other types of grains. In general, dislocation creep processes and subgrain rotation forming a strong LPO may be expected to result in a greater proportion of lower angle misorientations between grains, which may be reflected by a large peak of very low angle misorientations also on the neighbor-pair distribution (e.g. Trimby et al., 1998). The recrystallized amphiboles, however, mostly show high angles of misorientation. This may support their origin mostly from a more complicated, subgrain rotation unrelated process. Therefore, the mixed process of twinning and dislocation creep during the generation of the fine grains may have disrupted the original grain orientation relations as produced from subgrain rotation.

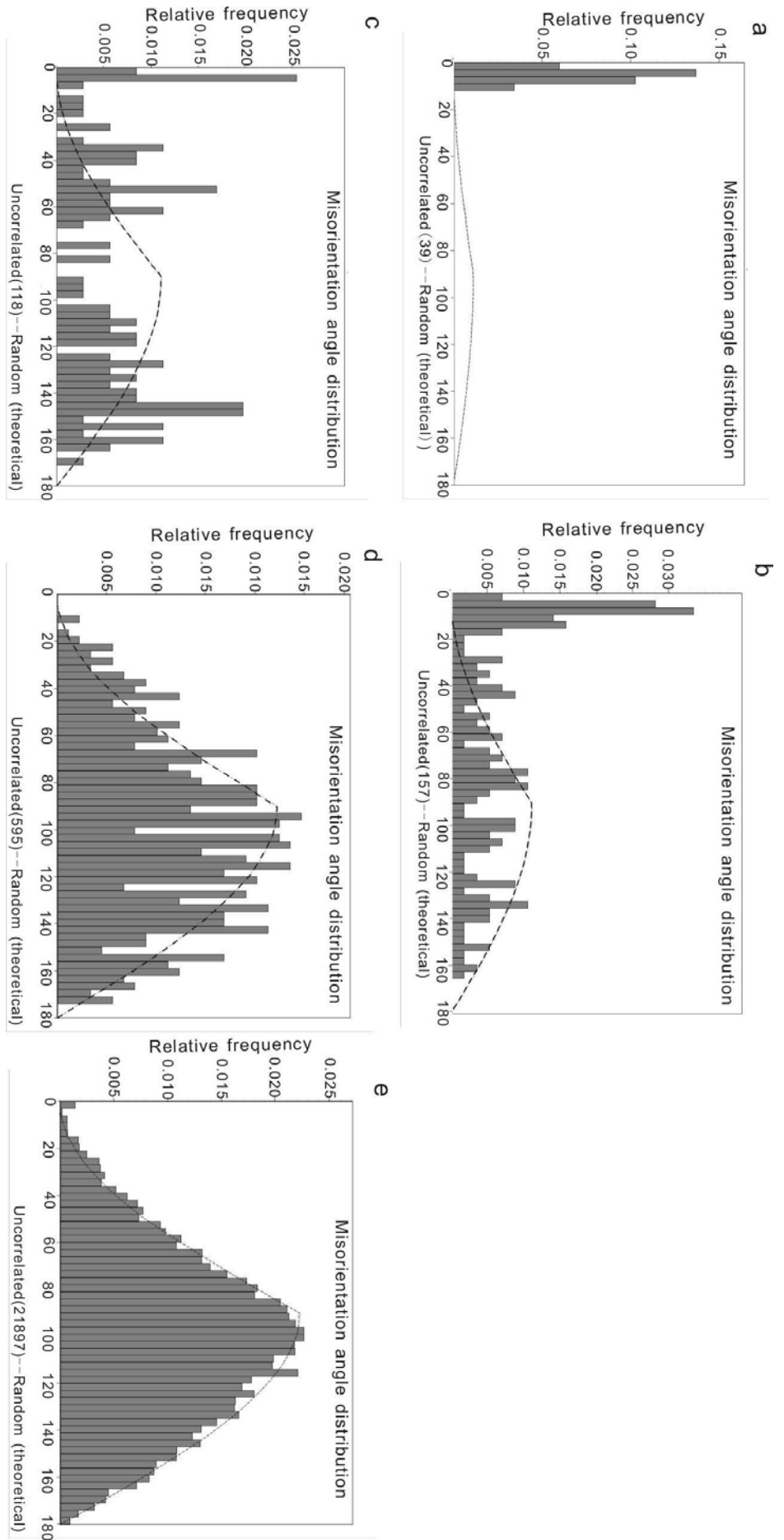
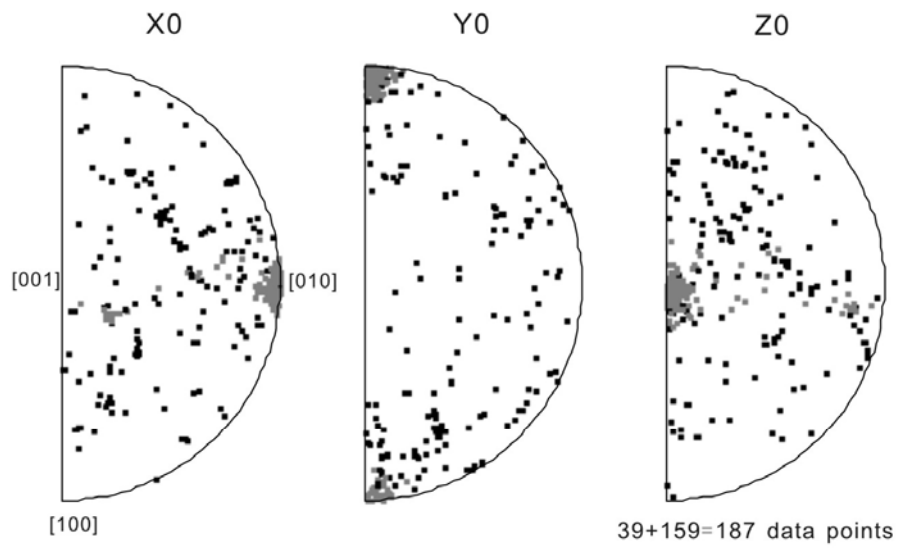
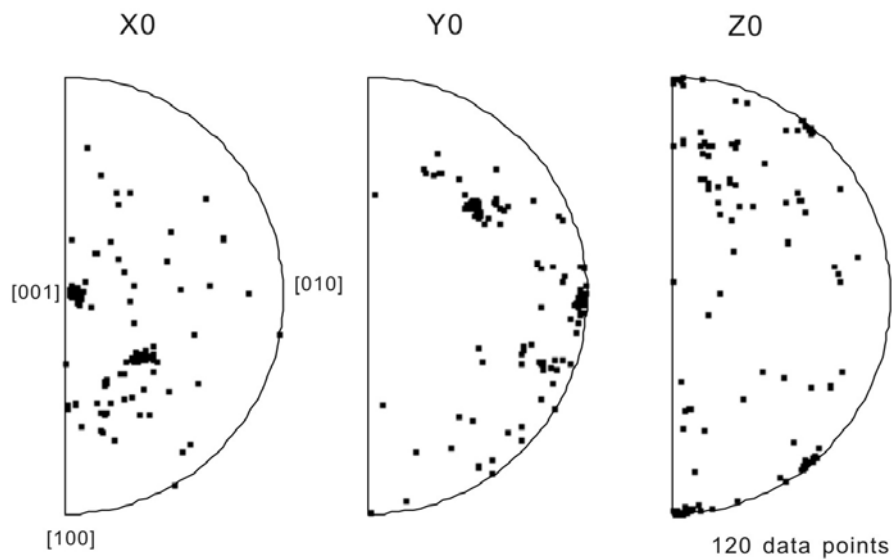


Fig. 2.8 Misorientation angle frequency distributions of amphiboles: a. type I porphyroclasts; b. fine grains around type I porphyroclasts and type I porphyroclasts; c. type II porphyroclasts; d. fine grains around type II porphyroclasts; e. fine grains in the matrix. The theoretical random distribution curve for amphibole is shown for comparative purposes.

a Type I porphyroclast and fine grains around type I porphyroclast



b Type II porphyroclasts



c Fine around type II porphyroclasts

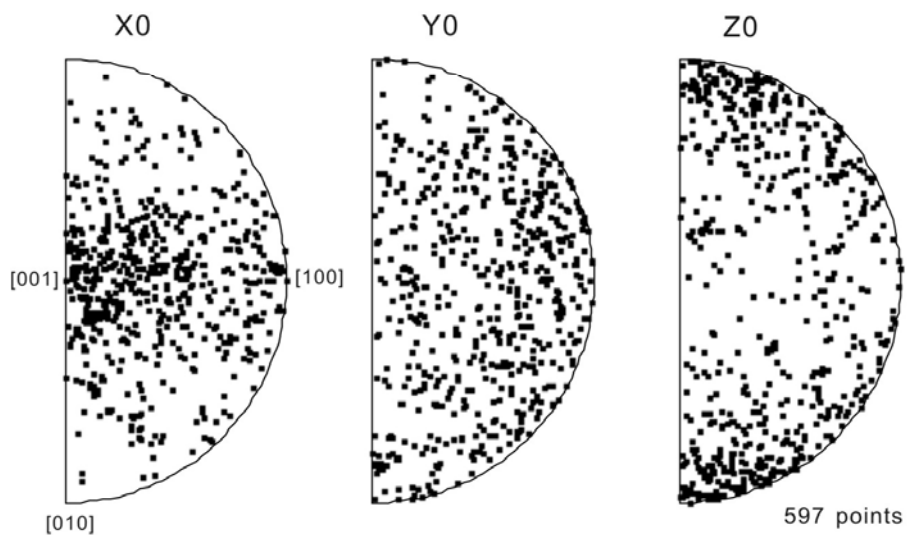


Fig. 2.1 EBSD inverse pole figure in the crystallographic reference frame [100], [010] and [001]. a. a type I porphyroclast and fine grains around it (the light color is from the type I porphyroclast); b. type II porphyroclasts; c. fine grains around type II porphyroclasts.

Inverse pole figures for both type I and type II porphyroclasts and their surrounding matrix (Fig. 2.9) provide further information on differences in the misorientation of the fine grains from the porphyroclasts. Data points from a type I porphyroclast shows strong clustering of X0 // [010], Y0 // [100] and Z0 // [001], but fine grains around them show scattered distributions (Fig. 2.9a). Type II porphyroclasts and fine grains around them, however, have similar distribution patterns in the inverse pole figure (Fig. 2.9b), X0 // [001], Y0 // [010] and Z0 // [100].

The inverse pole figure analyses provide clues to the close relationships between the fine grains and the type II porphyroclasts. The distribution pattern of data points of fine grains around the type II porphyroclasts is interpreted as derivation of the fine grains from the porphyroclasts. To the contrary, they also suggest that the orientation of the fine grains are not related to the type I porphyroclasts.

2.6 Mineral chemistry analysis of amphibole-plagioclase and P-T estimation

Metamorphic mineral assemblages, and deformation structures or microstructures suggest that the mylonitic amphibolites are primarily deformed under the amphibolite facies conditions. In metamafic rocks in which plagioclase and amphibole are in fabric equilibrium, amphibole mineral chemistry and thermobarometry (Table 2.2) provide the opportunity to constrain the P-T conditions of deformation. A first pressure estimation is based on the metamorphic mineral assemblages of garnet+plagioclase–muscovite–biotite in staurolite-grade pelitic schists outcropping near the mylonitic amphibolites, that gives lower to medium-pressure (e.g. about 5.0 kbar) metamorphic conditions during left lateral shearing (Leloup et al., 1993).

Electron microprobe analyses (Table 2.2) reveal a very slight variation in chemical compositions for the amphibole from the different types of grains (type I and II porphyroclasts, and fine matrix grains). In the amphiboles the cation distribution of Na in M4-site ranges from 0.07-0.23<0.5, in A-site between 0.20 to 0.49, and the (Ca+Na)M⁴ is above 1.5 for all the samples. Therefore, it is concluded that all amphibole grains analyzed are of calcium-amphibole composition. Si and A-site occupancy are important in evaluating the composition variation of amphiboles in the mylonitic amphibolites (e.g. Pe-Piper, 1988; Díaz Azpiroz et al, 2007). Si is 6.42-6.78 p.f.u. and (Na+K)^A ranges between 0.31-0.63. As shown in Table 2.2 and

Table 2.2 Mineral chemistry analyses of amphibole and P-T estimation/calculation. Fe^{3t} estimated using Holland and Blundy (1994); Temperatures calculated from Hb-Pl thermometer (Holland and Blundy, 1994) at a 6 kbar present highest temperatures registered by each sample. Names according to Leake et al. (1997) and Pe-Piper (1988).

Sample	JLDC1	JLDC2	JLDC3	JLDC4	JLDC5	JLDC6	DC0501	DC0502	DC0503
Amphibole	Type I porphyroclasts		Type II porphyroclasts		Fine-grained amphibole		Ultramylonites amphibole		
SiO ₂	44.13	44.35	44.54	43.25	43.07	43.10	45.60	43.13	42.51
Al ₂ O ₃	10.70	10.81	11.62	11.53	11.34	12.15	9.67	12.70	11.26
TiO ₂	0.35	0.47	0.26	0.47	0.27	0.17	0.46	0.56	0.51
Cr ₂ O ₃	0.00	0.43	0.00	0.00	0.00	0.00	0.00	0.00	0.00
FeO	18.12	17.74	19.10	18.16	19.07	19.48	18.57	18.08	18.96
MnO	0.14	0.52	0.45	0.23	0.23	0.43	0.00	0.19	0.54
MgO	9.70	9.60	8.59	8.76	9.35	8.84	9.77	8.89	9.08
CaO	11.77	11.73	10.71	12.16	11.70	11.54	11.82	12.16	11.75
Na ₂ O	1.82	2.22	1.50	2.00	2.10	1.62	1.40	1.85	1.91
K ₂ O	0.48	0.29	0.55	0.60	0.30	0.42	0.46	0.31	0.67
Total	97.21	98.16	97.32	97.16	97.43	97.75	97.77	97.87	97.19
Structural formulae in base of 23 oxygens									
Si	6.61	6.62	6.64	6.54	6.46	6.42	6.78	6.48	6.42
Al ^{IV}	1.39	1.38	1.36	1.46	1.54	1.58	1.22	1.52	1.58
T	8.00	8.00	8.00	8.00	8.00	8.00	8.00	8.00	8.00
Al ^{VI}	0.50	0.52	0.68	0.60	0.46	0.56	0.48	0.73	0.43
Al ^(total)	1.89	1.90	2.04	2.06	2.00	2.14	1.70	2.25	2.01
Ti	0.04	0.05	0.03	0.05	0.03	0.02	0.05	0.06	0.06
Cr	0.00	0.00	0.00	0.00	0.00	0.00	0.00	0.00	0.00
Fe ³⁺	0.41	0.32	0.55	0.20	0.57	0.71	0.38	0.36	0.56
Mg	2.19	2.14	1.91	1.98	2.09	1.96	2.17	1.97	2.04
Fe ²⁺	1.86	1.90	1.78	2.10	1.80	1.70	1.93	1.89	1.84
Mn	0.02	0.07	0.06	0.03	0.03	0.05	0.000	0.02	0.07
M1-3	5.00	5.00	5.00	5.00	5.00	5.00	5.00	5.00	5.00
Mg	0.00	0.00	0.00	0.00	0.00	0.00	0.00	0.00	0.00
Fe ²⁺	0.00	0.00	0.06	0.00	0.02	0.00	0.00	0.00	0.00
Mn	0.00	0.00	0.00	0.00	0.00	0.00	0.00	0.00	0.00
Ca	1.91	1.88	1.71	1.97	1.88	1.84	1.88	1.92	1.89
Na	0.11	0.12	0.23	0.07	0.12	0.14	0.12	0.09	0.11
M4	2.00	2.00	2.00	2.00	2.00	2.00	2.00	2.00	2.00
Ca	0.00	0.00	0.00	0.00	0.00	0.00	0.00	0.00	0.00
Na	0.42	0.49	0.20	0.51	0.49	0.33	0.29	0.45	0.45
K	0.09	0.06	0.11	0.12	0.06	0.08	0.09	0.06	0.13
A	0.51	0.54	0.31	0.63	0.55	0.41	0.38	0.51	0.58
Ca ^{M4}	1.888	1.867	1.711	1.926	1.880	1.842	1.883	1.915	1.894
Si (p.f.u.)	6.61	6.62	6.64	6.543	6.46	6.42	6.78	6.48	6.42
Mg#	0.52	0.53	0.51	0.49	0.54	0.54	0.52	0.51	0.53
(Na + k) ^A	0.51	0.54	0.31	0.63	0.55	0.41	0.38	0.51	0.58
Name			Mag-Hb	Fer-Hb		Schermakite	Mag-Hb		
Plagioclase Samples									
Plagioclase									
SiO ₂	59.40	61.05	64.51	61.38	61.30	63.82	61.48	61.71	61.92
Al ₂ O ₃	23.12	23.37	19.07	22.40	23.06	22.59	23.08	23.13	22.59
TiO ₂	0.23	0.00	0.00	0.00	0.00	0.03	0.00	0.21	0.45
FeO	0.01	0.28	0.00	0.00	1.08	0.00	0.00	0.66	0.70
MnO	0.00	0.11	0.00	0.00	0.17	0.00	0.00	0.00	0.00
CaO	5.89	5.13	4.28	4.83	4.54	3.24	4.96	4.22	4.05
Na ₂ O	10.52	9.82	12.62	10.86	8.79	10.58	9.58	10.11	10.93
K ₂ O	0.00	0.21	0.12	0.15	0.23	0.25	0.09	0.02	0.13
Total	99.17	99.97	100.60	99.62	99.17	100.07	99.19	100.08	100.76
Ca	0.29	0.25	0.20	0.23	0.23	0.15	0.24	0.20	0.19
Na	0.92	0.85	1.04	0.95	0.77	0.90	0.83	0.87	0.94
K	0.00	0.01	0.01	0.01	0.01	0.01	0.01	0.00	0.01
X _{ab}	0.76	0.77	0.84	0.80	0.77	0.84	0.77	0.81	0.82
X _{an}	0.24	0.22	0.16	0.20	0.22	0.14	0.22	0.19	0.17
P = 6 kbar	641.1	650.1	584.6	597.7	672.7	613.7	617.4	595.9	652.3
Temp. (°C)±20									

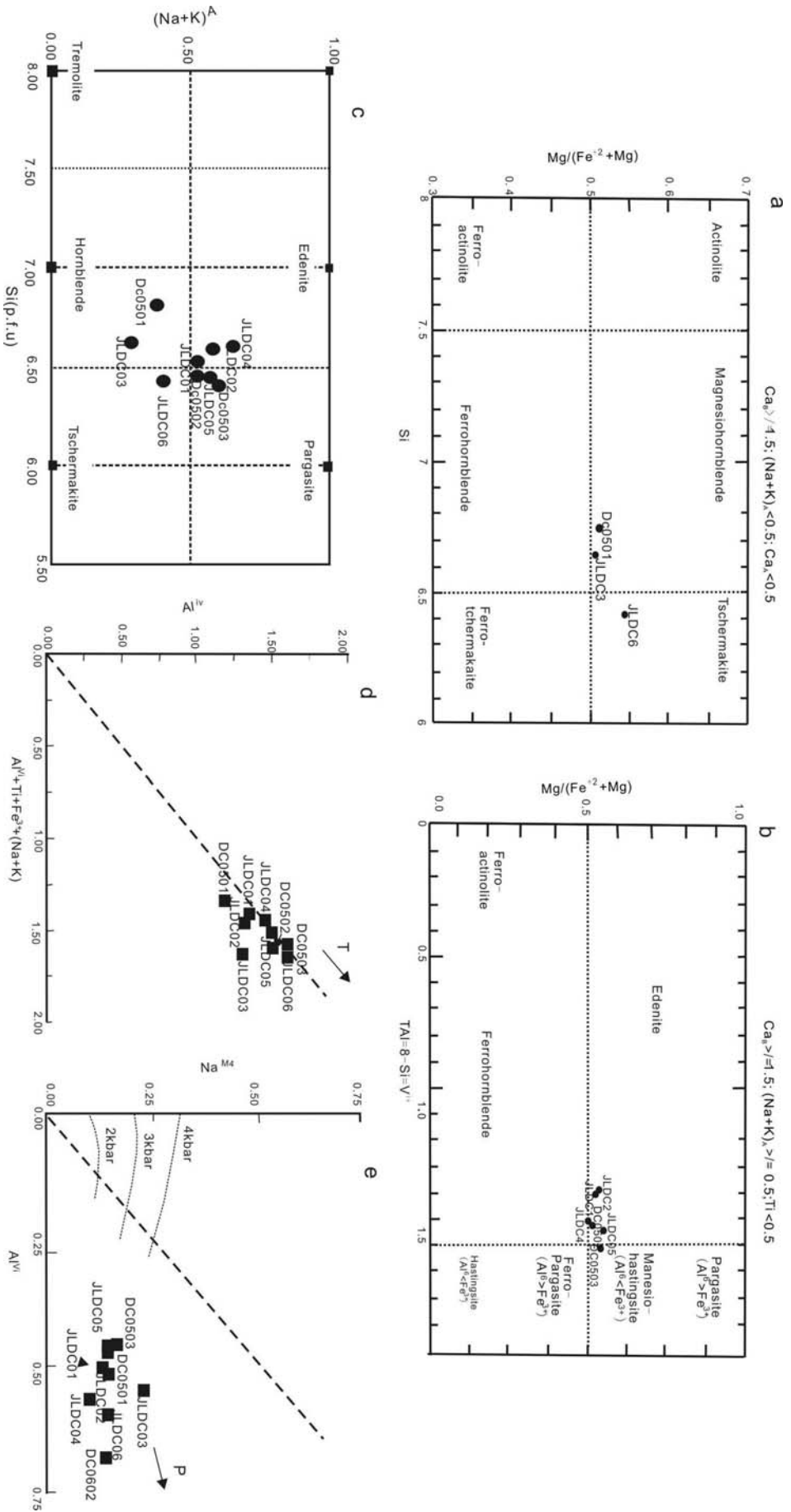


Fig. 2.2 Mineral chemistry of amphibole grains in the amphibolite mylonites. a. Si vs. Mg# diagram ($(Na+K)^4 < 0.5$); b. Al vs Mg# diagram ($(Na+K)^4 > 0.5$). Classification according to Leake et al. (1997); c. $(Na+K)^4$ vs. Si (p.f.u.) classification of calcic amphiboles according to Pe-Piper (1988). d. Al^{iv} vs. $Al^{vi} + Ti + Fe^{3+} + (Na+K)$ plot by Robinson et al. (1971) is depicted by a 1:1 line that intersects at (0, 0); increasing values along this line broadly indicates increasing temperature. e. Na^{M4} vs. Al^{vi} plot is indicated by a 1:1 line that intersects at (0, 0); increasing values along this line approximates a pressure increase; the isobarometric lines are deduced from the calibration by Brown (1977).

Fig. 2.10, in the Si-Mg# diagram ($(\text{Na}+\text{K})^{\text{A}} < 0.5$), JLDC7 and JLDC3 are plotted as magnesiohornblende and JLDC6 as tschermakite (Fig. 2.10a), and in the Al-Mg# diagram ($(\text{Na}+\text{K})^{\text{A}} > 0.5$), JLDC1, JLDC2, JLDC5, belong to edenite, and JLDC4 and DC0502 are plotted close to the edenite and ferrohornblende boundary. DC0503 is plotted in the area of the pargasite (Fig. 2.10b). Both the Si-Mg# diagram and Al-Mg# diagram are in coincidence with Si-(Na+K)^A # diagram (Fig. 2.10c). Thus the porphyroclasts and matrix grains can be grouped as edenite.

The Al^{iv}, Fe³⁺ and Ti in the octahedral sites, together with the A-site occupancy are balanced by Al^{vi} substituting (e.g., Spear, 1981; Blundy and Holland, 1990). Qualitative temperature estimations can be therefore presented on the basis of Al^{iv}, Ti and (Na+K)^A contents in amphiboles (e.g. Spear, 1981; Blundy and Holland, 1990; Spear, 1993; Díaz Azpiroz et al, 2007). For all samples, Ti contents are low (0.01-0.06) and do not show obvious variation from porphyroclasts to matrix. The amphibole grains are characterized by high Al (Al^{iv}=1.22-1.58, Al^{vi}=0.43-0.73). Such characteristics may suggest that they are deformed at relatively high grades (e.g. epidote amphibolite facies to amphibolite facies, Robinson et al., 1971; Spear, 1981; Anderson and Smith, 1995; Ernst and Liu, 1998). On the other hand, all the samples fall into a limited area on the Al^{iv}-Al^{vi}+Fe³⁺+Ti+(Na+K)^A plot (Fig. 10d), suggesting that the amphiboles meet the ideal substitution mechanism (e.g. Díaz Azpiroz et al, 2007). According to the calibration by Brown (1997), pressures of less than 6 kbar are estimated from the Na^{M4}-Al^{vi} plot for the studied amphiboles (Fig. 2.10e).

More precise estimation of temperature conditions of amphibolite deformation processes are further performed by applying Holland and Blundy (1994) amphibole-plagioclase geothermometer based on the edenite+albite=richterite+anorthite equilibrium (Holland and Blundy, 1994). The cores of Type I and Type II porphyroclasts, and the fine grains around the porphyroclasts and in the matrix give temperatures ranging from 585 to 673 °C, with an average of 625 °C. The calculated results (Table 2.2) are consistent with the mineral chemistry analysis, suggesting metamorphic conditions at lower amphibolite facies at relatively lower pressures conditions.

2.7 Discussion

2.7.1 "Soft" - "hard" behavior of amphibole porphyroclasts

Amphibole grains with "hard" or "soft" initial crystallographic orientations have strong effects on the rheological behavior of the minerals. Therefore, the two types of porphyroclasts (type I

and II porphyroclasts) tend to be deformed in a brittle manner at the very beginning of shearing under the prevailing conditions. The "soft" and "hard" behavior of a porphyroclast is proven by microstructural, SPO and LPO, and TEM submicrostructural analyses. Such behavior of the porphyroclast is mainly dependent on its initial crystallographic orientation with respect to applied shear stresses. When a grain is oriented with its slip system (100) [001] consistent with regional shearing, with an angle of 0° - 50° or 150° - 180° of the (100)- plane to the shearing direction, the slip system can be easily activated. However, when its slip system (100) [001] is inconsistent with regional shearing, with an angle of 50° to 150° of the (100)-plane to shearing direction, the slip system remains unactivated (e.g. Liu, 1999). The geometrical consistency or inconsistency of the (100) [001] slip system in respect to the applied shear stresses, leads to the "soft" or "hard" behavior of the porphyroclasts during shearing.

Type I porphyroclasts are typical "hard" porphyroclasts during shearing without any evidence for dynamic recrystallization. Mechanical rotation is responsible for the deformation and orientation pattern of the type I porphyroclasts. Matrix grains around them do not have any genetic, i.e. geometrical relationships with them and behave passively during shearing, shown by SPO and EBSD analyses. Therefore, tangled dislocations or walls of tangled dislocations are preserved either at grain margins, or in the cores. There are no regular dislocation walls, implying the incapability for dislocations to glide and climb. Type II porphyroclasts are typical "soft" porphyroclasts and have mantled microstructures. Tangled dislocations are partly developed in the cores of the porphyroclasts. Along the margins of the porphyroclasts, however, dislocations are generally well organized, that some dislocation glide or climb along the (100) [001] slip system towards the (001) direction to form (001) dislocation walls. (100) microtwinning extensively develops contemporaneously. Dynamic recrystallization by combined subgrain nucleation due to twinning and dislocation creep generates fine grains of amphibole in the matrix.

Differences in initial crystallographic orientations contribute to the "hard" and "soft" behaviors of the amphibole grains, characterized by the dislocation (im)mobility during deformation, revealed by TEM microstructural evidences. The different behaviors, on the other hand, have resulted in the similarities and differences in deformation microstructures, SPO and LPO fabrics. The type I porphyroclasts are rounded and subrounded, with a low aspect ratio and a more random ϕ distribution. They have also unique LPO fabrics and misorientation patterns. The other types of grains, however, show general similarities, either in the SPO and LPO fabrics, or in misorientation patterns. Such similarities are attributed to the generation of the new fine grains in the matrix (either surrounding type I or type II porphyroclasts in mylonites, or in the

matrix in ultramylonites) by crystal plastic deformation of the parent grains (e.g. the present type II porphyroclasts).

2.7.2 Twinning, subgrain nucleation and dynamic recrystallization

Lattice preferred orientations of minerals in a deformed rock are directly related to prevailing slip systems during deformation (e.g. Shelley, 1994; Fliervoet et al., 1999; Lee et al., 2002; Brenker et al., 2002; Díaz Azpiroz et al., 2007). It is generally accepted that during deformation a predominantly activated slip system tends to coincide with the flow direction and the flow plane, respectively (e.g. Mainprice and Nicolas, 1989). In this case, the parallelism of [001] crystallographic axes and (100) crystallographic planes of amphibole grains to the stretching lineation and foliation of the mylonites (Fig. 2.7c and d) implies that the lattice-preferred orientation of dynamically recrystallized amphibole grains resulted from a dominant activation of (100) [001] slip (twinning) system.

Most fine grains in the matrix have close relationships with the type II porphyroclasts. During the deformation and recrystallization, the type II porphyroclasts have initial crystallographic orientations that are propitious for the (100) [001] slip system to be activated and therefore (100) micro-twinning becomes the most dominant deformation mechanism. Twinning is assisted by dislocation mobility, inducing well-organized dislocations along twin boundaries. Dominant (100) twinning is also proven by micro- and submicrostructural analysis. The existence of twin boundaries constrains the mobility of dislocations in twins and their hosts. TEM observation reveals the existence of two groups of dislocation walls in the type II porphyroclasts, one along (100) that constitute most of the twin boundaries, the other along (001) that form dislocation walls or subgrain boundaries in another direction (Fig. 2.5c). The curving directions of dislocation dipoles observed in the deformation twins suggest that dislocations glide or climb towards dislocation walls in the [001] slip direction.

(100) twinning has accommodated the major strain that amphibole grains experienced. The most important role of twinning is that it contributes not only to deformation, but also to subgrain nucleation and subsequent dynamic recrystallization during shearing. Twins and their hosts are separated primarily by twin boundaries constituted by dislocations in (100) directions. In the twinned parts, dislocations glide or climb towards (100) twin boundaries or to (001) dislocation walls. The former enhances twin gliding, and the latter forms new boundaries that are subnormal to twin boundaries. Acicular to columnar shaped subgrains are formed by combination of these twin boundaries along (100) and the (001) dislocation walls. Subsequent

rotation of the subgrains is enhanced by progressive shearing and thus recrystallized new grains are formed. Both twins and their hosts evolve into fine grains that are parallel to each other. During this process, nucleation of the subgrains and subsequent formation of dynamically recrystallized fine grains are governed by both (100) twinning and dislocation creep. We call this mechanism *twinning nucleation recrystallization (TNR)*(Fig.2.11).

Fine grains formed by combined twinning and dislocation gliding/climbing are acicular to columnar in shape. They are homogeneously distributed in mylonitic matrix (more than 95% of the grains) and are aligned parallel to the shearing direction. It is optically very obvious that the generation of the fine grains in the matrix is related to the development of tails of type II mantled porphyroclasts; ϕ , σ or δ porphyroclasts. Some of the fine grains are further deformed during progressive shearing so that weak intragranular plastic deformation occurs in the grains.

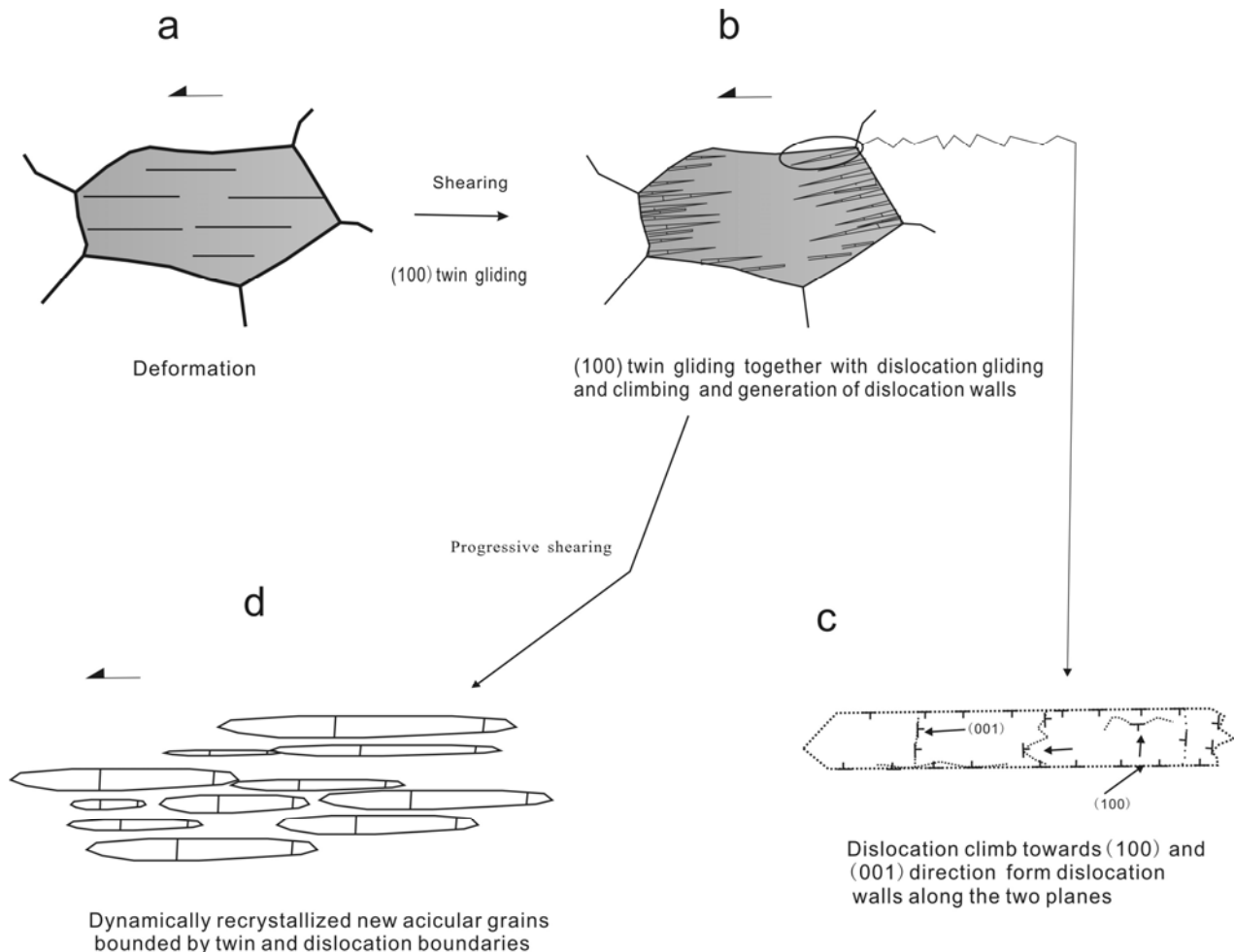


Fig. 2.3 Schematic diagram showing the dynamic recrystallization of amphibole by twinning nucleation recrystallization.

In the amphibole mylonitic rocks, subgrain rotation due to dislocation glide and climb has partly contributed to the dynamic recrystallization processes. Dislocation walls, subgrains and dynamically recrystallized grains due to subgrain rotation are observed with TEM. Fine grains formed by subgrain rotation recrystallization are characterized by equigranular shapes. No or rare free dislocations are observed in the grains. OM observation reveals that the fine grains formed by subgrain rotation are much fewer than those formed by combined twinning and dislocation creep.

2.7.3 Role of secondary phases: quartz and plagioclase

There is 30-35% plagioclase and 10-15% quartz in the amphibolite mylonitic rocks. They constitute quartzofeldspathic bands both in banded mylonites and in ultramylonites. Plagioclase grains in the mylonitic rocks are characterized by crystal plastic deformation and dynamic recrystallization. They are elongated or partly twinned, and some are dynamically recrystallized into fine grains in the matrix. Undulatory and inhomogeneous extinction, grain elongation, deformation twinning and subgrain formation are common in porphyroclastic plagioclase grains. Quartz grains may form monomineralic bands or constitute polymineralic bands with plagioclase grains. They are characterized by high temperature grain growth, forming equant grains with straight boundaries and triple junctions (Fig. 2.3e and f), or rectangular quartz ribbons parallel to the dominant foliation in the mylonites. The latter often occur in high temperature tectonites (e.g. Culshaw and Fyson, 1984; Hippertt et al., 2001). At the same time, the quartz grains do not show any evidence of intragranular plastic deformation, suggesting a quasi-static grain growth.

The following indications suggest that the quartzofeldspathic bands are the high strain zones in the banded mylonitic rocks. (1) Most plagioclase grains are dynamically recrystallized into very fine grains of less than 10 microns in sizes. Some relic porphyroclastic grains are observed and have high aspect ratios. They are intensively twinned and show abundant evidences for crystal plastic deformation. (2) Quartz grains occur as ribbon quartz (rectangular quartz grain aggregates) or augen-shaped grain aggregates, indicating intensive high temperature deformation. (3) Amphibole grains in the quartzofeldspathic bands are generally new fine grains formed by dynamic recrystallization. Their grain sizes are very small (less than 15 μm) in comparison with amphibole grains in the amphibole rich bands (greater than 100 μm). (4) Amphibole grains in the quartzofeldspathic bands are homogeneously distributed and strongly oriented, parallel to the macroscopic stretching lineation.

TEM observation is in agreement with high temperature deformation and recrystallization of quartz and plagioclase in high strain zones. Most quartz grains have polygonal shapes and sharp and straight grain boundaries. They are generally dislocation free or in some cases contain a few free dislocations, which are attributed to progressive deformation (Fig. 2.6a and b). In contrast, plagioclase grains contain many dislocation substructures that support crystal plastic deformation and dynamic recovery/recrystallization. In cores of plagioclase porphyroclasts there are rarely tangled dislocations (Fig. 2.6c). Dislocations are organized into arrays or walls, and the latter form subgrain boundaries. New fine grains of plagioclase with few free dislocations are formed by subgrain rotation (Fig. 2.6d). The new fine grains have typical characteristics of dynamically recrystallized fine grains.

Optical and TEM observations suggest that during deformation and dynamic recrystallization of amphibole grains in the mylonitic rocks high temperature ductile flow dominate the deformation of quartz and plagioclase grains. The existence of quartzofeldspathic components leads to strain localization and strain softening during mylonitization, which is possibly an important triggering for the deformation and dynamic recrystallization of amphibole grains.

2.8 Conclusions

1) Various microstructures and submicrostructures are developed in the amphibole mylonitic rocks from Diancang Shan. Different mineral phases in the rocks show distinct deformation characteristics. Amphibole and plagioclase grains are intensively deformed with obvious grain size reduction, but quartz grains are recrystallized dominantly by grain growth. Our observations suggest that amphibole grains from the mylonitic rocks are strongly deformed and dynamically recrystallized under low-pressure metamorphic conditions at temperature of 585 to 673°C, with an average of 625°C.

2) Two types of porphyroclasts, i.e. type I “hard” porphyroclasts and type II “soft” porphyroclasts can be observed in the mylonites. Type I “hard” porphyroclasts have their crystallographic orientation with [001]-axes normal or subnormal to the stretching lineation of the rocks. Type II porphyroclasts have their orientation with [001]-axes parallel or sub-parallel to the stretching lineation. The latter are easily deformed and recrystallized due to the crystallographic orientation which makes it easy to activate the (100) [001] slip system. The two types of porphyroclasts possess a diversity of micro- and submicrostructures that characterize their “hard” and “soft” behaviors during mylonitization. A close genetic relation of the fine grains to the type II “soft” porphyroclasts is proven by SPO, LPO and misorientation analysis.

3) Twinning nucleation recrystallization (TNR) is one of the most important processes that operate during dynamic recrystallization of amphibole. TEM and EBSD analysis reveals the dominant roles of (100) twinning during deformation and grain size reduction of amphiboles. Twinning along (100), in combination with dislocation creep (gliding and climbing) governs the nucleation of subgrains and subsequent formation of dynamically recrystallized new fine grains.

Acknowledgements

This study has received financial support from the National Natural Science Foundation of China (90814006, 40872139 and 40772133), the 111 Project (B07011) of the Ministry of Education and State Key Laboratory of Geological Processes and Mineral Resources (Grant No. GPMR200837). The authors acknowledge Prof. JIN Zhenmin and Dr. XU Haijun from China University of Geosciences at Wuhan for helpful discussions on apart of EBSD data analysis and Prof. Chunming Wu and Prof. Chunjing Wei for kindly help with the amphibolite geothermobarometri data analysis. The manuscript benefited immensely from the constructive reviews of one anonymous reviewer and Manuel Díaz Azpiroz as well as the journal editor Prof. Tom Blenkinsop.

References

- Allison, I., La Tour, T.E., 1977. Brittle deformation of amphibole in a mylonite: a direct geometrical analogue of ductile deformation by translation gliding. *Journal of Asian Earth Sciences* 14, 1953-1958.
- Anderson, J.L., Smith, D.R., 1995. The effects of temperature and f_{O_2} on the AL-in amphibole barometer. *American Mineralogist* 80, 549-559.
- Babai, H.A., La Tour, T.E., 1994. Semibrittle and cataclastic deformation of amphibole-quartz rocks in a ductile shear zone. *Tectonophysics* 229, 19-30.
- Barruol, G., Kern, H., 1996. Seismic anisotropy and shear-wave splitting in lower-crustal and upper-mantle rocks from the Ivrea Zone-experimental and calculated data. *Physics of the earth and planetary interiors* 95, 175-194.
- Berger, A., Stünitz, H., 1996. Deformation mechanisms and reaction of amphibole: examples from the Bergell tonalite (Central Alps). *Tectonophysics* 257, 149-174.
- Biermann, C., 1981. (100) Deformation twins in naturally deformed amphiboles. *Nature* 292, 821-823.

- Biermann, C., Van Roermund K.L.M., 1983. Defect structures in naturally deformed clinoamphiboles -a TEM study. *Tectonophysics* 95, 267-278.
- Blundy, J.D., Holland, T.J.B., 1990. Calcic amphibole equilibria and a new amphibole-plagioclase geothermometer. *Contributions to Mineralogy and Petrology* 104, 208-224.
- Brenker, F.E., Prior, D.J., Müller, W.F., 2002. Cation ordering in omphacite and effect on deformation mechanism and lattice preferred orientation (LPO). *Journal of Structural Geology* 24, 1991-2005.
- Brodie, K.H., Rutter, E., 1985. On the relationship between deformation and metamorphism with special reference to the behavior of basic rocks. In: Thompson, A.B., Rubie, D.C. (Eds.), *Metamorphic Reactions: Kinetics, Textures, and Deformation. Advances in Physical Geochemistry* 4, Berlin, Springer, 138-179.
- Brown, E.H., 1977. The crossite content of Ca-amphibole as a guide to pressure of metamorphism. *Journal of Petrology* 18, 53e72.
- Buck, P., 1970. Verformung von Amphibole-Einkristallen bei drucken bis 21kb. *Contributions to Mineralogy and Petrology* 28, 62-71.
- Burchfiel, B.C., Wang, E., 2003. Northwest-trending, middle Cenozoic, left-lateral faults in southern Yunnan, China, and their tectonic significance. *Journal of Structural Geology* 25, 781-792.
- Burg, J.P., Wilson, C.J.L, Mitchell, J.C., 1986. Dynamic recrystallization and fabric development during the simple shear deformation of ice. *Journal of Structural Geology* 8, 857-870.
- Culshaw, N., Fyson, W., 1984. Quartz ribbons in high grade gneiss: modifications of dynamically formed orientations by oriented grain growth. *Journal of Structural Geology* 6, 663-668.
- Cumbest, R.J., Drury, M.R., Van Roermund, H.L.M., Simpson, C., 1989. Dynamic recrystallization and chemical evolution of clinoamphibole from Senja Norway. *Contributions to Mineralogy and Petrology* 101, 339-349.
- De Meer, S., Drury, M.R., De Bresser, J.H.P., Pennock, G.M., 2002. (Eds.) *Deformation Mechanisms, Rheology and Tectonics: Current issues and new developments in deformation mechanisms, rheology and tectonics.* Geological Society, London, Special Publications, 200.
- Díaz Azpiroz, M., Lloyd, G.E., Fernández, C., 2007. Development of lattice preferred orientation in clinoamphiboles deformed under low-pressure metamorphic conditions. A SEM/EBSD study of metabasites from the Aracena metamorphic belt (SW Spain). *Journal of Structural Geology* 29, 629-645.

- Díaz Aspiroz, M., Fernández, C., 2003. Characterization of tectono-metamorphic events using crystal size distribution (CSD) diagrams. A case study from the Acebuches metabasites (SW Spain). *Journal of Structural Geology* 25, 935-947.
- Dollinger, G., Blacic, J.D., 1975. Deformation mechanisms experimentally and naturally deformed amphiboles. *Earth Planetary Science letters* 26, 409-416.
- Drury, M.R., Ural, J., 1990. Deformation-related recrystallization processes. *Tectonophysics* 172, 235-253.
- Ernst W.G., Liu J., 1998. Experimental phase-equilibrium study of Al- and Ti-contents of calcic amphibole in MORB-A semiquantitative thermobarometer. *American Mineralogist* 83, 952-969.
- Fliervoet, T.F., Drury, M.R., Chopra, P.N., 1999. Crystallographic preferred orientations and misorientations in some olivine rocks deformed by diffusion or dislocation creep. *Tectonophysics* 303, 1-27.
- Hacker, B.R., Christie, J.M., 1990. Brittle/ductile and plastic/cataclastic transition in experimentally deformed and metamorphosed amphibolite. In: Duba, A.G., Durham, W.B., Handin, J.W., Wang, H.F. (Eds.), *The Brittle-Ductile Transition in Rocks*. AGU Geophysical Monograph Series 56, 127-148.
- Hippertt, J., Rocha, A., Lana, C., Egydio-Silva, M., Takeshita, T., 2001. Quartz plastic segregation and ribbon development in high-grade striped gneisses. *Journal of Structural Geology* 23, 67-80.
- Holland, T.J.B., Blundy, J.D., 1994. Non-ideal interactions in calcic amphiboles and their bearing on amphibole-plagioclase thermometry. *Contributions to Mineralogy and Petrology* 116, 433-447.
- Imon, R., Okudaira, T., Fujimoto, A., 2002. Dissolution and precipitation processes in deformed amphibolites: an example from the ductile shear zone of the Ryoke metamorphic belt, SW Japan. *Journal of metamorphic Geology* 20, 297-308.
- Imon, R., Okudaira, T., Kanagawa, K., 2004. Development of shape- and lattice-preferred orientations of amphibole grains during initial cataclastic deformation and subsequent deformation by dissolution-precipitation creep in amphibolites from the Ryoke metamorphic belt, SW Japan. *Journal of Structural Geology* 26, 793-805.
- Jiang, Z., Skrotzki, W., 1996. Microstructure and texture of amphibole from an amphibolite of the KTB main borehole (NE-Bavaria). *Zeitschrift für Geologische Wissenschaften* 24, 657-669.

- Kenkmann, T., 2000. Processes controlling the shrinkage of porphyroclasts in gabbroic shear zones. *Journal of Structural Geology* 22, 471-487.
- Kitamura, K., 2006. Constraint of lattice-preferred orientation (LPO) on Vp anisotropy of amphibole-rich rocks. *Geophysical Journal International* 165, 1058-1065.
- Kruse, R., Stünitz, H., 1999. Deformation mechanisms and phase distribution in mafic high-temperature mylonites from the Jotun Nappe, southern Norway. *Tectonophysics* 303, 223-249.
- Lacassin R., Leloup P.H., Tapponnier P., 1993. Bounds on strain in large Tertiary shear zones of SE Asia from boudinage restoration. *Journal of Structural Geology* 15, 677-692.
- Lafrance, B., Vernon, R.H., 1993. Mass transfer and microfracturing in gabbroic mylonites of the Guadalupe igneous complex, California. In: Boland, J.N., Fitz Gerald, J.D. (Eds.), *Defects and Processes in the Solid State: Geoscience applications, the McLaren Volume. Developments in Petrology* 4, 151-167.
- Lapworth, T., Wheeler, J., Prior, D., 2002. The deformation of plagioclase investigated using electron backscatter diffraction crystallographic preferred orientation data. *Journal of structural Geology* 24, 387-399.
- Leake, B.E., Wolley, A.R., Arps, C.E.S., et al., 1997. Nomenclature of amphiboles. Report of the Subcommittee on Amphiboles of International Mineralogical Association, Commission on New Minerals and Mineral Names. *American Mineralogist* 82, 1019-1037.
- Lee, K.L., Jiang, Z., Karato, S., 2002. A scanning electron microscope study of the effects of dynamic recrystallization on lattice preferred orientation in olivine. *Tectonophysics* 351, 331–341.
- Leiss, B., Gröger, H.R. Ullemeyer, K., Lebit, H., 2002. Textures and microstructures of naturally deformed amphibolites from the northern Cascades, NW USA: methodology and regional aspects. In: De Meer, S., Drury, M.R. De Bresser, J.H.P., Pennock, G.M. (Eds). *Deformation Mechanisms, Rheology and tectonics: Current Status and Future Perspectives. Geological Society, London, Special Publications* 200, 219-238.
- Leloup, P. H., Harrison, T. M. Ryerson, F. J, Ryerson, F.J., Chen W. J., Li, Q., Tapponnier, P., and Lacassin, R., 1993. Structural, petrological and thermal evolution of a Tertiary ductile strike-slip shear zone, Diancang Shan, Yunnan. *Journal of Geophysical Research* 98, 6715-6743.
- Leloup, P.H., Arnaud, N., Lacassin, R., Kienast, J.R., Harrison, T.M., Pan Trong, T.T., Replumaz, A., Tapponnier, P., 2001, New constraints on the structure, thermochronology and timing of the Ailao Shan–Red River shear zone, SE Asia. *Journal of Geophysical Research* 106, 6683-6732.

- Leloup, P.H., Lacassin, R. Tapponnier, P., Urs Schärer, Zhong, D. l., Liu, X.H., Zhang, L.S., Ji, S.C., Trinh, P.T., 1995. The Ailao Shan-Red River shear zone (Yunnan, China), Tertiary transform boundary of Indochina. *Tectonophysics* 251, 3-84.
- Liu, J.L. Cao S.Y., Zhai, Y. F., Song, Z.J., Wang, A.J., Xiu, Q. Y. Cao, D.H., Gao, L., Guan, Y., 2007. Rotation of crustal blocs as an explanation of Oligo-Miocene extension in Southeastern Tibet-evidenced by the Diancang Shan and nearby metamorphic core complexes. *Earth Science frontiers* 14, 40-48.
- Liu, J.L., Song, Z.J., Cao, S. Y., Zhai, Y.F., Wang A.J., Gao, L., Xiu, Q.Y., Cao, D.H., 2006. The dynamic setting and processes of tectonic and magmatic evolution of the oblique collision zone between Indian and Eurasian plates: exemplified by the tectonic evolution of the Three River region, eastern Tibet (in Chinese). *Acta Petrologica Sinica* 22, 775-786.
- Liu, J.L., Wang, A.J., Cao S.Y., Zou, Y.X., Tang, Y., Chen, Y., 2008. Geochronology and tectonic implication of migmatites from Diancangshan, Western Yunnan, China. *Acta Petrologica Sinica* 24(3): 413-420
- Liu, Y.C., 1999. Crystallographic preferred orientation and slip system of amphibole in the Florence shear zone, Central Australia. *Journal of Mineralogy and Petrology* 19, 1-7.
- Lloyd, G.E., Farmer, A.B., Mainprice, D., 1997. Misorientation analysis and the formation of subgrain and grain boundaries. *Tectonophysics* 279, 55-78.
- Mainprice, D., Nicolas, A., 1989. Development of shape and lattice preferred orientations: application to the seismic anisotropy of the lower crust. *Journal of Structural Geology* 11, 175-189.
- Morley, C.K., 2007. Variations in Late Cenozoic–Recent strike-slip and oblique-extensional geometries, within Indochina: The influence of pre-existing fabrics. *Journal of Structural Geology* 29, 36-58.
- Morrison-Smith, D.J., 1976. Transmission electron microscopy of experimentally deformed hornblende. *American Mineralogist* 61, 272-280.
- Nyman, M.W., Law, R.D.S., Melik, E.A., 1992. Cataclastic deformation for the development of core mantle structures in amphibole. *Geology* 20, 455-458.
- Passchier, C.W., Trouw, R. A. J., 2005. *Microtectonics*. Springer-Verlag, Berlin.
- Pe-Piper, G., 1988. Calcic amphiboles of mafic rocks of the Jeffers Brook plutonic complex, Nova Scotia, Canada. *American Mineralogist* 73, 993-1006.
- Randle, V., 1993. *The Measurement of Grain Boundary Geometry*. Institute of Physics Publishing, Bristol, 169 pp.

- Robison P., Ross M., Jaffe H.W., 1971. Composition of the anthophyllite-gedrite series, comparisons of gedrite and amphibole, and the anthophyllite-gedrite solvus. *American Mineralogist* 56, 1005-1041.
- Rooney, T.P., Riecker, R.E., Ross, M., 1970. Deformation twins in amphibole. *Science* 169, 173-175.
- Rooney, T.P., Riecker, R.E., Gavasci, A.T., 1975. Amphibole deformation features. *Geology* 3, 364-366.
- Schärer, U., Zhang, L.S., Tapponnier P., 1994. Duration of strike-slip movements in large shear zones: The Red River belt. *Earth and Planetary Science Letters* 126, 379-397.
- Sha, S.L., 1998. The basic features of Diancang Shan M T metamorphic zone (in Chinese). *Yunnan Geology* 1, 1-16.
- Sha, S. L., Yin, G.H., Ao, D., Duan, G. X., 2002. Discovery and significance of ophiolitic mélanges at Diancang Shan Mountain in northwestern Yunnan. *Regional Geology of China* 29, 44-47.
- Shelley, D., 1994. Spider texture and amphibole preferred orientations. *Journal of Structural Geology* 16, 709-717.
- Skrotzki, W., 1992, Defect structures and deformation mechanisms in naturally deformed amphibole. *Physics Status Solid* 131, 605-624.
- Spear, F.S., 1981. An experimental study of amphibole stability and compositional variability amphibolite. *American Journal of Science* 281, 697-734.
- Spear, F.S., 1993. *Metamorphic Phase Equilibria and Pressure-Temperature-Time Paths*. Mineralogical Society of America, Washington, D.C.
- Stünitz, H., 1993. Transition from fracturing to viscous flow in a naturally deformed metagabbro. In: Boland, J.N., Fitz Gerald, J.D. (Eds.), *Defects and Processes in the Solid State: Geoscience Applications, the McLaren Volume*. *Developments in Petrology* 4, 121-150.
- Tatham, D.J., Lloyd, G.E., Butler, R.W.H., 2008. Amphibole and lower crustal seismic properties. *Earth and Planetary Science Letters* 267, 118-128.
- Trimby, P.W., Prior, D.J., Wheeler, J., 1998. Grain boundary hierarchy development in quartz mylonite. *Journal of Structural Geology* 20, 917-933.
- Zhong, D.L., Tapponnier, P., Wu, H.W., 1990. Large-scale strike-slip fault, the major structure of intracontinental deformation after collision. *Chinese Science Bulletin* 35, 304-309.

This chapter has been published as: Shuyun Cao, Junlai Liu, Bernd Leiss, 2009. Deformation microstructures and textures, and regional tectonic significance of high-temperature shearing of the Diancang Shan Complex, Yunnan, China. Trabajos de Geología Journal 29, 147-155.

3 Deformation microstructures, textures and regional tectonic significance of high-temperature shearing of the Diancang Shan Complex, Yunnan, China

Abstract

The Diancang Shan Complex located at the northwestern extension along the Ailao Shan-Red River (ASRR) shear zone, is a representative metamorphic complex of the ASRR tectonic belt. This complex is constituted by two units, a central high-grade metamorphic belt and an eastern low-grade superposed metamorphic belt. Structural, microstructural, sub-microstructural and texture analysis of sheared rocks in the high-grade metamorphic rocks reveal that deformation of rocks occurred at high-temperature condition. The related structures, micro-structures and textures are attributed to left-lateral shearing along the ASRR shear zone, which also helps to constrain the timing of initiation of left-lateral shearing at early Oligocene.

3.1 Introduction

As the eastern border of the IndoChina block, the Ailao Shan-Red River (ASRR) shear zone in Yunnan (Southwestern China), played important roles in accommodating southeastward extrusion of the Indochina block during Indian-Eurasian plate collision and post-collisional evolution from early Oligocene to early Miocene (e.g. Tapponnier et al. 1990; Searle 2006; Leloup et al. 2007) (Fig 3.1a). Several blocks of high grade metamorphic rocks (Xuelong Shan, Diancang Shan, Ailao Shan in China and Day Nui Con Voi in Vietnam, Fig 3.1b) are exposed along the ASRR shear zone. These blocks are narrow zones of high grade metamorphic rocks bounded by brittle faults against low grade metamorphic rocks to the west and unmetamorphosed or low grade metamorphic sedimentary rocks to the east. Within the blocks, the rocks are partly sheared resulting in widespread high-temperature mylonites with sub-horizontal stretching lineation. These mylonites provide constraints on large scale left-lateral strike-slip shearing displacements of at least 600 km along the shear zone. Due to the lack of

detailed studies of microstructures and textures of these deformed rocks, debates exist on the timing of the initiation of left-lateral shearing, the significance of high-temperature deformation and the mechanisms of exhumation of the high grade metamorphic rocks.

The Diancang Shan block, lying to the northwestern extension of the Ailao Shan metamorphic complex, is a typical metamorphic complex in the ASRR shear zone. The metamorphic complex is mainly constituted by two units, a central high grade metamorphic belt to the west and a low grade superimposed metamorphic belt to the east (Fig 3.1a).

The central high grade metamorphic belt, is constituted by a sequence of metamorphic rocks of amphibolites facies, including amphibolites, marbles, schists, gneisses and mylonites with typical high-temperature mineral assemblages: sillimanite + garnet + staurolite + kyanite, amphibole + plagioclase, and tremolite + diopside + olivine + calcite + dolomite. The metamorphic rocks together with multi-phase granitic dikes and intrusions are often mylonitized by intensive left-lateral strike-slip, resulting in the formation of typical L-tectonites (Fig 3.2 a, b and d).

A low-grade shear zone related to exhumation of the Diancang Shan metamorphic complex (or metamorphic core complex, Liu et al. 2007) in a later event occurs as a low-grade superimposed metamorphic belt along the eastern flank of the Diancang Shan range. The high-temperature metamorphic rocks are overprinted by the low grade shear deformation at greenschist facies conditions. Low temperature mineral assemblages and fabrics are well preserved. The resultant mylonites displaying L-S type fabrics and are characterized by retrogressive chloritic mylonites. Macro- and micro-shear sense indicators suggest a top to the east shearing.

3.2 Techniques

Standard thin sections are cut parallel to the lineation and perpendicular to the foliation of mylonite samples. Microstructures are analyzed by optical microscopy (OM) and sub-microstructures are observed by high resolution transmission electron microscope (TEM). Energy dispersion spectroscopy (EDS) is applied to identify the compositions of minerals. Shimadzu EPMA-1600 electron microprobe analysis is used to carry out quantitative analysis of mineral chemistry. Textures of amphibole are measured on a Hitachi 3400N scanning electron microscope (SEM) equipped with a HKL Channel 5 electron back-scattered diffraction (EBSD) detector. All the analyses were finished at the State Key Laboratory of Geological Processes and Mineral Resources (Beijing).

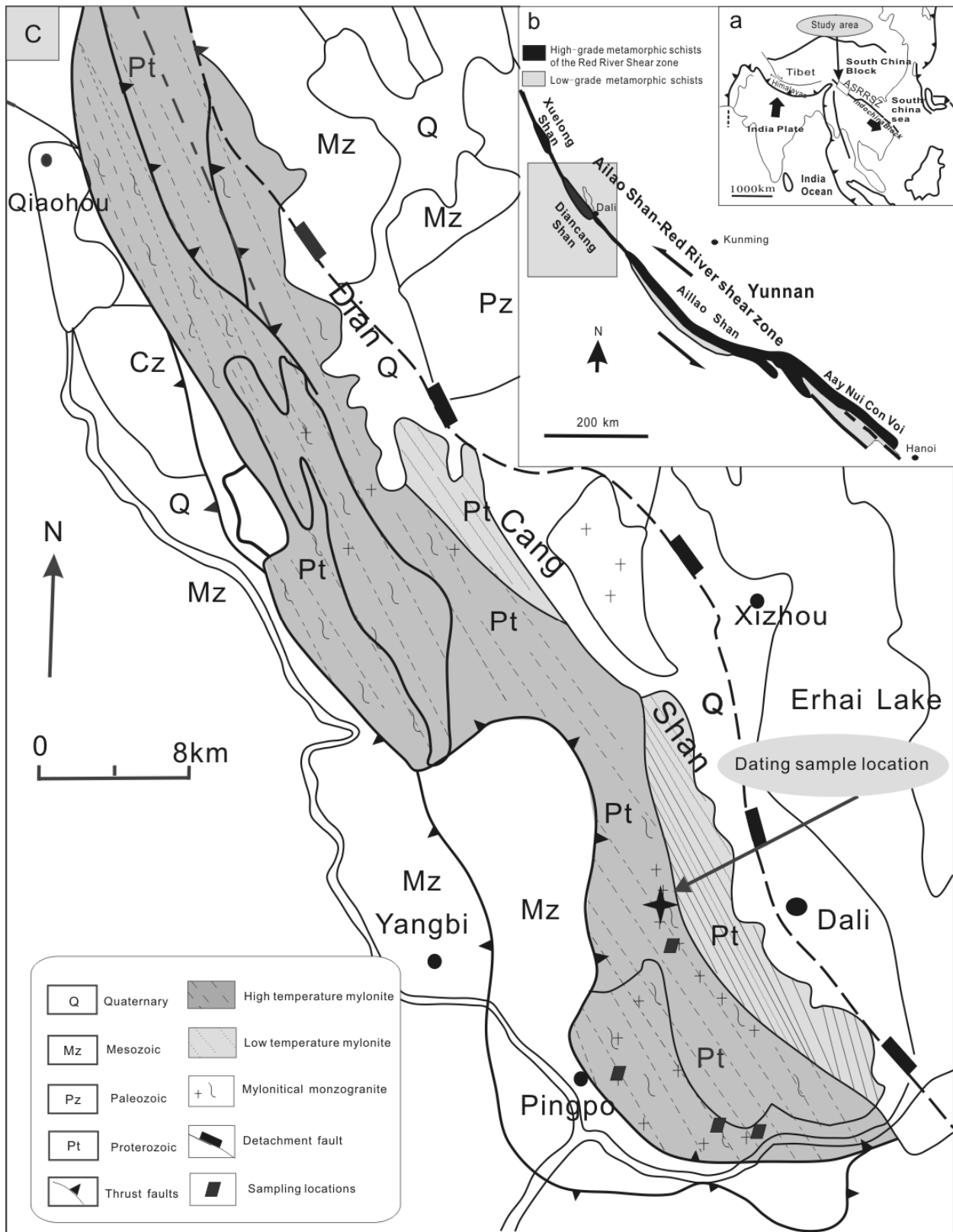


Fig. 3.1 Tectonic setting and structural outline of Diancang Shan area. a) Regional tectonic framework of Southeast Asia; b) Xuelong Shan, Diancang Shan, Ailao Shan and Day Noi Con Voi metamorphic blocks along the Ailao Shan-Red River shear zone; c) Structural framework of the Diancang Shan area. ASRRSZ= Ailao Shan-Red River shear zone.

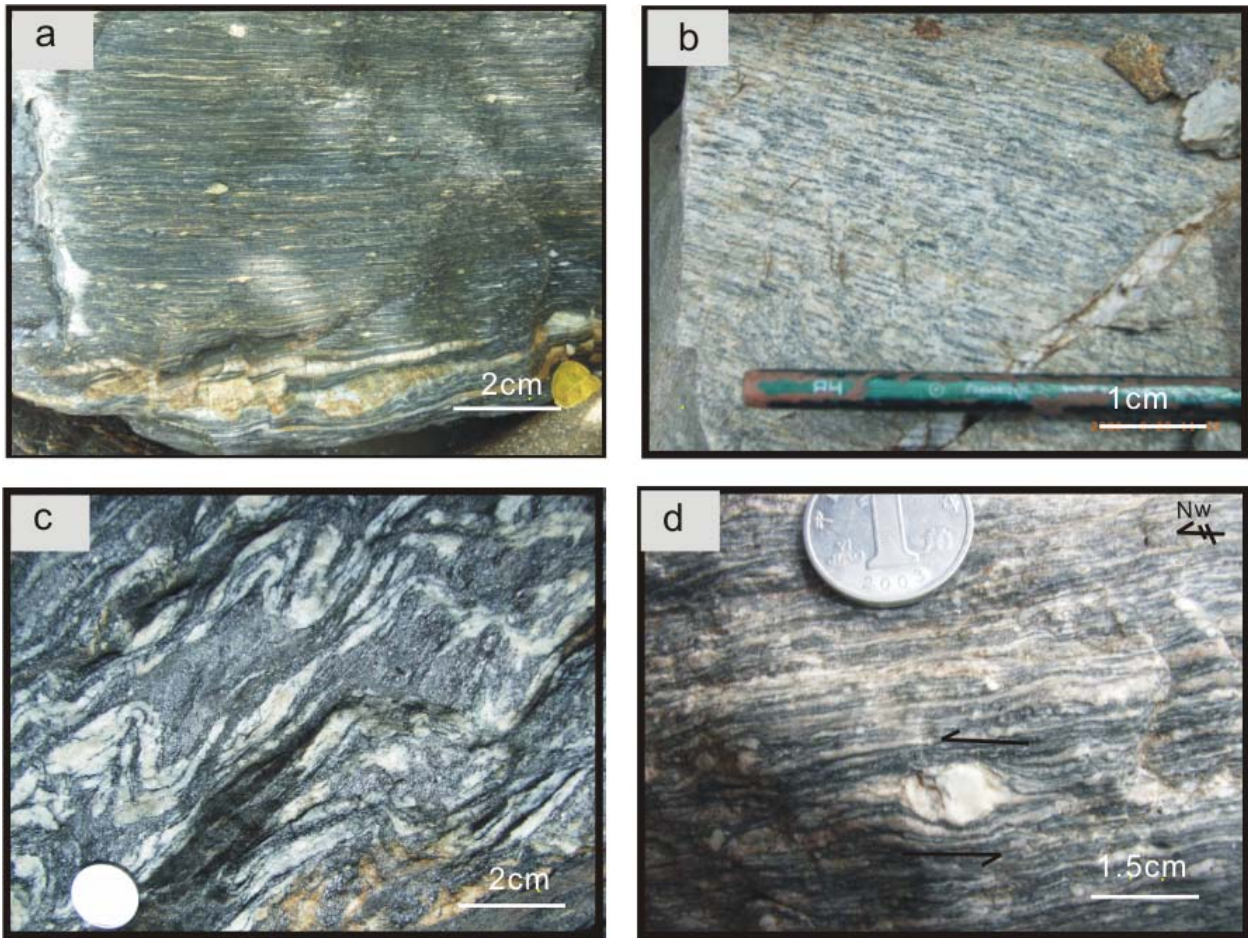


Fig. 3.2 Outcrop scale structural evidences of high-temperature ductile deformation, observed in high grade metamorphic rocks in Diancang Shan: a) Amphibolitic ultramylonite with strong stretching lineation (L-tectonite); b) Stretching lineation (L-tectonite) shown by diorite xenoliths in granite; c) tight folds in biotite gneiss; d) Feldspar porphyroclasts indicating left-lateral shear by asymmetric recrystallized tails

3.3 Results

3.3.1 Macro-and micro-structures of mylonites from high grade metamorphic complex

High-temperature mylonites derived from either granitic rocks or amphibolitic rocks constitute the main part of the shear zones in the high grade metamorphic complex. At the outcrop scale, asymmetric folds (e.g. hook-like folds) and tight folds (Fig. 3.2c) are well-developed in sheared gneisses (such as sillimanite or amphibolitic gneisses) and are characteristic for high-temperature ductile flow. Hinges of the folds are mostly parallel to subhorizontal NNW-SSE stretching lineation. Elongated quartz, feldspar and fine-grained biotite mineral aggregates form the extremely strongly developed stretching lineation fabrics, which is the most remarkable feature of high-temperature mylonite in the shear zone (Fig. 3.2 a, b and d). Such fabrics occur in both

sheared metamorphic rocks and sheared granitic dikes or monzogranitic intrusions. The widespread and penetrative occurrence of these structures suggests that the gneisses experienced very intense progressive left-lateral strike-slip deformation (Fig. 3.2b).

Augen structures in mylonitized monzogranite and amphibolites are also typical features of the high-temperature mylonites. They are composed of K-feldspar, plagioclase and amphibole porphyroclasts and fine matrix of feldspar, quartz, amphibole and other mineral phases. Microstructural features like σ , δ and S-C fabrics consistently document a left-lateral shear (Fig. 3.2d).

Different mineral phases show distinctive deformation structures. Quartz grain boundaries of equigranular grains often form triple junctions. Serrated grain boundaries are observed in some cases, suggesting local high-temperature grain boundary migration. Rectangular and sigmoidal quartz aggregates are parallel to the major foliation and lineation of the rocks. Rare occurrence of dislocation substructures in quartz grains points to the importance of high-temperature recovery and recrystallization during or after high-temperature shearing (Fig. 3.4d). Feldspar grains show typical characteristics of high-temperature plastic deformation (Fig. 3.3c): they are elongated or partly twinned, and some are partly or completely dynamically recrystallized into fine-grained matrix. The porphyroclastic cores show undulatory and inhomogeneous extinction, and have core-mantle structures and subgrains. Mechanical twinning and a few free dislocations near twin boundaries are also the effects of plastic deformation. TEM analyses show that some dislocations are organized into dislocation walls and form subgrains. Thus K-feldspar recrystallization seems to be dominated by the subgrain rotation process. Deformation of K-feldspar was associated with metasomatism by relatively calcium-rich plagioclase to form myrmekite structure (Fig. 3.3d), suggesting plastic deformation at feldspar recrystallization temperature above 550 °C (Vernon 1991; Menegon et al. 2006).

Amphibolitic mylonites have typical mylonitic microstructures, shown by coarse amphibole porphyroclasts and fine-grained matrix. Two distinct types of amphibole porphyroclasts are distinguished:

Type I porphyroclasts are oriented with their [001]-axis perpendicular to the stretching lineation, i.e. the shearing direction. They generally have regular shapes, and most retain euhedral shapes with rhombic or polygonal outlines in (100) section. Grain boundaries are typically straight and regular or slightly curved (Fig. 3.3e). The grains have rare evidences of weak crystal plastic deformation. Instead, they are characterized by frequent occurrence of microfractures (particularly along cleavage planes), and by sharp changes between porphyroclasts and new fine grains in the matrix.

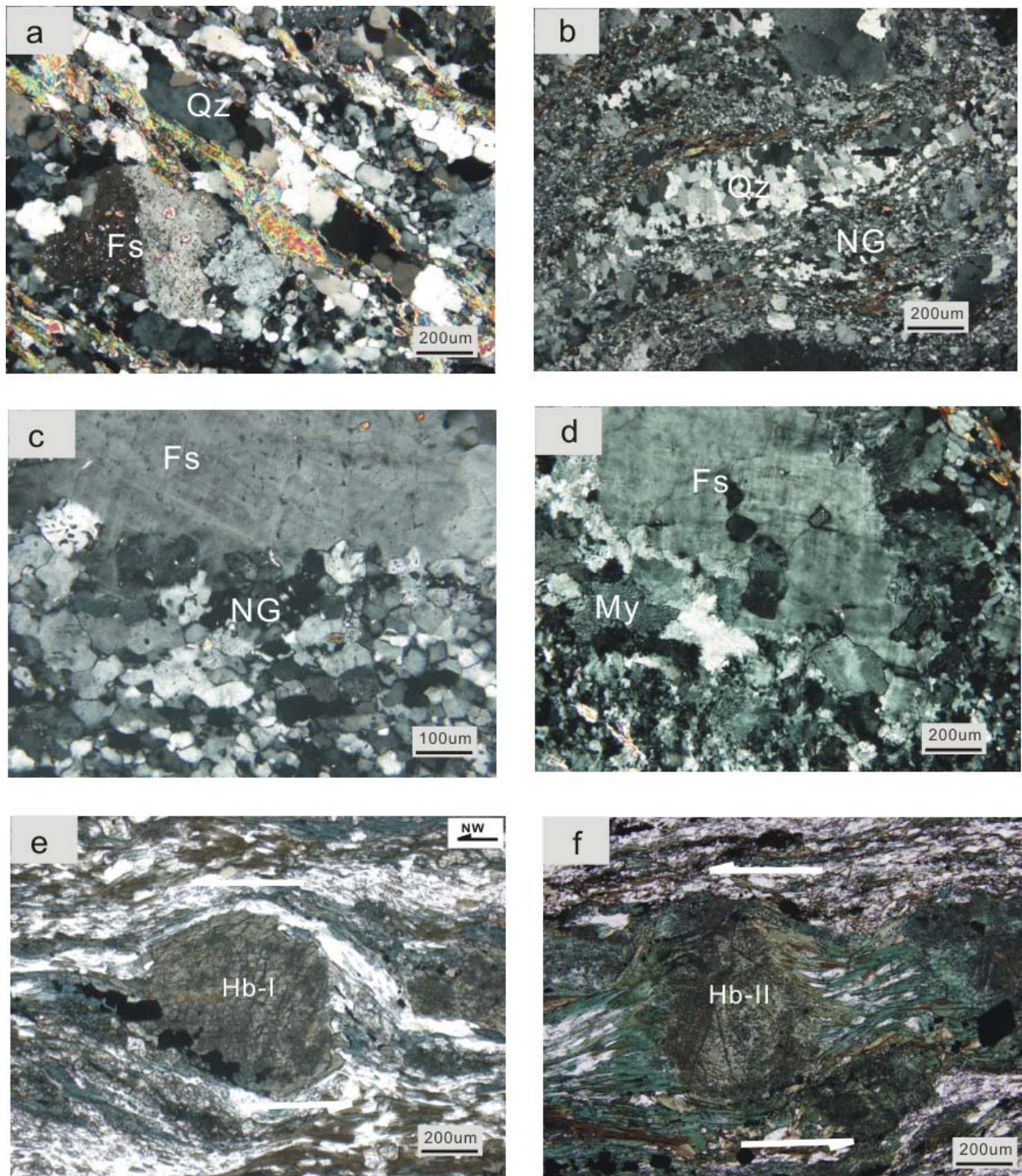


Fig. 3.3 Microscopic high-temperature deformation characteristics of high grade metamorphic rocks in Diancang Shan: a) Polycrystalline quartz (Qz) ribbons and fine-grained feldspar porphyroclasts (Fs); b) Sigmoidal quartz aggregate and new fine-grained feldspar (NG); c) K-feldspar porphyroclasts (Fs) and transition to recrystallized grains in the matrix; d) Myrmekites (My) around a K-feldspar porphyroclast (Fs); e) Amphibole type I porphyroclasts (Hb-I) with [001] normal to shear direction. f) Amphibole typical type II porphyroclast (Hb-II) with [001] parallel to the shearing direction.

Type II amphibole porphyroclasts are oriented with their [001]-axis parallel or subparallel to the stretching lineation or shearing direction (Fig. 3.3f). They are either lens-shaped or fish-shaped and show ϕ , σ or δ fabrics. Undulatory, partly discontinuous extinction, deformation twins, subgrains, core-mantle structures etc. are widespread in type II porphyroclasts. They generally show a gradual transition into fine recrystallized grains in the matrix. New fine grains are heterogeneously distributed, constituting alternating domains of amphibole-rich and quartzofeldspathic zones. TEM observation reveals that they generally have acicular shapes with long axes parallel to the stretching lineation. Various dislocation substructures are observed in amphibole grains, especially within deformed porphyroclasts. Free dislocations, dislocation dipoles, dislocation arrays, dislocation walls, subgrains formed by dislocation walls, and twin boundaries are the most commonly observed dislocation microstructures. Tangled dislocations are the dominant dislocation patterns in type I porphyroclasts (Fig. 3.4a). Variations of dislocation patterns are common in type II porphyroclasts. In the core of type II porphyroclasts, dislocations are irregularly organized into tangled dislocation walls and regularly organized towards marginal zones of the porphyroclasts. Twins of micron scale are generally straight and regular, and some twin boundaries are constituted by well-organized dislocations (Fig. 3.4b). New fine grains in the matrix show few free dislocations (Fig. 3.4c).

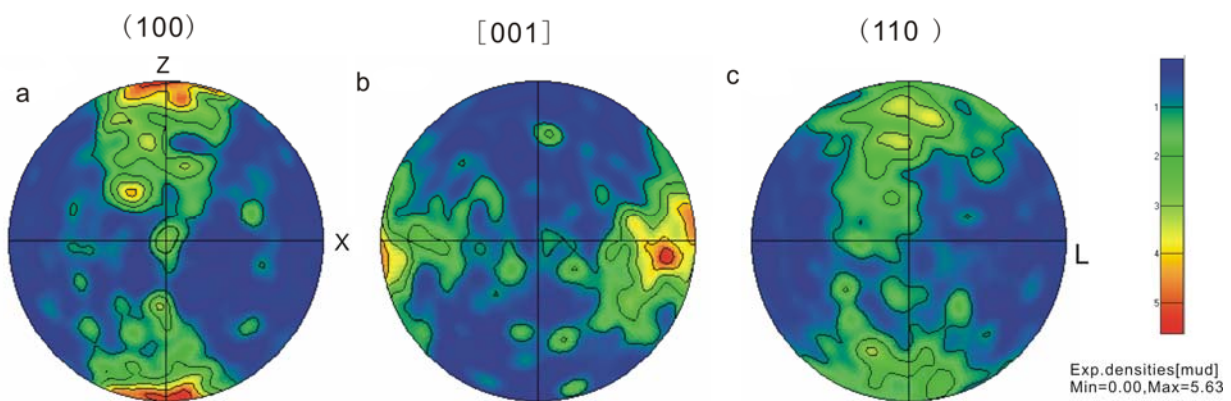


Fig. 3.4 Amphibole textures of recrystallized matrix grains of amphibolitic mylonite obtained by EBSD analysis: a) (100)-planes; b) [001]-axes. c) (110)-planes; Foliation- XY-solid line, lineation-X direction; Equal area projection and lower hemisphere.

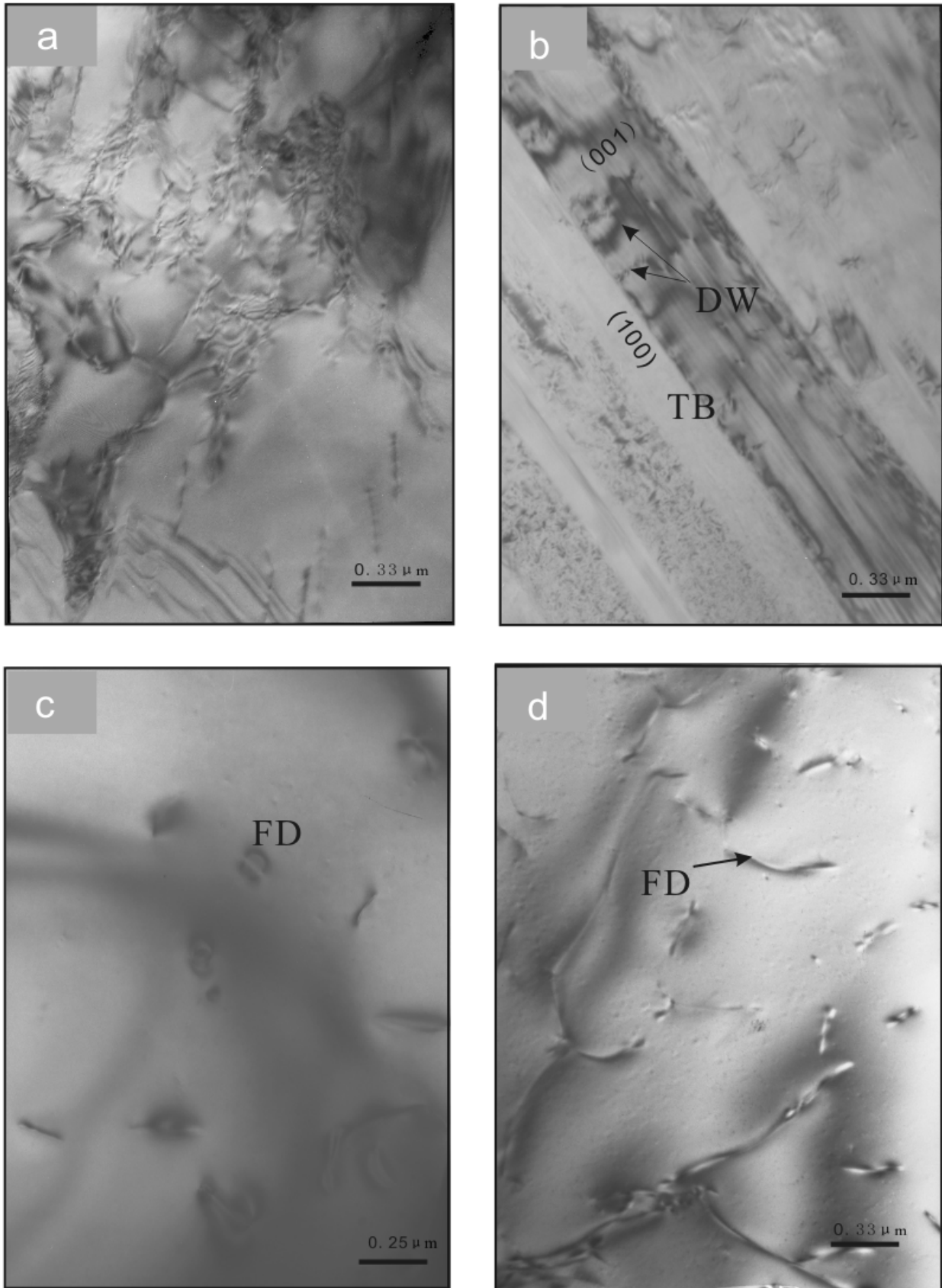


Fig. 3.5 TEM submicrostructural characteristics in amphibole and quartz from high grade metamorphic rocks: a) Tangled dislocations from the core of a type I amphibole porphyroclast; b) Regular twin boundaries (TB), dislocations in twins and twinned hosts, and dislocation walls (DW) perpendicular to twin boundaries from

margins of type II amphibole porphyroclasts; c) Matrix amphibole grains containing only a few free dislocations (FD); d) Some free dislocations (FD) in quartz grains.

3.3.2 Texture analysis of amphibole in amphibolitic mylonites

Textures of amphibole grains from the matrix of ultramylonites, cores of type I and type II porphyroclasts and matrix grains around the porphyroclasts are analyzed by EBSD. It is shown that [001] crystallographic axes and (100) crystallographic planes of dynamically recrystallized amphibole grains lie within these mylonitic foliation and parallel to the stretching lineation (Fig. 3.5a and b). Such a parallelism implies that the texture of dynamically recrystallized amphibole grains resulted from a dominant activation of (100) [001] slip system (twinning) (Fig. 3.5c), which is related to high-temperature deformation (Dollinger & Blacic, 1975, Cao et al., 2007).

3.3.3 Estimation and calculation of pressure and temperature during deformation

The estimation and calculation of pressure and temperature of deformation and metamorphism of type I porphyroclasts, type II porphyroclasts and matrix grains in the amphibole mylonites is made by applying the geobarometer of Schmidt (1992) and hornblende-plagioclase geothermometer of Holland and Blundy (1994). The estimated pressures are between 0.599 GPa - 0.710 GPa, with an average of 0.653 GPa and the calculated temperatures vary between 604 °C- 674 °C, with an average of 636 °C. These estimates indicate amphibolites facies conditions.

3.4 Discussions and Conclusions

3.4.1 Indication of high-temperature deformation

All the above described observations indicate high-temperature deformation in the Diancang Shan during left-lateral shearing along the ASRR. Macroscopic fold patterns and microstructural features are typical of high-temperature flow of rocks. OM and TEM analysis reveals the dominance of high-temperature recovery and recrystallization of quartz, feldspar and amphibole. Amphibole texture analyses give clues to the importance of (100) [001] slip systems during dynamic recrystallization. P/T calculations give pressures and temperatures of lower amphibolite facies.

3.4.2 Significance of high-temperature shearing

Whether left-lateral shearing occurred prior or postdated high-temperature metamorphism remains the key to understanding the timing of initiation and duration of left lateral shearing along the ASRR. Leloup et al. (1995, 2001) and Schärer et al. (1990, 1994) stressed on the simultaneity of shearing, the generation of granitic magma by shear heating, and the intrusion of the magma into veins. In combination of structural analysis of mylonitic rocks and U-Pb dating of zircon, monazite and xenotime in the intrusions, they suggested that large scale shearing along the ASRR initiated at about 35 Ma and lasted until 17 Ma. High-temperature left-lateral shear in the Ailao Shan and Diancang Shan is also documented by left-laterally sheared garnet-sillimanite bearing mylonitic paragneiss (e.g. Leloup et al. 2007). Tran et al. (1998), however, revealed that the peak metamorphism took place under amphibolite-facies conditions and the subsequent mylonitization occurred under greenschist-facies conditions. Searle (2006) also interpreted the ASRR shear zone as an upper crustal, left-lateral strike-slip fault that cuts through previous high grade metamorphic rocks and early formed granites. Metamorphism of the Day Nui Con Voi metamorphic rocks in Vietnam predated and is unrelated to shearing along the ASRR shear zone. Searle (2006) then argued that shear fabrics associated with left-lateral slip postdate peak metamorphism, constraining the timing of initiation of shearing to 21 Ma at relatively low temperature conditions.

Our observations on the Diancang Shan mylonites suggest that the deformation microstructures and textures resulted from high-temperature deformation and dynamic recrystallization are attributed to left-lateral shearing along the ASRR shear zone. The emplacement of magmatic dikes and mozogranitic intrusion are synkinematic. Our recent SHRIMP dating from a synkinematic mozogranitic intrusion displaying the above-mentioned high-temperature microstructures and textures give an age of 30.88 Ma (Cao et al., in prep.), which constrains the timing of initiation of left-lateral shearing at early Oligocene.

Acknowledgement

This study received financial support from the State Key Research “973” Plan of China (Grant No. 2002CB412607), National Natural Science Foundation of China (40872139), Ministry of Land and Resources (200811008) and State Key Laboratory of Geological Processes and Mineral Resources (Grant No. GPMR200637 and and No. GPMR200837). We thank Dr. A. Vollbrecht for helpful discussions and revision of early versions of the manuscript.

References

- Cao, S. Y., Liu, J. L., Hu, L. (2007): Micro- and submicrostructural evidence for high-temperature brittle-ductile transition deformation of amphibole: Case study of high-grade mylonites from Diancangshan, western Yunnan: *Science in China Series D: Earth Sciences*, 50(10): 1459-1470.
- Dollinger, G. and Blacic, J. D. (1975): Deformation mechanisms in experimentally and naturally deformed amphiboles: *Earth and Planetary Science Letters*, 26: 409-416.
- Holland, T. J. B. and Blundy, J. D. (1994): Non-ideal interactions in calcic amphiboles and their bearing on amphibole-plagioclase thermometry: *Contrib. Miner. Petrol.*, 116: 433-447.
- Leloup, P. H., Lacassin, R. and Tapponnier, P., Zhong, D., Liu, X., Zhang, L., Ji, S. and Trinh, P.T. (1995): The Ailao Shan-Red River shear zone (Yunnan, China), Tertiary transform boundary of Indochina. *Tectonophysics*, 251: 3-84.
- Leloup, P. H., Arnaud, N., Lacassin, R., Kienast, J. R., Harrison, T. M., Phan Trong, T. T., Replumaz, A. and Tapponnier, P. (2001): New constraints on the structure, thermochronology and timing of the Ailao Shan-Red River shear zone, SE Asia. *J. Geophys. Res.*, 66: 1083-6732.
- Leloup, P. H., Tapponnier, P. and Lacassin, R. (2007): Discussion on the role of the Red River shear zone, Yunnan and Vietnam, in the continental extrusion of SE Asia. *J. Geol. Soc., London*, 164:1253-1260.
- Liu, J. L., Cao, S. Y., Zhai, Y. F., Song, Z. J et al. (2007): Rotation of crustal blocks as an explanation of Oligo-Miocene extension in southeastern Tibet-evidenced by the Diancangshan and nearby metamorphic core complexes. *Earth Science Frontiers*, 14 (4): 40-48.
- Menegon, L., Pennacchioni, G. and Stünitz, H. (2006): Nucleation and growth of myrmekite during ductile shear deformation in metagranites. *J. metam. Geol.*, 24, 553-568.
- Schärer, U., Tapponnier, P., Lacassin, R. and Leloup, P. H., Zhong, D. and Ji, S. (1990): Intraplate tectonics in Asia: a precise age for large-scale Miocene movement along the Ailao Shan-Red River shear zone, China. *Earth and Planetary Sci. Lett.*, 97: 65-77.
- Schärer, U., Zhang, L. S and Tapponnier, P. (1994): Duration of strike-slip movements in large shear zones: The Red River belt, China. *Earth and Planetary Sci. Lett.*, 126: 379-397.
- Searle, M. (2006): Role of the Red River Shear zone, Yunnan and Vietnam, in the continental extrusion of SE Asia, *J. Geol. Soc., London*, 163:1025-1036.

- Schmidt, M. (1992): Amphibole composition in tonalite as a function of pressure: An experimental calibration of the Al-in hornblende barometer. *Contr. Miner. Petrol*, 110: 304-310.
- Tapponnier, P., Lacassin, R., Leloup, P. H., Schärer, U., Zhong, D. L., Liu, X. H., Ji, S. C., Zhang, L. S. and Zhong, J. Y. (1990): The Ailao Shan/Red River metamorphic belt: Tertiary left-lateral shear between Indochina and South China. *Nature*, 343: 431-437.
- Tran, N. N., Mitsuhiro, T. and Tetsumaru, I. (1998): P-T-t paths and post-metamorphic exhumation of the Day Nui Con Voi shear zone in Vietnam. *Tectonophysics*, 290: 299-318.
- Vernon, R. H. (1991): Questions about myrmekite in deformed rocks. *J. Struct. Geol.*, 13, 979–985.

This chapter has been published as: Shuyun Cao, Junlai Liu, Bernd Leiss, Axel Vollbrecht, Johann Genser, Franz Neubauer, Chunqiang Zhao, 2011. Initiation of left-lateral deformation along the Ailao Shan-Red River shear zone: new geochronological, microstructural and textural constraints from the Diancang Shan metamorphic massif, SW Yunnan, China. International Geology Review. DOI: 10.1080/00206814.2010.543789.

4 Initiation of left-lateral deformation along the Ailao Shan-Red River shear zone: new geochronological, microstructural and textural constraints from the Diancang Shan metamorphic massif, SW Yunnan, China

Aabstract

The Diancang Shan metamorphic massif, the northwestern extension of the Ailao Shan massif, is a typical metamorphic complex situated along the NW-SE trending Ailao Shan-Red River (ASRR) shear zone. Diancang Shan granitic and amphibolitic mylonites collected from sheared high-grade metamorphic rocks were studied using optical microscope and EBSD techniques. SHRIMP U–Pb dating of zircon grains from the granitic mylonites constrain the timing of shearing. Macro- and microstructural and textural analysis reveals intense plastic deformation of feldspar, quartz and amphibole under amphibolite-facies conditions, and all consistently document left-lateral shearing. Porphyritic monzogranitic mylonite along the shear zone possesses evidence supporting a sequential, progressive process from crystallization during magma emplacement, through submagmatic flow to solid-state plastic deformation. We suggested that the early-kinematic pluton subsequently underwent strong left-lateral strike-slip shearing. The development of complex textures of quartz, feldspar and amphibole from the granitic and amphibolitic mylonites apparently recorded a successive variation of deformation conditions during progressive shearing. They are coherent and reflect solid-state high-temperature ductile deformation during regional sinistral shearing. Relatively low-temperature modification of the quartz c-axis fabrics within the Diancang Shan massif are related to an exhumation and cooling event. All magmatic zircons give U-Pb ages of 30.95 ± 0.61 Ma for the crystallization of the granite. This age provides the timing of onset of left-lateral shearing along the ASRR shear zone in the Diancang Shan high-grade metamorphic massif.

4.1 Introduction

The current tectonic activity in Asia is widely cited as the consequence of continental collision between Indian and Eurasian plates since the Eocene. Lithospheric material of the Tibetan Plateau and adjacent regions has undergone significant intracontinental deformation, especially along a series of major strike-slip fault zones (e.g. Molnar and Tapponnier, 1975; Tapponnier et al. 1986; 1990; Wang et al., 1998; Burchfiel and Wang, 2003) (Fig. 4.1A and B). As the eastern boundary of the Indochina block, the NW-trending Ailao Shan-Red River (ASRR) shear zone in Southwest China (Fig. 4.1B) plays an important role in accommodating southeastward extrusion of the Indochina block during the plate collision and postcollisional evolution (e.g. Guo et al., 1986; Tapponnier et al., 1986, 1990; Zhong et al., 1990; Harrison et al., 1992, 1996; Wang and Burchfiel, 1997; Chung et al., 1997, 1998, 2008; Tran et al., 1998; Wang et al., 1998, 2000; Sun et al., 2003; Liu et al., 2004, 2006, 2007; Searle 2006; Yeh et al., 2008). Recent studies on the structural and tectonic aspects of the ASRR shear zone are mainly focused on the southern segment, i.e. the Ailao Shan in China and the Day Noi Con Voi in Vietnam, which has improved our understanding of the tectonothermal evolution of the shear zone and its role in regional tectonic evolution (e.g. Leloup et al., 1995, 2007; Tran et al., 1998; Jolivet et al., 2001; Searle, 2006; Anczkiewicz et al., 2007; Yeh et al., 2008; Sassier et al., 2009; Zhu et al., 2009; Fyhn et al., 2009). It is generally accepted that Late Oligocene-Early Miocene shearing along the ASRR shear zone leads to over 500 km southward displacement of the Indochina block (e.g. Huang, 1960; Tapponnier et al., 1986; Leloup et al., 1995; Chung et al., 1997; Searle, 2006) relative to the Yangtze-South China block. The process was accompanied by the opening of the South China Sea (e.g. Peltzer et al., 1988; Tapponnier et al., 1990; Briais et al., 1993; Leloup et al., 1995; Harrison et al., 1992, 1996; Chung et al., 1998). These were partly proven by the metamorphic, deformation and thermochronological analysis of the high-grade metamorphic rocks of the four massifs (e.g. Xuelong Shan, Diancang Shan, Ailao Shan and Day Nui Con Voi metamorphic massifs) exposed along the shear zone (e.g. Leloup et al., 1993, 1995; Tran et al., 1998; Liu et al., 2007).

There have been extensive discussions on the timing of initiation and duration of left-lateral shearing along the ASRR, the total finite offsets, and the scale of the fault (crustal or mantle) and the mechanism of exhumation of the high-grade metamorphic rocks (e.g. Molnar and Tappinnier, 1975; Tapponnier et al., 1982, 1990; Harrison et al., 1992, 1996; Lacassin et al., 1993; Leloup et al., 1995, 2001a, b, 2007; Wang et al., 1998, 2000, 2001; Nagy et al., 2001; Jolivet et al., 2001; Gilley et al., 2003; Searle, 2006, 2007; Viola and Anczkiewicz, 2008; Yeh et al., 2008). For example, Gilley et al. (2003), by dating monazite from the mylonitic fabric and synkinematic

garnet growths from the northern segments of the ASRR in Yunnan, revealed that the left-lateral strike-slip and high-temperature metamorphism along the ASRR shear zone occurred between 34 to 21 Ma. In the Ailao Shan and Diancang Shan, the total set of U–Pb ages from zircon, monazite, xenotime and sphene shows that magmatic activities occurred from 35 to 20 Ma (Schärer et al., 1994; Zhang and Schärer, 1999). Because left-lateral shearing was coeval with cooling, $^{40}\text{Ar}/^{39}\text{Ar}$ data documented the timing of ductile deformation in ASRR shear zone from 31 to 17 Ma (e.g. Harrison et al., 1992; 1996; Leloup and Kienast, 1993; Tran et al., 1998; Jolivet et al., 2001; Leloup et al., 2001a, 2001b; Maluski et al., 2001; Garnier et al., 2002). However, Wang et al. (2000) suggested that the exhumation of metamorphic massif by shearing along the ASRR shear zone began at 27 Ma and lasted until 22 Ma by applying $^{40}\text{Ar}/^{39}\text{Ar}$ dating of amphibole, muscovite, biotite and K-feldspar from the Day Nui Con Voi metamorphic massif. They proposed that, because the onset of the left-lateral shearing along the ASRR shear zone did not occur until 27 Ma, it might not related to the opening of the South China Sea (Chung et al., 1997). Recent studies by Sassier et al. (2009) revealed the monazite U–Pb ages of 30 Ma from the strongly deformed leucocratic dykes and of 22 Ma from the less deformed leucocratic dykes, and the ages of 24 and 26 Ma of monazite from intermediately deformed ones suggest that the left-lateral shearing at least started prior to 26 Ma. $^{40}\text{Ar}/^{39}\text{Ar}$ dating of amphibole, biotite and muscovite suggests that cooling during exhumation of the high-grade rocks in these massifs is related to the transtensional setting of the Ailao Shan range between 27 and 17 Ma, which progressively exhumed the shear zone rocks from southeast to northwest (e.g. Harrison et al., 1992, 1996; Leloup et al., 2001b).

Whether left-lateral shearing is prior to or postdating the high-temperature metamorphism also remains the key to the understanding of the timing of left lateral shearing along the ASRR. Leloup et al. (2001a, b) and Schärer et al. (1990, 1994) stressed on the simultaneity of shearing, the generation of granitic magma by shear heating, and the intrusion of the magma into veins. High-temperature left-lateral shearing along the Ailao Shan and Diancang Shan is also documented by left-laterally sheared garnet-sillimanite bearing mylonitic paragneiss (e.g. Leloup et al., 1995). Tran et al. (1998), however, revealed that the peak metamorphism took place under amphibolite-facies conditions and the subsequent mylonitization occurred under greenschist-facies conditions. Searle (2006) interpreted the ASRR shear zone as an upper crustal, left-lateral strike-slip fault that cuts through previous high-grade metamorphic rocks and early formed granites. Metamorphism of the Day Nui Con Voi metamorphic massif in Vietnam predated shearing and is, therefore, unrelated to shearing along the ASRR shear zone (Searle, 2006). These authors, therefore, argued that shear fabrics associated with left-lateral

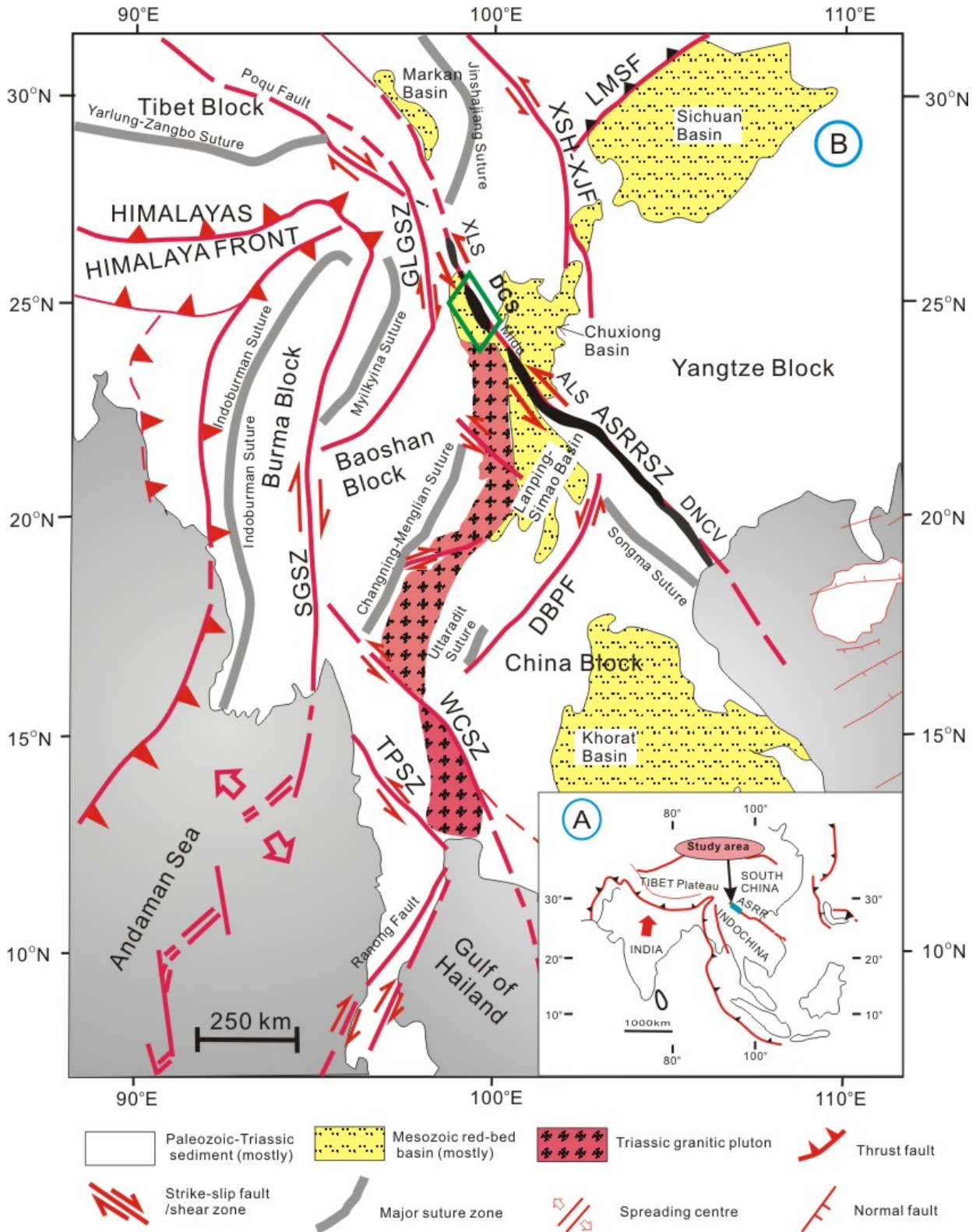


Fig. 4.1 Tectonic sketch map of major tectonic features of Southeast Asia (modified after Tapponnier et al., 1986, Leloup et al., 2005 and Morley, 2007). A - Geologic sketch of the extrusion of Indochina in response to northward penetration of India. B - Major fault and shear zones of Southeast Asia. ASRRSZ=Ailao Shan-Red River shear zone; GLGSZ=Gaoligong shear zone; SGSZ=Sagaing shear zone; WCSZ=Wang Chao shear zone; TPSZ=Three Pagoda shear zone; XLS=Xuelong Shan massif; DCS=Diancang Shan massif; ALS=Ailao Shan massif; DNCV=Day Nui Con Voi massif.

slip postdate peak metamorphism at relatively low-temperature conditions and suggested that the left lateral shearing initiated from 21 Ma, instead of 35 Ma. From this aspect, they questioned the role of the shear zone during postcollisional accommodation of southeast-directed lateral extrusion in eastern Tibet.

As a result, the age of the onset of shearing along the ASRR shear zone becomes the key to the understanding of the above arguments and therefore needs to be addressed in great detail. Due to the lack of minerals for direct dating of deformation events, the relation between magmatism and shearing has therefore become the solely important way to provide a means of determination of the age of the deformational event. In particular, the main mineral texture patterns and microstructures of plutonic bodies can help address the link between magma emplacement and tectonics. Abundant studies (e.g. Brown and Solar, 1998; 1999; Paterson et al., 1998; Rosenberg, 2004) indicate that emplacement can be considered either tectonically controlled (syn-tectonic) if the magmatic structure or microstructure and texture are consistent with the regional strain field, or magma-pressure driven if the pattern is independent (post-tectonic). Interpretation of the relative timing of plutonic crystallization and regional deformation is a complex problem because of the changing rheology of magma as it crystallizes, and because of incomplete understanding of the range of possible fabrics that can form in the transition from magma to crystalline solid (e.g. Paterson et al., 1989, 1991a, 1991b; Karstrom 1993; Miller and Paterson, 1994).

This paper presents results of a detailed study on the timing of plutonic intrusion and shearing in the rocks, with a case study from the Diancang Shan massif. We conducted integrated analysis of optical deformation microstructures, EBSD textures of the main mineral phases from the granitic mylonite and wall rocks e.g. amphibole mylonite, and SHRIMP zircon U/Pb dating of the early kinematic porphyritic monzogranitic mylonite, collected from the Diancang Shan massif. The results provide a better constraint on the timing of emplacement of the granitic intrusion and the initiation of the left-lateral shearing along the ASRR shear zone. It will also provide some clues to the exhumation mechanism and regional tectonic evolution of the ASRR shear zone.

4.2 Geological setting and structural geology

The high-grade metamorphic rocks are mostly amphibolites, amphibole-plagioclase gneisses, sillimanite schists, and migmatites (e.g. Sha, 1998; Sha et al., 2002), and plutonic intrusions of

various ages. High-temperature assemblages preserved in these mylonites include almandine + staurolite + kyanite + sillimanite in schists; tremolite + diopside + olivine + calcite + dolomite in marbles; and amphibole + garnet + plagioclase in amphibolites. They are highly mylonitized due to left-lateral ductile shearing. A remarkable feature of the mylonites (of both metamorphic and granitic derivations) is their extremely strong stretching lineation fabrics, in contrast to poorly developed mylonitic foliation, thus forming L and $L \gg S$ fabrics (Fig. 4.3a, c and e). When present, the mylonitic foliation strikes NNW–SSE. Lineation is subhorizontal or plunges gently either to the NNW or to the SSE (Fig. 2.2B). At the outcrop scale, sheath folds are common in the sheared gneisses, schists and marbles (Fig. 3d and f), which show characteristics of plastic flow and intense ductile shearing. Hinges of the sheath folds are mostly parallel to the subhorizontal NNW–SSE oriented stretching lineation. The incipient S–C fabrics are present in the mylonitic monzogranite and felsic veins (Fig. 4.3b). The S-plane is defined by grain aggregates of feldspar, quartz and mica, and C-plane mainly by strongly elongated grains of feldspar and amphibole. The acute angle between S and C is generally between 20 and 45°. Widespread occurrence of different shear criteria (e.g. sheared veins, S–C fabric and sigma- and delta-type porphyroclasts) suggests that these gneisses experienced intensive progressive left-lateral strike-slip shearing (Fig. 4.4 b and c).

Retrograde metamorphism overprinted the high-temperature metamorphic belt along the eastern flank of the Diancang Shan range and is possibly related to the exhumation of the Diancang Shan high-grade metamorphic complex (or metamorphic core complex, Liu et al., 2007) in a later event. Early high-temperature mylonites were sheared at greenschist facies conditions along margins of this zone, resulting in low-temperature mineral assemblages and fabrics in chloritic mylonites. Mafic minerals (e.g. amphibole and biotite) are chloritized, quartz grains deformed by crystal plasticity, and plagioclase grains deformed mainly by fracturing, forming domino and similar microstructures. Some granitic plutons are sheared into L–S fabrics instead of L and $L \gg S$ fabrics. S–C fabrics are also formed with S-planes defined by grain aggregates of elongated quartz and fractured plagioclase and C-plane by chlorite grains. Hot striae mostly defined by growth of fibrous chlorite grains are widely distributed at the easternmost marginal part of this belt. On the other hand, mylonitic foliation from the superimposed retrograde metamorphic belt has similar attitudes to that from the central high-strain shear zone, striking NW–SE and dipping to the E, but some weak stretching lineation show high pitch angles (70°–90°).

Mesozoic (Triassic and Jurassic) metasedimentary rocks occur in the western part of the DCS mountain. Farther west they grade into very-low grade Jurassic metasedimentary rocks and to

Cretaceous sedimentary rocks of the Lanping Basin. Metamorphic rocks include muscovite schists, two-mica-schists, sericite-phyllites, phyllites, metasandstones, and metalimestones/marbles. To the south, the Diancang Shan is separated from the Ailao Shan massif by the almost 80 km long “Midu Gap” of unmetamorphosed sedimentary rocks (Leloup et al., 1995).

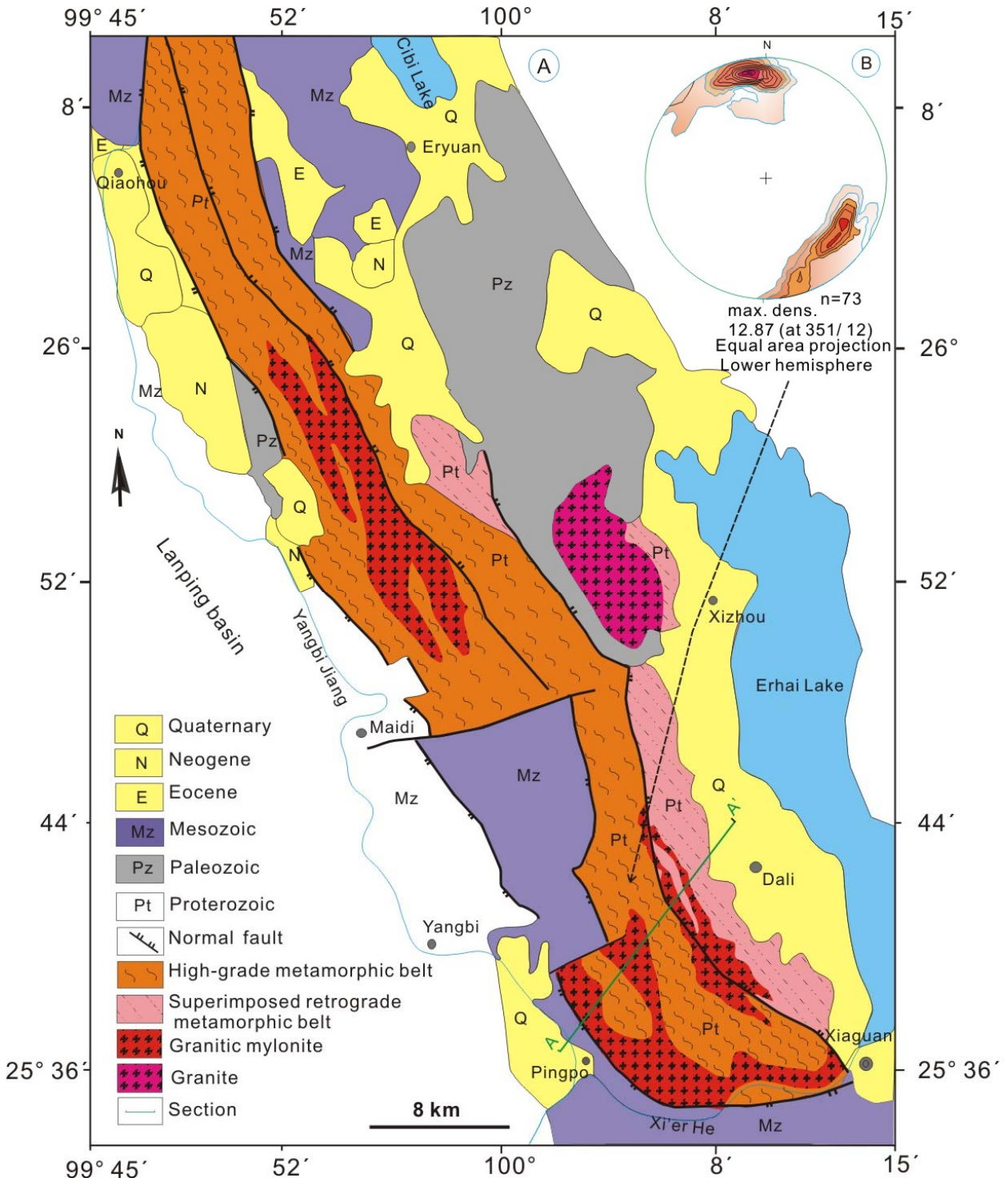


Fig. 4.2 Structural outline of the Diancang Shan area. A. Structural framework of the Diancang Shan area

(modified from Yunnan Bureau of Geology and Mineral Resources, 1994). B. Equal area projection of stretching lineation from high-temperature mylonites. Lower hemisphere equal area projection.

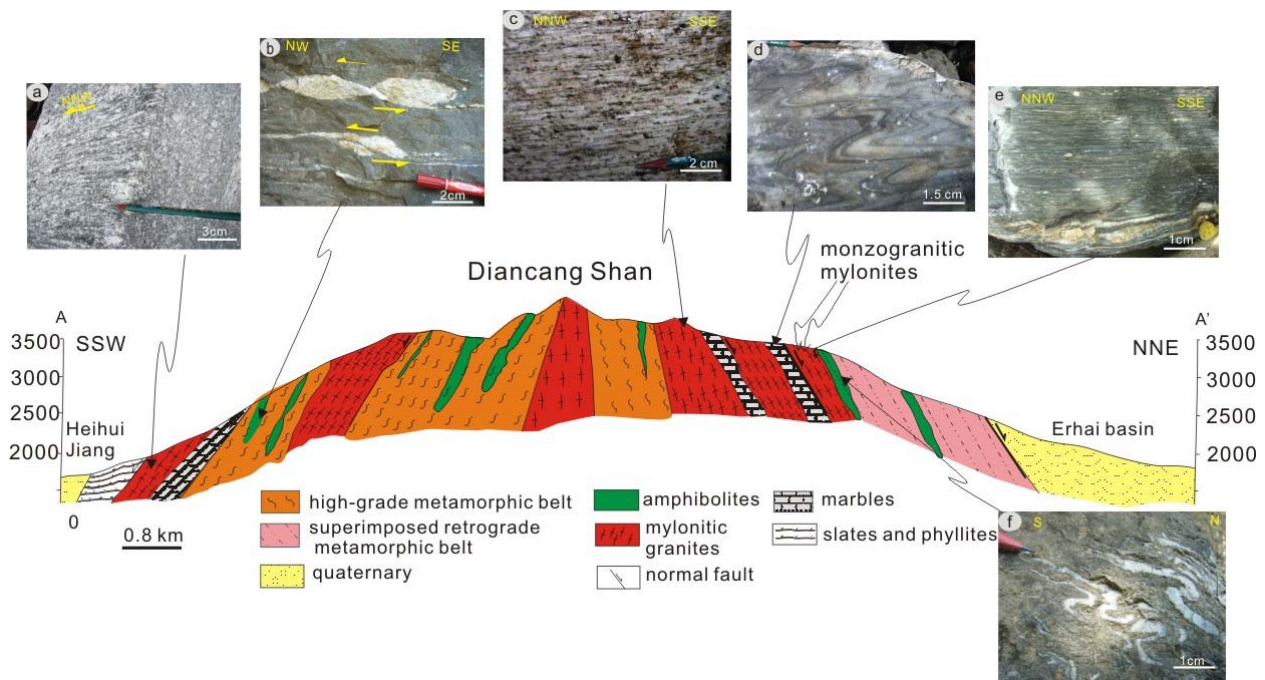


Fig. 4.3 Geological section across the Diancang Shan massif and macroscopic structural evidence of ductile deformation in high-grade metamorphic rocks in the Diancang Shan. a - Stretching lineation (L-fabric) in granitic mylonite. b - Felsic veins indicative of sense of shearing. c - Stretching lineation (L-fabric) in granitic mylonite. d - Strongly folded marble. e - Amphibolitic ultramylonite with strong stretching lineation (L-fabric). f - Sheath folds in garnet biotite gneiss.

4.3 Samples and techniques

4.3.1 Sample descriptions

Most of the granitic rocks spatially associated with shear zones in the Diancang Shan are exposed in the central belt of high-grade metamorphic rocks. The field appearance of the dated porphyritic monzogranitic mylonite is shown in Figure 4a. It is a tabular and elongate body exposing concordant relationships with the wall rocks, in both the overall configurations of the intrusions and the rock fabrics. The intrusion is restricted to the shear zone, where the granites experienced strong shearing deformation to form the granitic mylonites. Feldspar forms augen-shaped, sigma- and delta-type porphyroclasts (Fig. 4.4b and c). Although the monzogranite is strongly sheared, the magmatic texture and mineralogy can still be identified. The rocks have a medium to fine-grained inequigranular fabric and show early kinematic magmatic deformation structures. They contain K-feldspar (25–30 vol%), plagioclase (35–40%), quartz (25–30%) and

biotite (5–10%), and accessory minerals, e.g. apatite, zircon and monazite. Limited geochemical analysis results of the monzogranite samples show the SiO₂ abundance of 73.76 wt%, TiO₂ of 0.26 wt%, Al₂O₃ of 13.87 wt%, CaO of 1.3 wt%, Na₂O (3.8) + K₂O (4.25) > 8.05 wt%, K₂O > Na₂O. The Al/(Na + K + Ca) ratio is at 1.01.

Analyzed samples of amphibolite mylonite and ultramylonite are from the wall rocks of the dated monzogranite. Some quartzofeldspathic veins in the amphibolite rocks are sheared to form complex folds. Strongly deformed amphibole is associated with this foliation, again indicating initial high-temperature deformation. As the most fundamental structural characteristics of the amphibolite mylonites, the strong stretching lineation and weak foliation lead to alternating quartzofeldspathic and amphibole domains in thin sections. Elongated coarse amphibole grains, laminated biotite grains, lens-shaped plagioclase and quartz aggregates constitute the foliation and lineation to form L-fabric (Fig. 4.3e). Different mineral phases in the rocks show distinct deformation characteristics. Amphibole and plagioclase grains are intensely deformed with obvious dynamically recrystallization, but quartz grains are recrystallized dominantly by grain growth.

4.3.2 Analytical methods

Optical microscopy: Detailed optical microstructural observations and texture analysis were conducted on thin sections of the amphibolite mylonites and mylonitized porphyritic monzogranite. Polished thin sections were used for EBSD texture measurements. All thin sections were cut parallel to the kinematic XZ section, i.e. parallel to the stretching lineation and, where visible, normal to the foliation. Thin section samples from porphyritic monzogranite mylonites were selected for quartz and feldspar texture measurements and amphibole mylonites for amphibole texture measurements.

EBSD: Textures of quartz, amphibole and feldspar were measured using electron-backscatter diffraction (EBSD) detector mounted on a tungsten filament Hitachi S-3400N-II scanning electron microscope (SEM) in China University of Geosciences, Beijing. EBSP (electron-backscatter pattern) analyses were completed using the HKL CHANNEL5 software package. An acceleration voltage of 20 kV applied with an electron probe beam current of 3 nA and a working distance of 20 mm give rise to the 0.1 μm of spatial resolution and 0.5° of angular resolution. Data acquisition was done using both point scan and mapping modes. Indexing was accepted when at least six detected kikuchi bands matched with those in the standard reflector file for the analyzed mineral phases. The pole figures were plotted in an equal area of the lower

hemisphere with the trace of the mylonitic foliation (S) and the stretching lineation (L) as reference directions. Systematic mis-indexing was noted in automated orientation maps and such data was replaced by zero solution pixels. A detailed description of the EBSD technique can be found in e.g. Prior et al., 1996. EDS (Energy Dispersive Spectrometry, using an Oxford INCA Energy 350) attached to the SEM is the major technique identifying mineral phases and determining variation of mineral components during SEM/EBSD analysis.

SHRIMP II zircon U–Pb dating: All zircons were separated from whole-rock samples by grinding fresh rock samples in a ring mill. The crushed sample was passed through a 250 mesh sieve, washed and dried. Zircon grains were separated using heavy liquid and magnetic separation before representative grains were hand picked under a binocular microscope. Selected zircon grains were mounted in an epoxy disc with chips standard zircons (Black et al., 2003). They were polished until nearly half of each grain was removed. Microstructural photos were taken by transmitted and reflected light of microscopy, and cathodoluminescence under a scanning electron microscope. The mound was then cleaned and gold coated in preparation for SHRIMP analyses.

The entire process of zircon Th–U–Pb isotope analysis was finished using the Sensitive High-Resolution Ion Microprobe (SHRIMP II) machine at the Beijing Ion-probe Center, Chinese Academy of Geological Sciences (CAGS). Detailed analyzing processes are similar to Compston et al. (1984) and more recently stated by Williams et al. (1998). Using a 32 nA primary beam, circular to oval areas of 30 μm chosen within zircon grains were analyzed, together with replicate analyses of the TEM standard in the same epoxy mount. Both Pb/U and Pb/Th ratios and absolute Pb, Th and U abundances of the standards Sri Lanka zircon SL13 ($^{206}\text{Pb}/^{238}\text{U}=0.0928$ corresponding 572Ma, 238 ppm ^{238}U , Williams et al., 1998) and TEM with an age of 417 Ma (Black et al., 2003) have been used to monitor the analyses of the zircon. Corrections for common Pb were made using the measured ^{204}Pb isotopic composition. The uncertainty in all ages has a 95% confidence level, unless otherwise stated. Reduction of the measured data was done by using of SQUID1.03d (Ludwig, 2001) and ISOPLOT2.94h (Ludwig, 1999) programs. The data were plotted in the classical concordia diagram. The mean ages are weighted means at the 95% confidence level, and the single data point listed in Tables 1 is given at 1σ errors.

4.4. Microstructures

Microstructural investigations were concentrated on the mylonitic porphyritic monzogranites and amphibolites. Distinctive microstructures were obtained through feldspar, amphibole and quartz microstructural investigations. The microstructures are used to constrain the magmatic mineral crystallization, the operating slips systems of deforming minerals, and temperature and mechanisms of deformation.

4.4.1 Microstructures for late magmatic crystallization in the early kinematic monzogranite

Evidence for late-magmatic hydrothermal metasomatism is preserved in the dated porphyritic monzogranites. An early phase of K-metasomatism is evidenced by the replacement of plagioclase by K-feldspar to form K-feldspar phenocrysts, which is best documented by plagioclase left-over in marginal zones or internal parts of K-feldspar megacrysts (Fig. 4.4d). Patches of these left-over grains are often optically continuous and hence can be related to originally larger plagioclase grains. Some plagioclase crystals are replaced in their interiors by K-feldspar to form patchy microcline or perthite. In some cases, plagioclase crystals are almost completely replaced by K-feldspar. Most of the K-feldspar and remnant plagioclase grains show dynamic recrystallization tails or are completely recrystallized to form fine-grained subgrain aggregates (Fig. 4.4d–f, i). On the other hand, K-feldspar grains are further metasomatized by relatively Na-rich plagioclase. Very common K/Na metasomatism is indicated by widespread occurrence of myrmekite structures along the rims of albite lamellae or patches within large K-feldspar (Fig. 4.4e, g and h). Some myrmekites are surrounding almost the entire feldspar porphyroclast grain (Fig. 4.4g and h). During the progressive deformation, myrmekite extensively recrystallized to form the matrix (Fig. 4.4e and g). In most cases, the myrmekites seem to be stress-induced because their distribution and orientation can be attributed to bulk left-lateral shearing within the Diancang Shan zone (Fig. 4.4h).

Early crystallization is also demonstrated by the porphyritic structures, especially by oscillatory compositional growth zoning in feldspar grains (Fig. 4.4i), which is truncated by the matrix. In addition, exsolution lamellae of albite are widely developed in the K-feldspar phenocrysts. They are fine, stripe-shaped and nearly parallel to each other.

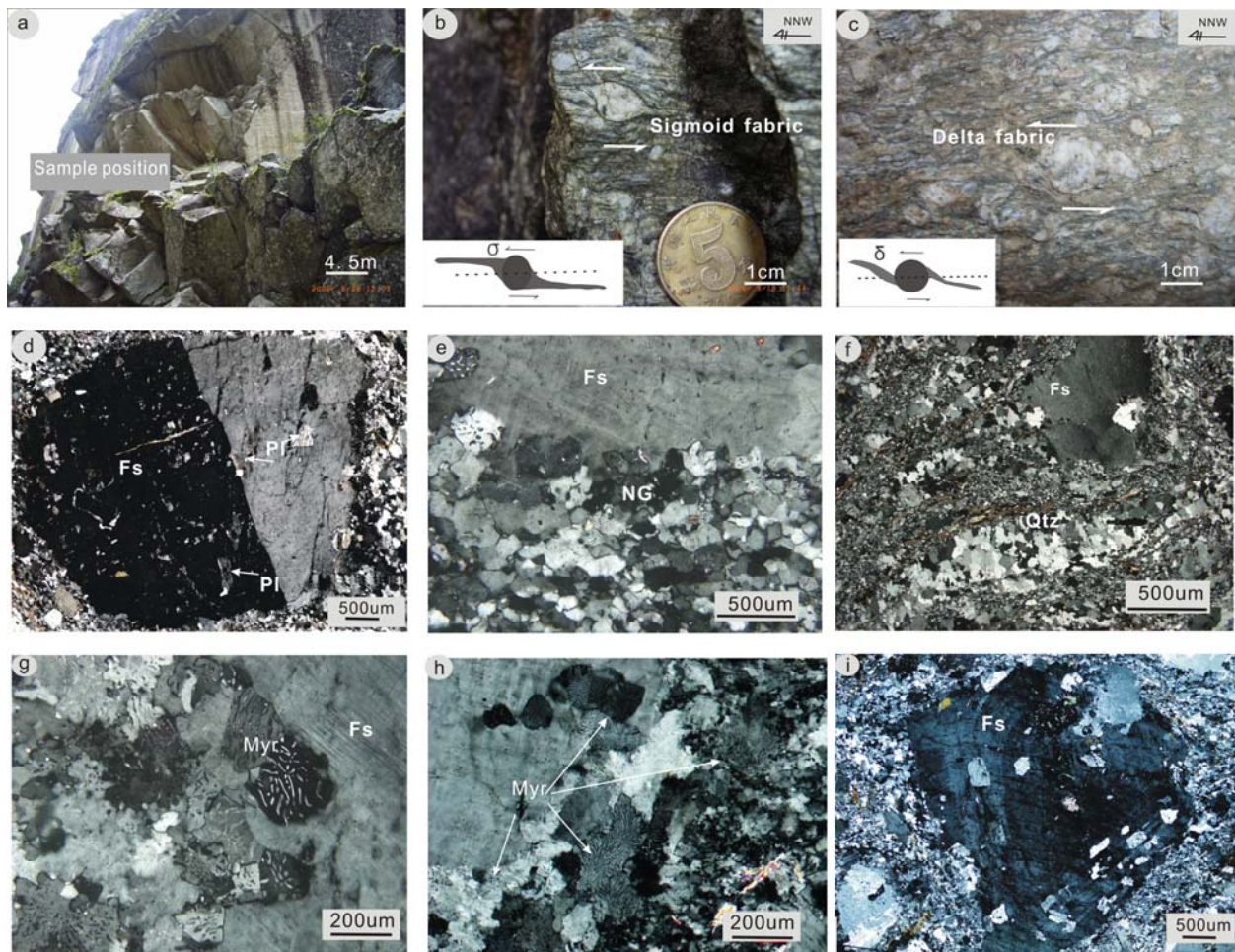


Fig. 4. 4 Macro- and microstructures of dated granitic mylonites from Diancang Shan. a - Sample location. b and c - Sigmoidal and delta-fabrics show left-lateral shearing deformation. d - Remnant plagioclase in K-feldspar. E - K-feldspar porphyroclasts (Fs) and transition to recrystallized grains (NG) in the matrix. f - Sigmoidal quartz aggregate (Qtz) at pressure fringes around feldspar porphyroclasts (Fs). g and h - Myrmekites (Myr) around feldspar porphyroclasts (Fs). i - Feldspar porphyroclasts with magmatic oscillatory zonation of crystal growth. NG - new fine-grained feldspar.

4.4.2 Plastic deformation of main mineral phases

4.4.2.1 Feldspar

Feldspar grains in the porphyritic monzogranite mylonites are characterized by solid-state crystal plastic deformation and strong dynamic recrystallization in the high strain zone (Figs. 4e, f and i, Fig. 4.5a–d). Most feldspar porphyroclasts are strongly elongated into lenticular shapes with irregular, serrated grain boundaries. They define the mylonitic foliation and partly control the orientations of quartz ribbons (Fig. 4.5c). Undulatory, inhomogeneous extinction and partial twinning are common in the porphyroclasts. Narrow needle-shaped deformation twins terminate

inside the grains. Flame perthites are rare and typically merge into albite at microcline grain boundaries. The most common deformation feature in the feldspars is the existence of a rim of recrystallized grains along the grain boundaries, producing a subgrain and core-mantle structures in highly deformed rocks (Fig. 4.4e; Fig. 4.5a–c). Large porphyroclasts have abundant subgrains and new fine grains are developed along their margins. The recrystallized grain size is uniform and varies in the range of 50–100 μm .

4.4.2.2 Amphibole

Amphibole grains from amphibolite mylonites are intensively deformed and dynamically recrystallized (Fig. 4.5e, f). Coarse porphyroclasts embedded in a fine-grained matrix are the most prominent characteristics of the amphibolite mylonites, although they constitute only a minor portion of the sample volume in both the mylonites to ultramylonites. Coarse amphibole grains mostly occur as porphyroclasts in amphibole-rich domains, while fine amphibole grains occur as matrix grains in quartzofeldspathic domains. The porphyroclasts with [001]-axes paralleling or sub-paralleling to stretching lineation are either augen and lens or fish-shaped (Fig. 4.5e). A group of parallel cleavages along (110) orientation are common in the porphyroclasts. The σ and ϕ tails are possibly formed in porphyroclasts in a stable position during general flow and δ tails are possibly around permanently rotated porphyroclasts (e.g. Passchier and Trouw, 2005). Abundant evidences for crystal plastic deformation is observed in the porphyroclasts. Undulatory or inhomogeneous extinction occur in most of the porphyroclasts, more abundant in the cores than in the marginal zones. Core-mantle structures are formed due to the occurrence of subgrains with different shapes (Fig. 4.5e). Most subgrains are strongly elongated in their shapes. Occasionally, lamellar subgrains are in the transition between deformed cores and fine grains in the matrix. Fine amphibole grains in the mylonites are characterized by the following features (Fig. 4.5f): (1) they form generally single crystals; (2) grains are acicular- or columnar-shaped; (3) they are homogeneously distributed and have strong shape preferred orientations, forming L-fabrics of the mylonites; (4) normal to the long axes of the grains there is a group of intragranular fractures; (5) fine grains in the ultramylonites rarely show obvious evidence of intragranular plastic deformation, although undulatory extinction can be occasionally observed.

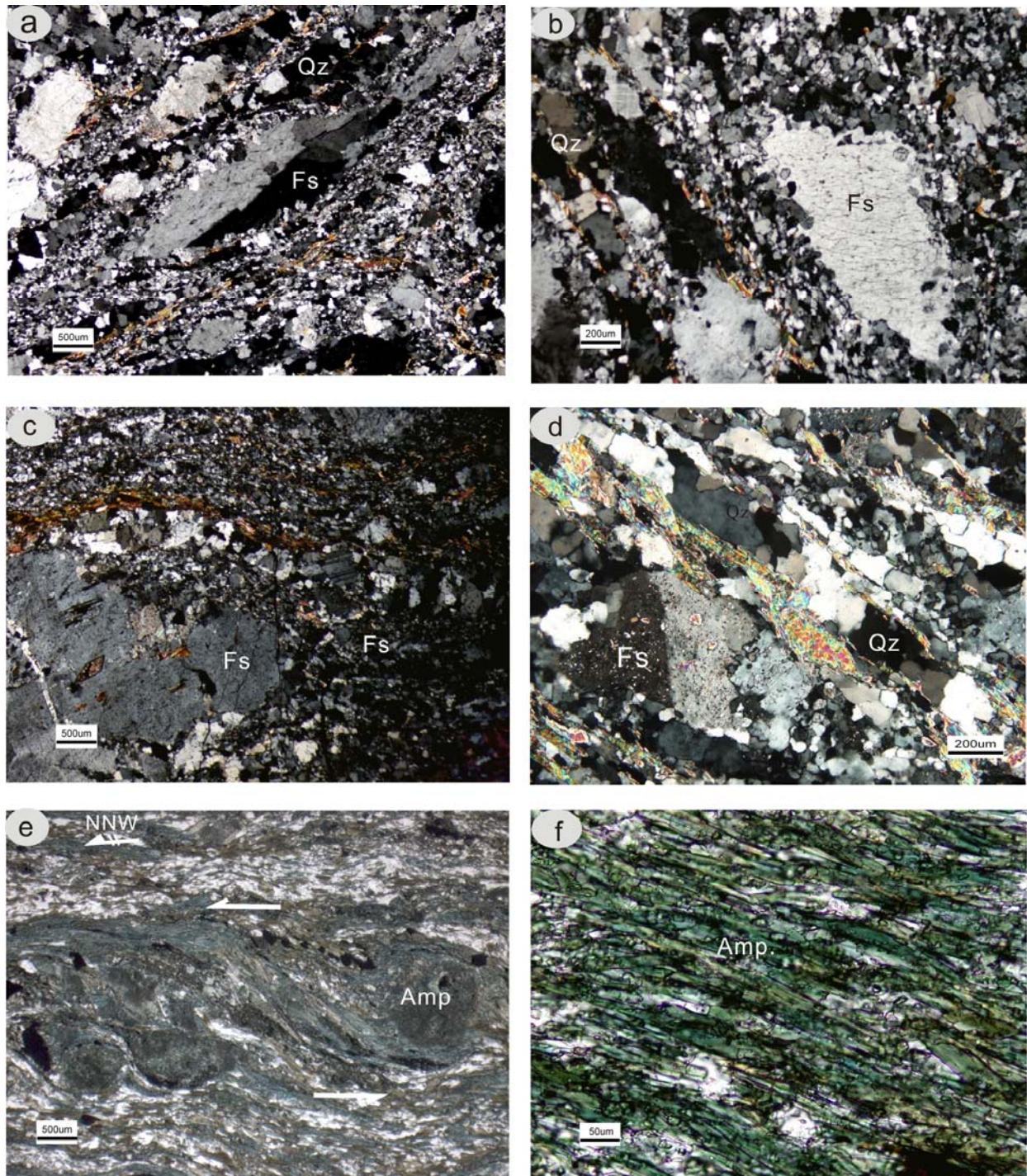


Fig. 4.5 Microscopic high-temperature plastic deformation characteristics of main minerals. a - Deformed feldspar porphyroclasts (Fs) with fine-grained tails in granite mylonite. b - Fine-grained feldspar porphyroclasts with core-mantle structures in granite mylonite. c - Deformed feldspar porphyroclasts (Fs) and quartz ribbons in granite mylonite. d - Polycrystalline quartz (Qz) ribbons and fine-grained feldspar porphyroclasts (Fs) in granite mylonites. e - Augen or δ -shaped amphibole (Amp) porphyroclasts and fine-grained amphibole grains with strong crystallography orientation in amphibolite mylonites. f - Fine-grained amphibole grains with strong preferred crystallographic orientation in amphibolitic ultramylonites.

shapes. Occasionally, lamellar subgrains are in the transition between deformed cores and fine grains in the matrix. Fine amphibole grains in the mylonites are characterized by the following features (Fig. 4.5f): (1) they form generally single crystals; (2) grains are acicular- or columnar-shaped; (3) they are homogeneously distributed and have strong shape preferred orientations, forming L-fabrics of the mylonites; (4) normal to the long axes of the grains there is a group of intragranular fractures; (5) fine grains in the ultramylonites rarely show obvious evidence of intragranular plastic deformation, although undulatory extinction can be occasionally observed.

4.4.2.3 Quartz

Quartz grains within the porphyritic monzogranites or amphibolite rocks commonly form polycrystalline aggregates due to recrystallization (Fig. 4.4f, Fig. 4.5a–d). They also occur in ribbons of elongate rectangular grains or sigma-type aggregates aligned parallel to the macroscopic foliation in the mylonites. Some large polygonized grains occur in pressure shadows on both sides of feldspar grains (Fig. 4.4f). Such features have been interpreted as either a major imprint of a late strain increment or a steady-state foliation (e.g. Brunel, 1980; Law et al., 1986). The ribbons are up to 100–200 μm thick and are mostly longer than the thin section (Fig. 4.5c and d). They are composed of predominantly non-equidimensional (50–100 μm) recrystallized grains of similar orientation (within individual ribbons) aligned oblique to the foliation. The senses of obliquity are consistent with the left-lateral shearing. Some irregular or sutured grain boundaries of the quartz grains imply the dominant role of grain boundary migration recrystallization. Undulatory extinction in some of the recrystallized quartz grains indicates a progressive deformation increment after their recrystallization.

4.5. Textures–EBSD analysis

4.5.1 Quartz texture

All textures of quartz were measured from the homogeneously distributed areas within the dated monzogranite samples and the textures results are shown in Figure 6. Measured quartz grains are parallel to the stretching lineation. Quartz grains or ribbons in contact with feldspar porphyroclasts were not measured to avoid contact strain effect. Quartz c-axes maxima in sample a, b and c, are concentrated near to Y-directions, but there are sub-maxima in the orientation oblique to the XZ-plane and close to the X-directions (the stretching lineation

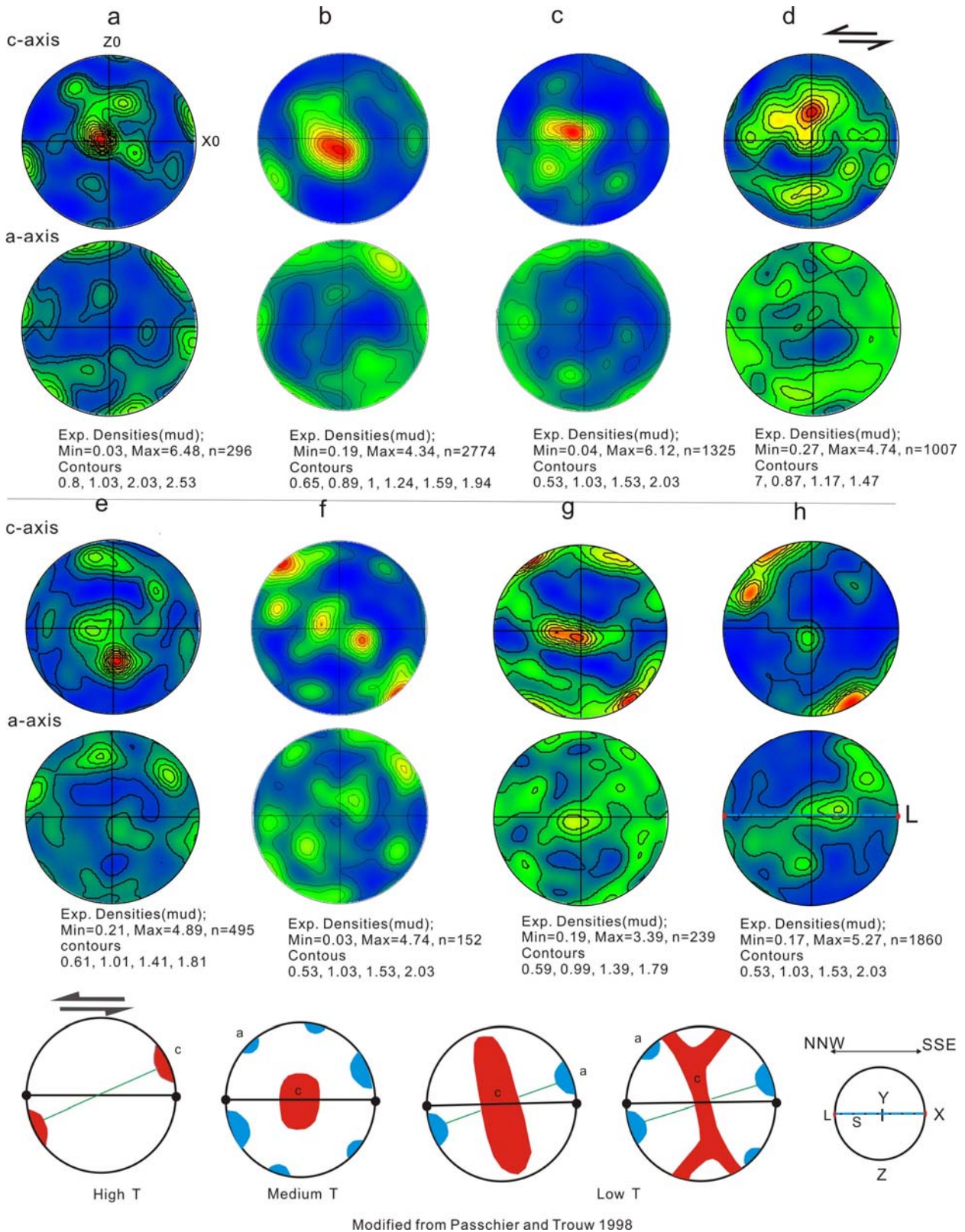


Fig. 4.6 Quartz c- and a-axis textures were measured in eight samples collected from mylonitic monzogranite (the dated samples). Textures are shown in the equal area and lower hemisphere projection. As shown in the small inset at the lower right corner of the illustration, XY represents the foliation(S)-spot line and X represents the lineation (L)- round spot. The second inset at the lowest side is the quartz texture model with temperature changes (modified from Passchier and Trauw, 1998).

direction). The a-axes in the three samples present maxima in the XZ-plane. This configuration of c-axis point maxima migrating from near X- to Y-directions, could be attributed to activation of prism $\langle c \rangle$ slip to $\langle a \rangle$ slip. The c-axes close to Y-direction, or between the Z- and X-directions indicate that prism $\langle a \rangle$ glide were operative, and the c-axis submaxima concentrating near the X-directions is attributed to activation of prism $\langle c \rangle$ slips (e.g. Lister and Dornsiepen, 1982; Mainprice et al., 1986). Such a situation could result from deformation under amphibolite facies conditions (e.g. Passchier and Trouw, 2005) or higher temperature ($T > 700^\circ\text{C}$) (Garbut and Teyssier, 1991).

In sample d, the quartz c-axes is mostly characterized by small circle near the Y-direction and the a-axes present broad great circle distributed. The c-axes in sample e represent maxima close the Y-direction and submaxima at intermediate position between the Y- and Z-directions. The a-axes form maxima close to the XZ-plane. They could suggest the main prism $\langle a \rangle$ slip to rhomb $\langle a \rangle$ slip systems becomes activated with decreasing temperature, causing a fabric maximum at an intermediate direction between the Y- and Z-directions. The c-axes of quartz from the sample f are characterized by an asymmetric single-girdle passing through Y-direction, at a high angle ($\sim 45^\circ$) to the foliation and lineation. The point maxima within the girdle contain a Y-sub-maximum together with developed maxima in XZ plane at an intermediate orientation to X and Z. In contrast, well developed cross girdles in samples g and h show the asymmetrically distributed maxima in relation to the Z-direction (inclined to foliation and stretching lineation) (e.g. Schmid and Casey, 1986; Law, 1990). These patterns suggest activation of the $\langle a \rangle$ basal slip, which is the glide system of quartz with lower activation energy at low to medium-grade conditions (e.g. Fueten, 1992). The asymmetry of the point maximum of c-axes directions in all samples also indicate the general left-lateral shear sense obtained with meso- and microscopic kinematic indicators.

4.5.2 Amphibole texture

Fig. 4.7 gives amphiboles textures measured from the homogeneously distributed fine grains and porphyroclasts from the amphibole mylonites and ultramylonites. In the mylonites the (100) poles of the amphibole exhibit maxima lying in the XY-plane, the $\langle 001 \rangle$ -axes dominantly form maxima lying in the X-directions, and the (010) poles form a maximum in the Y-direction (Fig. 4.7a). There is a slight dispersion of (100) and (010) of matrix grains towards a girdle parallel to the YZ-plane. Mapping of fine matrix amphibole grains from samples of ultramylonitic

amphibolites give similar texture patterns for both the porphyroclasts and fine grains around them (Fig. 4.7b). In this case, the parallelism of $\langle 001 \rangle$ crystallographic axes and (100) crystallographic planes of amphibole grains to the stretching lineation and foliation of the mylonites implies that the lattice-preferred orientation of dynamically recrystallized amphibole grains resulted from a dominant activation of (100) $\langle 001 \rangle$ slip (twinning) system at relatively high-temperatures (Cao et al., 2010).

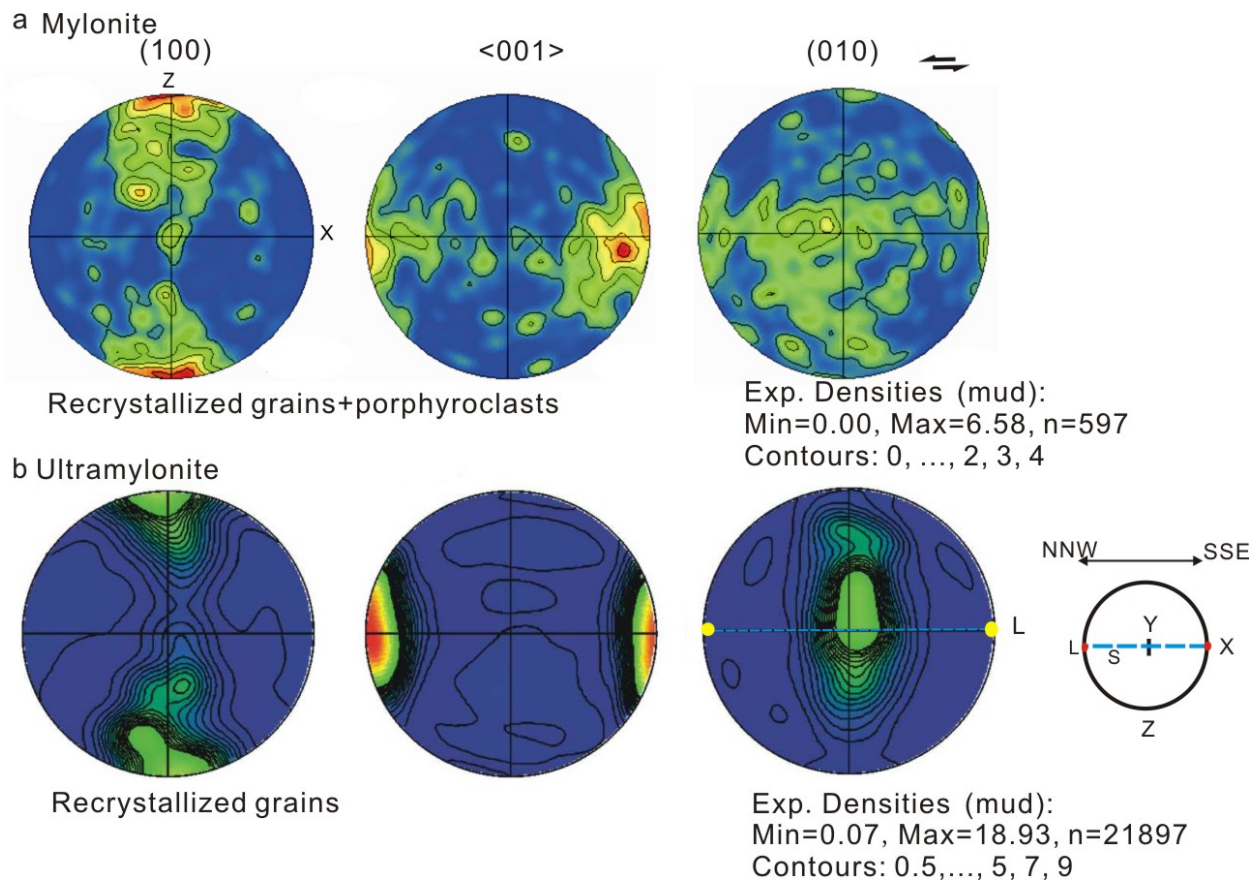


Fig. 4.7 Amphibole textures measured from amphibolitic mylonite (a) and ultramylonites (b). Textures are shown in the equal area and lower hemisphere projection. As shown in the small inset at the lower right corner of the illustration, XY represents the foliation(S)-spot line and X represents the lineation (L)- round spot.

4.5.3 Feldspar Texture

Textures of feldspar are shown in Fig. 4.8, from homogeneously distributed porphyroclasts and subgrains within the intensively deformed porphyritic monzogranite mylonite samples. Measured feldspar grains are strongly elongated parallel to the stretching lineation. The pole figures of feldspar from the sample show a maxima of the (010) poles at the Z-direction, indicating that the (010) crystal plane parallel to the foliation (XY-plane). The $\langle 001 \rangle$ and $\langle 101 \rangle$

crystallographic orientations show maxima distributed in the XY-plane, either near to the Y ($\langle 001 \rangle$) or X ($\langle 101 \rangle$)-directions. Experimental studies of feldspar have revealed that the most common active slip plane over a wide range of conditions is (010) and that slip directions are $\langle 101 \rangle$, $\langle 100 \rangle$, $\langle 001 \rangle$ and $\langle 010 \rangle$ (e.g. Tullis, 1983, Schulmann et al., 1996; Martelat et al., 1999; Franek et al., 2006; Ishii et al., 2007). Therefore, these textures may indicate that the lattice-preferred orientations of feldspar grains are developed by intragranular slipping with (010) as the main slip plane and $\langle 101 \rangle$ or $\langle 001 \rangle$ as the slip directions.

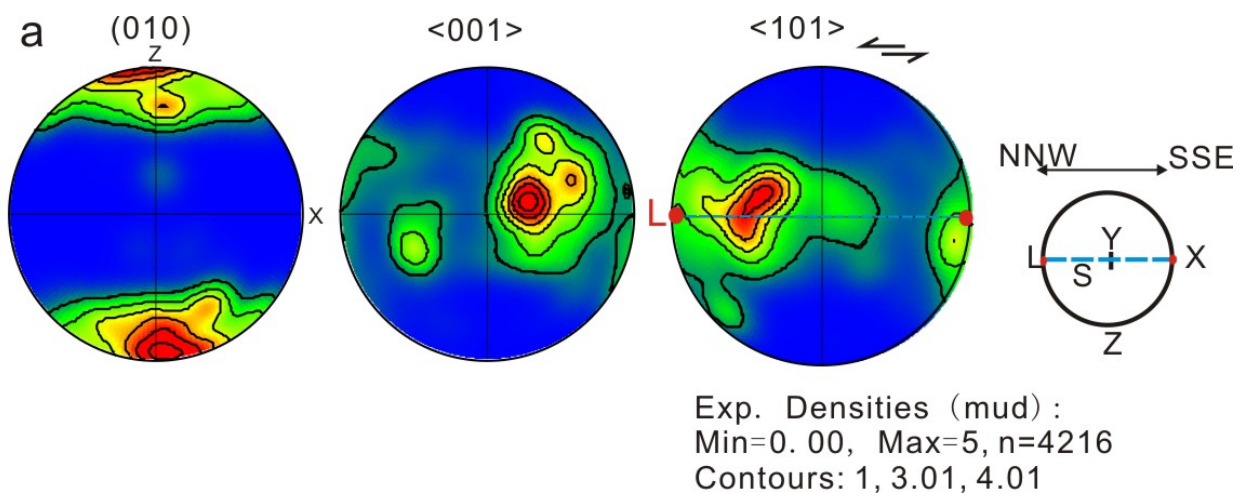


Fig. 4.8 Feldspar textures were measured from two mylonitic monzogranite (dated sample). Textures are shown in the equal area and lower hemisphere projection. As shown in the small inset at the lower right corner of the illustration, XY represents the foliation(S)-spot line and X represents the lineation (L)- round spot.

4.6 Thermochronology results

Zircon grains are elongated euhedral to subhedral prismatic crystals up to 200–300 μm long. They are clear and yellow or greenish yellow in color. Most zircons have internal cores with marginal oscillatory zoning, which resembles the zoning derived from magmatic growth (Fig. 4.9a). Euhedral zoning is more prominent towards the grain rims. The outer rims of the zircon population consist of euhedrally zoned crystals with well-defined pyramidal terminations.

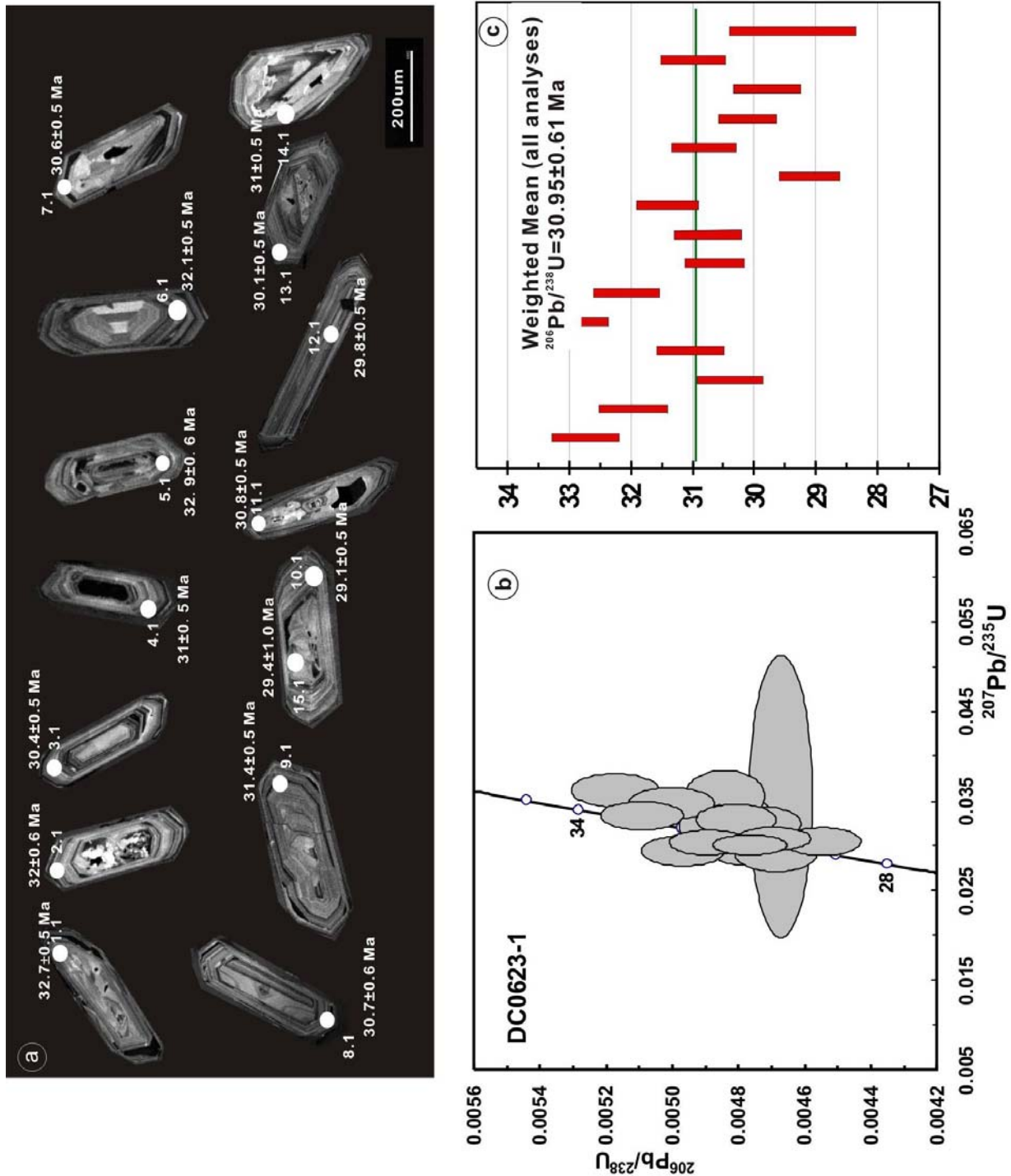


Fig. 4.9 a - Cathodoluminescence images of representative zircons, and sites of analyzed spots (b) and U-Pb Concordia diagram and $^{206}\text{Pb}/^{238}\text{U}$ weighted average age diagram (c) of the early kinematic porphyritic monzogranite.

Fifteen SHRIMP spots were dated in 14 zircon grains for this sample and the locations and results of dating are shown in the Figure 9a and Table 1. Th, U contents show perfect positive correlation with changes in Th of 2092–355 ppm, in U of 6736–799 ppm, and Th/U ratio between 0.2–0.5. Such variations of the Th–U ratio are characteristic of magmatic zircons. The

$^{206}\text{Pb}/^{238}\text{U}$, $^{207}\text{Pb}/^{235}\text{U}$ results are plotted on concordia diagram and the 15 data points show a consistent group distribution, with a $^{206}\text{Pb}/^{238}\text{U}$ weighted average age of 30.95 ± 0.61 Ma (MSWD = 4.1, 95% confidence level) (Fig. 4.9b and c). Since all these zircons have faint oscillatory zoning and pyramidal terminations, this age is interpreted, therefore, as the age of magmatic crystallization.

4.7 Discussion

4.7.1 Early-kinematic plutonism: magmatic crystallization

The nature of the transition from submagmatic to solid-state has important implications for emplacement models for plutons, for cooling and strain rates within solidifying plutons and their wall rocks, and for timing of emplacement relative to regional deformation (e.g. Miller et al., 1994). Although criteria for the timing of magma emplacement relative to regional deformation are commonly ambiguous, it is difficult to demonstrate unequivocally such timing for individual plutons (e.g. Paterson et al., 1988; Karlstrom 1991; Karlstrom et al., 1993; Miller et al., 1994; Searle, 2006). A variety of well-developed structures and microstructures for the transition from magmatic- or submagmatic flow to high-temperature solid-state deformation is still preserved in plutons in the Diancang Shan metamorphic massif. These structures can be used to indicate a continuous process from early emplacement to later shear deformation, which suggests that the early-kinematically emplaced pluton subsequently experienced strong left-lateral strike-slip shearing within solid-state conditions. The evidence of microstructures is as follows:

(1) Magmatic crystallization is characterized by porphyritic structures, especially by concentric growth zoning in feldspar grains, which are truncated by the matrix, confirming that deformation occurred after formation of the zoning (e.g. Vernon et al., 1987; Vernon, 2000). Evidence for late magmatic metasomatism is widespread in the mylonitic rocks. An early phase of K-metasomatism is succeeded by sodium metasomatism. Such hydrothermal alteration is mainly confined to the interior of the mylonitized monzogranite and is never observed in the nearby wall rocks. This is an indication that the hydrothermal activity is a late magmatic event, rather than a regional metasomatism related syn- or post-shearing stages. Some myrmekites may be related to the solid-state deformation (e.g. Simpson and Wintsch, 1989; Vernon, 2000), but they are confined to some special domains.

(2) Parallel to sub-parallel alignment of elongate euhedral feldspar crystals are not completely deformed internally which imply that there was sufficient freedom for the feldspar crystals to

grow and rotate before undergoing plastic deformation (e.g. Shelley, 1985, Blumenfeld and Bouchez, 1988; Vernon, 2000). Paterson et al. (1998) suggested that the alignment of crystals would not be preserved unless the magma reached a sufficiently high viscosity for it not to be removed by late flow. Therefore, they inferred that the preservation of such preferred orientations would occur most commonly in a later stage of magma crystallization.

(3) The albite flames are heterogeneously distributed through the microperthite. The recrystallized K-feldspar with exsolution lamellae indicates crystallization by solid-state deformation at hypersolvus temperatures (e.g. Vernon, 1999).

(4) K-feldspar possesses microcline twinning and show marginal replacement by myrmekite. Elongated feldspar grains with recrystallized tails of aggregates quartz, mica and feldspar are common. Subsolidus deformation appears to be a prerequisite for the formation of myrmekite (e.g. Vernon, 1991). The reactions involved appear to be complex and require transport of chemical components in fluids from one part of the rock to another (e.g. Simpson and Wintsch, 1989). Plagioclase in myrmekite replacing K-feldspar probably implies growth at relatively high-temperatures (e.g. Vernon, 1991). At such conditions, new elongate grains of K-feldspar precipitate in dilational domains within and around K-feldspar porphyroclasts as a part of the process of myrmekite formation that progressively consumed the porphyroclasts (e.g. Menegon et al., 2008).

(5) S-C fabric is defined by large feldspar crystal, fine-grained biotite and quartz. Recrystallization of feldspar to smaller equant grains is modest in both S and C surfaces. The limited solid-state deformation and recrystallization suggest that the S–C fabric formed primarily in the submagmatic state, that is, small amounts of melt allowed rotation and sliding of feldspar crystals into the C-orientation (e.g. Vernon, 2000). These also indicate the history of late magma crystallization. As magmatic minerals began to be locked, shear strain become concentrated in the narrow C-surfaces and this strain partitioning continued during plastic flow in the solid-state (Miller and Paterson, 1994). Thus the S-C arrangements with the similar sense of shear suggest that deformation was continuous from the magmatic to the solid-state (e.g., Blumenfeld and Bouchez, 1988; Miller and Paterson, 1994; Vernon, 1999, 2000).

(6) Most of feldspar megacrysts with recrystallized “tails” provide pronounced evidence for the existence of the megacryst prior to the mylonitic deformation. The compositions of coexisting recrystallized plagioclase and K-feldspar, give at least a general indication of high recrystallization temperatures (e.g. Vernon, 2000).

4.7.2 Solid-state plastic deformation

We reiterate that the microstructures of the granite from the Diancang Shan high-grade metamorphic massif provide evidences for a transition from magmatic through submagmatic to solid-state plastic deformation during the early-emplacment of the plutons. We also noted that to document this transition is important to prove that the solid-state plastic deformation occurred at high-temperature conditions. It is possible, therefore, to correlate the textures, microstructure and the field fabrics in order to understand whether there is any relation between the regional strain/kinematics and fabric development in the granites and host rocks. Microstructure and texture analyses suggest that the solid-state fabrics formed within amphibolites-facies metamorphic conditions, largely between about 700°C and 550°C.

(1) Feldspar grains are elongated or partly twinned with recrystallized tails, and some are completely dynamically recrystallized into fine-grained matrix. The porphyroclastic cores show undulatory and inhomogeneous extinction, and have core-mantle structures and subgrains. TEM analyses show that some dislocations are organized into dislocation walls and form subgrains. There are rarely free dislocations in fine grains (Cao et al., 2010). Thus K-feldspar recrystallization seems to have been dominated by the subgrain rotation process. According to Tullis & Yund (1987), the recrystallization-accommodated dislocation creep in feldspar is generally completed by moderately high-temperatures, or middle to upper amphibolite facies, although values are not tightly constrained. Deformation of K-feldspar was associated with metasomatism by relatively Na-rich plagioclase to form myrmekite structure, suggesting plastic deformation at feldspar recrystallization temperatures above 550°C (e.g. Vernon, 1991; Menegon et al., 2006). The texture of feldspar suggests that the prevailing intragranular slip systems are the (010) <101> or (010) <001>. Experimental studies of K-feldspar have revealed that the most common active slip plane over a wide range of conditions is (010) and that slip directions are <101>, <100>, <001> and <010> (e.g. Tullis, 1983; Schulmann et al., 1996; Martelat et al., 1999; Franek et al., 2006; Ishii et al., 2007), and these slip systems mainly occur by dislocation creep deformation mechanism within amphibolite facies to granulite facies deformation conditions in feldspar aggregates of granitic mylonite (e.g. Gandais et al., 1984; Olsen et al., 1984, 1985).

(2) It is generally accepted that amphibole is deformed by brittle processes and concomitant breakdown reactions under greenschist facies (e.g. Brodie and Rutter, 1985) or even at amphibolite facies (Lafrance and Vernon, 1993), or solution mass transfer (Brodie and Rutter, 1985; Stünitz, 1993; Shelley, 1994; Imon et al., 2002, 2004). Dominance of dislocation activity, subgrain formation and dynamic recrystallization may occur at higher temperature and pressure conditions (e.g. Biermann and Van Roermund, 1983; Cumbest et al., 1989; Skrotzki, 1992; Cao

et., 2007, 2010), although it is inferred that amphibole generally does not deform significantly by intracrystalline plasticity below 650–700°C in the presence of fluid (e.g. Berger and Stünitz, 1996). The amphibole grains from amphibolite mylonites and ultramylonites in the Diancang Shan massif show distinct plastic deformation characteristics. Amphibole grains are intensely deformed with obvious grain size reduction. Most fine grains are generated by combined twinning and dislocation creep of parent amphibole grains with specific preferred crystallographic and shape orientations. Twinning along (100), in combination with dislocation creep (gliding and climbing) governs the nucleation of subgrains and formation of dynamically recrystallized fine amphibole grains. Textures of amphibole show that <001> crystallographic axes and (100) crystallographic planes of dynamically recrystallized hornblende grains lie within these mylonitic foliation and parallel to the stretching lineation. Such a parallelism implies that the texture of dynamically recrystallized hornblende grains resulted from a dominant activation of (100) <001> slip system (twinning) (Cao et al., 2010), which is related to high-temperature deformation (e.g. Dollinger and Blacic, 1975; Cao et al., 2010). Our observations, therefore, suggest that amphibole grains from the mylonitic rocks are strongly deformed and dynamically recrystallized under amphibole facies conditions with an average temperature of 625°C (Cao et al., 2010).

(3) Most quartz grains have polygonal shapes and straight grain boundaries parallel to the major foliation and lineation of the rocks. Serrated grain boundaries are observed in some cases suggesting local high-temperature grain boundary migration. Some quartz grain boundaries of equigranular grains form triple junctions. Rare occurrence of dislocation substructures in quartz grains points to the importance of high-temperature recovery and recrystallization during or after high-temperature shearing. Activation of slip systems of quartz is temperature sensitive, the c-axes orientation of quartz changes with temperatures (e.g. Passchier and Trouw, 2005). Textures of quartz present the c-axes maxima near the Y-axes is attributed to the accommodation of intracrystalline deformation by <a> prismatic slips activated. Such texture patterns indicate the prism slip system activity at amphibolite facies conditions (e.g. Lister and Dornsiepen, 1982; Mainprice et al., 1986; Passchier and Trouw, 2005). Some textures show patterns for prism <c> slip, with c-axes concentrating near the X-axes (Fig. 4.6a–e), indicating deformation or recrystallization at temperatures higher than 700 °C (e.g. Bouchez et al., 1984; Hobbs, 1985; Blumenfeld et al., 1986; Mainprice et al., 1986; Garbutt and Teyssier, 1991; Stipp et al., 2002; Passchier and Trouw, 2005).

4.7.3 Timing of initiation of left-lateral shearing in the Diancang Shan massif

The granitic mylonite, originally a typical porphyritic monzogranite, is an important component unit of the high-grade metamorphic belt in the NNW–SSE extended central Diancang Shan massif. Although the strong shear deformation made the granite no longer retain enough original magmatic structural characteristics, the coarse feldspar porphyroclasts and relatively fine-grained matrix constitute a typical porphyritic structure. On the other hand, microstructural analysis shows that the dominant deformation of the granitic mylonite is a high-temperature solid-state deformation.

The above lines of microstructural evidences support an explanation of early-kinematic emplacement of the granitic magma before solid-state ductile shearing. Therefore, the intrusion of the magma gives a proper constraint on the initiation of the left lateral ductile shearing along the ASRR shear zone, at least at Diancang Shan. Zircons developed well crystal growth oscillatory zoning, and the majority of Th/U ratio generally higher than 0.3, characteristic of typical magmatic zircons. Therefore, the zircon grains give an age for emplacement and crystallization of the magma. At the same time, the U–Pb age of 30.95 ± 0.61 Ma of the magmatic zircons thus provides the lower timing of left-lateral shearing at Diancang Shan.

4.8 Conclusions

The new data from the Diancang Shan massif give rise to the following major conclusions:

- (1) Microstructural and textural analysis documents the intense solid-state plastic deformation of feldspar, quartz and amphibole of high-grade metamorphic rocks from the Diancang Shan massif. These rocks were sheared and metamorphosed at amphibolite-facies P-T conditions, attending left-lateral shearing along the ASRR shear zone.
- (2) Structural, microstructural and textural data of a large porphyritic monzogranite intrusion reveal that the emplacement was early-. The pluton underwent a progressive process from magma emplacement to solid-state high-temperature plastic deformation related to the regional sinistral strike-slip motion.
- (3) The U–Pb age of 30.95 ± 0.61 Ma of magmatic zircons in the early-kinematic porphyritic monzogranite indicates the onset of left-lateral shearing. Therefore, the initiation of ductile deformation along the ASRR shear zone began at ca. 31 Ma in the Diancang Shan.

Acknowledgements

This study received financial support from the National Natural Science Foundation of China (40872139), the 111 Project (B07011) of the Ministry of Education, State Key Laboratory of Geological Processes and Mineral Resources (Grant No. GPMR200837), and also was supported by the Fundamental Research Funds for the Central Universities (Grant No. GPMR2009PY01). We thank Dr Jian Zhang for a helpful scientific review of an earlier version of the manuscript and Prof. Dr. W. Gary Ernst is also appreciated for his constructive comments and reviews which substantially improved this work.

References

- Anczkiewicz, R., Viola, G., Muntener, O., Thirlwall, M.F., Villa, I.M., Quong, N.Q., 2007. Structure and shearing conditions in the DayNuiCon Voi massif: Implications for the evolution of the Red River shear zone in northern Vietnam. *Tectonics* 26, TC2002, doi:10.1029/2006TC001972.
- Berger, A., Stünitz, H., 1996. Deformation mechanisms and reaction of amphibole: examples from the Bergell tonalite (Central Alps). *Tectonophysics* 257, 149–174.
- Biermann, C., Van Roermund K.L.M., 1983. Defect structures in naturally deformed clinoamphiboles – a TEM study. *Tectonophysics* 95, 267–278.
- Black, L.P., Kamo, S.L., Williams, I.S., Mundil, R., Davis, D.W., Korsch, R.J., Foudoulis, C., 2003. The application of SHRIMP to Phanerozoic geochronology: a critical appraisal of four zircon standards. *Chemical Geology* 200, 171–188.
- Blumenfeld, P., Bouchez, J.L., 1988. Shear criteria in granite and migmatite deformed in the magmatic and solid states. *Journal of Structural Geology* 10, 361–372.
- Blumenfeld, P., Mainprice, D., and Bouchez, J.L., 1986, C-slip in quartz from subsolidus deformed granite. *Tectonophysics*, v. 127, pp. 97–115.
- Bouchez, J., Mainprice, D., Trepied, L., and Doukhan, J., 1984, Secondary lineation in a high-T quartzite (Galicia, Spain): an explanation for an abnormal fabric: *Journal of Structural Geology*, v. 6, p. 159-165.
- Burchfiel, B.C., Wang, E.C., 2003. Northwest-trending, middle Cenozoic, left-lateral faults in southern Yunnan, China, and their tectonic significance. *Journal of Structural Geology* 25, 781–792.

- Briais, A., Patriat, P., Tapponnier, P., 1993. Updated interpretation of magnetic anomalies and seafloor spreading stages in the South China Sea: implications for the Tertiary tectonics of Southeast Asia. *Journal of Geophysical Research* 98, 6299–6328.
- Brodie, K.H., Rutter, E., 1985. On the relationship between deformation and metamorphism with special reference to the behavior of basic rocks. In: Thompson, A.B., Rubie, D.C. (Eds.), *Metamorphic Reactions: Kinetics, Textures, and Deformation*. *Advances in Physical Geochemistry* 4, Berlin, Springer, pp. 138–179.
- Brown, M., Solar, G.S., 1998. Granite ascent and emplacement during contractional deformation in convergent orogens. *Journal of Structural Geology* 20, 1365–1393.
- Brown, M., Solar, G.S., 1999. The mechanism of ascent and emplacement of granite magma during transpression: a syntectonic granite paradigm. *Tectonophysics* 312, 1–33.
- Brunel, M., 1980. Quartz fabrics in shear-zone mylonites: evidence for a major imprint due to late strain increments. *Tectonophysics* 64, 33–44.
- Cao, S.Y., Liu, J.L., Hu, L., 2007. Micro- and submicrostructural evidence for high-temperature brittle-ductile transition deformation of hornblende: Case study of high-grade mylonites from Diancangshan, western Yunnan. *Science in China Series D-Earth Sciences* 50(10), 1459–1470.
- Cao, S.Y., Liu, J.L., Hu, L., 2010. Orientation-related deformation mechanisms of naturally deformed amphibole in amphibolite mylonites from the Diancang Shan, SW Yunnan, China. *Journal of structural geology* 32, 606–622.
- Chung, S.L., Lee, T.Y., Lo, C.H., Wang, P.L., Chen, C.Y., Yem, N.T., Hoa, T.T., Wu, G.Y., 1997. Intraplate extension prior to continental extrusion along the Ailao Shan Red River shear zone. *Geology* 25 (4), 311–314.
- Chung, S.L., Lo, C.H., Lee, T.Y., Zhang, Y. Q., Xie, Y.W., Li, X.H., Wang, K.L., Wang, P. L., 1998. Diachronous uplift of the Tibetan plateau starting from 40 Myr age. *Nature* 394, 769–773.
- Chung, S.L., Searle, M.P., Yeh, M.W., 2008. The age of the potassic alkaline igneous rocks along the Ailao Shan-Red River shear zone: Implications for the onset age of left-lateral shearing: A discussion. *Journal of Geology* 116 (2), 201–204.
- Compston, W., Williams, I.S., 1984. U-Pb geochronology of zircons from lunar breccias 73217 using a sensitive high mass resolution ion microprobe. *Journal of Geophysical Research* 89, 525–534.

- Cumbest, R.J., Drury, M.R., Van Roermund, H.L.M., Simpson, C., 1989. Dynamic recrystallization and chemical evolution of clinoamphibole from Senja Norway. *Contributions to Mineralogy and Petrology* 101, 339–349.
- Dollinger, G., Blacic, J.D., 1975. Deformation mechanisms experimentally and naturally deformed amphiboles. *Earth Planetary Science letters* 26, 409–416.
- Franek, J., Schulmann, K., Lexa, O., 2006. Kinematic and rheological model of exhumation of high pressure granulites in the Variscan orogenic root: example of the Blansky les granulite, Bohemian Massif, Czech Republic. *Mineralogy and Petrology* 86, 253–276.
- Fueten, F., 1992. Tectonic interpretations of systematic variations in quartz c-axis fabrics across the Thompson Belt. *Journal of Structural Geology* 14, 775–789.
- Fyhn, M.B.W., Boldreel, L.O., Nielsen, L.H., 2009. Geological development of the Central and South Vietnamese margin: Implications for the establishment of the South China Sea, Indochinese escape tectonics and Cenozoic volcanism. *Tectonophysics* 478, 184–214.
- Gandais, M., Willaim, C., 1984. Mechanical properties of feldspars. In: Brown, W.L. (Eds.), *Feldspars and feldspathoids*. NATO AST Series C 137, D. Reidel Publ Comp, Dordrecht Boston Lancaster, pp. 207–246.
- Garbut, J.M., Teyssier, C., 1991. Prism $\langle c \rangle$ slip in quartzites of the Okhurst mylonite belt, California. *Journal of Structural Geology* 13, 657–666.
- Garnier, V., Giuliani, G., Maluski, H., Ohnenstetter, D., Trong, T. P., Quang, V. H., Van, L. P., Van, T. V., Schwarz, D., 2002. Ar-Ar ages in phlogopites from marble-hosted ruby deposits in northern Vietnam: Evidence for Cenozoic ruby formation. *Chemical Geology* 188, 33–49.
- Gilley, L.D., Harrison, T.M., Leloup, P.H., Ryerson, F.J., Lovera, O.M., Wang, J.H., 2003. Direct dating of left-lateral deformation along the Red River shear zone, China and Vietnam. *Journal of Geophysical Research* 108, p. 2127, doi:10.1029/2001 JB001726
- Guo, S. M., Zhang, J., Li, X.G., Xiang, H.F., Chan, T.N., Zhang, G.W., 1986. Fault displacement and recurrence intervals of earthquakes on the northern segment of the Honghe River fault zone, Yunnan province. *Seismology and Geology* 8, 77–90.
- Harrison, T.M., Chen, W.J, Leloup, P.H., 1992. An early Miocene transition in deformation regime within the Red River fault zone, Yunnan, and its significance for Indo-Asian tectonics. *Journal of Geophysical Research* 97(B5), 7159–7182.
- Harrison, T.M, Leloup, P.H., Ryerson, F.J., Tapponnier, P., Lacassin, R., Chen, W.J., 1996. Diachronous initiation of transtension along the Ailao Shan-Red River Shear zone, Yunnan and Vietnam. In: Harrison, T.M., Yin, A., (Eds.), *The Tectonics of Asian* Cambridge University Press, New York, pp. 208–226.

- Hobbs, B.E., 1985, The geological significance of microfabric analysis. In: Wenk, H.R.,(Editor), Preferred Orientation in Deformed Metals and Rocks: An Introduction to Modern Texture Analysis, Academic Press, Orlando, pp. 463–484.
- Huang, T.K., 1960. Characteristics of the structure of China: Preliminary conclusions, *Scientica Sinica* 9(4), 492–544.
- Imon, R., Okudaira, T., Fujimoto, A., 2002. Dissolution and precipitation processes in deformed amphibolites: an example from the ductile shear zone of the Ryoke metamorphic belt, SW Japan. *Journal of metamorphic Geology* 20, 297–308.
- Imon, R., Okudaira, T., Kanagawa, K., 2004. Development of shape- and lattice-preferred orientations of amphibole grains during initial cataclastic deformation and subsequent deformation by dissolution–precipitation creep in amphibolites from the Ryoke metamorphic belt, SW Japan. *Journal of Structural Geology* 26, 793–805.
- Ishii, K., Kanagawa, K., Shigematsu, N., Okudaira, T., 2007. High ductility of K-feldspar and development of granitic banded ultramylonite in the Ryoke metamorphic belt, SW Japan, *Journal of structural Geology* 29, 1083–1098.
- Jolivet, L., Beyssac, O., Goffé, B., Avigad, D., Lèpvrier, C., Maluski, H., Thang, T.T., 2001. Oligo–Miocene midcrustal subhorizontal shear zone in Indochina, *Tectonics* 20, 46–57.
- Karlstrom, K.E., 1991. Towards a syntectonic paradigm for granites. EOS, Transactions of the American Geophysical Union 70, 762–770.
- Karlstrom, K.E., Miller, C.F., Kingsbury, J. A., Wooden, J.L., 1993. Pluton emplacement along an active ductile thrust zone, Piute Mountains, southeastern California: Interaction between deformational and solidification processes. *Bulletin geological Society of America* 10, 213–230.
- Lacassin, R., Leloup, P.H., Tapponnier, P., 1993. Bounds on strain in large Tertiary shear zones of SE Asia from boudinage restoration. *Journal of Structural Geology* 15, 677–692.
- Lafrance, B., Vernon, R.H., 1993. Mass transfer and microfracturing in gabbroic mylonites of the Guadalupe igneous complex, California. In: Boland, J.N., Fitz Gerald, J.D. (Eds.), *Defects and Processes in the Solid State: Geoscience applications, the McLaren Volume*. *Developments in Petrology* 4, pp. 151–167.
- Law, R.D., Casey, M., Knipe, R.J., 1986. Kinematic and tectonic significance of microstructures and crystallographic fabrics within quartz mylonites from the Assynt and Eriboll regions of the Moine thrust zone, NW Scotland. *Transactions Royal Society of Edinburgh, Earth Sciences* 77, 99–123.

- Law, R., 1990. Crystallographic fabrics: a selective review of their applications to research in structural geology. In: R.J. Knipe and E.H. Rutter, Editors, *Deformation Mechanisms, Rheology and Tectonics*, Geological Society Special Publication 54, 335–352.
- Leloup, P.H., Kienast, J.R., 1993. High-temperature metamorphism in a major strike-slip shear zone: the Ailao Shan–Red River, People’s Republic of China. *Earth and Planetary Science Letters* 118, 213–234.
- Leloup, P.H., Lacassin, R., Tapponnier, P., Schärer, U. Zhong, D.L., Liu, X.H., Zhang, L.S., Ji, S.C., Phan, T.T., 1995. The Ailao Shan-Red River shear zone (Yunnan, China), Tertiary transform boundary of Indochina. *Tectonophysics* 251, 3–84.
- Leloup, P. H., Lacassin, R., Tapponnier, P., Harrison, T.M., 2001a. Comment on “Onset timing of left-lateral movement along the Ailao Shan–Red River shear zone: $^{40}\text{Ar}/^{39}\text{Ar}$ dating constraint from the Nam Dinh area, northeastern Vietnam” by Wang et al., 2000, *Journal of Asian Earth Sciences* 18, 281–292. *Journal of Asian Earth Sciences* 20, 95–99.
- Leloup, P.H., Arnaud, N., Lacassin, R., Kienast, J. R., Harrison, T. M., Phan Trong, T.T., Replumaz, A., Tapponnier, P., 2001b. New constraints on the structure, thermochronology, and timing of the Ailao Shan-Red River shear zone, SE Asia, *Journal of Geophysical Research* 106, 6683–6732.
- Leloup, P. H., Tapponnier, P., Lacassin, R., 2007. Comment on “Discussion on the role of the Red River shear zone, Yunnan and Vietnam, in the continental extrusion of SE Asia” by Searle, M.P., 2006, *Journal of the Geological Society, London* 163, 1025–1036. *Journal of the Geological Society, London* 164, 1253–1260
- Liu, J.L., Wang, A.J., Cao, D.H., Xiu, Q.Y., 2004. Structure and evolution of the post-collisional fault structures in the Three River orogenic belt: exemplified by the Cenozoic Jianchuan-Lanping Basin. *Geological Journal of China Universities* 12 (4), 488–499.
- Liu, J.L., Song, Z.J., Cao, S. Y., Zhai, Y.F., Wang A.J., Gao, L., Xiu, Q.Y., Cao, D.H., 2006. The dynamic setting and processes of tectonic and magmatic evolution of the oblique collision zone between Indian and Eurasian plates: exemplified by the tectonic evolution of the Three River region, eastern Tibet (in Chinese). *Acta Petrologica Sinica* 22, 775–786.
- Liu, J.L., Cao, S.Y., Zhai, Y.F., Song, Z.J. Wang, A.J., Xiu, Q.Y., Gao, L., Guan, Y., 2007. Rotation of Crustal Blocks as an Explanation of Oligo–Miocene Extension in Southeastern Tibet–Evidenced by the Diancangshan and Nearby Metamorphic Core Complexes. *Earth Science Frontiers* 14 (4), 40–48
- Lister, G.S., Dornsiepen, U.L., 1982. Fabric transitions in the Saxony granulite terrane. *Journal of Structural Geology* 4, 81–92.

- Ludwig, K.R., 1999. User's Manual for Isoplot/Ex, version 2.06: A geochronological toolkit for Microsoft Excel. Berkeley Geochronology Center, Special Publication No. 1a, 49.
- Ludwig, K.R. 2001. SQUID 1.02: A user's manual. Berkeley Geochronology Center, Special Publication No. 2, 19.
- Mainprice, D., Bouchez, J.L., Blumenfeld, P., Tubia, J.M., 1986. Dominant c slip in naturally deformed quartz: implications for dramatic plastic softening at high temperature. *Geology* 14, 819–822.
- Maluski, H., Lepvrier, C., Jolivet, L., Carter, A., Roques, D., Beyssac, O., Tang, T.T., Thang, N.D., Avigad, D., 2001. Ar-Ar and fission-track ages in the Song massif: Early Triassic and Cenozoic tectonics in northern Vietnam. *Journal of Asian Earth Science* 19, 233–248.
- Martelat, J.E. Schulmann, K., Lardeaux, J.M., Nicollet, C., Cardon, H., 1999. Granulite microfabrics and deformation mechanisms in southern Madagascar. *Journal of Structural Geology* 21 (6), 671–687.
- Menegon, L., Pennacchioni, G., Stünitz, H., 2006. Nucleation and growth of myrmekite during ductile shear deformation in metagranites. *Journal of Metamorphic Geology* 24, 553–568.
- Menegon, L., Pennacchioni, G., Spiess, R., 2008. Dissolution-precipitation creep of K-feldspar in mid-crustal granite mylonites. *Journal of Structural Geology* 30 (5), 565–579.
- Miller, R.B, Paterson, S.R., 1994. The transition from magmatic to high-temperature solid-state deformation: implications from the Mount Stuart batholiths, Washington. *Journal of Structural Geology* 16(6), 853–865.
- Molnar, P., Tapponnier, P., 1975. Cenozoic tectonics of Asia: Effects of a continental collision. *Science* 189, 419–426.
- Morley, C.K., 2007. Variations in late Cenozoic-Recent strike-slip and oblique-extensional geometries, within Indochina: The influence of preexisting fabrics, *Journal of Structural Geology* 29, 36–58.
- Nagy, E.A., Maluski, H., Lepvrier, C., Schaerer, U., Phan, Truong Thi, Leyreloup, A., Vu, Van Thich, 2001. Geodynamic significance of the Kontum Massif in central Vietnam: composite $^{40}\text{Ar}/^{39}\text{Ar}$ and U–Pb ages from Paleozoic to Triassic. *Journal of Geology* 109 (6), 755–770.
- Olsen, T.S., Kohlstedt, D.L., 1984. Analysis of dislocations in some naturally deformed plagioclase feldspars. *Physics and Chemistry of Minerals* 11, 153–160.
- Olsen, T.S., Kohlstedt, D.L., 1985. Natural deformation and recrystallization of some intermediate plagioclase feldspars. *Tectonophysics* 111, 107–131.
- Passchier, C.W., Trouw, R. A. J., 2005. *Microtectonics*. Springer-Verlag, Berlin.

- Paterson, S.R., Tobisch, O.T., 1988. Using pluton ages to determine regional deformations: problems with commonly used criteria. *Geology* 16, 1108–1111.
- Paterson, S.R., Vernon, R.H., Tobisch, O.T., 1989. A review of criteria for the identification of magmatic and tectonic foliations in granitoids. *Journal of Structural Geology* 11, 349–363.
- Paterson, S.R., Tobisch, O.T., Vernon, R.H., 1991a. Emplacement and Deformation of Granitoids during Volcanic Arc Construction in the Foothills Terrane, Central Sierra–Nevada, California. *Tectonophysics* 191, 89–110.
- Paterson, S.R., Brudos, T., Fowler, T.K., Carlson, C., Bishop, K., Vernon, R.H., 1991b. Papoose Flat pluton: forceful expansion or post-emplacement deformation? *Geology* 19, 324–327.
- Paterson, S.R., Fowler, T.K., Schmidt, K.L., Yoshinobu, A.S., Yuan, E.S., Miller, R.B., 1998. Interpreting magmatic fabric patterns in plutons. *Lithos* 44, 53–82.
- Peltzer, G., Tapponnier, P., 1988. Formation and evolution of strike-slip faults, rifts, and basins during the India-Asia collision: an experimental approach. *Journal of Geophysical Research* 93(15), 085–117.
- Prior, D.J., Trimby, P.W., Weber, U.D., Dingley, D.J., 1996. Orientation contrast imaging of microstructures in rocks using forescatter detectors in the scanning electron microscope. *Mineralogical Magazine* 60, 859–869.
- Rosenberg, C.L., 2004. Shear zones and magma ascent: A model based on a review of the Tertiary magmatism in the Alps. *Tectonics* 23(3), 1–21.
- Sassier, C., Leloup, P.H., Rubatto, D., Galland, O., Yue, Y., Lin, D., 2009. Direct measurement of strain rates in ductile shear zones: A new method based on syntectonic dikes. *Journal of Geophysical Research-Solid Earth* 114, 1–32.
- Schärer, U., Tapponnier, P., Lacassin, R., Leloup, P.H., Dalai, Z., Ji, S.C., 1990. Intraplate tectonics in Asia: a precise age for large-scale Miocene movement along the Ailao Shan–Red River shear zone, China. *Earth and Planetary Science Letters* 97, 65–77.
- Schärer, U., Zhang, L.S., Tapponnier, P., 1994. Duration of strike-slip movements in large shear zones: The Red River belt, China. *Earth and Planetary Science Letters* 126, 379–397.
- Schmid, S.M., Casey, M., 1986. Complete fabric analysis of some commonly observed quartz c-axis patterns. In: Hobbs, B.E., Heard, H.C. (Eds.), *Mineral and Rocks Deformation: Laboratory Studies–The Patterson Volume*. American Geophysicists Union, *Geophysical Monograph* 36, pp. 263–286.
- Schulmann, K., Mlcoch, B., Melka, R., 1996. High-temperature microstructures and rheology of deformed granite, Erzgebirge, Bohemian Massif. *Journal of Structural Geology* 18(6), 719–733.

- Searle, M.P., 2006. Role of the Red River Shear zone, Yunnan and Vietnam, in the continental extrusion of SE Asia, *Journal of the Geological Society, London* 163, 1025–1036.
- Searle, M.P., 2007, Comment on ‘Discussion on the role of the Red River shear zone, Yunnan and Vietnam, in the continental extrusion of SE Asia’ by Searle, M.P., 2006, *Journal of the Geological Society, London*, v. 163, p. 1025–1036: *Journal of the Geological Society, London*, v. 164, p. 1253–1260.
- Sha, S.L., 1998. The basic features of Diancang Shan M T metamorphic zone (in Chinese). *Yunnan Geology* 1, 1–16.
- Sha, S.L., Yin, G.H., Ao, D., Duan, G. X., 2002. Discovery and significance of ophiolitic mélanges at Diancang Shan Mountain in northwestern Yunnan. *Regional Geology of China* 29, 44–47.
- Shelley, D., 1985. Determining paleo-flow directions from groundmass fabrics in the Lyttleton radial dykes, New Zealand. *Journal of Volcanology and Geothermal Research* 25, 69–79.
- Shelley, D., 1994. Spider texture and amphibole preferred orientations. *Journal of Structural Geology* 16, 709–717.
- Simpson, C., Wintsch, R.P., 1989. Evidence for deformation-induced K-feldspar replacement by myrmekite. *Journal of Metamorphic Geology* 7, 261–275.
- Skrotzki, W., 1992. Defect structures and deformation mechanisms in naturally deformed amphibole. *Physics Status Solid* 131, 605–624.
- Stipp, M., Stünitz, H., Heilbronner, R., and Schmid, S., 2002, The eastern Tonale fault zone: a ‘natural laboratory’ for crystal plastic deformation of quartz over a temperature range from 250 to 700 °C: *Journal of Structural Geology* 24, 1861–1884.
- Stipp, M., Heilbronner, R. 2002. The eastern Tonale fault zone: a nature laboratory for crystal plastic deformation of quartz over a temperature range from 250 to 700 °C. *Journal of Structural Geology* 5, 1–24.
- Stünitz, H., 1993. Transition from fracturing to viscous flow in a naturally deformed metagabbro. In: Boland, J.N., Fitz Gerald, J.D. (Eds.), *Defects and Processes in the Solid State: Geoscience Applications, the McLaren Volume. Developments in Petrology* 4, 121–150.
- Sun, Z., Zhong, Z. H., Zhou, D., Qiu, X. L., Wu, S. M., 2003. Deformation mechanism of Red River fault zone during Cenozoic and experimental evidences related to Yinggehai basin formation. *Journal of Tropical Oceanography* 22(2), 1–9.
- Tapponnier, P., Peltzer, G., Armijo, R., Le Dain, A.Y., Cobbold, P., 1982. Propagating extrusion tectonic in Asia: new insights from simple experiments with plasticine. *Geology* 10, 611–616.

- Tapponnier, P., Peltzer, G., Armijo, R., 1986. On the mechanics of the collision between India and Asia. In: Coward, M.P., Ries, A.C. (Eds.), *Collision Tectonics*. Geological Society of London Special Publication 19, pp. 115–157.
- Tapponnier, P., Lacassin, R., Leloup, P.H., Schärer, U., Zhong, D.L., Liu, X.H., Ji, S.C., Zhang, L.S., Zhong, J.Y., 1990. The Ailao Shan/Red River metamorphic belt: Tertiary left-lateral shear between Indochina and South China. *Nature* 343, 431–437.
- Tran, N.N., Mitsuhiro, T., Tetsumaru, I., 1998. P–T–t paths and post-metamorphic exhumation of the Day Nui Con Voi shear zone in Vietnam. *Tectonophysics* 290, 299–318.
- Tullis, J., 1983. Deformation of feldspars. In: Ribbe, P.H. (Eds.), *Feldspar Mineralogy*, Mineralogical Society of America 2, 297–323.
- Tullis, J., Yund, R.A., 1987. Transition from cataclastic flow to dislocation creep of feldspar: mechanisms and microstructures. *Geology* 15, 606–609.
- Vernon, R.H., 1987. Growth and concentration of fibrous sillimanite related to heterogeneous deformation in K-feldspar-sillimanite metapelites. *Journal of Metamorphic Geology* 5, 51–68.
- Vernon, R.H. 1991. Questions about myrmekite in deformed rocks. *Journal of Structural Geology* 13, 979–985.
- Vernon, R.H., 1999. Flame perthite in metapelitic gneisses in the Cooma Complex, SE Australia. *American Mineralogist* 84, 1760–1765.
- Vernon, R.H., 2000. Review of microstructural evidence of magmatic and solid-state flow. *Visual Geosciences* 5, 1–23.
- Viola, G., Anczkiewicz, R., 2008. Exhumation history of the Red River shear zone in northern Vietnam: new insights from zircon and apatite fission-track analysis. *Journal of Asian Earth Sciences* 33, 78–90.
- Wang, E., Burchfiel, B.C., 1997. Interpretation of Cenozoic tectonics in the right-lateral accommodation zone between the Ailao Shan shear zone and the eastern Himalayan syntaxis. *International Geology Review* 39, 191–219.
- Wang, P.L., Lan, C.Y., Yem, N.T., Lo, C.H., Lee, T.Y., Chung, S.L., 1998. Thermochronological evidence for the movement of the Ailao Shan-Red River shear zone: a perspective from Vietnam. *Geology* 26, 887–890.
- Wang, P.L., Lo, C.H., Chung, S.L., Lee, T.Y., Lan, C.Y., Thang, T.V., 2000. Onset timing of left-lateral movement along the Ailao Shan-Red River shear zone: $^{40}\text{Ar}/^{39}\text{Ar}$ dating constraint from the Nam Dinh area, northeastern Vietnam. *Journal of Asian Earth Science* 18, 281–292.

- Wang, P.L., Lo, C.H., Chung, S.L., Lee, T.Y., Lan, C.Y., Thang, T.V., 2001. Reply to comment on "Onset of the movement along the Ailao Shan-Red river shear zone: Constraint from Ar-40/Ar-39 dating results for Nam Dinh area, northern Vietnam". *Journal of Asian Earth Sciences* 18, 281–292.
- Williams, I.S., 1998. U-Th-Pb geochronology by ion microprobe. In: McKibben, M.A., Shanks W.C., Ridley, W.I. (Eds.), *Applications of Microanalytical Techniques to Understanding Mineralizing Processes*, *Reviews in Economic Geology* 7, pp. 1–35.
- Yeh, M.W., Lee, T.Y., Lo, C.H., Chung, S.L., Lan, C.Y., Anh, T.T., 2008. Structural evolution of the Day Nui Con Voi metamorphic complex: Implications on the development of the Red River Shear Zone, Northern Vietnam. *Journal of Structural Geology* 30(12), 1540–1553.
- Yunnan Bureau of Geology and Mineral Resources, 1994, 1:50000 scale geological maps of Fengyi, Eryuan, Zhoucheng, Xiaguan, Dali areas, Unpublished map sheets.
- Zhang, L.S., Schärer, U., 1999. Age and origin of magmatism along the Cenozoic Red River shear belt. *China. Contributions to Mineralogy and Petrology* 134, 67–85.
- Zhong, D.L., Tapponnier, P., Wu, H.W., Zhang, L.S., Ji, S.C., Zhong, J.Y., Liu, X.H., Schärer, U., Lacassiu, R., Leloup, P., 1990. Large-Scale Strike-Slip-Fault-the Major Structure of Intracontinental Deformation after Collision. *Chinese Science Bulletin* 35(4), 304–309.
- Zhu, M.Z., Graham, S., McHargue, T., 2009. The Red River Fault zone in the Yinggehai Basin, South China Sea. *Tectonophysics* 476, 397–417.

Table 4.1 Summary of SHRIMP U-Pb zircon results for porphyritic monzogranite from Diancang Shan massif.

Sample	com Pb	U	Th	Th/U	Ratios*						Age (Ma)	
Grain spot	%	ppm	ppm		$^{207}\text{Pb}/^{206}\text{Pb}$	$\pm(1\sigma)$	$^{207}\text{Pb}/^{235}\text{U}$	$\pm(1\sigma)$	$^{206}\text{Pb}/^{238}\text{U}$	$\pm(1\sigma)$	$^{206}\text{Pb}/^{238}\text{U}$	$\pm(1\sigma)$
1.1	0.67	3968	752	0.20	0.0475	4.9	0.0333	5.2	0.0051	1.6	32.7	0.5
2.1	1.24	2398	901	0.39	0.0450	7.5	0.0309	7.7	0.0050	1.8	32.0	0.6
3.1	1.14	1917	542	0.29	0.0486	7.8	0.0316	8.0	0.0047	1.8	30.4	0.5
4.1	1.52	2234	700	0.32	0.0429	10.9	0.0285	11.0	0.0048	1.8	31.0	0.5
5.1	1.03	2606	1237	0.49	0.0425	7.9	0.0300	8.1	0.0051	1.7	32.9	0.6
6.1	0.69	3016	1203	0.41	0.0463	4.4	0.0318	4.7	0.0050	1.7	32.1	0.5
7.1	0.31	6736	1941	0.30	0.0457	3.0	0.0300	3.4	0.0048	1.6	30.6	0.5
8.1	1.26	2148	804	0.39	0.0455	13.5	0.0300	13.6	0.0048	1.8	30.7	0.6
9.1	0.71	4035	839	0.21	0.0440	4.9	0.0296	5.1	0.0049	1.6	31.4	0.5
10.1	0.83	2845	974	0.35	0.0450	6.9	0.0281	7.1	0.0045	1.7	29.1	0.5
11.1	1.00	2827	812	0.30	0.0471	7.2	0.0311	7.4	0.0048	1.7	30.8	0.5
12.1	0.53	4109	1056	0.27	0.0450	4.4	0.0291	4.7	0.0047	1.6	30.1	0.5
13.1	1.71	1804	355	0.20	0.0357	13.4	0.0228	13.5	0.0046	1.8	29.8	0.5
14.1	1.52	1608	2092	1.34	0.0493	9.0	0.0327	9.2	0.0048	1.7	31.0	0.5
15.1	9.66	799	422	0.55	0.0363	84.8	0.0229	84.5	0.0046	3.4	29.4	1.0

* is the ratios corrected for common Pb

This chapter has been published as: CAO SHUYUN, LIU JUNLAI, BERND LEISS, ZHAO CHUNQIANG, 2010. Zircon U-Pb geochronology from the post-kinematic granitic plutons in the Diancang Shan metamorphic massif along the Ailao Shan-Red River shear zone and its geological implications. Acta Geologica Sinica, 84, 801-840.

5 Zircon U-Pb geochronology from the post-kinematic granitic plutons in the Diancang Shan metamorphic massif along the Ailao Shan-Red River shear zone and its geological implications

Abstract

The Ailao Shan-Red River fault zone is the boundary between the Yangtze block to the northeast and the Indochina block to the southwest. It is an important tectonic zone due to its role in the southeastward extrusion of the Indochina block during and subsequent to the Indian-Eurasian collision. Diancang Shan (DCS) high-grade metamorphic complex, located at the northwest extension along the Ailao Shan-Red River (ASRR) shear zone, is a representative metamorphic complex of the ASRR tectonic belt. Structural and microstructural analysis of sheared rocks in the high-grade metamorphic rocks reveals that they are coherent with solid-state high-temperature ductile deformation, which is attributed to left-lateral shearing along the ASRR shear zone. New LA-ICP-MS zircon U-Pb geochronological and microstructural studies of the post-kinematic granitic plutons provide a straightforward time constraint on the termination ductile left-lateral shearing and exhumation of the metamorphic massif in the ASRR shear zone. It is suggested that the left-lateral shearing along the ASRR shear zone ended at ca. 21 Ma at relative lower-temperature or decreasing temperature conditions. During or after the emplacement of the young dikes at ca. 21 Ma, rapid brittle deformation event occurred, which makes the DCS massif start fast uplift/exhumation and cooling to a shallow crustal level.

5.1 Introduction

The current tectonic activity in Asia is widely cited as the consequence of continental collision between the India and Eurasia plates since the Eocene (ca. 55-34 Ma) and interests focus on a series of major strike-slip fault zones (e.g. Molnar and Tapponnier, 1975; Patriat and Achahe, 1984; Peltzer and Tapponnier, 1988; Aitchison and Davis, 2004; Aitchison et al., 2007; Meng et

al., 2008; Yi et al., 2008; Fyhn et al., 2009) (Fig. 5.1a). The ASRR shear zone in southwestern China, as the eastern boundary of the Indochina plate, plays important roles in accommodating the southeastward extrusion of the Indochina block during the Indian-Eurasian plate collision and post-collisional evolution (e.g. Tapponnier and Molnar, 1977; Tapponnier et al., 1982, 1986, 1990; Zhong et al., 1990; Lacassin et al., 1997; Lee and Lawver, 1995; Leloup et al., 1995; 2001a, b; 2007; Harrison et al. 1992, 1996; Wang and Burchfiel, 1997; Wang et al., 1998a, 1998b, 2000, 2001); Tran et al., 1998; Sun et al., 2003; Liu et al., 2006, 2007; Searle, 2006; Sassi et al., 2009) (Fig. 5. 1). Researches spanning more than twenty years have provided a wealth of information on the structural and thermal evolution, and geometries of the ASRR shear zone and Red River fault (e.g. Harrison et al., 1992; Leloup and Kienast, 1993; Schärer et al., 1990, 1994; Leloup et al., 1995, 2001a, b; Harrison et al., 1996; Chung et al., 1997; Wang et al., 1998b, 2000; Zhang and Schärer, 1999; Schoenbohm et al., 2004; Sun et al., 2003; Liu et al., 2006; Yeh et al., 2008; Zhang and Wang, 2009). The metamorphic, structural and thermochronological analyses of the four metamorphic massifs suggest that left-lateral strike-slip shearing with a long-lasting accompanied exhumation occurred along the shear zone ca. 35 Ma to 16 Ma (e.g. Schärer et al., 1990, 1994; Harrison et al., 1992, 1996; Leloup and Kienast, 1993; Zhang and Schäre, 1999; Gilley et al., 2003). However, Searle (2006) interpreted the ASRR shear zone as an upper crustal, left-lateral strike-slip fault that cuts through previous high-grade metamorphic rocks and early formed granites, and he thought that metamorphism of the Day Nui Con Voi metamorphic rocks in Vietnam predates and is unrelated to the shearing along the ASRR shear zone, and then argued that shear fabrics associated with left-lateral slip postdate peak metamorphism at relatively low temperature conditions and suggested that the left lateral shearing along the ASRR shear zone initiated from 21 Ma, instead of 35 Ma, and therefore questioned the role of the shear zone during post-collisional accommodation in eastern Tibet. Recently, Liang et al. (2007) reported new U-Pb zircon ages measured from potassic alkaline intrusions along the ASRR shear zone and suggested that the onset age of the left-lateral movements along the ASRR shear zone began at or slightly before 36 Ma and that the movements lasted from ≥ 36 Ma to 17 Ma. However, Chung et al. (2008) and Searle (2006) argued that all the calc-alkaline and potassic alkaline granites and most leucogranites within the ASRR shear zone are pre-kinematic and there is no spatial or temporal link between the alkaline igneous intrusions and the ASRR strike-slip shearing, and thus their U-Pb ages cannot serve as direct time constraints on the initiation of the fault zone. Wang et al. (1998b, 2000, 2001) suggested that the exhumation of metamorphic massif due to shearing along the ASRR zone began at ca. 27 Ma and lasted until ca. 22 Ma based on the $^{40}\text{Ar}/^{39}\text{Ar}$ date on the outcrop of the

Day Nui Con Voi metamorphic massif and also proposed that the onset of the left-lateral of the shear zone did not occur until ca. 27 Ma (e.g. Tran et al., 1998; Wang et al., 1998b; Anczkiewicz et al., 2007).

It is obvious that controversy still exists over the ages of timing of strike-slip shearing, mechanisms of exhumation along the ASRR shear zone, and its tectonic implication, specifically due to unavailability of target minerals for direct dating of the shearing (e.g. Leloup et al., 1995; Wang et al. 2000 and their comment 2001; Gilley et al., 2003; Chung et al., 2005; Searle, 2006, and his comment 2007). Constraining the age of shearing along crustal-scale faults by dating the emplacements of plutons, therefore, is a fundamental problem to the understanding of the accommodation of tectonic plate due to the continental collision or post-collisional extension (e.g. Chung et al., 1997, 1998). Hence, it is becoming increasingly clear that detailed studies of structural, microstructural and textural analyses and precise dating of the relative ages of plutons can be used to better constrain the timing of regional tectonic events. Generally, the relative timing of plutonism and tectonic deformation can be demonstrated from detailed comparison of structure and fabrics developed within tectonic plutons with their host rocks (e.g. Paterson et al., 1989; Searle et al., 2007; Cao et al., 2010).

In this paper, we focus on the DCS metamorphic massif and present new results obtained with the LA-ICP-MS on zircon U-Pb dating from post-kinematic granitic plutons. The results from combined dating, structural and microstructural evidences allow us to constrain the timing relationships between emplacement and left-lateral strike-slip shearing in the DCS massif along the ASRR shear zone.

5.2 Geological Setting

The ASRR shear zone has recorded a complex structural evolution in which the kinematics of the deformation vary both spatially and temporally. The ASRR metamorphic belt comprises four principal narrow high-grade metamorphic complexes massifs: the Xuelong Shan, Diancang Shan, Ailao Shan massifs in China and Day Nui Con Voi massif in Vietnam. These massifs are exposed between Paleozoic and Mesozoic cover rocks and are bounded in many places by Neogene-Quaternary basins (e.g. Bureau of Geology and Mineral Resources of Yunnan, 1983) (Fig. 5.1b). The DCS metamorphic massif is located between the Lanping-Simao Basin and the Dali block, which is an elongated metamorphic massif (ca. 20 km wide and 80 km long). To the south it is separated from the Ailao Shan massif along the ASRR shear zone by the Midu Gap, an approximately 80-km segment of brittlely deformed, essentially unmetamorphosed sedimentary

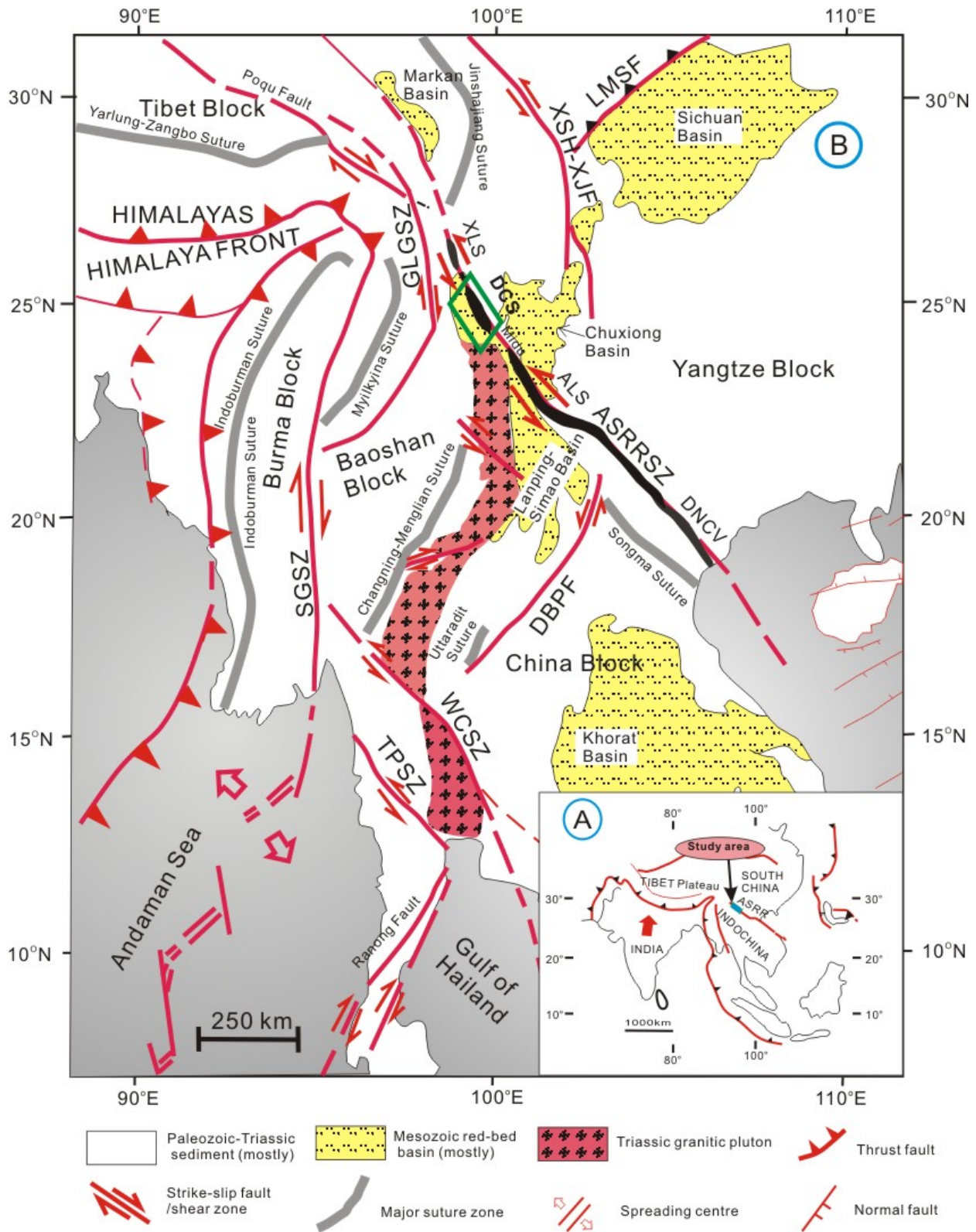


Fig. 5.1 Tectonic sketch map of Southeast Asia (modified after Tapponnier et al. (1986), Leloup et al. (2005) and Morley (2007)). (a) Geologic sketch of the extrusion of Indochina in response to northward penetration by India; (b) major sutures and shear zones/faults in Southeast Asia. GLGSZ-Gaoligong shear zone; SGSZ-Sagaing shear zone; TPSZ-Three Pagoda shear zone; WCSZ-Wang Chao shear zone; LMSF-Longmen Shan fault; XSH-XJF-Xianshuihe-Xiaojiang fault; DBPF-Dien Bien Phu fault; ASRRSZ-Ailao Shan-Red River shear

zone; XLS-Xuelong Shan metamorphic massif; DCS-Diancang Shan metamorphic massif; ALS-Ailao Shan metamorphic massif; DNCV-Day Nui Con Voi metamorphic massif.

rocks. Late Cenozoic and active normal faults and their associated basins bound the high grade metamorphic complexes on both sides of the DCS mountain range. The DCS massif consists of three tectono-metamorphic zones (western, central and eastern zones), which are based on integrated field, structural, petrological and geochronological data (Fig. 5.2a). The retrograde metamorphism (greenschist facies conditions) overprinted the high-temperature metamorphic belt (more than 1500 m thick) along the eastern edge of the DCS mountain range. Chloritic mylonites of upper greenschist to greenschist grade constitute a normal shear zone. Macro- and micro-shear sense indicators suggest a top-to-east shearing. The western and central zones are characterized by an intensely sheared high-grade metamorphic mylonitic unit. Paleo- to Mid-Proterozoic amphibolites, schists, gneisses, marbles and granitic intrusions have typically high-temperature mineral assemblages that include sillimanite + garnet + staurolite + kyanite, hornblende + plagioclase, tremolite + diopside + olivine + calcite + dolomite, and two feldspars + quartz + two micas.

At outcrop scale of the high-grade metamorphic rocks in the DCS massif, granitic rocks are ubiquitous and mostly occur as layered bodies. The high-grade metamorphic rocks and most plutons are highly mylonitized due to left-lateral shearing. Folds are often asymmetric (e.g. hook-like folds) and sheath folds are common in sheared gneisses (such as sillimanite and amphibolitic gneiss), which show characteristics of plastic flow and intense ductile shearing. The hinges of the sheath folds are mostly parallel or subhorizontal to the regional stretching lineation direction. The solid-state deformation of the granite is expressed by the widespread presence of mylonites, which are restricted to the vicinity of the DCS fault. A remarkable feature of the mylonites is their extremely strong stretching lineation fabrics, in contrast to poorly developed mylonitic foliation, thus forming L and L>>S tectonites. Some segments are composed predominantly of L-S-tectonites that are defined by a prominent stretching lineation and an equally well developed foliation. The mylonitic foliation, when present, strikes NNW-SSE. The lineation is subhorizontal or plunge gently either to the NNW or to the SSE direction (Fig. 5.2b). Shear zone segments record a significant component of NNW-directed non-coaxial strain. Widespread occurrence of different shear criteria (e.g. sheared veins, S-C fabric, C' shear bands, mica fish arrays, sigma- and delta-type feldspar porphyroclasts) suggests that these gneisses and pre- and syn-kinematic intrusions experienced intensive progressive left-lateral strike-slip shear deformation (Fig. 5.3a–c). The increased ductility of the area adjacent to the

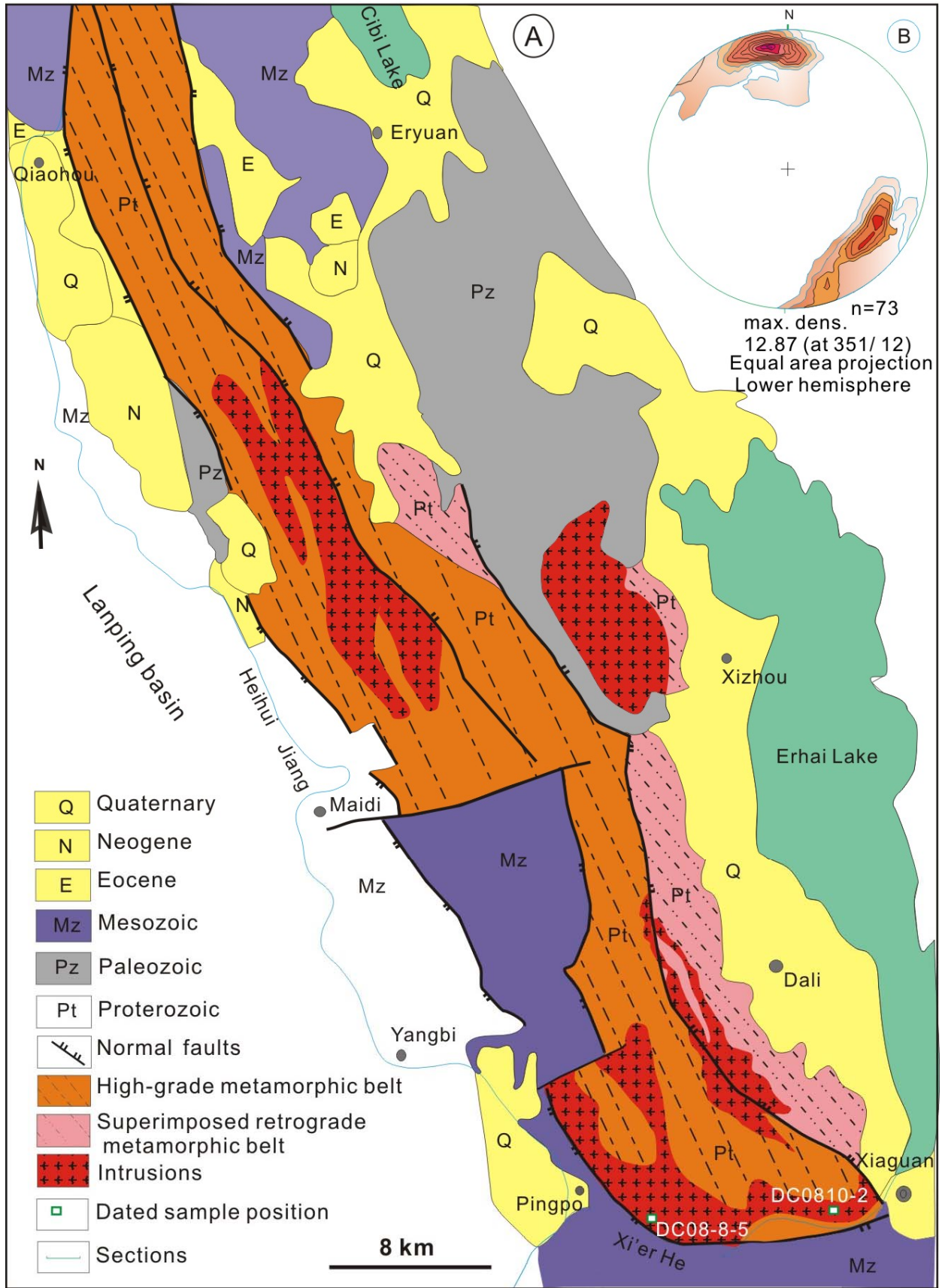


Fig. 5.2 Geological map of the Diancang Shan area (modified from Yunnan Bureau of Geology and Mineral Resources, 1994).

syn-kinematic emplacements suggests that emplacement of the granite was synchronous with mylonitization. However, post-kinematic plutonic intrusions or mostly granitic pegmatite and felsic dikes remain unsheared and show cutting-across relationship with the mylonitic foliation and lineation are also observed in the DCS massif.

5.3 High-temperature Ductile Deformation of Mylonites from the High-grade Metamorphic Belt

High-temperature mylonites derived from either pre- and syn-kinematic granitic rocks and amphibolitic rocks constitute the main part of the shear zone in the high-grade metamorphic complex. At outcrop scale, augen structures in mylonitized monzogranite and amphibolites are also typical features of the high-temperature mylonites. They are composed of porphyroclasts of K-feldspar, plagioclase and hornblende and fine matrix of feldspar, quartz, hornblende and other mineral phases (Fig. 5.3). Different mineral phases show distinctive deformation structures. Equigranular quartz grains often form triple junctions. Serrated grain boundaries are observed in some cases, suggesting local high-temperature grain boundary migration. Rectangular and sigmoidal quartz aggregates are parallel to the major foliation and lineation of the rocks (Fig. 5.3d–g). Rare occurrence of dislocation substructures in quartz grains points to the importance of high-temperature recovery and recrystallization during or after high-temperature shearing (Passchier and Trouw, 2005; Cao et al., 2010). Feldspar grains show typical characteristics of high-temperature plastic deformation. They are elongated or partly twinned, and some are partly or completely dynamically recrystallized into fine-grained matrix (Fig. 5.3a, b, g). The porphyroclastic cores show undulatory and inhomogeneous extinction, and have core-mantle structures and subgrains (Fig. 5.3a, b). Mechanical twinning and a few free dislocations near twin boundaries are also the effects of plastic deformation. TEM analyses show that some dislocations are organized into dislocation walls and form subgrains (Cao et al., 2010). Thus K-feldspar recrystallization seems to be dominated by subgrain rotation. Deformation of K-feldspar was associated with metasomatism by relatively calcium-rich plagioclase to form myrmekite structure, suggesting plastic deformation at feldspar recrystallization temperature above 550 °C (Vernon, 1991; Menegon et al., 2006) (Fig. 5.3f). The recrystallization-accommodated dislocation creep in feldspar is generally completed by moderately high temperatures, or middle to upper amphibolite facies (e.g. Tullis, 1983; Tullis and Yund, 1987; Gandais et al., 1984; Olsen et al., 1984, 1985). Amphibolitic mylonites have typical mylonitic microstructures, shown by coarse hornblende porphyroclasts and fine-grained matrix. They generally show a gradual

transition into fine recrystallized grains in the matrix. New fine grains are heterogeneously distributed constituting alternating domains of hornblende-rich and quartzofeldspathic zones (Cao et al., 2007, 2010) (Fig. 5.3d, e).

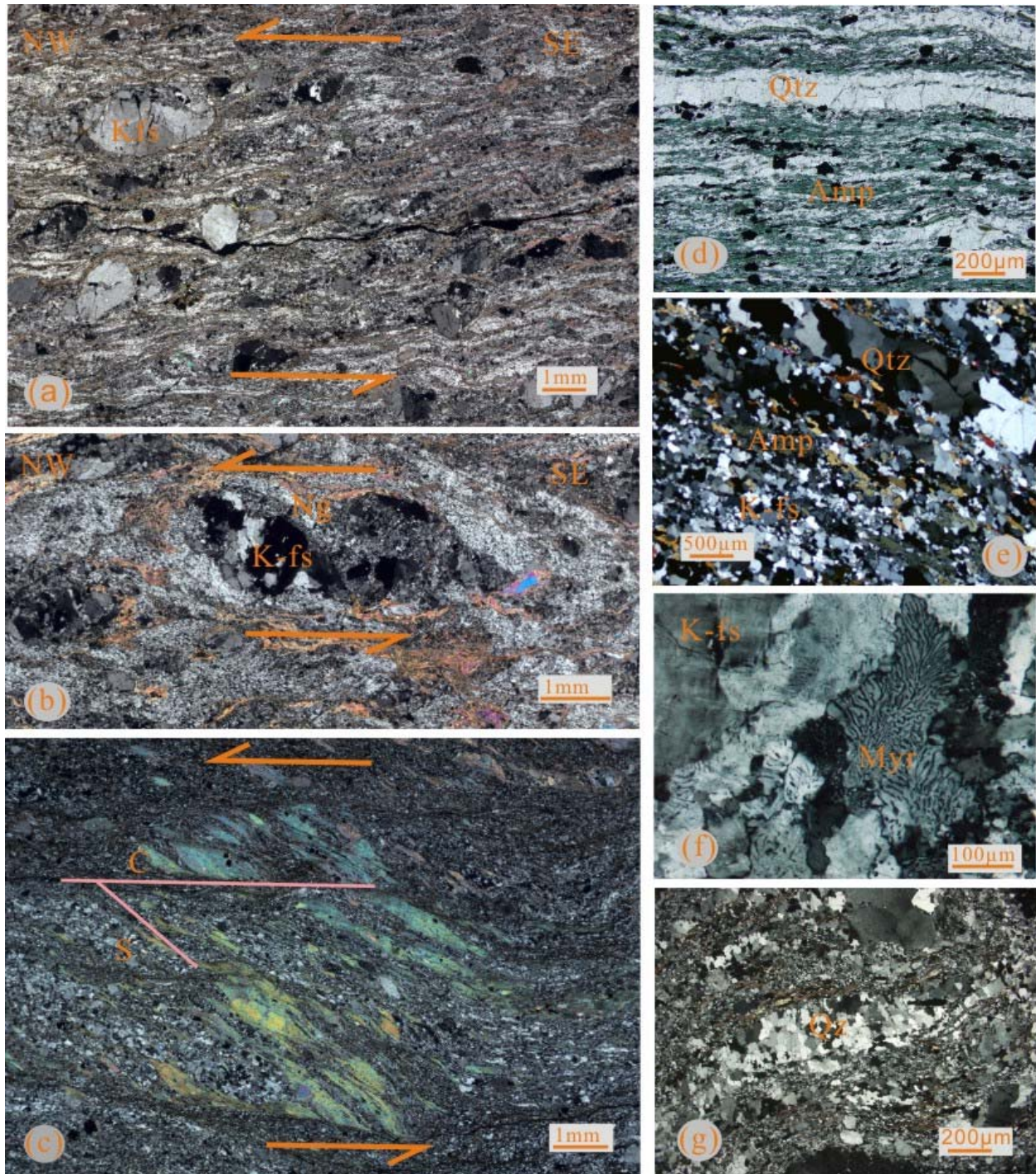


Fig. 5.3 Microscopic high-temperature plastic deformation characteristics of mylonites from the high-grade metamorphic belt. (a) Microstructural observations from the full thin section scanned from the sample in granite mylonite. Fine-grained feldspar porphyroclasts with core-mantle structures in granite mylonite. Deformed bands of feldspar porphyroclasts in quartz-biotite mylonitic matrix suggesting an early high-

temperature deformation. (b) Deformed feldspar porphyroclasts with fine-grained tails in granite mylonite (the thin section scanned). Fine-grained feldspar porphyroclasts with core-mantle structures in granite mylonite. Shear-sense is consistently left-lateral shearing. (c) S-C and fish-shaped fabrics in muscovite-gneiss, indicating the left-lateral shearing sense (the thin section scanned). (d) Fine-grained amphibole grains with strong preferred crystallographic orientation in amphibolitic ultramylonites. (e) Polycrystalline quartz (Qz) ribbon, fine-grained feldspar and amphibolite. (f) Myrmekites (Myr) on the edge of K-feldspar (K-fs) porphyroclasts in the monzogranite mylonite. (g) Sigmoidal polycrystalline quartz aggregate (Qtz) at pressure fringes around K-feldspar porphyroclasts (K-fs) in granite mylonites.

5.4 Relationships between the Post-kinematic Intrusions and Deformation

5.4.1 Mesoscopic deformation within the syn- and post-kinematic granitic dikes and veins

The post-kinematic intrusions within the DCS area are represented by granitic pegmatite dikes (DC08-8-5 and DC0810-2) (Fig. 5.4a, b). In individual outcrops, all these form steeply dipping, weakly to undeformed dikes of variable width (a few centimeters to meters). All the intrusions cut the high-temperature mylonitic foliation and lineation at high angles, and are generally neither unfoliated nor lineated. They are straight and parallel-sided dikes. Non-deformation or very weak-deformation features suggest that all these intrusions were emplaced after the cessation of the ductile shearing in the DCS range. They are composed of variable proportions of k-feldspar, plagioclase, quartz, biotite and muscovite, with accessory magnetite, apatite and zircon.

5.4.2 Microfabrics in the thin sections

Most of the feldspar grains are euhedral-subhedral in crystal shapes. In contrast to syn-kinematic plutons, the microstructures of the minerals in the post-kinematic intrusions generally occur randomly. No clear evidence links them to the main ductile deformation, but they may have been involved in a later stage of brittle deformation. Microstructural evidence of brittle deformation consists of extensive fracturing of all primary minerals. Fracturing is especially noticeable in plagioclase, which locally shows extensive networks of healed fractures. Most fractures within the grains are randomly orientated. Quartz exhibits undulose extinction and equate to slightly elliptical grains, showing weak deformation. The quartz in the highest strain zones presents as clusters of slightly elongate, polygonal grains of about 20 μm in diameter, in lens-shaped domains. The brittle deformation microstructures may be related to progressive

deformation/exhumation at relative low-temperature faulting in the DCS massif after the final stage of left-lateral shearing.

5.5 Zircons and U-Pb LA-ICP-MS Data

5.5.1 Analytical techniques

Zircons from post-kinematic granitic intrusions from the DCS high-grade metamorphic belt were analyzed using the LA-ICP-MS (Multi-collector Inductively Coupled Plasma Mass Spectrometer) method, in order to place constraints on the timing of post-kinematic intrusions. All the post-kinematic samples do not contain any evidence of ductile deformation, so they intruded during the latest stage of left-lateral strike-slip deformation.

All zircons were separated from the whole-rock samples using conventional techniques. After crushing and sieving of the powdered samples, heavy minerals were concentrated by panning and then by magnetic separation. Zircon grains were hand picked and then the selected grains were mounted into an epoxy disc with chip standard zircons of a standard material (G91500) (Wiedenbeck et al., 1995). They are carefully polished until their cores exposed. Cathodoluminescence (CL) images of zircons combined with reflected light and transmitted light were used to morphologically target distinct areas on the zircons for LA-ICP-MS analyses. CL images were obtained at a Mono CL3+ attached under a scanning electron microscope (HITACHI S3000-N). Before SHRIMP analysis, samples were coated with high-purity Au to prevent charging.

Analyses for zircon U-Pb isotopic compositions of samples in this study were carried out at the State Key Laboratory of Lithospheric Evolution, Institute of Geology and Geophysics, Chinese Academy of Sciences (Beijing). The applied laser beam is 60 μm in diameter with a frequency of 8 Hz and a model of spot ablation. Helium was used as the carrier gas through Y-type tube into Q-ICP-MS and MC-ICPM machines to enhance the transport efficiency of the ablated materials. Standards of zircon 91500 and NIST SRM 610 (^{29}Si) were analyzed after every 5 sample analyses respectively. Collection times of signal and gas background were 40 and 20 s, respectively. Isotopic ratios of $^{207}\text{Pb}/^{206}\text{Pb}$, $^{206}\text{Pb}/^{238}\text{U}$, $^{207}\text{U}/^{235}\text{U}$ ($^{235}\text{U}=^{238}\text{U}/137.88$) and $^{208}\text{Pb}/^{232}\text{Th}$ were calculated using the GLITTER 4.0 software after fractionation correcting using zircon 91500 ($^{207}\text{Pb}/^{206}\text{Pb}$ age of 1065.4 ± 0.6 Ma) (Wiedenbeck et al., 1995) as external standard. During the error calculation of the isotope ratios, the standard deviation of the

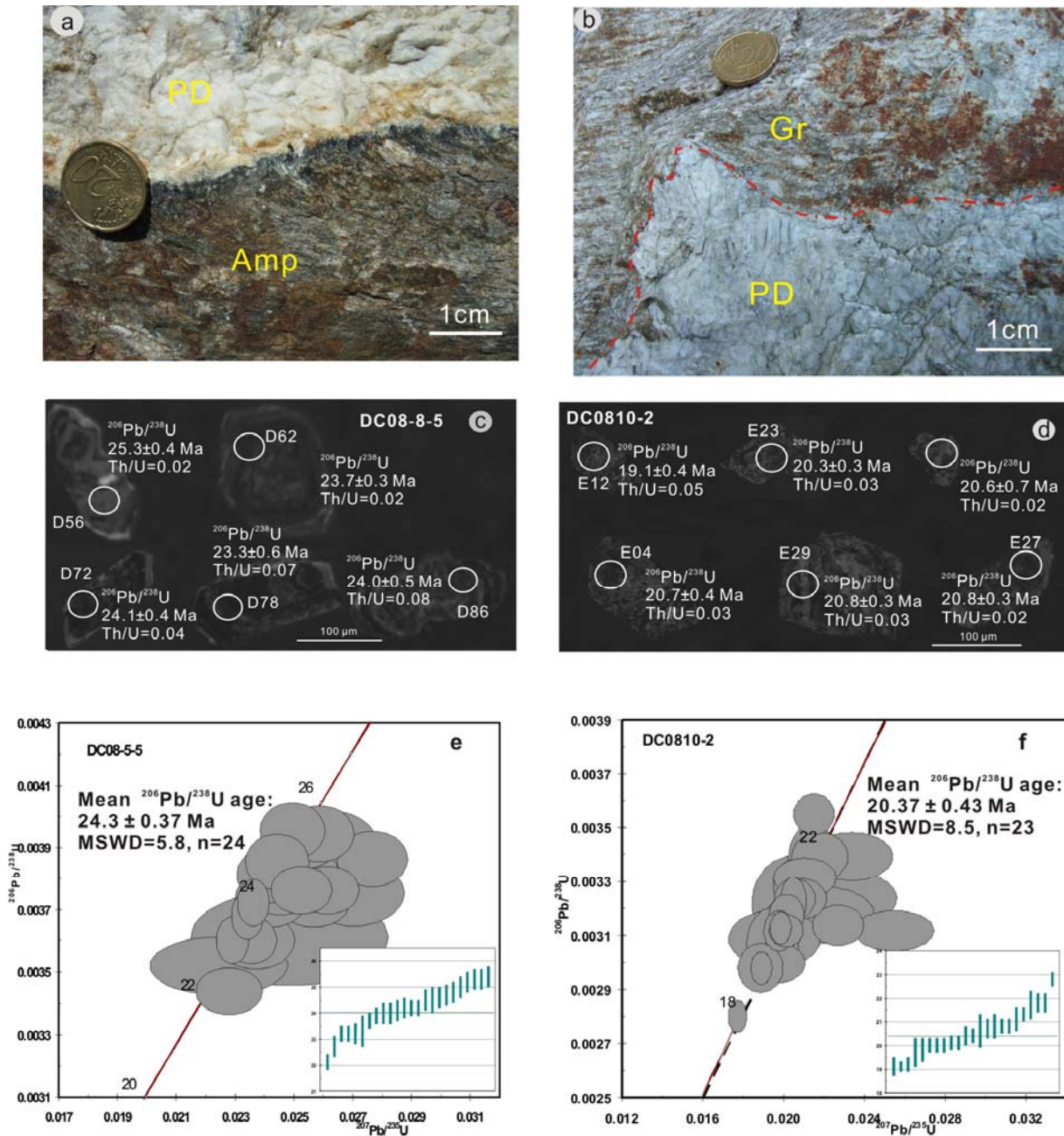


Fig. 5.4 (a) and (b) show meso-structural relationships between post-kinematic rocks and their wall rocks. (a) Weakly deformed mica pegmatite (sample DC08-8-5) crosscutting mylonitic amphibole (Amp.) with a NNW trending stretching lineation. (b) Undeformed pegmatoid dike (PD) (sample DC0810-2) crosscutting syn-kinematic mylonitic granite (Gr) with a NNW trending stretching lineation. (c) and (d) show cathodoluminescence (CL) images of representative zircons from (c) granitic pegmatite (sample DC08-8-5) and (d) granitic pegmatite (sample DC0810-2). Circles indicate the locations of LA-ICP-MS analyses. The spot numbers presented above the zircon images are the same number as listed in Tables 1. (e) and (f) show zircon U-Pb LA-ICP-MS concordia diagrams and $^{206}\text{Pb}/^{238}\text{U}$ weighted average age diagrams. (e) Age diagrams of granitic pegmatite (sample DC08-8-5); (f) Age diagrams of granitic pegmatite (sample DC0810-2).

standard zircon 91500 and targeted samples have been considered, 2% standard deviation of the recommended isotopic values for 91500 has been merged as well. Because ^{204}Pb could not be measured due to low signal and the interference from ^{204}Hg in the gas supply, common lead correction was carried out using the EXCEL program ComPbCorr#3 15G (Andersen, 2002).

All of the U-Th-Pb age calculations and plotting of concordia diagrams and weighted mean ages were made using the ISOPLOT/Ex program of Ludwig (2003). The reported ages are based on radiogenic $^{207}\text{Pb}/^{235}\text{Pb}$ or $^{238}\text{U}/^{206}\text{Pb}$ with errors given as 1σ confidence limits. The mean ages are weighted means at the 95% confidence level, and the single data point listed in Tables 1 is given at 1σ error. LA-ICP-MS U-Pb isotopic data are listed in Table 5.1.

5.5.2 Zircon and geochronology results

Granitic pegmatite sample (DC08-8-5)

Sample DC08-8-5 is from coarse-grained and weakly deformed granitic muscovite-pegmatite (Fig. 5.4a). The zircon grains are subhedral with a few having a stubby grain shape, and mostly gray and light-brown to pink color in transmitted light. They have aspect ratios of between 1:1 and 2:1, and grain sizes are commonly between 100–150 μm . On CL images they are dark in the cores and rims, indicative of U-rich. Most of the cores or rims still exhibit oscillatory zoning (Fig. 5.4c).

All analyzed zircons have Th of 105-570 ppm and U of 5437-13026 ppm, with low Th/U ratios ranging from 0.01 to 0.08. All 24 spots analyzed on zircons are concordant $^{206}\text{Pb}/^{238}\text{U}$ ages ranging from 25.4 ± 0.4 to 22.1 ± 0.3 Ma. The $^{206}\text{Pb}/^{238}\text{U}$ and $^{207}\text{Pb}/^{235}\text{U}$ results are plotted on an concordia diagram and show very consistent single age population distribution, with a $^{206}\text{Pb}/^{238}\text{U}$ weighted average age of 24.03 ± 0.37 Ma (MSWD=5.8, n=24) (Fig. 5.4e). This age is interpreted as the best estimate for the crystallization age of granitic pegmatite.

Coarse-grained pegmatite sample (DC0810-2)

Sample DC0810-2 is the undeformed granitic pegmatite dike collected from the south of DCS (Fig. 5.4b). Zircon grains from this sample are mostly euhedral with a few having a stubby grain shape, opaque dark to yellow in color in transmitted light. They have aspect ratios of between 1:1 and 1:2, and grain sizes are commonly 100-150 μm long (Fig. 5.4d). The zircon crystals are dark in color, and some are darker at the rims than at the cores indicative of differences in U-content. All analyzed zircons have Th content of 105-7849 ppm and U of 3638-29874 ppm, with low Th/U ratios ranging from 0.02 to 0.67. Analyses were conducted at 35 spots for 35 zircons in this sample. All analyses are entirely concordant and yield concordia $^{206}\text{Pb}/^{238}\text{U}$ ages ranging

from 22.8 ± 0.3 to 19.1 ± 0.4 Ma (Table 5.1). They are very close to the concordia and gave a weighted apparent mean $^{206}\text{Pb}/^{238}\text{U}$ age of 20.37 ± 0.43 Ma (MSWD = 8.5, n= 23) (Fig. 5.4f). Therefore, they represent the intrusion and crystallization ages of the granitic pegmatite, indicating that the intrusion occurred at ca. 21 Ma.

5.6 Discussion

5.6.1 *The timing of termination and duration of ductile strike-slip shearing*

The post-kinematic granitic intrusions sharply cut the high-temperature mylonitic foliation at high angles, and are generally unfoliated, straight and parallel-sided. They are very weakly deformed or nearly undeformed, suggesting that the intrusions were emplaced within a preexisting high-temperature mylonitic belt. Development of solid-state brittle deformation fabrics documents continued progressive deformation at relative low temperature during the latest stage of magma crystallization and cooling. The ICP-MS zircon ages obtained from all plutons and dikes are considered to reflect the age of their emplacement due to the magmatic texture of the analyzed zircons. Zircons from the weakly deformed granitic dike (DC08-8-5) produced a concordant weighted mean U-Pb age of 24.03 ± 0.37 Ma. Zircons from the undeformed pegmatite samples (DC010-2) produced concordant weighted mean U-Pb ages of 20.37 ± 0.43 Ma. Such age results are also consistent with microstructural observations, which confirm that they are post-kinematic plutons and dikes, and that their weak deformation occurred under decreasing temperatures. From all these analyses, we reasonably suggest that the final stage of progressive shearing can be constrained by these zircon crystallization ages. Hence, the ages of ca. 24 Ma should represent an upper limit for the termination of the left-lateral strike-slip shearing. The youngest age of ca. 21 Ma (DC0810-2) is inferred to date the final phase of regional deformation and left lateral shearing at least in the DCS massif along the ASRR shear belt. From the analyses, we reasonably suggest that the ages of ca. 21 Ma should represent the timing of termination of the left-lateral strike-slip shearing, at least in the DCS massif along the ASRR shear belt.

It is important to note that the youngest and undeformed dike (ca. 21 Ma) is significantly older than that proposed for the age of 16 Ma suggested in literature (e.g. Harrison et al., 1992, 1996; Leloup and Kienast, 1993; Tran et al., 1998; Wang et al., 1998a, b, 2000; Jolivet et al., 1999, 2001; Leloup et al., 2001a, b; Maluski et al., 2001; Garnier et al., 2002; Leloup et al., 2007). It does not support the proposal that the left-lateral shearing started after ca. 21 Ma (Searle, 2006)

as well. Therefore, all the new results suggest that the large-scale displacement along the ASRR shear zone in the DCS massif started before 21 Ma. Our data, combined with Wang et al. (1998b, 2000, 2001) suggest that the onset of the left-lateral movement of the shear zone did not occur until ca. 27 Ma (e.g. Tran et al., 1998; Wang et al., 1998b; Anczkiewicz et al., 2007). The most straightforward interpretation of our data indicate that the main periods between 27 Ma and 21 Ma were at high-temperature conditions (amphibolite facies) and terminated at about 21 Ma at low temperature.

5.6.2 Implications for the exhumation of the high-grade metamorphic complex

Structural, microstructural and geochronological data from the DCS metamorphic complex along the ASRR shear zone also show that the deformation history of the shear zone is considerably more complex than that shown in the model of Leloup et al. (1995, 2001b) and Searle (2006) (e.g. Wang et al., 2001; Chung et al., 2008). Our new observations have revealed a complex but seemingly consistent picture for the emplacement of the plutons and dikes that allows to reconcile the U-Pb results.

Geochronological data have shown a complicated cooling-exhumation history of these massifs. Debate exists on the ages of exhumation of the high-grade metamorphic massifs, e.g. XLS, DCS, ALS and DNCV along the ASRR shear zone. The first appearance of the major NE-directed extension and exhumation of the entire Bu Khang complex in central Vietnam began at 36 Ma and peaked at 21 Ma (e.g. Lepvrier et al., 1997; Jolivet et al., 1999), which was accompanied by syn-kinematic magmatic emplacement and deformation (ca. 26-24 Ma) (e.g. Nagy et al., 2000, 2001). Left-lateral transtensional deformation and cooling of the DNCV metamorphic complex in North Vietnam occurred between ca. 29 and 22 Ma (e.g. Tran et al., 1998; Wang et al., 1998b; Tran et al., 2001; Anczkiewicz et al., 2007). In the Ailao Shan, rapid cooling occurred diachronously along strike from 25 Ma at the SE end to 17 Ma at the NW end (e.g. Harrison et al., 1996) or 33-17 Ma (e.g. Tapponnier et al., 1990; Leloup et al., 2001b). Successively exhumed metamorphic massifs also include the Mogok gneiss dome (26-14 Ma), and Doi-Inthanon-Doi-Suthep metamorphic complex (27-16 Ma) (e.g. Morley, 2002; Barr et al., 2002). Left-lateral shearing in Thailand along the NW-striking Three Pagodas (ca. 36–33 Ma) and Wang Chao (ca. 33-31 Ma) faults experienced subsequent rapid uplift during E-W extension at 25-23 Ma (Lacassin et al., 1997). For the DCS metamorphic complex, Schärer et al. (1990) analyzed U-Pb ages of zircon, monazite and xenotime, from slightly sheared granitic rocks, with ages from ca. 24 Ma to 22 Ma, and Leloup and Kienast (1993) reported ^{40}Ar - ^{39}Ar cooling ages of

23 Ma to 17 Ma for amphibole, biotite, muscovite, and k-feldspar in the sheared felsic rocks. From all these data, it is suggested that the exhumation of metamorphic complexes in SE Asia is diachronous, broadly in the range from 36 Ma to 17 Ma. The above ages may have recorded an early Oligo-Miocene phase of transtensional left-lateral deformation and partial exhumation (and syn-kinematic emplacement of plutonic intrusions) of the DCS metamorphic complex in the RSRR shear zone.

As outlined above, the shear sense indicators (C-S fabrics, asymmetric tails of feldspar porphyroclasts, shear bands and veins) indicate a left-lateral movement. The local variations of lineation plunges (from 0° to 30°) could have created small deviations in the shear direction which helped some deep crustal rocks to be exhumed. Differences of cooling ages can be attributed to Miocene extension. Ages from the post-kinematic plutons and dikes can be interpreted as a decreasing or cooling event postdating high-temperature plastic deformation. We have emphasized high-temperature solid-state plastic deformation in the high-temperature conditions (Cao et al., 2007, 2010), but also show penetrative low- to moderate-temperature (<500°C) solid-state deformation. The brittle, low-temperature deformation clearly postdates the crystallization of principal magmatic phases and probably reflects the later E-W exhumation-related fabrics. On the other hand, east-dipping lineation is also observed locally on the eastern flank of the DCS from our recent field observations. This may also give clues to the young-phase intrusion activity that may suggest temporally relation between the exhumation of the metamorphic complexes and low-temperature extension in the ASRR shear zone and also in the southeast Tibet plateau since the Miocene. Early phase of Miocene cooling of the DCS can be connected to ductile extensional exhumation while the low-temperature part was associated with brittle normal faulting.

Our zircon U-Pb data and microstructural results demonstrate that the DCS metamorphic massif underwent a rapid cooling during or after ca. 24-21 Ma. This may provide a straightforward constraint on the left-lateral shearing and exhumation in the entire ASRR shear zone. This leads us to interpret the ductile exhumation during ca. 27-23 Ma from the results of $^{40}\text{Ar}/^{39}\text{Ar}$ dating for amphibole (e.g. Leloup and Kienast, 1993; Wang et al., 2000). During or after the emplacement of the younger dikes at 24-21 Ma, a rapid brittle deformation event occurred, which made the DCS massif start fast uplift/exhumation and cooling to a shallow crustal level. We would suggest that more $^{40}\text{Ar}-^{39}\text{Ar}$ and fission track (FT) dating could be used as a proxy for timing of cooling during transtensional or transpressional exhumation of the DCS high-grade metamorphic massifs, and also the whole ASRR shear zone.

5.7 Conclusions

Our observations on the DCS high-grade metamorphic massif suggest that the deformation macro- and microstructures that resulted from high-temperature deformation and dynamic recrystallization are attributed to left-lateral shearing along the ASRR shear zone. The ages of ca. 24 Ma should represent an upper age for the termination of the left-lateral strike-slip shearing, and the youngest age of ca. 21 Ma is inferred to date the final phase of regional ductile deformation and left lateral shearing at least in the DCS massif along the ASRR shear belt. From the analyses, we reasonably suggest that the ages of ca. 21 Ma should represent the timing of the termination of left-lateral strike-slip shearing, at least in the DCS massif along the ASRR shear belt. Therefore, the high-temperature ductile deformation (amphibolite facies) occurred at the main periods between 27 Ma and 21 Ma. During or after the emplacement of the young dikes at ca. 21 Ma, a rapid brittle deformation event occurred, which made the DCS massif start fast uplift/exhumation and cooling to a shallow crustal level.

Acknowledgements

This study has received joint financial support from the State Key Research “973” Plan of China (No. 2009CB421001), National Natural Science Foundation of China (40872139), the 111 Project (B07011) of the Ministry of Education, State Key Laboratory of Geological Processes and Mineral Resources (GPMR200837) and the Fundamental Research Funds for the Central Universities (GPMR2009PY01).

References

- Aitchison, J.C., and Davis, A.M., 2004. Evidence for the multiphase nature of the India–Asia collision from the Yarlung Tsangpo suture zone, Tibet. In: Malpas, J., Fletcher, C.J.N., Ali, J.R., and Aitchison, J.C. (eds.), *Aspects of the Tectonic Evolution of China*. London: Special Publication Geological Society of London, 226: 217–233.
- Aitchison, J.C., Ali, J.R., and Davis, A.M., 2007. When and where did India and Asia collide? *J. Geophys. Res.*, 112, B05423. doi:10.1029/2006JB004706.
- Anczkiewicz, R., Viola, G., Muntener, O., Thirlwall, M.F., Villa, I.M., and Quong, N.Q., 2007. Structure and shearing conditions in the DayNuiCon Voi massif: Implications for the

- evolution of the Red River shear zone in northern Vietnam. *Tectonics*, 26, TC2002, doi:10.1029/2006TC001972.
- Andersen, T., 2002. Correlation of common lead in U-Pb analyses that do not report ^{204}Pb . *Chemical Geol.*, 192: 59–79.
- Barr, S.M., MacDonald, A.S., Miller, B.V., Reynolds, P.H., Rhodes, B.P., and Yokart, B., 2002. New U-Pb and $^{40}\text{Ar}/^{39}\text{Ar}$ ages from the Doi Inthanon and Doi Suthep metamorphic core complexes, northwestern Thailand. In: Mantajit, N. (eds.), *Proceedings of the Symposium on Geology of Thailand*. Department of Mineral Resources, Bangkok, Thailand: 284–294.
- Bureau of Geology and Mineral Resources of Yunnan, 1983. *Geological Map of Yunnan*, Kunming, China.
- Cao, S.Y., Liu, J.L., and Hu, L., 2007. Micro- and submicrostructural evidence for high-temperature brittle-ductile transition deformation of hornblende: Case study of high-grade mylonites from Diancangshan, western Yunnan. *Sci. China (D)-Earth Sci.*, 50(10): 1459–1470.
- Cao, S.Y., Liu, J.L., and Leiss, B., 2010. Orientation-related deformation mechanisms of naturally deformed amphibole in amphibolite mylonites from the Diancang Shan, SW Yunnan, China. *J. Struct. Geol.*, 32, 606–622.
- Chung, S.L., Lee, T.Y., Lo, C.H., Wang, P.L., Chen, C.Y., Yem, N.T., Hoa, T.T., and Wu, G.Y., 1997. Intraplate extension prior to continental extrusion along the Ailao Shan Red River shear zone. *Geology*, 25 (4): 311–314.
- Chung, S.L., Lo, C.H., Lee, T.Y., Zhang, Y. Q., Xie, Y.W., Li, X.H., Wang, K.L., and Wang, P. L., 1998. Diachronous uplift of the Tibetan plateau starting from 40 Myr age. *Nature*, 394: 769–773.
- Chung, S.L., Chu, M.F., Zhang, Y., Xie, Y., Lee, T.Y., Lo, C.H., Li, X.H., Lan, C.Y., Zhang, Q., and Wang, Y., 2005. Tibetan tectonic evolution inferred from spatial and temporal variations in post-collisional magmatism. *Earth Sci. Rev.*, 68:173–196.
- Chung, S.L., Searle, M.P., and Yeh, M.W., 2008. Discussion and reply on “The age of the potassic alkaline igneous rocks along the Ailao Shan-Red River shear zone: Implications for the onset age of left-lateral shearing: A discussion. *J. Geol.*, 116 (2), 201–204.
- Fyhn, M.B.W., Boldreel, L.O., and Nielsen, L.H., 2009. Geological development of the Central and South Vietnamese margin: Implications for the establishment of the South China Sea, Indochinese escape tectonics and Cenozoic volcanism. *Tectonophysics*, 478: 184–214.
- Gandais, M., Willaim, C., 1984. Mechanical properties of feldspars. In: Brown, W.L. (Eds.), *Feldspars and feldspathoids*. NATO AST Series C 137, D. Reidel Publ Comp, Dordrecht Boston Lancaster, pp. 207–246.

- Garnier, V., Giuliani, G., Maluski, H., Ohnenstetter, D., Trong, T. P., Quang, V. H., Van, L. P., Van, T.V., and Schwarz, D., 2002. Ar-Ar ages in phlogopites from marble-hosted ruby deposits in northern Vietnam: Evidence for Cenozoic ruby formation. *Chemical Geol.*, 188: 33–49.
- Gilley, L.D., Harrison, T.M., Leloup, P.H., Ryerson, F.J., Lovera, O.M., and Wang, J.H., 2003. Direct dating of left-lateral deformation along the Red River shear zone, China and Vietnam. *J. Geophys. Res.*, 108, doi:10.1029/2001 JB001726.
- Harrison, T.M., Chen, W.J., and Leloup, P.H., 1992. An early Miocene transition in deformation regime within the Red River fault zone, Yunnan, and its significance for Indo-Asian tectonics. *J. Geophys. Res.*, 97(B5): 7159–7182.
- Harrison, T.M., Leloup, P.H., Ryerson, F.J., Tapponnier, P., Lacassin, R., and Chen, W.J., 1996. Diachronous initiation of transtension along the Ailao Shan-Red River Shear zone, Yunnan and Vietnam. In: Harrison, T.M., and Yin, A., (eds.), *The Tectonics of Asian*. New York: Cambridge University Press, 208–226.
- Jolivet, L., Maluski, H., Beyssac, O., Gpffé, B., Lepvrier, C., Thi, P.T., and Vuong, N.V., 1999. Oligocene-Miocene Bu Khang extensional gneiss dome in Vietnam: geodynamic implications. *Geology*, 27: 67–70.
- Jolivet, L., Beyssac, O., Goffé, B., Avigad, D., Lepvrier, C., Maluski, H., and Thang, T.T., 2001. Oligo-Miocene midcrustal subhorizontal shear zone in Indochina. *Tectonics*, 20: 46–57.
- Lacassin, R., Maluski, H., Leloup, P.H., Tapponnier, P., Hinthong, C., Siribhakdi, K., Chuaviroj, S., and Charoenravat, A., 1997. Tertiary diachronic extrusion and deformation of western Indochina: structural and $^{40}\text{Ar}/^{39}\text{Ar}$ evidence. *J. Geophys. Res.*, 102 (B5): 10,013–10,037.
- Lee, T.Y., and Lawver, L.A., 1995. Cenozoic plate reconstruction of Southeast Asia. *Tectonophysics*, 251: 85–138.
- Leloup, P.H., and Kienast, J.R., 1993. High-temperature metamorphism in a major strike-slip shear zone: the Ailao Shan–Red River, People’s Republic of China. *Earth Planet. Sci. Lett.*, 118: 213–234.
- Leloup, P.H., Lacassin, R., Tapponnier, P., Schärer, U., Zhong, D.L., Liu, X.H., Zhang, L.S., Ji, S.C., and Phan, T.T., 1995. The Ailao Shan-Red River shear zone (Yunnan, China), Tertiary transform boundary of Indochina. *Tectonophysics*, 251: 3–84.
- Leloup, P.H., Lacassin, R., Tapponnier, P., and Harrison, T.M., 2001a. Comment on “Onset timing of left-lateral movement along the Ailao Shan–Red River shear zone: $^{40}\text{Ar}/^{39}\text{Ar}$ dating constraint from the Nam Dinh area, northeastern Vietnam” by Wang et al., 2000 in *Journal of Asian Earth Sciences*, 18: 281–292. *J. Asian Earth Sci.*, 20: 95–99.

- Leloup, P.H., Arnaud, N., Lacassin, R., Kienast, J.R., Harrison, T.M., Phan, T.T., Replumaz, A., and Tapponnier, P., 2001b. New constraints on the structure, thermochronology, and timing of the Ailao Shan-Red River shear zone, SE Asia. *J. Geophys. Res.*, 106: 6683–6732.
- Leloup, P.H., Tapponnier, P., and Lacassin, R., 2007. Comment on “Discussion on the role of the Red River shear zone, Yunnan and Vietnam, in the continental extrusion of SE Asia” by Searle, M.P., 2006 in *Journal of the Geological Society, London* 163, 1025–1036. *J. Geol. Soc., London*, 164: 1253–1260.
- Lepvrier, C., Maluski, H., Vuong, N.V., Roques, D., Axent, V., and Rangin, C., 1997. Indosinian NW-trending shear zones within the Truong Son belt (Vietnam) $^{40}\text{Ar}/^{39}\text{Ar}$ Triassic ages and Cretaceous to Cenozoic overprints. *Tectonophysics*, 283: 105–127.
- Liang, H.Y., Campbell, I.H., Allen, C.M., Sun, W.D., Yu, H.X., Xie, Y.W., and Zhang, Y.Q., 2007. The Age of the Potassic Alkaline Igneous Rocks along the Ailao Shan–Red River Shear Zone: Implications for the Onset Age of Left-Lateral Shearing. *J. Geol.*, 115: 231–242.
- Liu, Junlai, Song, ZhiJie, Cao, Shuyun, Zhai, Yunfeng, Wang, Anjian, Gao, Lan, Xiu, Qunye and Cao, Dianhua, 2006. The dynamic setting and processes of tectonic and magmatic evolution of the oblique collision zone between Indian and Eurasian plates: exemplified by the tectonic evolution of the Three River region, eastern Tibet. *Acta Petrologica Sinica*, 22: 775–786 (in Chinese with English abstract).
- Liu, J.L., Cao, S.Y., Zhai, Y.F., Song, Z.J. Wang, A.J., Xiu, Q.Y., Gao, L., and Guan, Y., 2007. Rotation of Crustal Blocks as an Explanation of Oligo–Miocene Extension in Southeastern Tibet–Evidenced by the Diancangshan and Nearby Metamorphic Core Complexes. *Earth Sci. Frontiers*, 14 (4): 40–48.
- Ludwig, K.R., 2003. *ISOPLOT 3.00: A Geochronological Toolkit for Microsoft Excel*. Berkeley Geochronology Center Special Publication: 1–70.
- Maluski, H., Lepvrier, C., Jolivet, L., Carter, A., Roques, D., Beyssac, O., Tang, T.T., Thang, N.D., and Avigad, D., 2001. Ar-Ar and fission-track ages in the Song massif: Early Triassic and Cenozoic tectonics in northern Vietnam. *J. Asian Earth Sci.*, 19: 233–248.
- Menegon, L., Pennacchioni, G., Stünitz, H., 2006. Nucleation and growth of myrmekite during ductile shear deformation in metagranites. *J. Metamorph. Geol.*, 24: 553–568.
- Meng, X.G., Zhu, D.G., Shao, Z.G., Yang, C.B., Han, J.E., Yu, J., Meng, Q.W., and Lu, R.P., 2008. Late Cenozoic Stratigraphy and Paleomagnetic Chronology of the Zanda Basin, Tibet, and Records of the Uplift of the Qinghai-Tibet Plateau. *Acta Geologica Sinica*, 1: 63–72.
- Molnar, P., and Tapponnier, P., 1975. Cenozoic tectonics of Asia: Effects of a continental collision. *Science*, 189: 419–426.

- Morley, C.K., 2002. A tectonic model for the Tertiary evolution of strike-slip faults and rift Basins in SE Asia. *Tectonophysics*, 347: 189–215.
- Nagy, E.A., Schärer, U., and Minh, N.T., 2000. Oligo-Miocene granitic magmatism in central Vietnam and implications for continental deformation in Indochina. *Terra Nova*, 12: 67–76.
- Nagy, E.A., Maluski, H., Lepvrier, C., Schärer, U., Phan, T.T., Leyreloup, A., and Vu, Van Thich, 2001. Geodynamic significance of the Kontum Massif in central Vietnam: composite $^{40}\text{Ar}/^{39}\text{Ar}$ and U-Pb ages from Paleozoic to Triassic. *J. Geol.*, 109 (6): 755–770.
- Olsen, T.S., Kohlstedt, D.L., 1984. Analysis of dislocations in some naturally deformed plagioclase feldspars. *Phys. Chem. Miner.*, 11: 153–160.
- Olsen, T.S., Kohlstedt, D.L., 1985. Natural deformation and recrystallization of some intermediate plagioclase feldspars. *Tectonophysics* 111 : 107–131.
- Passchier, C.W., Trouw, R.A.J., 2005. *Microtectonics*. Springer-Verlag, Berlin. P56.
- Paterson, S.R., Vernon, R.H., and Tobisch, O.T., 1989. A review of criteria for the identification of magmatic and tectonic foliations in granitoids. *J. Struct. Geol.*, 11: 349–363.
- Patriat, P., and Achache, J., 1984. India-Eurasia collision chronology has implications for crustal shortening and driving mechanism of plates. *Nature*, 311: 615–621.
- Peltzer, G., and Tapponnier, P., 1988. Formation and evolution of strike-slip faults, rifts, and basins during the India-Asia collision: an experimental approach. *J. Geophys. Res.*, 93(15): 85–117.
- Sassier, C., Leloup, P.H., Rubatto, D., Galland, O., Yue, Y., and Lin, D., 2009. Direct measurement of strain rates in ductile shear zones: A new method based on syntectonic dikes. *J. Geophys. Res.-Solid Earth*, 114: 1–32.
- Schärer, U., Tapponnier, P., Lacassin, R., Leloup, P.H., Dalai, Z., and Ji, S.C., 1990. Intraplate tectonics in Asia: a precise age for large-scale Miocene movement along the Ailao Shan-Red River shear zone, China. *Earth Planet. Sci. Lett.*, 97: 65–77.
- Schärer, U., Zhang, L.S., and Tapponnier, P., 1994. Duration of strike-slip movements in large shear zones: The Red River belt, China. *Earth Planet. Sci. Lett.*, 126: 379–397.
- Schoenbohm, L.M., Whipple, K.X., Burchfiel, B.C., and Chen, L., 2004. Geomorphic constraints on surface uplift, exhumation and plateau growth in the Red River region, Yunnan Province, China. *Geol. Soc. Am. Bull.*, 116(7): 895–909.
- Searle, M., 2006. Role of the Red River Shear zone, Yunnan and Vietnam, in the continental extrusion of SE Asia. *J. Geol. Soc. London*, 163: 1025–1036.

- Searle, 2007. Comment on “Discussion on the role of the Red River shear zone, Yunnan and Vietnam, in the continental extrusion of SE Asia” by Searle, M.P., 2006 in *J. Geol. Soc.*, London, London 163, 1025–1036. *J. Geol. Soc.*, London, 164: 1253–1260.
- Sun, Z., Zhong, Z.H., Zhou, D., Qiu, X.L., and Wu, S.M., 2003. Deformation mechanism of Red River fault zone during Cenozoic and experimental evidences related to Yinggehai basin formation. *J. Tropical Oceanogr.*, 22(2): 1–9.
- Tapponnier, P., and Molnar, P., 1977. Active faulting and tectonics of China. *J. Geophys. Res.*, 82: 2905–2930.
- Tapponnier, P., Peltzer, G., Armijo, R., Le Dain, A.Y., and Cobbold, P., 1982. Propagating extrusion tectonic in Asia: new insights from simple experiments with plasticine. *Geology*, 10: 611–616.
- Tapponnier, P., Peltzer, G., and Armijo, R., 1986. On the mechanics of the collision between India and Asia. In: Coward, M.P., Ries, A.C. (eds.), *Collision Tectonics*. Geological Society of London Special Publication, 19: 115–157.
- Tapponnier, P., Lacassin, R., Leloup, P.H., Schärer, U., Zhong, D.L, Liu, X.H, Ji, S.C., Zhang, L.S., and Zhong, J.Y., 1990. The Ailao Shan/Red River metamorphic belt: Tertiary left-lateral shear between Indochina and South China. *Nature*, 343: 431–437.
- Tran, N.N., Mitsuhiro, T., and Tetsumaru, I., 1998. P–T–t paths and post-metamorphic exhumation of the Day Nui Con Voi shear zone in Vietnam. *Tectonophysics*, 290: 299–318.
- Tran, N.N., Sano, Y., Terada, K., Toriumi, M., Quynh, P.V., and Dung, L.T., 2001. First SHRIMP U–Pb zircon dating of granulites from the Kontum massif (Vietnam) and tectonothermal implications, *J. Asian Earth Sci*, 19: 77–84.
- Tullis, J., 1983. Deformation of feldspars. In: Ribbe, P.H. (Eds.), *Feldspar Mineralogy*, Mineralogical Society of America, pp. 297–323.
- Tullis, J., Yund, R.A., 1987. Transition from cataclastic flow to dislocation creep of feldspar: mechanisms and microstructures. *Geology*, 15: 606–609.
- Vernon, R.H. 1991. Questions about myrmekite in deformed rocks. *J. Struct. Geol.*, 13, 979–985.
- Wang, E., and Burchfiel, B.C., 1997. Interpretation of Cenozoic tectonics in the right-lateral accommodation zone between the Ailao Shan shear zone and the eastern Himalayan syntaxis. *Intl Geol. Rev.*, 39: 191–219.
- Wang, E., Burchfiel, B.C., Royden, L.H., Chen, L., Chen, J., Li, W., and Chen, Z., (eds.) 1998a. Late Cenozoic Xianshuihe-Xiaojiang, Red River, and Dali Fault Systems of Southwestern Sichuan and Central Yunnan, China. *Spec. Pap. Geol. Soc. Am.*, 327.

- Wang, P.L., Lan, C.Y., Yem, N.T., Lo, C.H., Lee, T.Y., and Chung, S.L., 1998b. Thermochronological evidence for the movement of the Ailao Shan-Red River shear zone: a perspective from Vietnam. *Geology*, 26: 887–890.
- Wang, P.L., Lo, C.H., Chung, S.L., Lee, T.Y., Lan, C.Y., and Thang, T.V., 2000. Onset timing of left-lateral movement along the Ailao Shan-Red River shear zone: $^{40}\text{Ar}/^{39}\text{Ar}$ dating constraint from the Nam Dinh area, northeastern Vietnam. *J. Asian Earth Sci.*, 18: 281–292.
- Wang, P.L., Lo, C.H., Chung, S.L., Lee, T.Y., Lan, C.Y., and Thang, T.V., 2001. Reply to comment on "Onset of the movement along the Ailao Shan-Red river shear zone: Constraint from Ar-40/Ar-39 dating results for Nam Dinh area, northern Vietnam". *J. Asian Earth Sci.*, 18: 281–292.
- Wiedenbeck, M., Alle, P., Corfu, F., Griffin, W.L., Meier, M., Oberli, F., Vonquadt, A., Roddick, J.C., and Speigel, W., 1995. Three natural zircon standards for U-Th-Pb, Lu-Hf, trace-element and REE analyses. *Geostand. Newsl.*, 19: 1–23.
- Yeh, M.W., Lee, T.Y., Lo, C.H., Chung, S.L., Lan, C.Y., and Anh, T.T., 2008. Structural evolution of the Day Nui Con Voi metamorphic complex: Implications on the development of the Red River Shear Zone, Northern Vietnam. *J. Struct. Geol.*, 30(12): 1540–1553.
- Yi, Haisheng, Wang, Chengshan, Shi, Zhiqiang, Lin, Jinhui, and Zhu, Lidong, 2008. Early Uplift History of the Tibetan Plateau: Records from Paleocurrents and Paleodrainage in the Hoh Xil Basin. *Acta Geologica Sinica (English edition)*, 1: 206–213.
- Zhang, L.S., and Schärer, U., 1999. Age and origin of magmatism along the Cenozoic Red River shear belt. *China. Contribu. Mineral. Petrol.*, 134: 67–85.
- Zhang, X., and Wang, Y.H., 2009. Crustal and upper mantle velocity structure in Yunnan, Southwest China. *Tectonophysics*, 471: 171–185.
- Zhong, D.L., Tapponnier, P., Wu, H.W., Zhang, L.S., Ji, S.C., Zhong, J.Y., Liu, X.H., Schaerer, U., Lacassiu, R., and Leloup, P., 1990. Large-Scale Strike-Slip-Fault-the Major Structure of Intracontinental Deformation after Collision. *Chinese Sci. Bull.*, 35(4): 304–309.

Table 5.1 Zircon U-Pb LA-ICP-MS analytical data of the post-kinematic intrusions in the Diancang Shan metamorphic massif

No.	Th (ppm)	U (ppm)	Th/U	$^{207}\text{Pb}/^{206}\text{Pb}$		$^{207}\text{Pb}/^{235}\text{U}$		$^{206}\text{Pb}/^{238}\text{U}$		$^{207}\text{Pb}/^{235}\text{U}(\text{Ma})$		$^{206}\text{Pb}/^{238}\text{U}(\text{Ma})$	
				Ratio	1 σ	Ratio	1 σ	Ratio	1 σ	Age	1 σ	Age	1 σ
DC08-8-5 Pegmatite													
D85	214.46	11152.37	0.01923	0.04796	0.00164	0.02276	0.00075	0.00344	0.00005	22.9	0.7	22.1	0.3
D75	163.25	9390.52	0.01738	0.04612	0.00333	0.02241	0.00156	0.00352	0.00006	22.0	2.0	22.7	0.4
D65	448.14	9748.50	0.04597	0.04745	0.00122	0.02352	0.00058	0.00360	0.00005	23.6	0.6	23.2	0.3
D76	164.59	9460.45	0.01740	0.04605	0.00093	0.02288	0.00036	0.00360	0.00005	23.0	0.4	23.2	0.3
D84	141.92	8385.20	0.01693	0.04764	0.00184	0.02367	0.00088	0.00360	0.00006	23.8	0.9	23.2	0.4
D78	573.32	8088.39	0.07088	0.04985	0.00468	0.02483	0.00223	0.00361	0.00010	25.0	2.0	23.3	0.6
D62	213.85	8925.02	0.02396	0.04605	0.00092	0.02339	0.00036	0.00368	0.00005	23.5	0.4	23.7	0.3
D70	254.85	12570.70	0.02027	0.04605	0.00091	0.02360	0.00036	0.00372	0.00005	23.7	0.4	23.9	0.3
D73	203.28	6886.46	0.02952	0.04993	0.00181	0.02566	0.00084	0.00373	0.00006	25.7	0.8	24.0	0.4
D82	177.99	9465.44	0.01880	0.04703	0.00172	0.02419	0.00080	0.00373	0.00006	24.3	0.8	24.0	0.4
D72	289.17	8087.92	0.03575	0.05243	0.00229	0.02705	0.00113	0.00375	0.00007	27.0	1.0	24.1	0.4
D60	211.37	13020.09	0.01623	0.04723	0.00161	0.02454	0.00075	0.00377	0.00006	24.6	0.7	24.2	0.4
D63	207.16	7846.69	0.02640	0.04880	0.00138	0.02524	0.00068	0.00376	0.00005	25.3	0.7	24.2	0.3
D69	105.67	7066.38	0.01495	0.05052	0.00143	0.02615	0.00071	0.00376	0.00005	26.2	0.7	24.2	0.3
D83	127.48	7551.29	0.01688	0.04605	0.00162	0.02418	0.00075	0.00381	0.00006	24.3	0.7	24.5	0.4
D86	570.43	6804.29	0.08383	0.05020	0.00283	0.02642	0.00142	0.00381	0.00008	26.0	1.0	24.5	0.5
D74	112.84	6394.45	0.01765	0.04773	0.00182	0.02515	0.00088	0.00382	0.00006	25.2	0.9	24.6	0.4
D59	195.41	6625.45	0.02949	0.04605	0.00155	0.02441	0.00072	0.00385	0.00006	24.5	0.7	24.7	0.4
D61	383.95	13026.31	0.02947	0.05210	0.00159	0.02768	0.00080	0.00386	0.00006	27.7	0.8	24.8	0.4
D77	115.95	5951.50	0.01948	0.04886	0.00192	0.02623	0.00099	0.00389	0.00006	26.3	1.0	25.0	0.4
D58	279.20	7432.91	0.03756	0.04893	0.00179	0.02639	0.00092	0.00392	0.00006	26.4	0.9	25.2	0.4
D56	105.20	5437.33	0.01935	0.04777	0.00153	0.02587	0.00079	0.00394	0.00006	25.9	0.8	25.3	0.4
D64	148.34	7623.13	0.01946	0.04674	0.00164	0.02529	0.00081	0.00392	0.00006	25.4	0.8	25.3	0.4
D57	122.40	6839.65	0.01790	0.04590	0.00141	0.02494	0.00074	0.00395	0.00006	25.0	0.7	25.4	0.4
DC0810-2 Pegmatite													
E12	6410.87	9583.20	0.66897	0.04605	0.00206	0.01884	0.00074	0.00297	0.00006	19.0	0.7	19.1	0.4
D90	1013.02	23992.19	0.04222	0.04605	0.00100	0.01887	0.00034	0.00297	0.00004	19.0	0.3	19.1	0.2
E11	676.22	12791.46	0.05286	0.04760	0.00240	0.01961	0.00094	0.00299	0.00005	19.7	0.9	19.2	0.3
E18	116.95	3638.64	0.03214	0.04605	0.00244	0.01945	0.00084	0.00306	0.00009	19.6	0.8	19.7	0.6
E10	1703.20	7018.22	0.24268	0.04605	0.00369	0.01954	0.00150	0.00308	0.00007	20.0	1.0	19.8	0.5
E23	199.80	6605.08	0.03025	0.04605	0.00133	0.01975	0.00049	0.00311	0.00005	19.9	0.5	20.0	0.3
E24	7849.32	29874.16	0.26275	0.04689	0.00142	0.02010	0.00055	0.00311	0.00004	20.2	0.6	20.0	0.3
D91	1440.21	18827.72	0.07649	0.05933	0.00318	0.02544	0.00130	0.00311	0.00005	26.0	1.0	20.0	0.3
E09	356.71	8944.31	0.03988	0.05253	0.00212	0.02267	0.00084	0.00313	0.00005	22.8	0.8	20.1	0.3
E17	771.69	11999.96	0.06431	0.04605	0.00102	0.01983	0.00034	0.00312	0.00004	19.9	0.3	20.1	0.3
E31	155.13	5155.92	0.03009	0.04994	0.00414	0.02181	0.00175	0.00317	0.00007	22.0	2.0	20.4	0.4
D89	125.16	4486.56	0.02790	0.04605	0.00152	0.02012	0.00057	0.00317	0.00005	20.2	0.6	20.4	0.3
E03	90.01	5215.91	0.01726	0.04605	0.00333	0.02035	0.00127	0.00321	0.00012	20.0	1.0	20.6	0.7
E04	149.42	4293.14	0.03480	0.04605	0.00129	0.02045	0.00042	0.00322	0.00006	20.6	0.4	20.7	0.4
E26	252.64	5611.67	0.04502	0.04956	0.00535	0.02207	0.00231	0.00323	0.00008	22.0	2.0	20.8	0.5
E27	122.70	5578.09	0.02200	0.04605	0.00169	0.02053	0.00067	0.00323	0.00005	20.6	0.7	20.8	0.3
E29	153.76	5557.75	0.02767	0.04700	0.00186	0.02091	0.00077	0.00323	0.00005	21.0	0.8	20.8	0.3
E05	105.18	5447.02	0.01931	0.04605	0.00219	0.02080	0.00088	0.00328	0.00007	20.9	0.9	21.1	0.5
E22	811.41	7705.83	0.10530	0.04605	0.00234	0.02103	0.00102	0.00331	0.00005	21.0	1.0	21.3	0.3
E13	194.89	5939.59	0.03281	0.04605	0.00214	0.02143	0.00080	0.00338	0.00009	21.5	0.8	21.7	0.6
E16	201.36	6267.33	0.03213	0.04658	0.00209	0.02178	0.00091	0.00339	0.00006	21.9	0.9	21.8	0.4
E28	271.49	6946.70	0.03908	0.05001	0.00298	0.02335	0.00133	0.00339	0.00006	23.0	1.0	21.8	0.4
D88	93.80	7382.97	0.01270	0.04391	0.00140	0.02148	0.00066	0.00355	0.00005	21.6	0.7	22.8	0.3

This chapter has been published as: Shuyun Cao, Junlai Liu, Bernd Leiss, Franz Neubauer, Johann Genser, Chunqiang Zhao, 2011. Oligo-Miocene shearing along the Ailao Shan-Red River shear zone: constraints from structural analysis and zircon U/Pb geochronology of magmatic rocks in the Diancang Shan massif, SE Tibet, China. Gondwana Research 19, 975-993. DOI: 10.1016/j.gr.2010.10.006.

6 Oligo-Miocene shearing along the Ailao Shan-Red River shear zone: constraints from structural analysis and zircon U/Pb geochronology of magmatic rocks in the Diancang Shan massif, SE Tibet, China

Abstract

The left-lateral strike-slip shearing along the Ailao Shan-Red River (ASRR) shear zone in the Southeastern Tibet, China, has been widely advocated to be a result of the Indian-Eurasian plate collision and post-collisional processes. The Diancang Shan (DCS) massif, which occurs at the northwestern extension of the Ailao Shan massif, is a typical high-grade metamorphic complex aligned along the ASRR tectonic belt. Structural and microstructural analysis of the plutonic intrusions in the DCS revealed different types of granitic intrusions spatially confined to the shear zone and temporally related to the left-lateral shearing along the ASRR shear zone in the DCS massif. The combined structural and geochronological results of SHRIMP-II and LA-ICP-MS zircon U/Pb isotopic dating have revealed successive magmatic intrusions and crystallization related to the Oligo-Miocene shearing in the DCS massif. The pre-, early- and syn-kinematic emplacements are linked to regional high-temperature deformation (lower amphibolite facies) at relatively deep crustal levels. The zircon U/Pb geochronological results suggest that the left-lateral ductile shearing along the ASRR shear zone was initiated at ca. 31 Ma, culminated between ca. 27 and 21 Ma resulting in high-temperature metamorphic conditions and slowed down at ca. 20 Ma at relatively low-temperatures.

6.1 Introduction

Combined tectonic and geomorphologic studies have yielded valuable insights into the tectonic evolution of Southeast Asia. As indicated by paleomagnetic data, the area is dominated by southeastward displacement and rotation of the Indochina Block. The displacement and block rotation is a consequence of the extrusion of the blocks from the India-Eurasian collision zone

along major fault zones, e.g. the Gaoligong and Sagaing shear zones in the west, and the Ailao Shan-Red River (ASRR) shear zone in the east (Tapponnier and Molnar, 1977; Tapponnier et al., 1982, 1986; Huang and Opdyke, 1993; Yang and Besse, 1993; Yang et al., 1995; Chung et al., 1997, 1998; Wang et al., 1998a, b, 2000, 2001; Sato et al., 1999; Burchfiel and Wang, 2003; Tanaka et al., 2008) (Fig. 6.1A, B). Shearing along the ASRR shear zone is assumed to have led to over 500 km southeastward displacement of the Indochina block relative to the Yangtze-South China block, and accompanied by the opening of the South China Sea (Huang, 1960; Tapponnier et al., 1986, 1990; Harrison et al., 1992, 1996; Briais et al., 1993; Leloup et al., 1995; Chung et al., 1997, 1998; Pelzer and Tapponnier, 1988; Searle, 2006; Fyhn et al., 2009).

The ASRR shear zone is geographically located in the Southeastern Tibet, where intensive Gondwana-Eurasian interactions took place. The shear zone has tectonically displaced and superimposed on the Jinshajiang-Ailao Shan Suture zone which is representative of a branch of the Paleotethys Ocean (e.g. Wang et al., 2000). A deep understanding of the shear zone evolution will both provide insight into the Cenozoic tectonics of Southeast Asia and help understanding and revealing the early history of the Gondwana-Eurasian interactions. Research spanning more than twenty years has provided a wealth of information on the geometry of the ASRR shear zone and its structural and thermal evolution. Recent geophysical studies have provided further evidence of the deep structure of the ASRR fault (Lee and Watkins, 1998; Clift et al. 2008; Zhang and Wang, 2009; Zhu et al., 2009).

One particular and otherwise important topic of interest is the thermochronological signature of left-lateral shearing, with the aim of constraining the timing and rate of shearing along the ASRR (Schärer et al., 1994; Zhang and Schärer, 1999; Sassi et al., 2009). Controversy still exists over the age of initiation and the duration of strike-slip shearing, the mechanisms of exhumation along the ASRR shear zone, and its tectonic implications. Early metamorphic, structural, and thermochronological (e.g. Ar/Ar and FT) analysis revealed that the left-lateral strike-slip of the ASRR shear zone started at least ca. 35 Ma ago (Schärer et al., 1990, 1994; Harrison et al., 1992; Leloup and Kienast, 1993b; Zhang and Schärer, 1999; Gilley et al., 2003) and lasted until ca. 16 Ma (Harrison et al., 1996; Wang et al., 2000, 2001; Leloup et al., 2001a, b, 2007; Gilley et al., 2003). However, Wang et al., (1998b, 2000, 2001) suggested that the exhumation of metamorphic massifs by shearing along the ASRR zone began ca. 27 Ma and lasted until ca. 22 Ma by $^{40}\text{Ar}/^{39}\text{Ar}$ dating of the metamorphic minerals (e.g. amphibole, muscovite, biotite and k-feldspar) from the Day Nui Con Voi massif. The authors proposed that the onset of the left-lateral movement in the shear zone did not occur until ca. 27 Ma (see also Tran et al., 1998; Anczkiewicz et al., 2007) and may not be responsible for the opening of the

South China Sea. Searle (2006) interpreted that the metamorphism of the Day Nui Con Voi metamorphic rocks in Vietnam predated and is unrelated to shearing along the ASRR shear zone, and then argued that the shear fabrics associated with the left-lateral slip postdated peak metamorphism at relatively low temperature conditions. He then suggested that the left-lateral shearing along the ASRR shear zone initiated from 21 Ma, instead of 35 Ma, and therefore questioned the role of the shear zone during post-collisional accommodation in eastern Tibet. These various constraints on the timing of onset shearing have been proposed from different places. Recent studies are mainly focused on the southern segment, i.e. the Ailao Shan massif in China and the Day Nui Con Voi massif in Vietnam. Recently, Liang et al. (2007) reported new U/Pb zircon ages from high potassic alkaline intrusions along the ASRR shear zone and suggested that the onset age of the left-lateral movements along the ASRR shear zone began at or slightly before 36 Ma and that the left-lateral movement continued from $\cong 36$ to 17 Ma. However, Chung et al. (2008) and Searle (2006) argued that all the calc-alkaline and high potassic alkaline granites, and most leucogranites within the ASRR shear zone are pre-kinematic and there is no spatial or temporal link between the alkaline igneous intrusions and the ASRR strike-slip shearing. Thus their U/Pb ages cannot serve as direct time constraints on the initiation of the shear zone. The Diancang Shan (DCS) metamorphic massif, an important part of the ASRR shear zone, is still poorly studied to date. Schärer et al. (1990) analyzed U/Pb ages of zircon, monazite and xenotime, from slightly sheared granitic rocks, with ages from ca. 24 to 22 Ma, and Leloup et al. (1993a) reported $^{40}\text{Ar}/^{39}\text{Ar}$ cooling ages of 23 Ma to 17 Ma for amphibole, biotite, muscovite, and K-feldspar in the sheared felsic rocks.

The relation between magmatism and shearing is a fairly important way to provide a means of determination of the age of the deformational event. It may provide an efficient means of determining the ages of the shearing, as if the temporal relations between the shear zone structures and magmatic intrusions are still not clearly shown. In particular, the main mineral microstructures of plutonic bodies can help address the link between magma emplacement and tectonics. Abundant studies (e.g. Paterson et al., 1998; Brown and Solar, 1998; 1999; Rosenberg, 2004) indicated that the emplacement can be considered either tectonically controlled (syn-tectonic) if the magmatic structure or microstructure and texture are consistent with the regional strain field, or magma-pressure driven if the pattern is independent (post-tectonic). Although criteria for the timing of magma emplacement in high-grade terranes relative to regional deformation are commonly ambiguous, and it is difficult to demonstrate unequivocally such timing for individual plutons (e.g. Paterson and Tobisch, 1988; Karlstrom, 1991; Karlstrom et al., 1993; Miller and Paterson, 1994; Searle, 2006), a variety of well-developed structures and

microfabrics are still preserved in plutons to determine whether the granites are pre-, syn- or post- shearing. They can be used to determine a record of a continuum in emplacement to deformation.

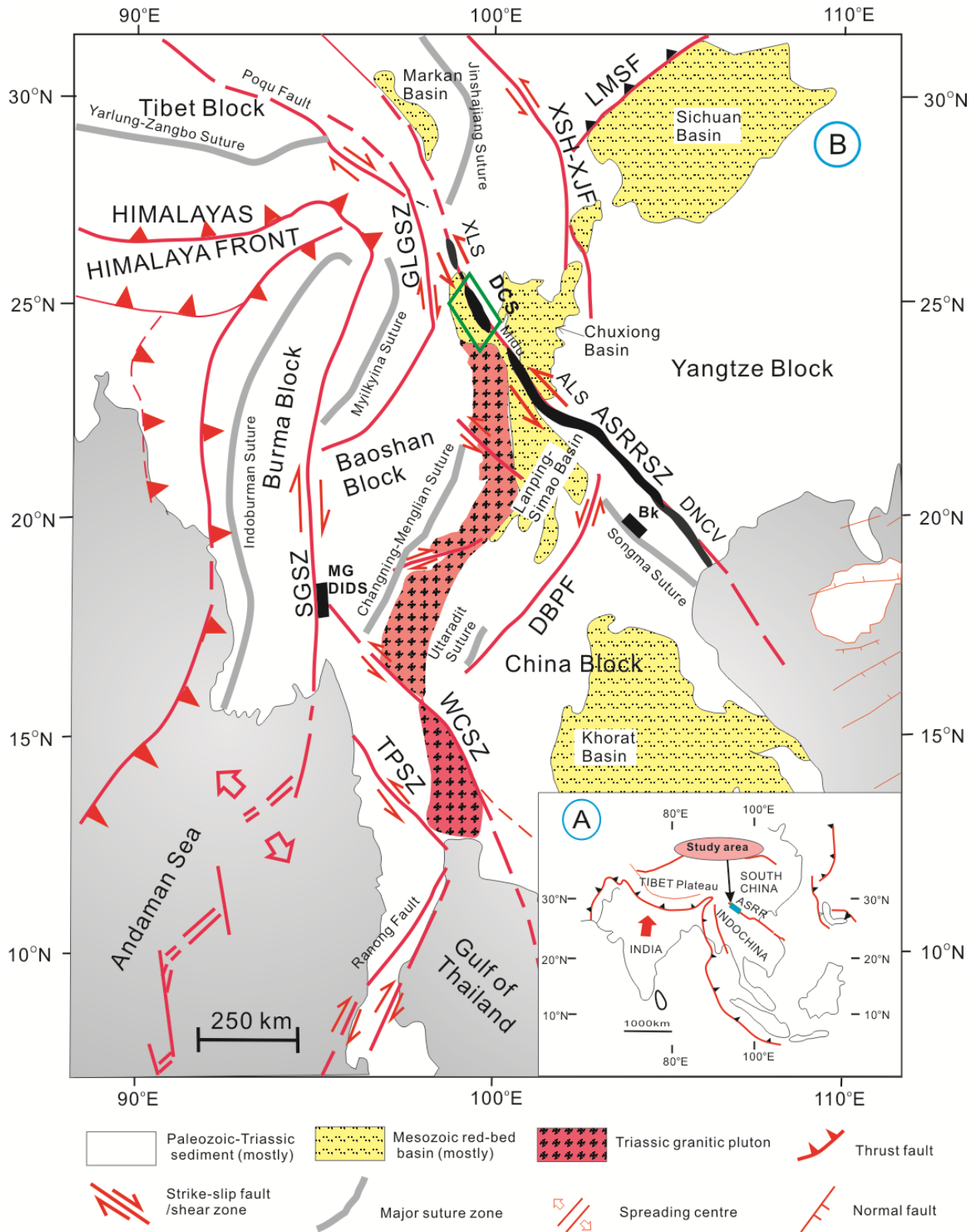


Fig. 6.1 Tectonic sketch of Southeast Asia (modified after Tapponnier et al. (1986), Leloup et al. (1995) and

Morley (2007)). A) Geologic sketch of the tectonic extrusion of the Indochina block in relation of the Indian-Eurasian continental collision. B) Major sutures and shear zones/faults in Southeast Asia. GLGSZ = Gaoligong shear zone; SGSZ = Sagaing shear zone; TPSZ = Three Pagoda shear zone; WCSZ = Wang Chao shear zone; LMSF = Longmen Shan Fault; XSH-XJF = Xianshuihe-Xiaojiang Faults; DBPF = Dien Bien Phu Fault; ASRRSZ = Ailao Shan-Red River shear zone; XLS = Xuelong Shan metamorphic massif; DCS = Diancang Shan metamorphic massif; ALS = Ailao Shan metamorphic massif; DNCV = Day Nui Con Voi metamorphic massif.; BK = Bu Khang complex; MG = Mogok gneiss dome; DIDS = Doi-Inthanon-Doi-Suthep metamorphic complex

In this paper, we present a series of new results obtained by SHRIMP and LA-ICP-MS U/Pb dating of single zircon grains from granitic plutons and dykes of different stages during shearing at the DCS massif. The new age data, coupled with our meso- and microstructural observations on pre-, syn- and post-kinematic plutons, not only allow us to establish the age framework of Cenozoic magmatic activities in the DCS massif, but can be used to better constrain the timing and duration of ASRR shearing. The data presented could also allow us to improve the current geodynamic models for the exhumation of the massifs along the ASRR shear zone, in particular during the post-collisional stage of the Indian-Eurasian plate interactions in Southeast Asia.

6.2. Geological setting and macro-structural analysis

The over 1000 km NW-trending ASRR shear zone is the boundary of the Yangtze block to the northeast and the Indochina block to the southwest. It is the most pronounced geological discontinuity in Southeast Asia (e.g. Huang, 1960; Tapponnier and Molnar, 1977; Bureau of Geology and Mineral Resources of Yunnan, 1983; Allen et al., 1984; Zhong et al., 1990; Chung et al., 1997; Wang et al., 1998b). Four narrow NW–SE oriented high-grade metamorphic massifs (mainly of Middle Proterozoic gneisses) e.g. Xuelong Shan (XLS); Diancang Shan (DCS); Ailao Shan (ALS) metamorphic complexes in China and Day Nui Con Voi (DNCV) metamorphic complex in Vietnam, are exposed along the ASRR shear zone. The metamorphic rocks show intense ductile deformation with a well-developed foliation that bears a strong sub-horizontal stretching lineation, both being parallel to the trend of the gneissic cores. Numerous shear criteria indicate that the high-grade metamorphic rocks have undergone an intense left-lateral ductile shearing (e.g. Tapponnier et al., 1986, 1990; Leloup et al., 1993a, 1995; Jolivet et al., 2001; Leloup et al., 2001b; Liu et al., 2007; Anczkiewicz et al., 2007) (Fig. 6.1B).

The DCS metamorphic massif is a narrow and elongated metamorphic massif (c. 20 km wide and 80 km long) trending NNW and SSE (Fig. 6.2A). Proterozoic high-grade metamorphic rocks,

e.g. amphibolite, marble, schist, minor quartzite and sillimanite schist, as well as plutonic intrusions of various ages are widely exposed in the central high strain shear zone. The high-temperature metamorphic assemblages (up to amphibolite facies) preserved in the massif include: almandine, staurolite, kyanite and sillimanite in schists; tremolite, diopside, olivine, calcite and dolomite in marbles; and amphibole, garnet and plagioclase in amphibolites. In the DCS massif, deformation and recrystallization and accompanied anatectic melting can unequivocally be described to left-lateral ductile shearing under high temperature metamorphic conditions along the ASRR shear zone. Deformation is characterized by subhorizontal stretching lineation, sub-vertical foliation, and isoclinal folds with lineation-parallel hinges in mylonites. Lineation predominates over foliation in the fabric components of the mylonites, which show typical $L \gg S$ fabrics. Locally there are L-S-tectonites that are defined by a prominent stretching lineation and an equally developed foliation. High temperature mylonites (mostly of granitic and amphibolitic in composition) compose the core of the metamorphic massif (Fig. 6.3b–f). In the mylonites, well-developed L stretching lineation is constituted by linear arrangement of mineral aggregates of elongated quartz-feldspar, amphibolite and biotite grains. The strong stretching mineral lineation L is plunging subhorizontally to the NW–SE or NNW–SSE with a pitch angle of less than 30° (Fig. 6.2B). When present, the mylonitic foliation is commonly parallel to compositional layering, and strikes approximately NNW–SSE, with variable dip angles. The mylonitic foliation dips steeply west along the western side of the zone and steepens to nearly vertical in the narrow central zone. Along the eastern and southeastern sides, the foliation in the hornblende-plagioclase gneiss and mica-schist dips gently to the east and southeast. Asymmetric sheath folds are common both in sheared gneisses (such as sillimanite or amphibolitic gneiss) and granitic rocks, which suggest intense ductile shearing in the entire shear zone.

Granitic rocks are ubiquitous and occur mostly as layered bodies in the DCS massif. Three main types of intrusions, pre-kinematic, syn-kinematic and post-kinematic, were observed within the DCS massif, which show variable degrees of deformation ranging from undeformed pegmatitic dykes to strongly sheared layered granites with foliations and lineation. Field and microscopic observations reveal that the pre- and syn-kinematic intrusions are coeval with high-temperature mylonitization. Widespread shear senses, including sheared veins (Fig. 6.3a), S-C/C' mylonitic fabric (Fig. 6.3c), shear bands, mica fish arrays, asymmetric fabrics (e.g. sigma- and delta-types of feldspar and hornblende porphyroclasts) (Fig. 6.3d–g) and asymmetric pressure shadows, suggest that the high-grade metamorphic rocks and most

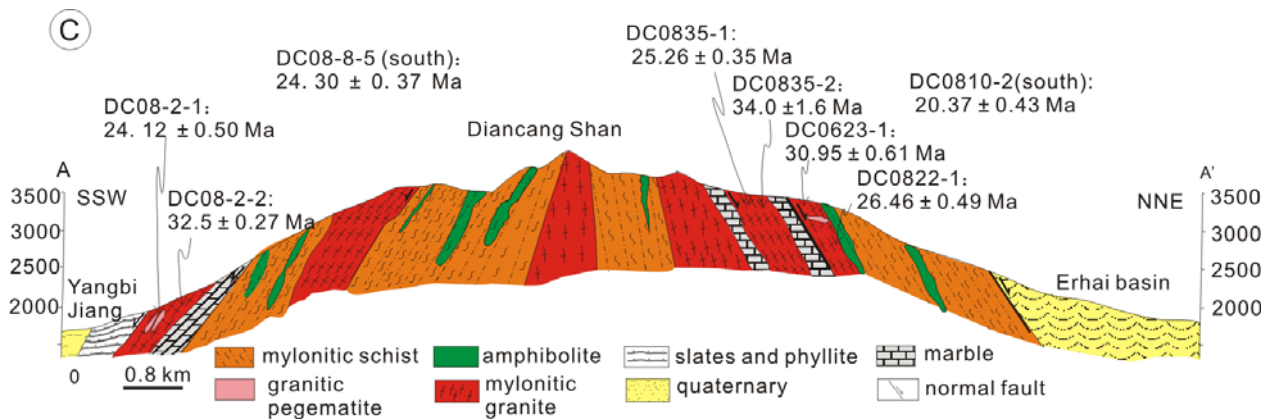
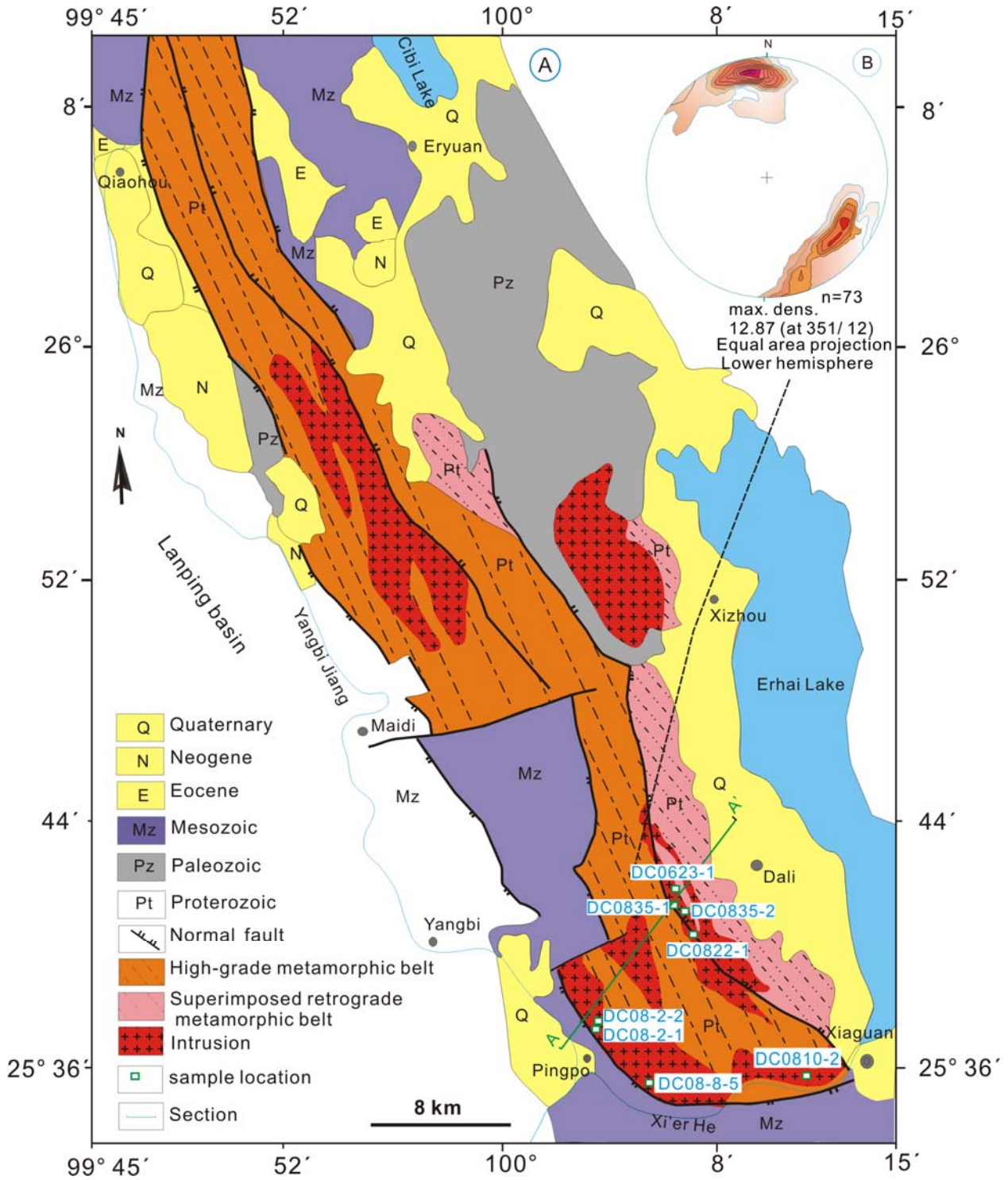


Fig. 6.2 Structural outline of the Diancang Shan area. A) Geological map of the Diancang Shan area (modified from Yunnan Bureau of Geology and Mineral Resources, 1994). B) Projection of stretching lineation from high-temperature mylonites. Lower hemisphere equal area projection. A–A' is the position of the structural section in figure 2C. U/Pb sample locations and ages are shown with arrows and two ages of samples (DC08-8-5 and DC0810-2) from the south part are also presented here.

leucocratic intrusions experienced progressive left-lateral shearing. However, post-kinematic granitic pegmatite dykes remain weakly deformed or unsheared, which show cross-cutting relationship with the mylonitic foliation and stretching lineation (Fig. 6.3h–i).

6.3. Analytical techniques

6.3.1 Optical microscopy

The detailed optical microstructural observations and measurements were conducted on thin sections from the metamorphic complex. All thin sections were cut standard parallel to the kinematic XZ section, i.e. parallel to the stretching lineation and, where visible, normal to the foliation. Microscopic observations are applied to characterize the deformation of the minerals in the rocks, and the deformation processes that affected the emplacements of the plutonic rocks. They are also used to estimate the deformation conditions e.g. temperature, and to unravel the deformation mechanisms of the main mineral phases.

6.3.2 U/Pb zircon dating

The granitic plutons and dykes from the DCS high-grade metamorphic belt were collected for SHRIMP-II and LA-ICP-MS zircon U/Pb dating. All zircons were separated from whole-rock samples using conventional techniques. After crushing and sieving of the samples, heavy minerals were concentrated by panning and then by magnetic separation. Zircon grains were hand picked and then the grains were mounted in an epoxy disc with chips of standard zircons of the TEM SL (Temora-417Ma) (Black et al., 2003) and the G91500 zircon age standard (G91500; Wiedenbeck et al., 1995) for SHRIMP-II and LA-ICP-MS analyses, respectively. These are then carefully polished until their cores were exposed. Cathodoluminescence (CL) images of zircons combined with reflected light and transmitted light images, were used to morphologically target distinct areas on the zircons for SHRIMP-II and LA-ICP-MS analyses. CL images were obtained at a Mono CL3+ attached to a scanning electron microscope (HITACHI S3000-N). Before SHRIMP-II analysis, samples were coated with high-purity Au to prevent charging.

6.3.2.1 SHRIMP-II U/Pb zircon dating

The zircon U/Pb isotopes of sample (DC0623-1) were analyzed using the Sensitive High-Resolution Ion Microprobe (SHRIMP-II) machine at the Beijing SHRIMP Ion-probe Center, Chinese Academy of Geological Sciences (CAGS). Detailed analyzing processes are similar to the description by Compston et al. (1984; 1992) and more recently stated by Williams et al. (1998); Wan et al. (2004) and Wang et al., 2004. A 3.2 nA primary beam, c. 30 μm diameter, was used for ion production within zircon grains, together with replicate analyses of the TEM standard zircon in the same epoxy mount. Both Pb/U and Pb/Th ratios and absolute Pb, Th and U abundances of the standards Sri Lanka zircon SL13 ($^{206}\text{Pb}/^{238}\text{U}=0.0928$ corresponding 572 Ma, 238 ppm ^{238}U ; Williams et al., 1998) and TEM with an age of 417 Ma ($^{206}\text{Pb}/^{238}\text{U}=0.06683$; Black et al., 2003) have been used to monitor the analyses of the zircon. Corrections for common ^{204}Pb were made using the measured ^{204}Pb isotopic composition and data processing was carried out using the SQUID 3.0 (Ludwig, 2003) and PRAWN programs (Williams et al., 1998). SHRIMP-II U-Th-Pb isotopic data are listed in Table 6.1.

6.3.1.2 LA-ICP-MS zircon dating

Zircon U/Pb isotopic measurements of seven samples (DC08-2-2, DC0835-2; DC0822-1, DC0835-1; DC08-2-1, DC0810-2, DC08-8-5) were done using the Laser Inductively Coupled Plasma Mass Spectrometer (LA-ICP-MS) method (e.g. Xie et al., 2008; Wu et al., 2010). All analyses in this study were carried out at the MC-ICPMS laboratory of the State Key Laboratory of Lithospheric Evolution, Institute of Geology and Geophysics, Chinese Academy of Sciences (IGGCAS) in Beijing. An Agilent 7500a quadrupole (Q)-ICPMS and a Neptune multi-collector (MC)-ICPMS were used for simultaneous collection of U–Pb isotopes, trace elements and Lu–Hf isotopes with an attached 193 nm excimer ArF laser-ablation system (GeoLas Plus). During analyses, the ablated aerosol was carried by helium and split into two transport tubes using a three-way pipe and therefore simultaneously introduced into the QICPMS and MC-ICPMS. The proportion of ablated material carried into the two instruments was controlled by three mass flow controllers. There is no significant mass fractionation when different proportions of ablated material were carried into the Q-ICPMS and MC-ICPMS. The detailed analytical procedure,

identical to those described by Yuan et al. (2008), can also be found in Xie et al. (2008) and Wu et al., (2010), partly described as follows (from Wu et al., 2010):

The Agilent 7500a Q-ICPMS has an abaxial Omega II lens system. Under normal operating mode, the sensitivity is better than 20 Mcps/ppm for ^{89}Y , using a 100 $\mu\text{L}/\text{min}$ PFA nebulizer and Scott spray chamber. In the case of laser ablation, the sensitivity of ^{238}U in NIST SRM 610 is 14000 cps/ppm using a spot size of 40 μm with laser repetition rate of 10 Hz and laser energy density of 25 J/cm^2 . The mass stability is better than 0.05 amu/24 h.

The GeoLas PLUS 193 nm excimer ArF laser ablation system consists of a COMPex 102 ArF excimer laser generator with wavelength of 193 nm, laser optical system with a laser beam homogenizing system, and Geolas standard software. The highest possible energy density on the sample is 35 J/cm^2 , but only 15 J/cm^2 was used in this study. Helium was used as the carrier gas to enhance transport efficiency of the ablated material. The sample cell has a diameter of \square 5.8 cm and height of 1.5 cm. This large cell yields a response time of \square 10 s, defined as the time the signal takes to decay by a factor of 10 (e.g. Wang et al., 2009, Wu et al., 2010).

All the gas lines were purged for over 1 h prior to each analytical session to reduce Pb on the surface to $^{204}\text{Pb} < 50$ cps in the gas blank. The measurements were carried out using time resolved analysis operating in a fast, peak hopping sequence in DUAL detector mode. Raw count rates for ^{29}Si , ^{204}Pb , ^{206}Pb , ^{207}Pb , ^{208}Pb , ^{232}Th and ^{238}U were collected for age determination. ^{202}Hg is usually < 10 cps in the gas blank, therefore the contribution of ^{204}Hg to ^{204}Pb is negligible and is not considered further. The integration time for the four Pb isotopes was 62.76 ms, whereas for the other isotopes (including ^{29}Si , ^{232}Th and ^{238}U) it was 30 ms. Data were acquired over 30 s with the laser off and 40 s with the laser on, giving ca. 340 (=170 reading/replicate \times 2 sweeps) mass scans for a penetration depth of ca. 20 μm . The average gas blank is typically < 4000 cps for ^{29}Si ; < 10 cps for ^{204}Pb , ^{206}Pb , ^{207}Pb and ^{208}Pb ; < 1 cps for ^{232}Th and ^{238}U .

Before analysis, the sample surface was cleaned with ethanol to eliminate possible contamination. Every 5 sample analyses were followed by measurements of one zircon 91500, one TEMORA-2 and one NIST SRM 610. $^{207}\text{Pb}/^{206}\text{Pb}$ and $^{206}\text{Pb}/^{238}\text{U}$ ratios were calculated using GLITTER 4.0 (Jackson et al., 2004; Griffin et al., 2008), which was then corrected using the Harvard zircon 91500 as an external standard. The $^{207}\text{Pb}/^{235}\text{U}$ ratio was calculated from the values of $^{207}\text{Pb}/^{206}\text{Pb}$ and $^{206}\text{Pb}/^{238}\text{U}$ ($^{235}\text{U} = ^{238}\text{U}/137.88$). The relative standard deviations of reference values for 91500 were set at 2%. Common Pb was corrected according to the method proposed by Andersen (2002). The weighted mean U–Pb ages and concordia plots were processed using ISOPLOT 3.0. Analyses of the Australian National University zircon standard TEMORA-2 as an unknown yielded a weighted $^{206}\text{Pb}/^{238}\text{U}$ age of 416 ± 2 Ma (2σ , $n=50$), which is

in good agreement with the recommended value (Black et al., 2003). Reported ages are based on radiogenic $^{207}\text{Pb}/^{235}\text{Pb}$ or $^{238}\text{U}/^{206}\text{Pb}$ with errors given as 1σ confidence limits. The LA-ICP-MS U–Pb isotopic data are listed in the table 2.

6.4. Petrology, microfabrics and geochronology

Several generations of granitic intrusions are exposed in the highly sheared metamorphic rocks in the DCS massif. Field and microscopic observations reveal the existence of pre-kinematic, syn-kinematic and post-kinematic plutons, that the ages of crystallization of the granitic rocks can be suitably applied to constrain the timing of ductile shearing along the shear zone in the DCS. Sample locations are given in Fig. 6.2A and C. The meso-structural relationships between granitic rocks and their wall rocks, and the deformation microstructures in the intrusions are presented in Fig. 6.3, 4 and Fig. 6.5 respectively. The selected zircon CL images and age diagrams are shown in Fig. 6.6 and Fig. 6.7, respectively.

6.4.1. Pre-kinematic plutons

6.4.1.1 Mesoscopic deformation within the pre-kinematic plutons

The hornblende-bearing granite (DC008-2-2), granite (DC0835-2) and porphyritic monzogranite (DC0623-1) were exposed within the southwest and central parts of the DCS massif respectively as shown in Fig. 6.2A and C. The hornblende-bearing granite (DC08-2-2) (Fig. 6.3d) contains mainly K-feldspar, hornblende, pyroxene and mica with accessory apatite, zircon, titanite, monazite, zircon, magnetite and ilmenite. The granite (DC0835-2) is fine-grained and contains K-feldspar, plagioclase, quartz with accessory zircon and apatite. The porphyritic monzogranite (DC0623-1) contains mainly K-feldspar, plagioclase, quartz and mica, and less common hornblende. The opaque minerals, apatite, zircon and monazite compose the magmatic accessory phases (Fig. 6.3e). The hornblende-bearing granite shows discordant relationships with the wall rocks. It was crosscut by the weakly deformed syn-kinematic granitic pegmatite (DC08-2-1). However, the granite and porphyritic monzogranite occur in the centre of the shear zone as tabular bodies and show concordant relationships with the wall rocks, in both the overall configurations of the intrusions and their fabrics. They experienced strong shear deformation to

form granitic mylonites. This is indicated by the progressive rotation of the magmatic foliation parallel to the mylonitic fabric. In the porphyritic

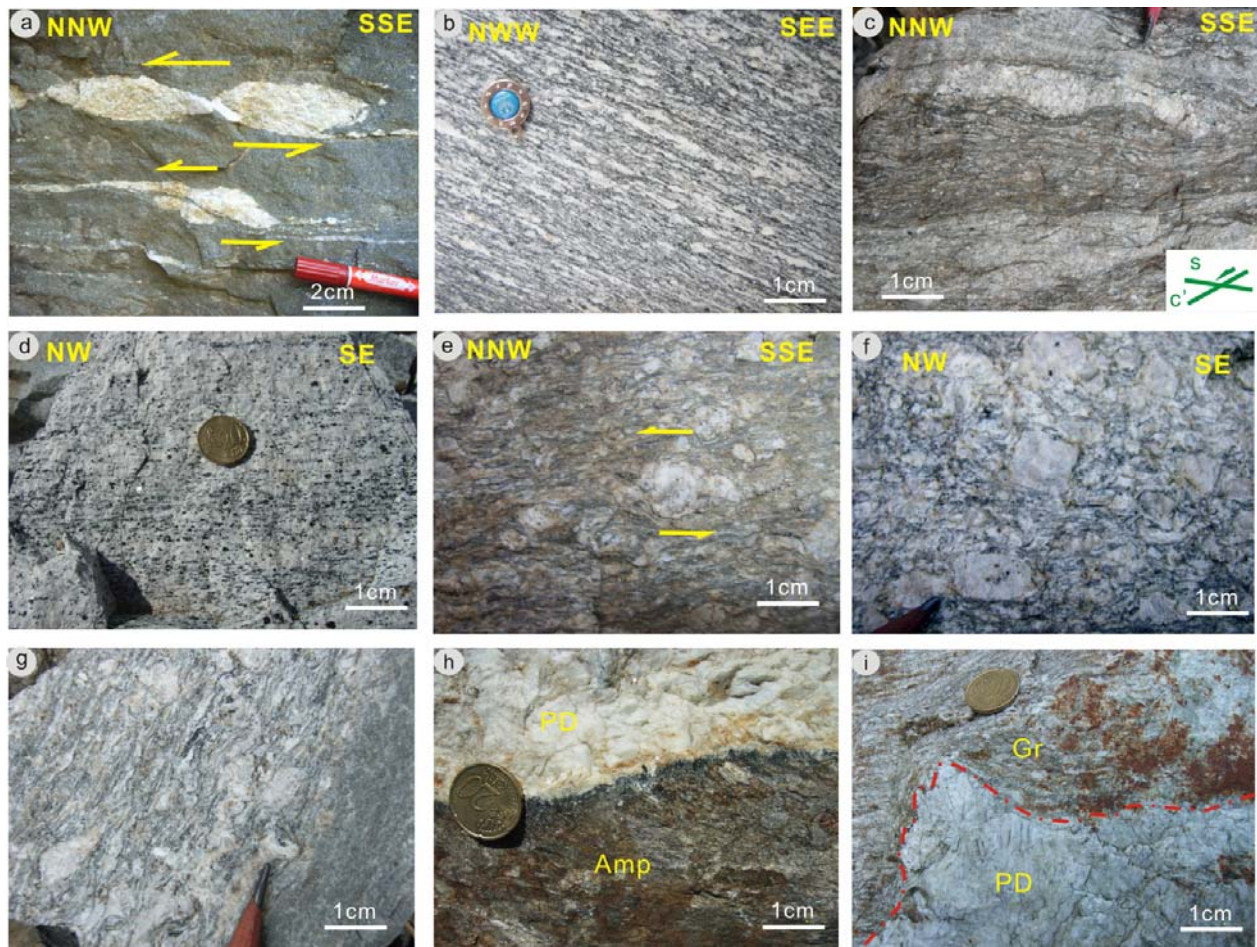


Fig. 6.3 Meso-structural relationships between granitic rocks and their wall rocks. a) Mylonitic amphibolites with felsic dykes. The felsic veins exhibit boudinage, S-C and sigmoid fabrics and top to the NNW shear criteria; b) The granitic mylonite with penetrative foliation and a NNW trending stretching lineation; c) S-C/C' fabrics developed in the granitic mylonite showing top to the NW shearing; d) Highly deformed pre-kinematic granite with stretching lineation (sample DC08-2-2); e) Pre-kinematic porphyritic porphyroclasts with delta-type mantled clasts of feldspar, the asymmetry indicates sinistral shear (site of sample DC0623-1); f) Syn-kinematic granitic mylonite (sample DC0822-1); g) Syn-kinematic granite with feldspar clasts (sample DC0835-1); h) Weakly deformed mica pegmatite (sample DC08-8-5) crosscutting mylonitic amphibolite (Amp.) with a NNW trending stretching lineation; i) Undeformed pegmatite dyke (PD) (DC0810-2) crosscutting syn-kinematic mylonitic granite (Gr) with a NNW trending stretching lineation.

monzogranite, the mineral porphyroclasts, e.g. feldspar and amphibole are either lens-shaped or fish-shaped, σ , δ and S-C fabrics, which consistently document a left-lateral deformation. The incipient S-C fabrics are present in the granitic mylonites with S-plane defined by grain aggregates of feldspar, quartz and mica, and C-plane defined by strongly elongated grains of

feldspar and amphibole. The acute angle between S and C is generally 10–25 degrees. The monzogranite is strongly altered, but the magmatic texture and mineralogy can still be identified. Evidence of shear zone activity prior to these magma emplacements is lacking. For example, these granitic mylonites do not contain any xenoliths of shear zone mylonites, which would indicate shear zone deformation postdate magma emplacement (Fig. 6.4a). The rocks have medium- to fine-grained fabrics and mostly show pre-kinematic magmatic structures.

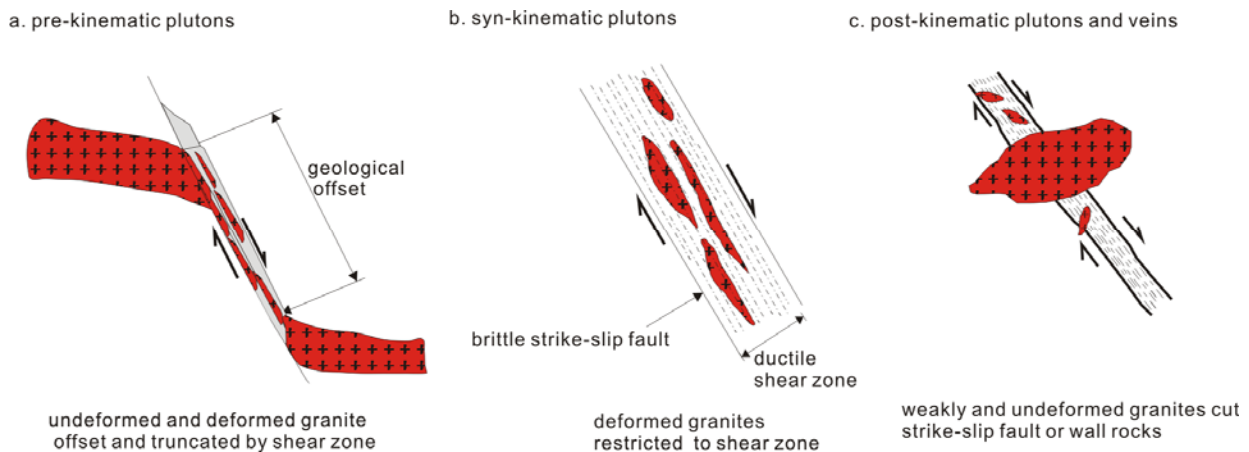


Fig. 6.4 Sketch maps of diagnostic features of pre-, syn- and post-kinematic granites in strike-slip fault zones (modified after Searle, 2006).

6.4.1.2 Microfabrics in thin sections

In the sample DC08-2-2, microstructures show strong dynamic recrystallization of the main mineral phases during retrograde metamorphic conditions (Fig. 6.5a–d). The original magmatic pyroxene grains have almost disappeared, and pyroxene relics set in a fine-grained polymineralic matrix of feldspar, quartz, amphibole and biotite. The relic porphyroclastic cores of pyroxene are locally isolated by the presence of rims of amphibole and biotite (Fig. 6.5 b and c). Pyroxene porphyroclasts commonly contain deformation lamellae and exhibit undulose extinction. However, subgrains and bulging grain boundaries are not observed. Asymmetric tails composed of elongated amphibole, biotite and apatite grains show lens-shaped or fish-shaped and σ -fabrics, which consistently document a left-lateral sense of shearing. Quartz grains are distributed in the matrix and around pyroxene porphyroclasts. The perthite (K-feldspar and albite) grains are characterized by crystal-plastic deformation and strong dynamic recrystallization. Plagioclase porphyroclasts are nearly absent. The microstructures indicate that during strike-slip deformation,

the early high-temperature magmatic fabric was superimposed by relative low temperatures (lower amphibolite facies) fabrics.

The felsic granite (DC0835-2) is a strongly deformed ultramylonite (Fig. 6.5e). Feldspar grains were completely recrystallized to form fine-grained feldspar aggregates. Few porphyroclasts are observed in the whole thin section.

In the sample DC0623-1, early magma crystallization is characterized by porphyritic structures, especially by oscillatory compositional growth zoning in feldspar grains (Fig. 6.5h), which is truncated by the matrix, confirming that deformation occurred after formation of the zoning (e.g. Vernon, 1987, 2000). In addition, exsolution lamellae of albite are developed widely in the K-feldspar phenocrysts. The exsolution lamellae are fine stripe shaped and nearly parallel to each other (Fig. 6.5i). Parallel to sub-parallel alignment of elongate euhedral feldspar crystals that are not completely internally deformed implies that there is sufficient freedom for the feldspar crystals to grow and rotate before undergoing plastic deformation (e.g. Shelley, 1985, Blumenfeld and Bouchez, 1988; Vernon, 2000). Paterson et al. (1998) suggested that the alignment of crystals would not be preserved unless the magma reached a sufficiently high viscosity for it not to be removed by late flow. Therefore, it is inferred that the preservation of such preferred orientations would occur most commonly in a later stage of magma crystallization. Some myrmekites are almost surrounding the entire porphyroclastic feldspar grain and may be related to solid-state deformation (e.g. Simpson and Wintsch, 1989; Vernon, 2000) (Fig. 6.5g). During the progressive deformation, myrmekite extensively recrystallized to form new fine grains in the matrix. In some cases, myrmekites seem to be stress-induced because their distribution and orientation can be attributed to bulk left-lateral shearing sense within the DCS zone.

Microstructures in the porphyritic monzogranite reveal mostly solid-state deformation features (Fig. 6.5f, h and i). Feldspar grains are characterized by crystal-plastic deformation and strong dynamic recrystallization in the high strain zone. Elongated feldspar grains define the mylonitic foliation and partly control the quartz ribbon orientation (Fig. 6.5i). Many porphyroclastic feldspar grains have serrated boundaries. Most of them have rims of recrystallized grains (Fig. 6.5f) formed by subgrain rotation dynamic recrystallization. The boundaries of adjacent feldspar grains are highly serrated, indicating dynamic recrystallization also through grain-boundary migration which accommodated dislocation creep. Most of the feldspar megacrysts with recrystallized “tails” provide pronounced evidence for the existence of the megacrysts prior to the mylonitic deformation. The compositions of coexisting recrystallized plagioclase and K-feldspar, give at least a general indication of high temperatures (e.g. Vernon, 2000). Most quartz

grains have typically polygonal aggregate shapes and are parallel or subparallel to the major foliation and lineation of the rocks. Some quartz ribbons or

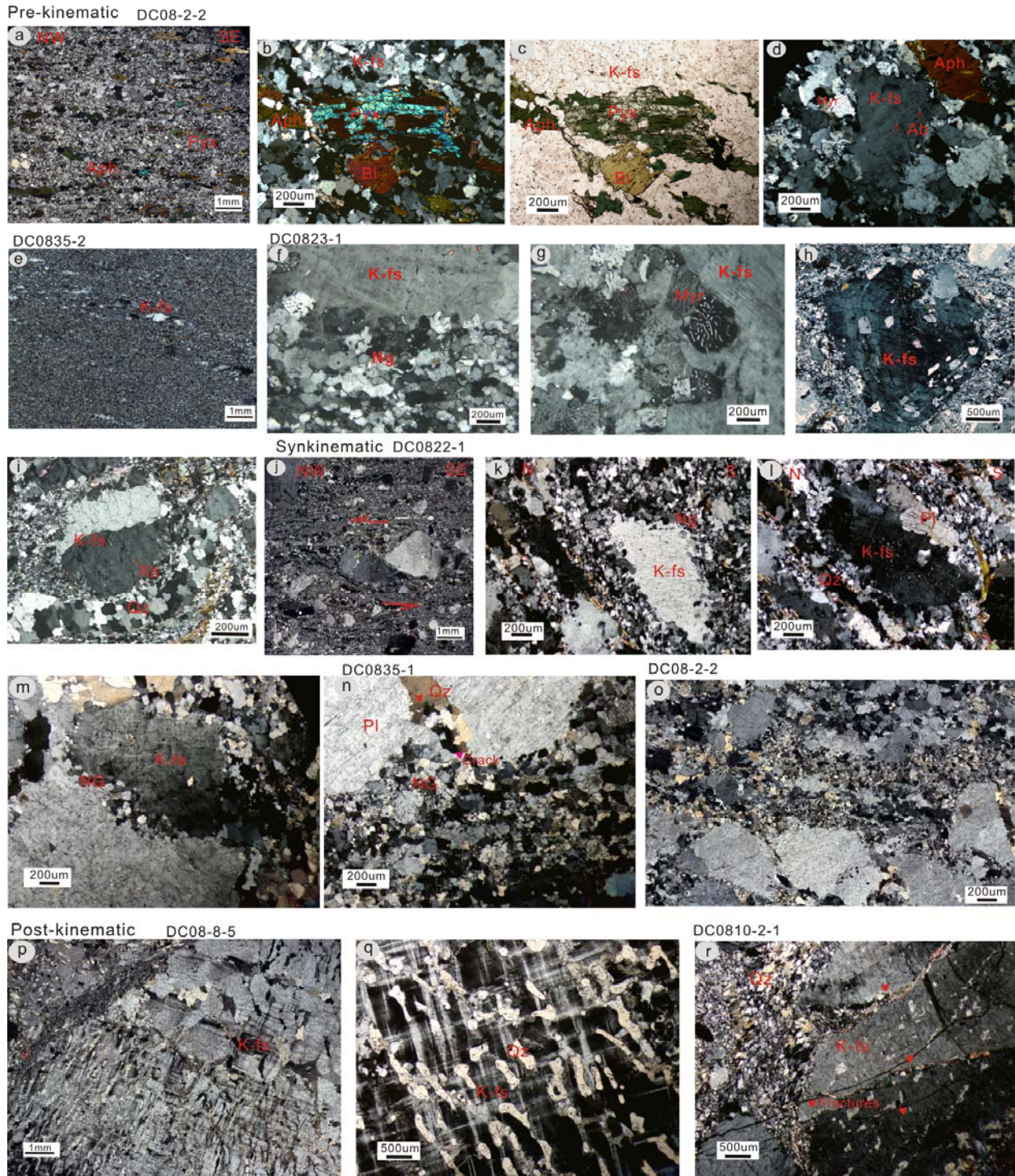


Fig. 6.5 Deformation microstructures of intrusions. a–d: Microstructures of pre-kinematic amphibolite-bearing granite (sample DC08-2-2). a) Microstructural observations from the full thin section scanned from the sample. Progressive grain size reduction of K-feldspar by dynamic recrystallization; b and c) Amphibolite, mica and the remnant pyroxene under cross- and parallel polarized light, respectively; d) Amphibolite porphyroclasts, perthite (K-feldspar and albite) surrounded by myrmekites (Myr) and fine-grained matrix. e) Complete

recrystallization of feldspar in the scanned thin-section of granitic ultramylonite (sample DC0835-2). f-i: Pre-kinematic porphyritic monzogranitic mylonite microstructures (sample DC0623-1). f) Typical core-mantle texture defined by K-feldspar cores surrounded by small subgrains and dynamically recrystallized new grains along their margins; g) Myrmekites (Myr) around K-feldspar porphyroclasts (Fs); h) K-feldspar porphyroclasts with magmatic oscillatory zonation of crystal growth; i) Perthite (K-feldspar and albite) surrounded by fine-grained matrix and quartz ribbons around the feldspar porphyroclast boundary. j-m: syn-kinematic granite microstructures (sample DC0822-1). j) Microstructural observations from scanned thin-section of the syn-kinematic granite mylonite. Microfault fabrics showing left-lateral shear sense; k and l) K-feldspar porphyroclasts with a typical core-and-mantle texture and quartz ribbons. The long axes are parallel to the foliation. m) Weakly deformed K-feldspar porphyroclasts; n) Microcracks in feldspar porphyroclasts with infillings of quartz. K-feldspar porphyroclasts (Fs) and transition to recrystallized grains (NG) in the matrix (Sample DC0835-1). o) K-feldspar porphyroclasts (Fs) and transition to recrystallized grains (NG) in the matrix (sample DC08-2-2). p-r: Post-kinematic intrusion microstructures. p) Graphic texture (alkali feldspar with exsolved quartz) in the weakly deformed alkali leucocratic granitic pegmatite; q) Graphic microstructure in large microcline (sample DC08-8-5); r) Fragmented plagioclase showing weakly undulatory extinction. Quartz undulose extinction and equate to slightly elliptical grains, showing weakly brittle deformation (DC0810-2).

aggregates with serrated grain boundaries occur in pressure shadows on both sides of the feldspar grains. Serrated grain boundaries are observed in some cases suggesting local high-temperature grain boundary migration (e.g. Passchier and Trouw, 2005). Quartz preferred orientation shows dislocation creep on prism $\langle c \rangle$ planes consistent with amphibolite-facies conditions (Cao et al., 2010). Rare occurrence of dislocation substructures in quartz grains points to the importance of high-temperature recovery and recrystallization during or after high-temperature shearing. Very few free dislocations may be attributed to progressive deformation (Cao et al., 2010).

All these features indicate that the shearing started after the crystallization of the granitic plutons, which argue for a pre-kinematic emplacement and subsequent high-temperature left-lateral strike-slip shearing. However, they still record deformation at relatively lower temperature conditions than melting of the melting temperature of the granites. Hence U/Pb ages of these deformed granites can be earlier than strike-slip shearing.

6.4.1.3 Zircon U/Pb results

The sample DC08-2-2 is the alkaline granite collected at the southwest of DCS. The zircon grains acquired from this sample bear subhedral shapes with straight grain margins, and are mostly clear and colorless to light brown in color in transmitted light image. They have aspect ratios of between 1:1 and 3:1, and grainsizes between 100 and 200 μm in length (Fig. 6.6a). The zircon grains show well-developed oscillatory zoning in the CL image. Twenty-three U/Pb laser-spot analyses were conducted on twenty-one zircon grains for this sample. They have Th of 88–371 ppm, U of 137–592 ppm, and Th/U ratio between 0.25 and 1 (mostly between 0.5 and 0.9), indicating a magmatic origin of the zircons. All analyses are entirely concordant and yield concordia $^{206}\text{Pb}/^{238}\text{U}$ ages ranging from 37 ± 2 Ma to 28 ± 2 Ma (Table 2). The $^{206}\text{Pb}/^{238}\text{U}$ and $^{207}\text{Pb}/^{235}\text{U}$ results are plotted on the concordia diagram and show nearly consistency group distribution, with a $^{206}\text{Pb}/^{238}\text{U}$ weighted average age of 32.5 ± 1.0 Ma (MSWD = 1.1, n=23) (Fig. 6.7a). The weighted mean age could be interpreted as the age of zircon crystallization.

The sample DC0835-2 is the most deformed alkaline granite collected from the central sector of the DCS massif. The zircons acquired from the sample show euhedral to subhedral grain shapes with straight grain boundaries, and are clear and colorless in transmitted light image. They have aspect ratios of between 2:1 and 3:1 with long axes of 150–250 μm (Fig. 6.6b). The zircon grains show oscillatory zoning in the CL image. Ten U/Pb laser-spot analyses were conducted on eight zircon grains for this sample. They have Th of 31–744 ppm, U of 166–1055 ppm, and Th/U ratio between 0.11 and 0.78, indicating a magmatic origin of the zircons. All analyses are concordant and yield concordia $^{206}\text{Pb}/^{238}\text{U}$ ages ranging from 38 ± 3 Ma to 32 ± 0.9 Ma (Table 1). The $^{206}\text{Pb}/^{238}\text{U}$ and $^{207}\text{Pb}/^{235}\text{U}$ results are plotted on a concordia diagram and show consistency group distribution, with a $^{206}\text{Pb}/^{238}\text{U}$ weighted average age of 33.4 ± 1.7 Ma (MSWD = 1.3, n = 10) (Fig. 6.7b). The weighted mean age is interpreted as the age of zircon crystallization from the magma.

The sample DC0623-1 is the strongly deformed porphyritic monzogranite from the central DCS massif and is crosscut by the syn-kinematically deformed fine-grained granitic dykes. Zircon grains acquired from the sample are mostly euhedral prismatic crystals and clear, yellow or greenish yellow in color in transmitted light image. They have aspect ratios of between 2:1 and 3:1, and long axes are commonly of 200–300 μm size (Fig. 6.6c). The zircons show well-developed oscillatory zoning in the CL image. Fifteen SHRIMP-II laser-spot analyses were conducted on fourteen zircon grains for this sample. They have Th of 355–2092 ppm, U of 799–6736 ppm, and Th/U ratio between 0.10 and 1.24, indicating a magmatic origin of zircons. All analyses are entirely concordant and yield concordia $^{206}\text{Pb}/^{238}\text{U}$ ages ranging from 32.9 ± 0.5 Ma

to 29.4 ± 0.5 Ma (Table 1). The $^{206}\text{Pb}/^{238}\text{U}$ and $^{207}\text{Pb}/^{235}\text{U}$ results are plotted on a concordia diagram and show a consistent age distribution, with a $^{206}\text{Pb}/^{238}\text{U}$ weighted average age of 30.95 ± 0.61 Ma (MSWD = 4.1, $n = 15$) (Fig. 6.7c). The weighted mean age is interpreted as the age of zircon crystallization from the magma.

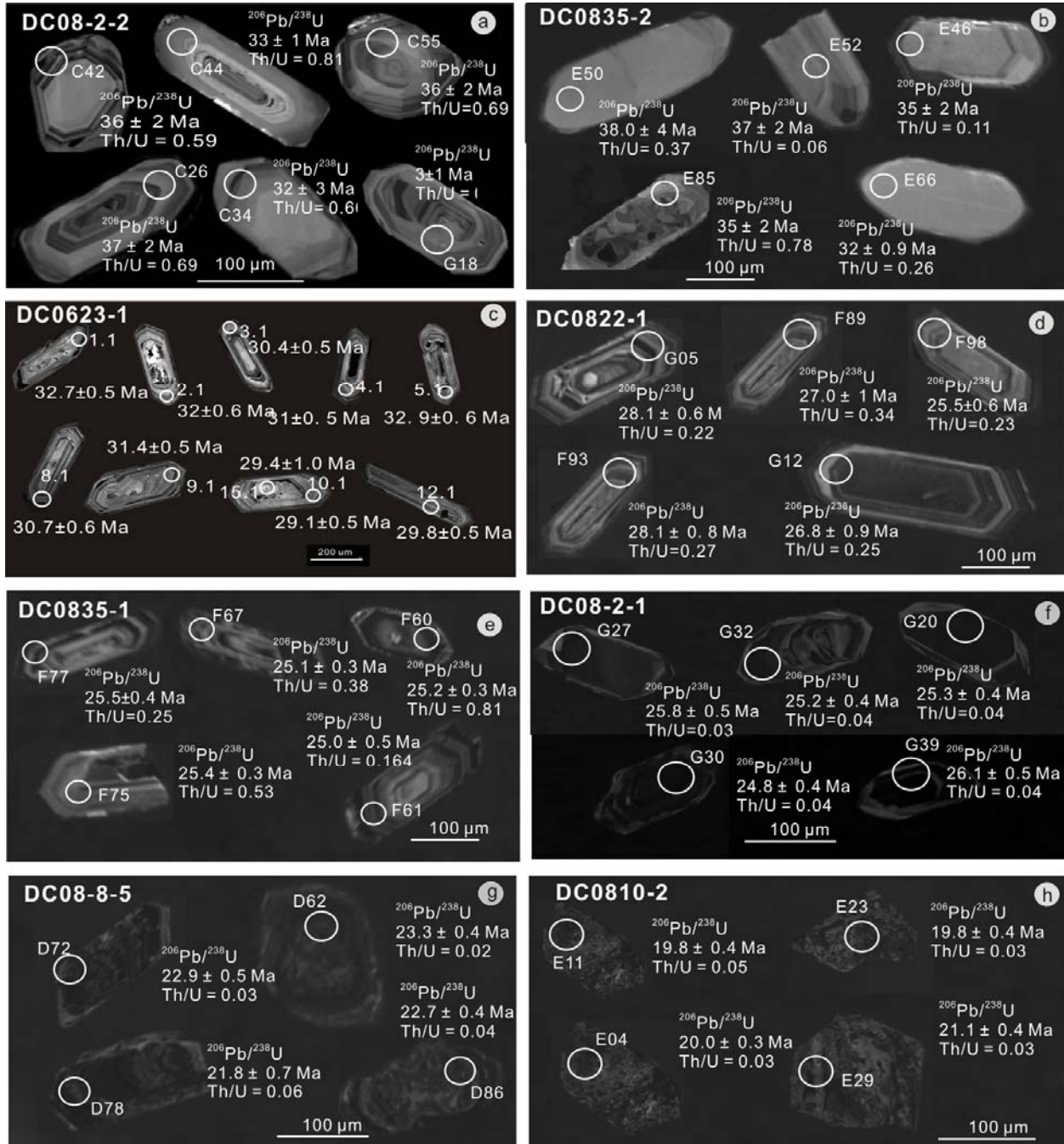


Fig. 6.6 Cathodoluminescence (CL) images of representative zircons from a) Diorite (sample DC08-2-2); b) granite (sample DC0835-2); c) Porphyritic monzogranite (sample DC0623-1); d) Two-mica granite (sample DC0822-1); e) Granite (sample DC0835-1); f-h) Granitic pegmatite (f-sample DC08-2-1; g-sample DC08-8-5; h-sample DC0810-2). Circles indicate the locations of SHRIMP (sample DC0623-1) and LA-ICP-MS analyses. The spot numbers presented above the zircon images are the same number as listed in Tables 1 and 2.

6.4.2 Syn-kinematic plutons

6.4.2.1 Mesoscopic deformation within the syn-kinematic pluton

Samples of a two-mica granite (DC0822-1), a granite (DC0835-1) and a granitic pegmatite (DC08-2-1) are exposed within the high-strain zones in the central DCS massif (Fig. 6.2A and C). The sample DC0822-1 contains mainly K-feldspar, plagioclase, quartz and two micas (Fig. 6.3f). The sample DC0835-1 contains mainly K-feldspar, plagioclase, quartz and a few small mica grains (Fig. 6.3g). The granitic pegmatite (DC08-2-1) intruded the pre-kinematic hornblende-bearing granite (DC08-2-2) and both experienced strong strike-slip shearing when they are close to the major mylonitic shear zone. Crystallization in the plutons was coeval with deformation in the shear zones. Early deformation fabrics are overprinted by high-T solid-state deformation structures to form the mylonites and local ultramylonitic bands. Evidence for syn-kinematic magmatic flow is inferred from their close relationship with the shear zone and the gradual decrease of foliation development from the margin to the interior (Fig. 6.4b). The magmatic foliation is defined by the parallel arrangement of euhedral K-feldspar grains, mica and quartz aggregates. They are regionally paralleling to the mylonitic foliation, suggesting that intrusion and cooling took place under left-lateral strike-slip conditions. The pronounced subhorizontal to horizontal stretching lineation is penetrative in hand specimen. They are defined by the parallel alignment of feldspar grains and by stringers of quartz. The mylonitic fabric shows a progressive increase in pervasiveness with a decrease in the size of the feldspar porphyroclasts. The granites locally contain xenoliths of mylonites. The syn-kinematic granite exhibits excellent S-C fabrics related to the late low temperature conditions. The C-planes are defined by planar discontinuities with a marked offset of the grain shape fabric (S-foliation) defined by preferred dimensional orientation of deformed feldspar aggregates, quartz ribbons and micas. Both C- and S-planes are subvertical and contain subhorizontal lineation defined by mineral elongation. Various kinematic indicators, including asymmetrical feldspar porphyroclasts, S-C fabrics, extensional crenulation cleavage and asymmetrical quartz fabrics within the mylonites, imply the dominant role of regional left-lateral shearing (e.g. Passchier and Trouw, 2005). These observations are consistent with emplacement, crystallization and subsequent deformation of a intrusion in an active shear zone.

6.4.2.2 *Microfabrics*

Microscopic structures in the feldspar grains in the two-mica granite (DC0822-1), granite (DC0835-1) and granitic pegmatite (DC08-2-1) preserve evidence for progressive deformation over a range of conditions from magmatic flow, sub-magmatic flow to plastic deformation (Fig. 6.5j–o). Evidences for late-magmatic hydrothermal metasomatism are preserved in the porphyritic monzogranite samples. An early phase of K-metasomatism is evidenced by the replacement of plagioclase by K-feldspar to form K-feldspar phenocrysts, which is best documented by plagioclase relic grains in marginal zones or inside K-feldspar megacrysts. Patches of these relic grains are often optically continuous and hence can be related to originally larger plagioclase grains. Some plagioclase crystals are replaced in their interiors by K-feldspar to form patchy microcline or perthite. In some cases, plagioclase crystals are completely replaced and only relics of the original grains remain unchanged. With decreasing temperature and melt fraction, deformation accompanied rigid body rotation of magmatic feldspar crystals to produce a grain-shape preferred orientation. The alignment of the feldspar crystals suggests that the fabric partly represents a magmatic foliation, but recrystallization of quartz and biotite indicates that solid-state deformation has been superimposed on the magmatic crystals. In the high strain zone, most feldspar grains in the mylonites are characterized by crystal plastic deformation and dynamic recrystallization. Recrystallization occurs around porphyroclasts with asymmetric fabrics, indicating a left-lateral or top-to-the-northwest shear sense (Fig. 6.5j). Undulatory and inhomogeneous extinction, twins, and subgrains are common in porphyroclastic feldspar grains. In the shear direction, feldspar porphyroclasts are strongly elongated, lenticular in shape with irregular, serrated grain boundaries. They are surrounded by a matrix of recrystallized grains. The new grains have been separated from their host, and most new grains appear to have been formed by subgrain rotation recrystallization (Fig. 6.5k and l). The recrystallized grain size is uniform and in the range of 50–100 μm . The well-rounded porphyroclasts, as well as the cores of many mantled augens, show very little evidence of internal deformation. In the two-mica granite samples, few myrmekites developed locally around feldspar grains at sites of high stress concentration (e.g. Simpson, 1985), which formed possibly due to shearing under subsolidus (e.g. Hibbard, 1987) or at least high-temperature conditions. This additionally suggests that these microstructures developed synchronously during the left-lateral strike-slip shearing. Quartz consists of polycrystalline aggregates that were derived from the recrystallization (Fig. 6.5k and l). The elongated (ribbon- or sigmoid-type) aggregates are common in mylonites and are aligned parallel to the macroscopic foliation. These have been interpreted as either a major imprint of a late strain increment or a steady-state foliation. The ribbons are up to 100–200 μm thick and

some are longer than the thin section. But in some low-strain domains, mica fishes are parallel to the foliation, forming a typical S-C fabric. The primary host biotite has been progressively deformed by recrystallization to an aggregate of fine-grained crystals of new biotite. Hence primary grains can no longer be observed optically. In contrast, semi-brittle microstructures are characterized by the micro-cracks in some feldspar porphyroclasts. The micro-cracks often have infillings of quartz and mica grains. The latter also define a strong penetrative fabric in the matrix, indicating that strain associated with subsolid state phase transformation at near solidus conditions (e.g. Bouchez et al., 1992; Blenkinsop, 2000). Some feldspar porphyroclasts show short and discontinuous micro-fractures. Fractures occur at the boundary or are isolated within a crystal or along crystal cleavage planes. Some fractures are oriented nearly anisotropically due to late stage of brittle deformation under decreasing temperature conditions.

Therefore, based on the field and microstructural evidence mentioned above, such rocks reveal high-temperature solid-state plastic deformation to ductile-brittle deformation features during and after the magma emplacement and cooling. It is concluded that the granite is a syn-kinematic intrusion that underwent syn- and post-magmatic deformation.

6.4.2.3 Zircon U/Pb results

The sample DC0822-1 is a deformed porphyritic granite collected from the central DCS. Zircon grains acquired from this sample are mostly euhedral with straight grain boundaries. They are clear, colorless or weakly greenish-yellow under transmitted light. Their aspect ratios vary between 2:1 to 3:1, with general grain long axes of 100 to 300 μm size (Fig. 6.6d). The zircons show well-developed oscillatory zoning in the CL image. Seventeen laser-spot analyses were conducted on seventeen zircon grains for this sample. They have Th of 311–1379 ppm, U of 1211–5541 ppm, and Th/U ratio between 0.17 and 0.46, indicating a magmatic origin of the zircons. All analyses are entirely concordant and yield concordia $^{206}\text{Pb}/^{238}\text{U}$ ages ranging from 27.0 ± 1 to 25.5 ± 0.6 Ma (Table 2). They are very close to the concordia and give a weighted apparent mean $^{206}\text{Pb}/^{238}\text{U}$ age of 26.95 ± 0.34 Ma (MSWD = 1.0, n = 17). Therefore, these ages represent the age of intrusion and crystallization of the porphyritic granite.

The sample DC0835-1 is a deformed porphyritic granite collected from the central DCS. Zircon grains acquired from this sample most are mostly euhedral. The rims are darker than the cores, which is indicative of higher U-content along their margins. The cores or rims exhibit clear oscillatory zoning. Only few zircon crystals present uniform oscillatory zoning patterns over the whole grain without any rim-core transition. They have aspect ratios of between 2:1 and 3:1.

Grain lengths are commonly between 100 and 200 μm (Fig. 6.6e). The zircons show a well-developed oscillatory zoning in the CL images. Seventeen laser-spot analyses were conducted on seventeen zircon grains from this sample. They have Th of 1508–43814 ppm, U of 6414–69924 ppm, and Th/U ratio between 0.14 and 0.54 indicative for a magmatic origin of the zircons. Most analyses are concordant and yield concordia $^{206}\text{Pb}/^{238}\text{U}$ ages ranging from 25.8 ± 0.4 to 25.0 ± 0.3 Ma (Table 1). The $^{206}\text{Pb}/^{238}\text{U}$ and $^{207}\text{Pb}/^{235}\text{U}$ results are plotted on a concordia diagram and show consistent group distribution, with a $^{206}\text{Pb}/^{238}\text{U}$ weighted average age of 25.31 ± 0.18 Ma (MSWD = 0.63, n = 14) (Fig. 6.7e). The weighted mean age is interpreted as the age of zircon crystallization from the magma. Two analyses are plotted to the right of the concordia and three analyses are slightly away from the concordant line. These discordant analyses are interpreted to be due to Pb-loss, and/or the presence of undetected common Pb.

The sample DC08-2-1 is a weakly deformed granitic pegmatite collected from the southwestern sectors of the DCS. Most zircon grains acquired from this sample are subhedral. They are colorless in transmitted light image. Their aspect ratios range from 1:1 to 2:1, and grain lengths are commonly 100–150 μm (Fig. 6.6f). The zircons are dark in the CL image indicating of higher U-contents and some cores or rims exhibit a clear oscillatory zoning. Nine laser-spot analyses were conducted on nine zircon grains for this sample. They have Th of 158–550 ppm, U of 4680–9928 ppm, and low Th/U ratio between 0.02 and 0.06. All analyses are entirely concordant and yield concordia $^{206}\text{Pb}/^{238}\text{U}$ ages ranging from 26.8 ± 0.6 to 25.3 ± 0.4 Ma (Table 2). The $^{206}\text{Pb}/^{238}\text{U}$ and $^{207}\text{Pb}/^{235}\text{U}$ results are plotted in the concordia diagram and they show an internally consistent age distribution, with a $^{206}\text{Pb}/^{238}\text{U}$ weighted average age of 25.49 ± 0.41 Ma (MSWD = 1.4, n = 9) (Fig. 6.7f). This age is interpreted as the best estimate for the crystallization age of the granitic pegmatite.

6.4.3 Post-kinematic intrusions

6.4.3.1 Mesoscopic deformation within the post-kinematic granitic dykes

The post-kinematic intrusions within the DCS area are represented by leucocratic granitic pegmatites (samples DC08-8-5 and DC0810-2). They are composed of variable proportions of K-feldspar, plagioclase, quartz, biotite and muscovite, with accessory magnetite, apatite and zircon. In individual outcrops, these weakly to undeformed dykes have variable widths (a few centimeters to meters) (Fig. 6.3g–i, Figs. 6.4–3). All the intrusions cut the high-temperature mylonitic foliation and lineation of their country rocks at small or high angles. They are straight-

and parallel-sided dykes. Weak-deformation or non-deformation features suggest that these intrusions were emplaced postdating the main stage of ductile shearing in the DCS massif.

6.4.3.2 Microfabrics

In contrast to the syn-kinematic plutons, the microstructures of the post-kinematic intrusions mainly show cataclastic deformation characteristics (Fig. 6.5o–p). In the sample DC08-8-5, there are typical graphic microstructures formed during rapid cooling after the magmatic stage. Puzzling intergrowths of quartz grains occur in the alkali feldspar hosts. Most K-feldspar grains are of subhedral crystal shape. Fine-grained recrystallization occurred locally at the boundaries. In the sample DC0810-2, microstructures show that most of feldspar grains are of euhedral or subhedral shape. Some exhibit intragranular randomly-orientated fractures. Quartz grains are slightly elliptical and exhibit undulose extinction. The quartz grains with the highest strain occur as slightly elongated, lens-shaped grain aggregates of about 20 μm in diameter. Some of the rocks show very weak solid-state brittle deformation microstructures, which may be related to progressive extension deformation/exhumation during relative low temperature faulting after the final stages of left-lateral ductile shearing in the DCS massif.

6.4.3.3 Zircon U/Pb results

The Sample DC08-8-5 is a coarse-grained, undeformed granitic muscovite-pegmatite collected in the southern DCS. Most zircon grains acquired from this sample are generally of euhedral shape, while a few grains have stubby grain shapes. They have aspect ratios between 1:1 and 2:1 with grain lengths commonly between 100–150 μm (Fig. 6.6g). The zircon grains show oscillatory zoning in the CL image. Twenty-three laser-spot analyses were conducted on twenty-three zircon grains for this sample. They have Th of 105–547 ppm, U of 5437–9797 ppm, and Th/U ratio between 0.01 and 0.06, indicating a magmatic origin of the zircons. All analyses are concordant and yield concordant $^{206}\text{Pb}/^{238}\text{U}$ ages ranging from 23.6 ± 0.4 to 22.1 ± 0.3 Ma (Table 2). The $^{206}\text{Pb}/^{238}\text{U}$ and $^{207}\text{Pb}/^{235}\text{U}$ results are plotted on the concordia diagram and show a $^{206}\text{Pb}/^{238}\text{U}$ weighted average age of 22.91 ± 0.19 Ma (MSWD = 1.9, n = 23) (Fig. 6.7g). This age is interpreted as the best estimate for the crystallization age of granitic pegmatite.

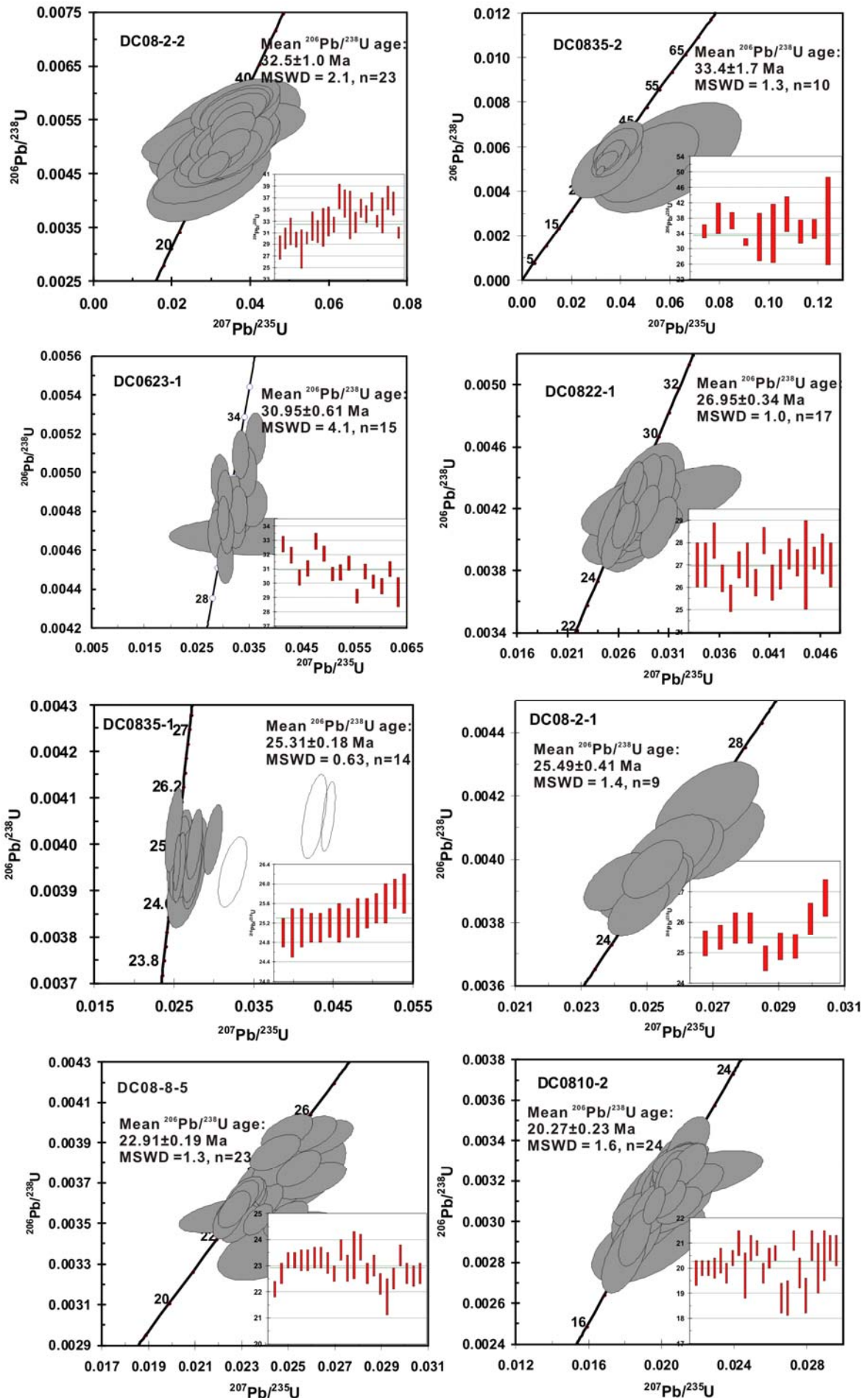


Fig. 6.7 U/Pb SHRIMP-II and LA-ICP-MS concordia diagrams and $^{206}\text{Pb}/^{238}\text{U}$ weighted average age diagrams. a) Diorite (sample DC08-2-1); b) Granite (sample DC0835-2); c) Porphyritic monzogranite (sample DC0623-1); d) Porphyritic granite (sample DC0822-1); e) Granite (sample DC0835-1); f) Granitic pegmatite (sample DC08-2-1); g) Granitic pegmatite (sample DC08-8-5); h) Granitic pegmatite (sample DC0810-2).

The sample DC0810-2 is another undeformed granitic pegmatite dyke collected from the southern DCS massif. Most zircon grains acquired from this sample are euhedral and a few zircons exhibit relatively stubby grain shapes. Grains are opaque, dark to yellow in color in transmitted light image. They have aspect ratios ranging from 1:1 to 1:2, and are commonly 100–150 μm long (Fig. 6.6h). Most crystals are dark, and some crystals show darker rims and brighter cores indicative of higher U-content along their rims. Thirty-four laser spot analyses were conducted on twenty-four zircon grains for this sample. The analyzed zircons have Th of 61–1102 ppm, U of 4293–7539 ppm and low Th/U ratios ranging from 0.02 to 0.20. All analyses are concordant and yield concordant $^{206}\text{Pb}/^{238}\text{U}$ ages ranging from 21.0 ± 0.5 to 18.8 ± 0.6 Ma (Table 2). They are close to the concordia and give a weighted mean apparent $^{206}\text{Pb}/^{238}\text{U}$ age of 20.27 ± 0.23 Ma (MSWD = 1.6, n = 24) (Fig. 6.7h). Therefore, this age represent the age of intrusion and crystallization of the granitic pegmatite at ca. 20 Ma.

The results of some samples (DC0835-1 and DC08-8-5) indicate that there exist a large amount of magmatic zircons characterized by high U and Th contents in the granitic rock. Although this “high-U effect” had been identified for many years, there is still no logical reason for its mechanism (e.g. Li et al., 2010). We therefore presented the data in the paper and used their results as references during the age characterization.

6.5. Discussion

6.5.1 U/Pb ages and the timing of shearing along the ASRR shear zone

Relative timing of magmatic crystallization and regional deformation is a complex problem because of the changing rheology of magma as it crystallizes and also because of our incomplete understanding of the range of possible fabrics that can form in the transition from magma to crystalline solid (e.g. Paterson et al., 1989; Karlstrom, 1991; Karlstrom et al., 1993; Searle, 2006). Consequently, the use of granitic rocks as structural time markers requires detailed petrological and structural control, including consideration of their rheological properties (e.g. Paterson and Tobisch, 1988; Paterson et al., 1989). It is important to distinguish different

intrusions, e.g. the pre-kinematic, syn-kinematic and post-kinematic intrusions, which can commonly constrain the timing of deformational events in high-grade metamorphic massifs. Numerous scattered outcrops of granitic intrusions and wall rocks in the DCS massif present the structural relationships of magma emplacement and tectonic shearing. The plutons range from concordant to discordant relationships with their wall rocks and their internal deformational state from thoroughly mylonitized over weakly deformed to undeformed.

The Eocene-Miocene tectonic-magmatic evolution of the DCS massif is proposed mainly based on our structural analysis and new SHRIMP-II and LA-ICP-MS zircon U/Pb ages from the different granitic rocks. The ages are considered to reflect the age of crystallization due to the magmatic texture of the analyzed zircons. All the samples record Eocene to Miocene ages between ca. 34 and 20 Ma. The structural characteristics of these plutons and dykes allow us to discuss a three stage successive kinematic evolution of the shear zone.

Late Eocene to Early Oligocene pre-kinematic magmatic event (ca. 31-34 Ma):

The alkaline granites, e.g. the hornblende-bearing granite (DC08-2-2), granite (DC0835-2) and porphyritic monzogranite (DC0623-1) are pre-kinematic relative to the left-lateral shearing. They preserve structures and microstructures of intense shearing. Magmatic zircons give U/Pb crystallization age of 32.5 ± 1.0 Ma, 33.4 ± 1.7 Ma and 30.95 ± 0.61 Ma, respectively. These ages are roughly similar to the U/Pb and Ar/Ar dating results by early authors (e.g. Schärer et al., 1990, 1994; Harrison et al., 1992; Leloup and Kienast, 1993). Ignoring the well-developed strain fabrics in the pre-kinematic magmatic intrusions with ages greater than 30 Ma along the ASRR, Liang et al. (2006) attributed the magmatic activities to ductile shearing. We reiterate, however, the pre-kinematic mineral assemblages have undergone high temperature re-equilibration during ductile shearing. Therefore, the ages of ca. 31 Ma possibly record a maximum age of the initiation of Early Oligocene strike-slip shearing.

Oligo- Miocene syn-kinematic magmatic event (ca. 27-21Ma):

Several samples of deformed granite and pegmatite (DC0822-1, DC08-2-1 and DC0835-1) give U/Pb crystallization ages of 26.95 ± 0.34 Ma, 25.49 ± 0.41 Ma and 25.31 ± 0.18 Ma, respectively. The U contents in zircons from the sample DC0835-1 is high, the age is therefore set as a reference. Thus they are the result of a second stage of late Oligocene-early Miocene (ca. 27–25 Ma) syn-kinematic magmatism. The rocks are directly affected by the high-temperature magmatic crystallization and partly overprinted by ductile-brittle deformation related to the left-lateral ductile shearing. Chung et al. (1997) bracketed the age span of 27 to 21 Ma as the age of

duration of shearing from a few U-Pb dating results. Similar ages from Ar/Ar dating of amphiboles and muscovite from the metamorphic rocks in the Day Nui Con Voi were interpreted as the result of shearing and exhumation along the ASRR shear zone (e.g. Wang et al., 1998b). The macro- and microstructural analysis suggested that the high-temperature deformation and dynamic recrystallization are attributed to progressive left-lateral shearing. Therefore, all these U/Pb ages of zircons from these plutons spanning from ca. 27 to 21 Ma recorded the duration of the main ductile shearing.

Miocene post-kinematic magmatic event (after ca. 21 Ma):

Zircons from the samples DC08-8-5 and DC0810-2 give ages of 22.91 ± 0.19 Ma and 20.27 ± 0.23 Ma respectively. The U contents in zircons from the sample DC08-8-5 is also high (mostly higher than 6000ppm). Although all the data points are plotted on the Concordia, the age is also set as a reference. These age results are also consistent with the field and microstructural observations, which confirm that they are post-kinematic plutons and dykes. The weak deformation occurred under decreasing temperatures. Final stages of progressive shearing can be constrained by the youngest zircon crystallization age (of the least deformed dykes). Hence, the age of ca. 20 Ma (DC0810-2) is inferred to date the final phase of left lateral shearing at least in the DCS massif. From the analyses, we reasonably suggest that the ages of ca. 20 Ma should represent the termination of left-lateral strike-slip ductile shearing. The conclusion is also consistent with the Ar/Ar thermochronological dating by Wang et al. (1998b).

To sum up, the period of left-lateral strike-slip shearing in the DCS massif can be precisely defined by the ages from the pre-kinematic alkaline granites, syn-kinematic granites and post-kinematic granitic pegmatites. The recognition of shearing microstructures and metamorphic assemblages in the syn-kinematic granitic intrusions in the DCS imply a transition from magmatic through submagmatic to solid-state plastic deformation during the emplacement of the plutons. To document this transition is important to prove that the solid-state plastic deformation occurred at high-temperature conditions, given that the plutonic process within the strike-slip shear zone system is synkinematic. The most straightforward interpretation of our data indicate that magmatism of the DCS shearing recorded a maximum age of the initiation at ca. 31 Ma, culmination during the main period between 27 and 21 Ma at high temperature ductile deformation condition (amphibolite facies) and termination at about 23 or 20 Ma at a low temperature conditions. It is more reasonable to argue that the left-lateral shearing underwent a main ductile deformation from ca. 27 to 21 Ma. Our view is well consistent with the point made

by Chung et al. (1997). Therefore, the shear strain developed over a period of about 6–10 Ma as a maximum. It is important to note that the youngest and undeformed dyke (ca. 20 Ma) is significantly older than the termination of left-lateral deformation that occurred at 16 Ma suggested in the literature (e.g. Harrison et al., 1992, 1996; Leloup and Kienast, 1993; Tran et al., 1998; Wang et al., 1998b, 2000; Jolivet et al., 1999, 2001; Leloup et al., 2001a, b, 2007; Maluski et al., 2001; Garnier et al., 2002). It does not support the idea that the left-lateral shearing started after ca. 21 Ma (see arguments by Searle, 2006 for the Ailao Shan) as well. Therefore, all our new results suggest that the large-scale displacement along the ASRR shear zone in the DCS massif at least started at ca. 27 Ma. However, it is not in agreement with the point that the left-lateral movements along the ASRR shear zone began at or slightly before 36 Ma age from high potassic alkaline rocks along the ASRR shear zone (Liang et al., 2007). Our analysis from the intensively deformed high potassic alkaline granites in the DCS massif show high-temperature solid-state ductile fabrics formed after crystallization of the magma. The results support the conclusion that magmatic activities at ca. 34–31 Ma are prior to the initiation of shearing (Chung et al., 2008).

6.5.2 Exhumation and magmatism during transpression/transension in the high-grade metamorphic massif

Debate exists on the ages and processes of exhumation of these high-grade metamorphic massifs, e.g. XLS, DCS, ALS and DNCV, along the ASRR shear zone (Fig. 6.1). The relationship between granitic magmatism and tectonic deformation of the DCS metamorphic complex bears important information on its exhumation. Most early hypotheses assume that the exhumation of the high-grade metamorphic complexes in SE Asia were related to the left-lateral strike-slip shearing during the extrusion of the Indochina block (e.g. Tapponnier et al., 1990; Leloup et al., 1993a, 2001b). Geochronological data have shown a complicated cooling-exhumation history of these massifs. The first appearance of major NE-directed extension and exhumation of the entire Bu Khang (BK) complex in central Vietnam (BK in Fig. 6.1) began at 36 Ma and culminated at 21 Ma (e.g. Lepvrier et al., 1997; Jolivet et al., 1999), which was accompanied by syn-kinematic magmatic emplacement and deformation (ca. 26–24 Ma) (e.g. Nagy et al., 2000, 2001). Left-lateral transtensional deformation and cooling of the DNCV metamorphic complex in North Vietnam occurred between ca. 29 and 22 Ma (e.g. Wang et al., 1998b, Tran et al., 1998, 2001; Anczkiewicz et al., 2007). In Ailao Shan, rapid cooling occurred diachronously along strike from 25 Ma in the SE end to 17 Ma in the NW end (e.g. Harrison et

al., 1996) or 33–17 Ma (e.g. Tapponnier et al., 1990; Leloup et al., 2001b). Successively exhumed metamorphic massifs also include the Mogok (MG) gneiss dome (26–14 Ma, MG in Fig. 6.1), and the Doi-Inthanon-Doi-Suthep (DIDS) metamorphic complex (27–16 Ma, DIDS in Fig. 6.1) (e.g. Morley, 2002; Barr et al., 2002). Left-lateral shearing in Thailand along the NW-striking Three Pagodas (ca. 36–33 Ma) and Wang Chao faults (ca. 33–31 Ma, WCSZ in Fig. 6.1) experienced subsequent rapid uplift during E-W extension at 25–23 Ma (Lacassin et al., 1997). For the DCS metamorphic complex, Schärer et al. (1990) analyzed U/Pb ages of zircon, monazite and xenotime, from slightly sheared granitic rocks, with ages from ca. 24 to 22 Ma, and Leloup et al. (1993a) reported $^{40}\text{Ar}/^{39}\text{Ar}$ cooling ages of 23 Ma to 17 Ma for amphibole, biotite, muscovite, and K-feldspar in the sheared felsic rocks. The above ages may have recorded a diachronous early Oligo-Miocene phase of transtensional left-lateral deformation and partial exhumation of deep crustal rocks in SE Asia.

In the case of the DCS massif, high-grade metamorphic rocks and mylonitic plutons display a foliation, which strikes NNW-SSE, and dips steeply ($>60^\circ$), with lineation that plunges between 0–30 degrees. As outlined above, the shear sense indicators (C-S fabrics, asymmetric tails of feldspar porphyroclasts, shear bands and veins) indicate a left-lateral movement. The local variations of lineation plunges could have created small deviations in the shear direction which contributed to the exhumation of deep crustal rocks. Differences of cooling ages can be attributed to Miocene extension. It is possible that syn-extensional magmatic emplacement occurred through the entire period of shearing and exhumation. Ages from the post-kinematic plutons and dykes can be interpreted as a decreasing or cooling event postdating high-temperature plastic deformation. We have emphasized submagmatic and high-temperature solid-state plastic deformation in the high-temperature conditions, but also show low- to moderate-temperature ($<500^\circ\text{C}$) penetrative solid-state deformation. The low-temperature brittle deformation clearly postdates the crystallization of principal magmatic phases and probably reflects the later E-W exhumation-related fabrics. On the other hand, east-dipping lineation is also observed locally on the eastern flank of the DCS from our recent field observations. This may also give clues to the young-phase intrusion activity that may suggest temporal relations between the exhumation of the metamorphic complexes and low-temperature extension. An early phase of Miocene cooling of the DCS can be connected with ductile extensional exhumation, while low-temperature part was associated with brittle normal faulting.

Our zircon U/Pb data and microstructural results provide a straightforward two-stage exhumation history of the DCS massif. An early stage is related to the ductile left-lateral shearing along the ASRR shear zone, which may also best interpret the exhumation of the massif

during ca. 27–23 Ma from the results of $^{40}\text{Ar}/^{39}\text{Ar}$ dating for amphibole (e.g. Leloup et al., 1993a; Wang et al., 2000). During or after the emplacement of the younger dykes at 23–20 Ma, rapid brittle deformation occurred. There was therefore a stage of fast uplift/exhumation and cooling of the DCS massif to the shallow crustal level. A coeval extensional event is possibly the formation of the Early Miocene sedimentary basins to the Northeast and Southwest of the DCS massif. However, we would suggest that more low temperature thermochronological data (e.g. FT or U-Th-He) could be used as a proxy for the timing of cooling during transtensional exhumation of the DCS high-grade metamorphic massifs, and also of the whole ASRR shear zone.

6.5.3 Regional tectonic implications

The continental collision between the Indian and Eurasian plate since the Eocene has been generally accepted as one of the most important processes in the Cenozoic tectonic evolution of Tibetan Plateau and East Asia (e.g. Tapponnier et al., 1982). Several hypotheses have been proposed to explain the tectonic evolution, such as clockwise rotation accompanied by plate-scale lateral extrusion and left-lateral strike-slip motion along the SE Asia area (e.g. Zhang and Zhong, 1996; Wang et al., 1998a; Tan, 1999; Chen et al., 2000; Guo, et al., 2001). Thrusting, crustal thickening/thinning, uplift and strike-slip transpression/transtention in the Tibetan Plateau and its adjacent regions, e.g. the southeastern part of the Tibetan Plateau, are the direct consequences of the collisional and postcollisional deformation. It is widely accepted that the majority of collision-related granites are best described as post-collisional, in the sense that they were emplaced commonly postdating an early collision-related metamorphic event, and are instead associated with a regional extensional and strike-slip fault movements (e.g. Chung et al., 1997). Constraining the ages of shearing along crustal-scale faults by emplacement of the plutons is a fundamental problem to the understanding of the accommodation of the crustal of the SE Asian plate to the continental collision or post-collisional extension. Along the ASRR shear zone, numerous small-volume Cenozoic intrusions are exposed, ranging from mafic to felsic composition (e.g. Liang et al., 2007). The present results reveal that the pre-kinematic granites (including the hornblende-bearing granite, monzogranite and felsic granite) in the DCS massif are dominated by high potassic alkaline magmatism, which is consistent with geochemical analysis by Chung et al., 1997; Wang et al., 2001). The high potassic alkaline magmatism is characterized by relatively low $\text{TiO}_2 < 1.3$, high Na_2O and K_2O ($\text{K}_2\text{O} + \text{Na}_2\text{O}$) $> 5\%$, Al_2O_3 (9%–20%), coupled with high contents of incompatible trace elements (Wang et al., 2001).

It has recently been reported that the highly potassic magmas were emplaced between ca. 40 and 30 Ma in the northwestern Yunnan (e.g. along and on both sides of the ASRR shear zone) and northwest Vietnam (e.g., Chung et al., 1997, 1998; Zhang and Schärer, 1999; Liang et al. 2007). Most high potassic alkaline igneous rocks are found in adjacent unmetamorphosed rocks, the orientation of these granitoid layers is paralleling to the shearing direction in the high-grade metamorphic belt (e.g. Chung et al., 1997; Liang et al., 2007).

Our new U/Pb data from the highly deformed high potassic alkaline granites in the DCS massif suggests that the magmatic rocks of ca. 34-31 Ma were emplaced prior to the initiation of shearing. The emplacement of these pre-shearing magmatic rocks in the ASRR shear zone appears to have been accompanied by development of Eocene to Oligocene rifted sedimentary basins. In the DCS massif, for example, the Eocene sedimentary rocks occurred in the west and northeast (e.g. Leloup et al., 1995; Chung et al., 1997). It is generally accepted that generation of such high potassic alkaline magmas resulted from a consequence of extensional setting (e.g. Chung et al., 2007). Similarly, we also propose that the short time span of emplacement of pre-kinematic plutons occurred during late Eocene to Oligocene, which can be related to the high-alkaline magmatic activity in response to the post-collisional extension. The delamination of a thickened continental lithosphere possibly caused late Eocene to early Oligocene regional extension and the potassic magmatism in the southeast of Tibetan Plateau occur as a response to the post-collision extension (Chung et al., 2008), or removal of the crustal root. The high potassic magmatism and the associated extension occurred before the initiation of the ASRR, thus suggesting that the onset of left-lateral shearing occurred after 31 Ma. We suggest that the shear zone underwent the main ductile deformation between ca. 27 and 21 Ma, which accommodated the successive southeastward extrusion of the crustal fragments. The youngest-phase magmatism activity is related to brittle shearing continued after 20 Ma, possibly until 17 Ma (cooling history analysis from Ar-Ar results) (e.g. Leloup et al., 1995). Understanding the timing sequence of tectonic event in SE Asia is of significance in revealing the mechanism of extrusion tectonics (Wang et al. 2000). On the other hand, it has also been widely accepted that the resultant strike-slip movement along the ASRR shear zone is the key process responsible for opening the South China Sea (e.g. Leloup et al. 1995). Our results also argue that the ductile phase of the left-lateral shearing along the ASRR shear zone has a maximum initiation age at ca. 31 Ma, which possibly postdated the onset of the opening of the South China Sea (ca. 32) (e.g. Taylor and Hayes, 1980, 1983; Briais et al. 1993; Cande and Kent, 1995).

6.6. Conclusions

1) Our U/Pb dating of magmatic zircons from leucocratic intrusions in the DCS metamorphic massif, constrain the timing of deformation related to the left-lateral shearing along the ASRR shear zone. There are three successive magmatic-tectonic deformation phases over the entire duration of left-lateral strike-slip shearing.

2) The granitic intrusions of different stages have distinct structural and microstructural characteristics. The early intrusions show regional high-temperature solid-state plastic deformation, which may characterize the pre-kinematic emplacement of the intrusions. Some intrusions are dominated by subsolidus deformation that resulted in widespread appearance of diagnostic structures and microstructures for syn-kinematic emplacement. The late intrusions postdate the ductile shearing, which formed dykes crosscutting the mylonitic foliation. The emplacement of the three stages of granitic intrusions is spatially confined and temporally related to a continuum of ductile to brittle deformation, which may indicate a change in the rheology of the crust evolving from ductile to brittle state.

3) The most straightforward interpretation of our data suggests that the left-lateral ductile shearing is initiated at ca. 31 Ma, reached its peak between 27 and 21 Ma at high temperatures related to the slow cooling and terminated at about 20 Ma at low temperatures related to the rapid cooling.

Acknowledgements

This study has received financial support from the National Natural Science Foundation of China (40872139), the 111 Project (B07011) of the Ministry of Education, State Key Laboratory of Geological Processes and Mineral Resources (Grant No. GPMR200837) and supported by the Fundamental Research Funds for the Central Universities (Grant No. GPMR2009PY01). Thanks are also due to the help by Dr. Zhang YB and Dr. Yang JH for helpful comments on the first draft of the manuscript. Two anonymous reviewers and the associate editor Dr. Inna Safonova and the chief editor Dr. M. Santosh are appreciated for their thoughtful and constructive comments and reviews which substantially improved this work, both in science and in English.

References

- Allen, C.R., Gillespie, A.R., Han, Y., Sieh, K.E., Zhang, B., Zhu, C., 1984. Red River and associated faults, Yunnan province, China: Quaternary geology, slip rates, and seismic hazard. *Geological Society of American Bulletin*, 95, 686–700.
- Anczkiewicz, R., Viola, G., Muntener, O., Thirlwall, M.F., Villa, I.M., Quong, N.Q., 2007. Structure and shearing conditions in the Day Nui Con Voi massif: Implications for the evolution of the Red River shear zone in northern Vietnam. *Tectonics*, 26, TC2002, doi:10.1029/2006TC001972.
- Andersen, T., 2002. Correlation of common lead in U-Pb analyses that do not report ²⁰⁴Pb. *Chemical Geology*, 2002, 192, 59–79.
- Barr, S.M., MacDonald, A.S., Miller, B.V., Reynolds, P.H., Rhodes, B.P., Yokart, B., 2002. New U–Pb and ⁴⁰Ar/39Ar ages from the Doi Inthanon and Doi Suthep metamorphic core complexes, northwestern Thailand. In: Mantajit, N. (ed.) *Proceedings of the Symposium on Geology of Thailand*. Department of Mineral Resources, Bangkok, 284–294.
- Black, L.P., Kamo, S.L., Williams, I.S., Mundil, R., Davis, D.W., Korsch, R.J., Foudoulis, C., 2003. The application of SHRIMP to Phanerozoic geochronology: a critical appraisal of four zircon standards. *Chemical Geology* 200, 171–188.
- Blenkinsop, T., 2000. *Deformation microstructures and mechanisms in minerals and rocks*. Kluwer Academic Publishes, Dordrecht.
- Blumenfeld, P., Bouchez, J.L., 1988. Shear criteria in granite and migmatite deformed in the magmatic and solid states. *Journal of Structural Geology*, 10, 361–372.
- Bouchez, J.L., Delas, C., Gleizes, G., Nedelec, A., Cuney, M., 1992. Submagmatic microfractures in granites. *Geology*, 20, 35–38.
- Briais, A., Patriat, P., Tapponnier, P., 1993. Updated interpretation of magnetic anomalies and seafloor spreading stages in the South China Sea: implications for the Tertiary tectonics of Southeast Asia. *Journal of Geophysical Research*, 98, 6299–6328.
- Brown, M., Solar, G.S., 1998. Granite ascent and emplacement during contractional deformation in convergent orogens. *Journal of Structural Geology*, 20, 1365–1393.
- Brown, M., Solar, G.S., 1999. The mechanism of ascent and emplacement of granite magma during transpression: a syntectonic granite paradigm. *Tectonophysics*, 312, 1–33.
- Burchfiel, B.C., Wang, E.C., 2003. Northwest-trending, middle Cenozoic, left-lateral faults in southern Yunnan, China, and their tectonic significance. *Journal of Structural Geology*, 25, 781–792.

- Bureau of Geology and Mineral Resources of Yunnan, 1983. Geological map of Yunnan, Kunming, China.
- Cande, S.C., Kent, D.V., 1995. Revised calibration of the geomagnetic polarity timescale for the late Cretaceous and Cenozoic, *Journal of Geophysical Research*, 100, 6093–6095.
- Cao, S.Y., Liu, J.L., Leiss, B., 2010. Orientation-related deformation mechanisms of naturally deformed amphibole in amphibolite mylonites from the Diancang Shan, SW Yunnan, China. *Journal of Structural Geology*, 32, 606–622.
- Chen, Z., Burchfiel, B.C., Liu, Y., King, R.W., Royden, L.H., Tang, W., Wang, E., Zhao, J., Zhang, X., 2000. Global positioning system measurements from eastern Tibet and their implications for India/Eurasia intercontinental deformation. *Journal of Geophysical Research*, 105 (B7), 16215–16227.
- Chung, S.L., Lee, T.Y., Lo, C.H., Wang, P.L., Chen, C.Y., Yem, N.T., Hoa, T.T., Wu, G.Y., 1997. Intraplate extension prior to continental extrusion along the Ailao Shan Red River shear zone. *Geology*, 25, 311–314.
- Chung, S.L., Lo, C.H., Lee, T.Y., Zhang, Y. Q., Xie, Y.W., Li, X.H., Wang, K.L., Wang, P. L., 1998. Diachronous uplift of the Tibetan starting from 40 Myr age. *Nature*, 394, 769–773.
- Chung, S.L., Searle, M.P., Yeh, M.W., 2008. Discussion and reply on “The age of the potassic alkaline igneous rocks along the Ailao Shan-Red River shear zone: Implications for the onset age of left-lateral shearing: A discussion. *The Journal of Geology*, 116, 201–204. *The Journal of Geology* 115, 231-242.
- Clift, P.D., Lee, G.H., Duc, N.A., Barckhausen, U., Long, H.V., 2008. Seismic reflection evidence for a dangerous grounds miniplate: no extrusion origin for the South China Sea. *Tectonics*, 27. doi:10.1029/2007TC002216.
- Compston, W., Williams, I.S., 1984. U-Pb geochronology of zircons from lunar breccias 73217 using a sensitive high mass resolution ion microprobe. *Journal of Geophysical Research*, 89, 525–534.
- Compston, W., Williams, I.S.; Kirschvink, J.L.; Zhang, Z., Ma, Guogan., 1992. Zircon U-Pb ages for the Early Cambrian time-scale. *Journal of the Geological Society of London*, 149, 171–184.
- Fyhn, M.B.W., Boldreel, L.O., Nielsen, L.H., 2009. Geological development of the Central and South Vietnamese margin: Implications for the establishment of the South China Sea, Indochinese escape tectonics and Cenozoic volcanism. *Tectonophysics*, 478, 184–214.
- Garnier, V., Giuliani, G., Maluski, H., Ohnenstetter, D., Trong, T. P., Quang, V. H., Van, L. P., Van, T. V., Schwarz, D., 2002. Ar-Ar ages in phlogopites from marble-hosted ruby deposits

- in northern Vietnam: Evidence for Cenozoic ruby formation. *Chemical Geology*, 188, 33–49.
- Gilley, L.D., Harrison, T.M., Leloup, P.H., Ryerson, F.J., Lovera, O.M., Wang, J.H., 2003. Direct dating of left-lateral deformation along the Red River shear zone, China and Vietnam. *Journal of Geophysical Research*, 108, doi:10.1029/2001 JB001726.
- Griffin, W.L., Powell, W.J., Pearson, N.J., O'Reilly, S.Y., 2008. GLITTER: data reduction software for laser ablation ICP-MS. In: Sylvester, P. (Ed.), *Laser Ablation-ICP-MS in the Earth Sciences: Current Practices and Outstanding Issues*: Mineral. Assoc. Canada Short Course, vol. 40, pp. 308–311.
- Guo, L., Zhong, Z., Wang, L., Shi, Y., Li, H., Liu, S., 2001. Regional tectonic evolution around Yinggehai basin of South China Sea. *Geological Journal of China Universities*, 7, 1–12.
- Harrison, T.M., Chen, W.J., Leloup, P.H., 1992. An early Miocene transition in deformation regime within the Red River fault zone, Yunnan, and its significance for Indo-Asian tectonics. *Journal of Geophysical Research*, 97(B5), 7159–7182.
- Harrison, T.M., Leloup, P.H., Ryerson, F.J., Tapponnier, P., Lacassin, R., Chen, W.J., 1996. Diachronous initiation of transtension along the Ailao Shan-Red River Shear zone, Yunnan and Vietnam. In: Harrison, T.M., Yin, A. (Eds.), *The tectonics of Asian*. Cambridge University Press, New York, pp. 208–226.
- Hibbard, M.J., 1987. Deformation of incompletely crystallized magma systems: granitic gneisses and their tectonic implications. *Journal of Geology*, 95, 543–561.
- Huang, T.K., 1960. Characteristics of the structure of China: Preliminary conclusions. *Scientica Sinica*, 9, 492–544.
- Huang, K., Opdyke, N.D., 1993. Paleomagnetic results from Cretaceous and Jurassic rocks of South and Southwest Yunnan: evidence for large clockwise rotations in the Indochina and Shan-Thai-Malay terranes. *Earth and Planetary Science Letters*, 117, 507–524.
- Jackson, S.E., Pearson, N.J., Griffin, W.L., Belousova, E.A., 2004. The application of laser ablation-inductively coupled plasma-mass spectrometry (LA-ICP-MS) to in situ U–Pb zircon geochronology. *Chemical Geology*, 211, 47–69.
- Jolivet L., Maluski H., Beyssac O., Goffé B., Lepvrier C., Phan Truong T., Nguyen Van V., 1999. Oligocene-Miocene Bu Khang extensional gneiss dome in Vietnam: Geodynamic implications. *Geology*, 27, 67–70.
- Jolivet, L., Beyssac, O., Goffé, B., Avigad, D., Lepvrier, C., Maluski, H., Thang, T.T., 2001. Oligo–Miocene midcrustal subhorizontal shear zone in Indochina. *Tectonics*, 20, 46–57.

- Karlstrom, K.E., 1991. Towards a syntectonic paradigm for granites. EOS, Transactions of the American Geophysical Union, 70, 762–770.
- Karlstrom, K.E., Miller, C.F., Kingsbury, J. A., Wooden, J.L., 1993. Pluton emplacement along an active ductile thrust zone, Piute Mountains, southeastern California: Interaction between deformational and solidification processes. Bulletin Geological Society of America, 10, 213–230.
- Lacassin, R., Maluski, H., Leloup, P.H., Tapponnier, P., Hinthong, C., Siribhakdi, K., Chuaviroj, S., Charoenravat, A., 1997. Tertiary diachronic extrusion and deformation of western Indochina: structural and $^{40}\text{Ar}/^{39}\text{Ar}$ evidence. Journal of Geophysical Research, 102 (B5), 10013–10037
- Lee, G.H., Watkins, J.S., 1998. Seismic stratigraphy and hydrocarbon potential of the Phu Khan Basin, offshore Central Vietnam, South China Sea. AAPG Bulletin, 82, 1711–1735.
- Leloup, P.H., Harrison, T.M., Ryerson, F.J., Chen, W.J., Li, Q., 1993a. Structural, petrological and thermal evolution of a Tertiary Ductile strike-slip shear zone, Diancang Shan, Yunnan. Journal of geophysical research, 98, 6715–6743.
- Leloup, P.H., Kienast, J.R., 1993b. High-temperature metamorphism in a major strike-slip shear zone: the Ailao Shan–Red River, People’s Republic of China. Earth and Planetary Science Letters, 118, 213–234.
- Leloup, P.H., Lacassin, R., Tapponnier, P., Schärer, U. Zhong, D.L., Liu, X.H., Zhang, L.S., Ji, S.C., Phan, T.T., 1995. The Ailao Shan-Red River shear zone (Yunnan, China), Tertiary transform boundary of Indochina. Tectonophysics, 251, 3–84.
- Leloup, P.H., Lacassin, R., Tapponnier, P., Harrison, T.M., 2001a. Comment on “Onset timing of left-lateral movement along the Ailao Shan–Red River shear zone: $^{40}\text{Ar}/^{39}\text{Ar}$ dating constraint from the Nam Dinh area, northeastern Vietnam” by Wang et al., 2000, Journal of Asian Earth Sciences, 18, 281–292. Journal of Asian Earth Sciences, 20, 95–99.
- Leloup, P.H., Arnaud, N., Lacassin, R., Kienast, J.R., Harrison, T.M., Phan Trong, T.T., Replumaz, A., Tapponnier, P., 2001b. New constraints on the structure, thermochronology, and timing of the Ailao Shan-Red River shear zone, SE Asia, Journal of Geophysical Research, 106, 6683–6732.
- Leloup, P.H., Tapponnier, P., Lacassin, R., 2007. Comment on “Discussion on the role of the Red River shear zone, Yunnan and Vietnam, in the continental extrusion of SE Asia” by Searle, M.P., 2006, Journal of the Geological Society, London, 163, 1025–1036. Journal of the Geological Society, London, 164, 1253–1260

- Lepvrier, C., Maluski, H., Vuong, N.V., Roques, D., Axent, V., Rangin, C., 1997. Indosinian NW-trending shear zones within the Truong Son belt (Vietnam) $^{40}\text{Ar}/^{39}\text{Ar}$ Triassic ages and Cretaceous to Cenozoic overprints. *Tectonophysics*, 283, 105–127.
- Li, Q.L., Li, X.H., Liu, Y., Tang, G.Q., Yang, J.H., Zhu, W.G., 2010. Precise U–Pb and Pb–Pb dating of Phanerozoic baddeleyite by SIMS with oxygen flooding technique.
- Liang H.Y., Campbell, I.H., Allen, C.M., Sun, W.D., Yu, H.X., Xie, Y.W., Zhang, Y.Q., 2007. The Age of the Potassic Alkaline Igneous Rocks along the Ailao Shan–Red River Shear Zone: Implications for the Onset Age of Left-Lateral Shearing. *The Journal of Geology*, 115, 231–242.
- Liu, J.L., Song, Z.J., Cao, S. Y., Zhai, Y.F., Wang A.J., Gao, L., Xiu, Q.Y., Cao, D.H., 2006. The dynamic setting and processes of tectonic and magmatic evolution of the oblique collision zone between Indian and Eurasian plates: exemplified by the tectonic evolution of the Three River region, eastern Tibet (in Chinese). *Acta Petrologica Sinica*, 22, 775–786.
- Liu, J.L., Cao, S.Y., Zhai, Y.F., Song, Z.J. Wang, A.J., Xiu, Q.Y., Gao, L., Guan, Y., 2007. Rotation of Crustal Blocks as an Explanation of Oligo–Miocene Extension in Southeastern Tibet–Evidenced by the Diancangshan and Nearby Metamorphic Core Complexes. *Earth Science Frontiers*, 14, 40–48.
- Ludwig, K.R., 2003, ISOPLOT 3.00: A Geochronological Toolkit for Microsoft Excel. Berkeley Geochronology Center Special Publication, 1–70
- Maluski, H., Lepvrier, C., Jolivet, L., Carter, A., Roques, D., Beyssac, O., Tang, T.T., Thang, N.D., Avigad, D., 2001. Ar–Ar and fission-track ages in the Song massif: Early Triassic and Cenozoic tectonics in northern Vietnam. *Journal of Asian Earth Science*, 19, 233–248.
- Miller, R.B, Paterson, S.R., 1994. The transition from magmatic to high-temperature solid-state deformation: implications from the Mount Stuart batholiths, Washington. *Journal of Structural Geology*, 16(6), 853–865.
- Morley, C.K., 2002. A tectonic model for the Tertiary evolution of strike-slip faults and rift Basins in SE Asia. *Tectonophysics*, 347, 189–215.
- Morley, C.K., 2007. Variations in Late Cenozoic–Recent strike-slip and oblique extensional geometries, within Indochina: The influence of pre-existing fabrics. *Journal of Structural Geology*, 29, 36–58.
- Nagy, E.A., Schärer, U., Minh, N.T., 2000. Oligo-Miocene granitic magmatism in central Vietnam and implications for continental deformation in Indochina. *Terra Nova*, 12, 67–76.

- Nagy, E.A., Maluski, H., Lepvrier, C., Schärer, U., Thi, P.T., Leyreloup, A., Thich, V.V., 2001. Geodynamic significance of the Kontum Massif in central Vietnam: composite $^{40}\text{Ar}/^{39}\text{Ar}$ and U–Pb ages from Paleozoic to Triassic. *Journal of Geology*, 109 (6), 755–770.
- Passchier, C.W., Trouw, R.A.J., 2005. *Microtectonics*. Springer-Verlag, Berlin. p56.
- Paterson, S.R., Tobisch, O.T., 1988. Using pluton ages to determine regional deformations: problems with commonly used criteria. *Geology*, 16, 1108–1111.
- Paterson, S.R., Vernon, R.H., Tobisch, O.T., 1989. A review of criteria for the identification of magmatic and tectonic foliations in granitoids. *Journal of Structural Geology*, 11, 349–363.
- Paterson, S.R., Fowler, T.K., Schmidt, K.L., Yoshinobu, A.S., Yuan, E.S., Miller, R.B., 1998. Interpreting magmatic fabric patterns in plutons. *Lithos*, 44, 53–82.
- Peltzer, G., Tapponnier, P., 1988. Formation and evolution of strike-slip faults, rifts, and basins during the India-Asia collision: an experimental approach. *Journal of Geophysical Research*, 93(15), 85–117.
- Rosenberg, C.L., 2004. Shear zones and magma ascent: A model based on a review of the Tertiary magmatism in the Alps. *Tectonics*, 23(3), 1–21.
- Sassier, C., Leloup, P.H., Rubatto, D., Galland, O., Yue, Y., Lin, D., 2009. Direct measurement of strain rates in ductile shear zones: A new method based on syntectonic dykes. *Journal of Geophysical Research-Solid Earth*, 114, 1–32.
- Sato, K., Liu, Y.Y., Zhu, Z.C., Yang, Z.Y., Otofujii, Y.I., 1999. Paleomagnetic study of middle Cretaceous rocks from Yunlong, western Yunnan, China: evidence of southward displacement of Indochina. *Earth and Planetary Science Letters*, 165, 1–15.
- Schärer, U., Tapponnier, P., Lacassin, R., Leloup, P.H., Dalai, Z., Ji, S.C., 1990. Intraplate tectonics in Asia: a precise age for large-scale Miocene movement along the Ailao Shan-Red River shear zone, China. *Earth and Planetary Science Letters*, 97, 65–77.
- Schärer, U., Zhang, L.S., Tapponnier, P., 1994. Duration of strike-slip movements in large shear zones: The Red River belt, China. *Earth and Planetary Science Letters*, 126, 379–397.
- Searle, M., 2006. Role of the Red River Shear zone, Yunnan and Vietnam, in the continental extrusion of SE Asia. *Journal of the Geological Society, London*, 163, 1025–1036.
- Shelley, D., 1985. Determining paleo-flow directions from groundmass fabrics in the Lyttleton radial dykes, New Zealand. *Journal of Volcanology and Geothermal Research*, 25, 69–79.
- Simpson, C. 1985. Deformation of granitic rocks across the brittle-ductile transition. *Journal of Structural Geology*, 7, 503–511.
- Simpson, C., Wintsch, R.P., 1989. Evidence for deformation-induced K-feldspar replacement by myrmekite. *Journal of Metamorphic Geology*, 7, 261–275.

- Tan, X.H., 1999. Characteristics and formation mechanism of Cenozoic structural basins in the three-river area of west Yunnan. *Yunnan Geology*, 18, 112–121.
- Tanaka, K, Mu C, Sato, K., Takemoto, K., Miura, D., Liu, Y., Zaman, H., Yang, Z., Yokoyama, M., Iwamoto, H., Uno, K., Otofujii, Y., 2008. Tectonic deformation around the eastern Himalayan syntaxis: constraints from the Cretaceous palaeomagnetic data of the Shan-Thai Block. *Geophysical Journal International*, 175, 713–728.
- Tapponnier, P., Molnar, P., 1977. Active faulting and tectonics of China, *Journal of Geophysical Research*, 82, 2905– 2930.
- Tapponnier, P., Peltzer, G., Armijo, R., Le Dain, A.Y., Cobbold, P., 1982. Propagating extrusion tectonics in Asia: new insights from simple experiments with plasticine. *Geology*, 10, 611–616.
- Tapponnier, P., Peltzer, G., Armijo, R., 1986. On the mechanics of the collision between India and Asia. In: Coward, M.P., Ries, A.C. (Eds.), *Collision Tectonics*. Geological Society of London Special Publication, 19, 115–157.
- Tapponnier, P., Lacassin, R., Leloup, P.H., Schärer, U., Zhong, D.L, Liu, X.H, Ji, S.C., Zhang, L.S., Zhong, J.Y., 1990. The Ailao Shan/Red River metamorphic belt: Tertiary left-lateral shear between Indochina and South China. *Nature*, 343, 431–437.
- Taylor, B., Hayes, D.E., 1983. Origin and history of South China Sea Basin, in Hayes D.E., (Eds.). *The Tectonic and Geologic Evolution of Southeast Asian Seas and Islands*, 2, AGU, Geophysical Monograph, Washington, DC, 23–56.
- Taylor, B., Hayes, D.E., 1980. The tectonic evolution of the South China basin. In: Hayes D.E. (Eds.). *The tectonic and geological evolution of southeast Asian Seas and islands*. AGU, Geophysical Monograph, 23, 89–104.
- Tran, N.N., Mitsuhiro, T., Tetsumaru, I., 1998. P–T–t paths and post-metamorphic exhumation of the Day Nui Con Voi shear zone in Vietnam. *Tectonophysics*, 290, 299–318.
- Tran, N.N., Sano, Y., Terada, K., Toriumi, M., Quynh, P.V., and Dung, L.T., 2001. First SHRIMP U–Pb zircon dating of granulites from the Kontum massif (Vietnam) and tectonothermal implications, *Journal of Asian Earth Sciences*, 19, 77–84.
- Vernon, R.H., 1987. Growth and concentration of fibrous sillimanite related to heterogeneous deformation in K-feldspar-sillimanite metapelites. *Journal of Metamorphic Geology*, 5, 51–68.
- Vernon, R.H., 2000. Review of microstructural evidence of magmatic and solid-state flow. *Electronic Geosciences*. Springer, 2000.

- Wan, Y.S., Liu, D.Y., Jian, P., 2004. Comparison between monazite dating and zircon dating. *Chinese Science Bulletin*, 49, 1185-1190.
- Wang, C.Y., Campbell, I.H., Allen, C.M., Williams, I.S., Eggins, S.M., 2009. Rate of growth of the preserved North American continental crust: evidence from Hf and O isotopes in Mississippi detrital zircons. *Geochimica et Cosmochimica Acta*, 73, 712–728.
- Wang, E., Burchfiel, B.C., Royden, L.H., Chen, L.Z., Chen, J.S., Li, W.X., Chen, Z.L. (Eds.), 1998a, Late Cenozoic Xianshuihe-Xiaojiang, Red River, and Dali Fault Systems of Southwestern Sichuan and Central Yunnan, China, Special Paper, Geological Society of America, 327.
- Wang, J.H., Yin, A., Harrison, T.M., Grove, M., Zhang, Y.Q., Xie, G.H., 2001. A tectonic model for Cenozoic igneous activities in the eastern Indo-Asian collision zone. *Earth and Planetary Science Letters*, 188, 123–133.
- Wang, P.L., Lan, C.Y., Yem, N.T., Lo, C.H., Lee, T.Y., Chung, S.L., 1998b. Thermochronological evidence for the movement of the Ailao Shan-Red River shear zone: a perspective from Vietnam. *Geology*, 26, 887–890.
- Wang, P.L., Lo, C.H., Chung, S.L., Lee, T.Y., Lan, C.Y., Thang, T.V., 2000. Onset timing of left-lateral movement along the Ailao Shan-Red River shear zone: $^{40}\text{Ar}/^{39}\text{Ar}$ dating constraints from the Nam Dinh area, northeastern Vietnam. *Journal of Asian Earth Science*, 18, 281–292.
- Wang, P.L., Lo, C.H., Chung, S.L., Lee, T.Y., Lan, C.Y., Thang, T.V., 2001. Reply to comment on "Onset of the movement along the Ailao Shan-Red river shear zone: Constraint from $^{40}\text{Ar}/^{39}\text{Ar}$ dating results for Nam Dinh area, northern Vietnam". *Journal of Asian Earth Sciences*, 18, 281–292.
- Wang, Y.B., Liu, D.Y., Tang, S.H., 2004. Isotopic geochemistry and SHRIMP U-Pb geochronology of mafic-felsic granulites from Larsemann Hills, East Antarctica. *Geochimica et Cosmochimica Acta*, 68, 663.
- Wiedenbeck, M., Alle, P., Corfu, F., Griffin, W.L., Meier, M., Oberli, F., Vonquadt, A., Roddick, J.C., Spiegel, W., 1995. Three natural zircon standards for U–Th–Pb, Lu–Hf, trace-element and REE analyses. *Geostandards Newsletter*, 19, 1–23.
- Williams, I.S., 1998. U-Th-Pb geochronology by ion microprobe. In: McKibben, M.A., Shanks W.C., Ridley, W.I. (Eds.), *Applications of Microanalytical Techniques to Understanding Mineralizing Processes*, *Reviews in Economic Geology*, 7, 1–35.

- Wu, F.Y., Ji, W.Q., Liu, C.X., Chung, S.L., 2010. Detrital zircon U-Pb and Hf isotopic data from the Xigaze fore-arc basin: Constraints on Transhimalayan magmatic evolution in southern Tibet. *Chemical Geology*, 271, 13–25.
- Wang, X.F., Metcalfe, I., Jian, P., He, L.Q., Wang, C.S., 2000. The Jinshajiang–Ailaoshan Suture Zone, China: tectonostratigraphy, age and evolution. *Journal of Asian Earth Sciences*, 18, 675–690.
- Xie, L.W., Zhang, Y.B., Zhang, H.H., Sun, J.F., Wu, F.Y., 2008. In situ simultaneous determination of trace elements, U–Pb and Lu–Hf isotopes in zircon and baddeleyite. *Chinese Science Bulletin*, 53, 1565–1573.
- Yang, Z., Besse, J., 1993. Paleomagnetic study of Permian and Mesozoic sedimentary rocks from northern Thailand supports the extrusion model for Indochina. *Earth and Planetary Science Letters*, 117, 525–552.
- Yang, Z., Besse, J., Suteethorn, V., Bassoulet, J.P., Fontaine, H., Buffetaut, E., 1995. Lower-Middle Jurassic paleomagnetic data from the Mae Sot area (Thailand), Paleogeographic evolution and deformation history of Southeastern Asia. *Earth and Planetary Science Letters*, 136, 325–341.
- Yeh, M.W., Lee, T.Y., Lo, C.H., Chung, S.L., Lan, C.Y., Anh, T.T., 2008. Structural evolution of the Day Nui Con Voi metamorphic complex: Implications on the development of the Red River Shear Zone, Northern Vietnam. *Journal of Structural Geology*, 30(12), 1540–1553.
- Yuan, H.L., Gao, S., Dai, M.N., Zong, C.L., Günther, D., Fontaine, G.H., Liu, X.M., Diwu, C.R., 2008. Simultaneous determinations of U–Pb age, Hf isotopes and trace element compositions of zircon by excimer laser-ablation quadrupole and multiple collector ICP-MS. *Chemical Geology*, 247, 100–118.
- Zhang, L.S., Schärer, U., 1999. Age and origin of magmatism along the Cenozoic Red River shear belt, China. *Contributions to Mineralogy and Petrology*, 134, 67–85.
- Zhang, L., Zhong, D., 1996. View on the Cenozoic tectonics of the Southeast Asia based on the strike–slip motion of the Red River shear zone. *Scientia Geologica Sinica*, 31, 327–339.
- Zhang, X., Wang, Y.H., 2009. Crustal and upper mantle velocity structure in Yunnan, Southwest China. *Tectonophysics* 471, 171–185.
- Zhong, D.L., Tapponnier, P., Wu, H.W., Zhang, L.S., Ji, S.C., Zhong, J.Y., Liu, X.H., Schärer, U., Lacassiu, R., Leloup, P., 1990. Large-Scale Strike-Slip-Fault-the Major Structure of Intracontinental Deformation after Collision. *Chinese Science Bulletin*, 35(4), 304–309.
- Zhu, M.Z., Graham, S., McHargue, T., 2009. The Red River Fault zone in the Yinggehai Basin, South China Sea. *Tectonophysics*, 476, 397–417.

Table 6. 1 Zircon U/Pb SHRIMP-II analytical data of the monzogranite sample in the Diancang Shan metamorphic massif.

Sample	com Pb	U	Th	Th/U	Ratios*						Age (Ma)	
Grain spot	%	ppm	ppm		$^{207}\text{Pb}/^{206}\text{Pb}$	$\pm(1\sigma)$	$^{207}\text{Pb}/^{235}\text{U}$	$\pm(1\sigma)$	$^{206}\text{Pb}/^{238}\text{U}$	$\pm(1\sigma)$	$^{206}\text{Pb}/^{238}\text{U}$	$\pm(1\sigma)$
1.1	0.67	3968	752	0.20	0.0475	4.9	0.0333	5.2	0.0051	1.6	32.7	0.5
2.1	1.24	2398	901	0.39	0.0450	7.5	0.0309	7.7	0.0050	1.8	32.0	0.6
3.1	1.14	1917	542	0.29	0.0486	7.8	0.0316	8.0	0.0047	1.8	30.4	0.5
4.1	1.52	2234	700	0.32	0.0429	10.9	0.0285	11.0	0.0048	1.8	31.0	0.5
5.1	1.03	2606	1237	0.49	0.0425	7.9	0.0300	8.1	0.0051	1.7	32.9	0.6
6.1	0.69	3016	1203	0.41	0.0463	4.4	0.0318	4.7	0.0050	1.7	32.1	0.5
7.1	0.31	6736	1941	0.30	0.0457	3.0	0.0300	3.4	0.0048	1.6	30.6	0.5
8.1	1.26	2148	804	0.39	0.0455	13.5	0.0300	13.6	0.0048	1.8	30.7	0.6
9.1	0.71	4035	839	0.21	0.0440	4.9	0.0296	5.1	0.0049	1.6	31.4	0.5
10.1	0.83	2845	974	0.35	0.0450	6.9	0.0281	7.1	0.0045	1.7	29.1	0.5
11.1	1.00	2827	812	0.30	0.0471	7.2	0.0311	7.4	0.0048	1.7	30.8	0.5
12.1	0.53	4109	1056	0.27	0.0450	4.4	0.0291	4.7	0.0047	1.6	30.1	0.5
13.1	1.71	1804	355	0.20	0.0357	13.4	0.0228	13.5	0.0046	1.8	29.8	0.5
14.1	1.52	1608	2092	1.34	0.0493	9.0	0.0327	9.2	0.0048	1.7	31.0	0.5
15.1	9.66	799	422	0.55	0.0363	84.8	0.0229	84.5	0.0046	3.4	29.4	1.0

* is the ratios corrected for common Pb

Table 6. 2 Zircon U/Pb LA-ICP-MS analytical data of the intrusions in the Diancang Shan metamorphic massif

No.	Pb _{rad} (ppm)	Th (ppm)	U (ppm)	Th/U	Isotopic Ratio						Age (Ma)			
					²⁰⁷ Pb/ ²⁰⁶ Pb	±1σ	²⁰⁷ Pb/ ²³⁵ U	±1σ	²⁰⁶ Pb/ ²³⁸ U	±1σ	²⁰⁷ Pb/ ²³⁵ U	±1σ	²⁰⁶ Pb/ ²³⁸ U	±1σ
DC08-2-2 Granodiorite														
C26	0.982	104.79	179.04	0.59	0.0457	0.0141	0.0279	0.0084	0.0044	0.00031	28.0	8.27	28.4	1.99
C27	1.098	155.52	177.97	0.87	0.0450	0.0090	0.0291	0.0056	0.0047	0.00028	29.2	5.51	30.0	1.82
C28	1.242	147.61	215.22	0.69	0.0490	0.0108	0.0329	0.0068	0.0049	0.00036	32.8	6.72	31.2	2.32
C29	1.710	177.37	324.45	0.55	0.0463	0.0060	0.0297	0.0036	0.0046	0.00021	29.7	3.57	29.8	1.33
C30	1.605	90.02	149.55	0.60	0.0486	0.0180	0.0295	0.0104	0.0044	0.00052	29.5	10.22	28.2	3.35
C31	3.505	529.08	591.78	0.89	0.0475	0.0043	0.0307	0.0026	0.0047	0.00016	30.7	2.54	30.1	1.05
C32	2.829	231.39	409.54	0.56	0.0530	0.0097	0.0366	0.0061	0.0050	0.00039	36.5	5.92	32.1	2.49
C33	2.917	291.59	416.23	0.70	0.0522	0.0083	0.0351	0.0052	0.0049	0.00030	35.0	5.08	31.2	1.94
C34	2.115	133.10	220.31	0.60	0.0466	0.0158	0.0319	0.0103	0.0050	0.00051	31.9	10.16	31.9	3.27
C38	0.972	86.85	137.24	0.63	0.0479	0.0130	0.0339	0.0088	0.0051	0.00040	33.9	8.66	32.9	2.55
C39	2.604	371.31	369.91	1.00	0.0498	0.0054	0.0347	0.0036	0.0050	0.00020	34.6	3.49	32.4	1.30
C41	1.240	111.91	173.78	0.64	0.0453	0.0096	0.0363	0.0075	0.0058	0.00032	36.2	7.30	37.2	2.08
C42	1.315	106.90	179.86	0.59	0.0473	0.0097	0.0367	0.0072	0.0056	0.00037	36.6	7.03	36.0	2.34
C43	1.408	114.50	180.10	0.64	0.0458	0.0182	0.0335	0.0127	0.0053	0.00064	33.5	12.48	34.0	4.11
C44	2.817	339.71	421.58	0.81	0.0441	0.0064	0.0310	0.0042	0.0051	0.00027	31.0	4.15	32.8	1.74
C45	2.420	166.39	381.38	0.44	0.0466	0.0051	0.0352	0.0036	0.0055	0.00024	35.1	3.50	35.2	1.54
C53	5.903	182.10	444.65	0.41	0.0488	0.0053	0.0358	0.0036	0.0053	0.00023	35.7	3.54	34.2	1.45
C55	1.668	159.40	232.68	0.69	0.0471	0.0066	0.0367	0.0049	0.0057	0.00024	36.6	4.82	36.3	1.56
G18	2.648	149.44	426.41	0.35	0.0461	0.0059	0.03238	0.00391	0.0051	0.00022	32.0	4.00	33.0	1.00
G24	3.215	92.62	193.92	0.48	0.0461	0.01932	0.03327	0.01374	0.00524	0.00039	33.0	14.00	34.0	3.00
G26	3.283	261.43	378.48	0.69	0.0461	0.00799	0.03651	0.0061	0.00575	0.00027	36.0	6.00	37.0	2.00
G31	2.269	129.75	309.57	0.42	0.0461	0.00788	0.03604	0.00589	0.00568	0.00028	36.0	6.00	36.0	2.00
G43	4.523	150.72	611.03	0.25	0.0461	0.00846	0.03031	0.0054	0.00477	0.00022	30.0	5.00	31.0	1.00
DC0835-2 Granite														
E46	2.772	58.45	511.97	0.11	0.0467	0.0046	0.0345	0.0029	0.0054	0.00028	34.5	2.87	34.5	1.79
E50	1.926	109.19	298.11	0.37	0.0467	0.0089	0.0380	0.0060	0.0059	0.00062	37.9	5.88	37.9	3.97
E52	4.012	39.27	699.59	0.06	0.0466	0.0047	0.0373	0.0031	0.0058	0.00033	37.2	3.06	37.3	2.11
E66	8.662	276.32	1055.77	0.26	0.0471	0.0021	0.0319	0.0012	0.0049	0.00014	31.9	1.16	31.6	0.90
E67	2.627	244.07	397.89	0.61	0.0486	0.0162	0.0345	0.0094	0.0051	0.00097	34.4	9.26	33.0	6.23
E69	1.106	31.27	181.39	0.17	0.0704	0.0244	0.0513	0.0135	0.0053	0.00119	50.8	13.03	33.9	7.64
E71	3.564	142.94	512.81	0.28	0.0470	0.0095	0.0394	0.0066	0.0061	0.00071	39.2	6.40	39.0	4.54
E80	4.110	236.93	741.49	0.32	0.0486	0.0081	0.0359	0.0050	0.0054	0.00049	35.8	4.94	34.4	3.12
E85	6.158	744.72	959.68	0.78	0.0466	0.0060	0.0350	0.0038	0.0055	0.00040	35.0	3.68	35.1	2.57
E92	2.427	203.41	320.69	0.63	0.0781	0.0380	0.0638	0.0232	0.0059	0.00192	62.8	22.13	38.0	12.29

Chapter 6: Oligo-Miocene shearing, structure, U/Pb geochronology and magmatic rocks

DC0822-1 Granite

F89	5.619	414.23	1211.45	0.34	0.0469	0.0037	0.0268	0.0018	0.0042	0.00018	27.0	2.00	27.0	1.00
F92	20.941	533.09	2182.38	0.24	0.0496	0.0034	0.0292	0.0017	0.0043	0.00018	29.0	2.00	27.0	1.00
F93	12.061	750.77	2749.95	0.27	0.0476	0.0021	0.0287	0.0011	0.0044	0.00012	29.0	1.00	28.1	0.80
F94	17.696	921.16	4317.11	0.21	0.0470	0.0017	0.0265	0.0008	0.0041	0.00010	26.6	0.80	26.4	0.60
F98	11.119	632.91	2751.00	0.23	0.0466	0.0018	0.0255	0.0008	0.0040	0.00010	25.6	0.80	25.5	0.60
F99	20.210	1114.64	4595.44	0.24	0.0496	0.0018	0.0287	0.0009	0.0042	0.00010	28.8	0.80	27.0	0.60
G01	15.273	311.37	1173.44	0.27	0.0491	0.0035	0.0285	0.0017	0.0042	0.00018	29.0	2.00	27.0	1.00
G03	15.288	980.17	3626.18	0.27	0.0477	0.0017	0.0268	0.0008	0.0041	0.00010	26.9	0.80	26.2	0.60
G05	24.432	1238.48	5541.37	0.22	0.0457	0.0013	0.0275	0.0007	0.0044	0.00009	27.5	0.70	28.1	0.60
G06	13.045	1298.37	2848.55	0.46	0.0533	0.0026	0.0300	0.0012	0.0041	0.00013	30.0	1.00	26.2	0.80
G12	15.065	824.19	3333.35	0.25	0.0477	0.0026	0.0274	0.0013	0.0042	0.00014	27.0	1.00	26.8	0.90
G13	22.851	991.55	5387.91	0.18	0.0465	0.0019	0.0274	0.0009	0.0043	0.00011	27.5	0.90	27.5	0.70
G14	8.56	314.18	1865.32	0.16843	0.04911	0.00610	0.02734	0.00327	0.00404	0.00013	28.0	2.0	27.1	0.6
G17	13.752	1379.23	2647.55	0.52	0.0486	0.0062	0.0285	0.0030	0.0043	0.00030	29.0	3.00	27.0	2.00
G19	5.89	395.12	1262.84	0.31288	0.04674	0.00577	0.02720	0.00325	0.00422	0.00013	30.0	1.0	27.3	0.5
G20	8.62	628.50	1749.53	0.35924	0.05694	0.00759	0.03344	0.00433	0.00427	0.00014	33.0	4.0	27.5	0.9
G21	20.263	1033.53	4325.12	0.24	0.0466	0.0036	0.0265	0.0017	0.0041	0.00018	27.0	2.00	27.0	1.00

DC0835-1 Granite

F60	102.625	16081.00	19915.29	0.81	0.0487	0.0021	0.0263	0.0011	0.0039	0.00005	32.0	1.00	25.0	0.30
F61	60.086	2080.15	13307.03	0.16	0.0493	0.0034	0.0265	0.0017	0.0039	0.00008	27.0	2.00	25.0	0.50
F64	105.112	9924.63	25907.97	0.38	0.0601	0.0024	0.0322	0.0012	0.0039	0.00005	27.2	0.80	25.1	0.40
F65	190.767	13314.94	46338.30	0.29	0.0501	0.0014	0.0273	0.0007	0.0040	0.00005	25.5	0.60	25.1	0.30
F66	76.673	1508.75	17579.40	0.09	0.0473	0.0012	0.0254	0.0006	0.0039	0.00005	27.1	0.80	25.1	0.30
F67	129.263	11341.34	29723.62	0.38	0.0546	0.0016	0.0297	0.0008	0.0040	0.00005	25.2	0.30	25.2	0.30
F72	132.313	16142.41	26217.43	0.62	0.0806	0.0012	0.0443	0.0006	0.0040	0.00005	25.5	0.80	25.2	0.40
F73	68.557	2090.60	15582.75	0.13	0.0461	0.0015	0.0253	0.0008	0.0040	0.00006	26.0	1.00	25.2	0.30
F74	155.985	4304.60	38191.43	0.11	0.0503	0.0016	0.0270	0.0008	0.0039	0.00005	25.0	1.00	25.3	0.40
F75	110.796	14847.86	27999.61	0.53	0.0774	0.0021	0.0425	0.0011	0.0040	0.00006	27.4	0.70	25.4	0.30
F77	28.044	1577.11	6414.28	0.25	0.0469	0.0021	0.0252	0.0011	0.0039	0.00006	29.7	0.80	25.5	0.30
F78	324.660	43814.34	69924.03	0.63	0.0470	0.0006	0.0251	0.0003	0.0039	0.00004	25.3	0.70	25.6	0.40
F80	39.753	2452.42	10080.34	0.24	0.0509	0.0017	0.0271	0.0009	0.0039	0.00006	44.0	0.60	25.8	0.30
F85	49.096	1177.81	12087.13	0.10	0.0471	0.0017	0.0254	0.0009	0.0039	0.00006	42.0	1.00	25.8	0.40

Chapter 6: Oligo-Miocene shearing, structure, U/Pb geochronology and magmatic rocks

DC08-2-1 Pegmatite

G20	23.654	234.41	6606.72	0.04	0.0444	0.0013	0.0241	0.0007	0.0039	0.00006	24.2	0.67	25.3	0.41
G25	28.422	391.83	8162.64	0.05	0.0459	0.0012	0.0252	0.0006	0.0040	0.00006	25.2	0.60	25.5	0.40
G27	15.506	162.77	4680.64	0.03	0.0466	0.0019	0.0259	0.0010	0.0040	0.00008	25.9	0.95	25.8	0.51
G29	29.911	306.02	9034.96	0.03	0.0461	0.0018	0.0256	0.0009	0.0040	0.00008	25.7	0.90	25.8	0.51
G30	28.535	376.96	8879.95	0.04	0.0464	0.0012	0.0247	0.0006	0.0039	0.00006	24.8	0.61	24.8	0.41
G32	33.036	360.56	8814.25	0.04	0.0465	0.0014	0.0252	0.0007	0.0039	0.00007	25.2	0.70	25.2	0.44
G37	20.881	158.63	6454.97	0.02	0.0457	0.0018	0.0249	0.0010	0.0039	0.00007	27.7	0.72	25.2	0.40
G39	24.847	323.63	8285.01	0.04	0.0484	0.0017	0.0272	0.0009	0.0041	0.00008	27.2	0.89	26.1	0.52
G42	32.298	550.15	9927.71	0.06	0.0465	0.0020	0.0268	0.0010	0.0042	0.00009	26.9	1.03	26.8	0.60

DC08-8-5 Pegmatite

D56	20.22	105.20	5437.33	0.02	0.0478	0.0015	0.0259	0.0008	0.0039	0.00006	22.9	0.7	22.1	0.3
D57	25.76	122.40	6839.65	0.02	0.0459	0.0014	0.0249	0.0007	0.0040	0.00006	22.0	2.0	22.7	0.4
D58	29.20	279.20	7432.91	0.04	0.0489	0.0018	0.0264	0.0009	0.0039	0.00006	23.6	0.6	23.2	0.3
D59	24.40	195.41	6625.45	0.03	0.0461	0.0016	0.0244	0.0007	0.0039	0.00006	23.0	0.4	23.2	0.3
D60	46.41	211.37	9302.09	0.02	0.0472	0.0016	0.0245	0.0008	0.0038	0.00006	23.8	0.9	23.2	0.4
D61	84.108	317.89	9553.85	0.03	0.0478	0.0016	0.0237	0.0007	0.0036	0.00007	23.8	0.70	23.2	0.40
D62	32.733	220.45	9414.17	0.02	0.0463	0.0015	0.0231	0.0006	0.0036	0.00007	23.2	0.60	23.3	0.40
D63	26.413	210.26	7622.72	0.03	0.0461	0.0012	0.0230	0.0005	0.0036	0.00006	23.1	0.50	23.3	0.40
D64	26.036	138.74	7320.30	0.02	0.0466	0.0016	0.0231	0.0007	0.0036	0.00007	23.1	0.70	23.1	0.40
D65	36.555	454.44	9797.21	0.05	0.0487	0.0010	0.0237	0.0004	0.0035	0.00005	23.8	0.40	22.7	0.30
D69	24.983	101.19	6938.52	0.01	0.0495	0.0014	0.0257	0.0006	0.0038	0.00006	25.8	0.60	23.6	0.40
D72	22.028	158.28	5978.43	0.03	0.0467	0.0019	0.0230	0.0008	0.0036	0.00008	23.1	0.80	22.9	0.50
D73	24.527	183.67	6925.88	0.03	0.0483	0.0035	0.0253	0.0016	0.0037	0.00014	25.0	2.00	23.4	0.90
D74	22.998	112.06	6568.21	0.02	0.0487	0.0021	0.0247	0.0009	0.0037	0.00008	24.8	0.90	23.7	0.50
D75	39.981	163.25	9390.52	0.02	0.0461	0.0033	0.0224	0.0016	0.0035	0.00006	22.0	2.0	22.7	0.4
D76	32.405	160.18	9402.87	0.02	0.0461	0.0012	0.0227	0.0005	0.0036	0.00006	22.7	0.50	23.0	0.40
D77	22.37	115.95	5951.50	0.01948	0.04886	0.00192	0.02623	0.00099	0.00369	0.00006	24.5	0.7	22.3	0.4
D78	31.251	547.32	9016.38	0.06	0.0531	0.0041	0.0248	0.0018	0.0034	0.00011	25.0	2.00	21.8	0.70
D82	32.133	178.09	9501.45	0.02	0.0474	0.0014	0.0229	0.0006	0.0035	0.00006	23.0	0.50	22.5	0.4
D83	31.346	149.74	8782.34	0.02	0.0461	0.0013	0.0231	0.0006	0.0036	0.00006	23.2	0.50	23.4	0.40
D84	28.819	137.06	8483.27	0.02	0.0461	0.0013	0.0224	0.0005	0.0035	0.00007	22.5	0.50	22.7	0.4
D85	28.758	202.51	9164.91	0.02	0.0469	0.0015	0.0228	0.0006	0.0035	0.00006	22.8	0.60	22.6	0.4
D86	21.442	237.97	5697.12	0.04	0.0513	0.0015	0.0249	0.0006	0.0035	0.00006	25.0	0.60	22.7	0.4

This chapter has been published as: Shuyun Cao, Franz Neubauer, Junlai Liu, Johann Genser, Bernd Leiss, 2011. Exhumation of the Diancang Shan metamorphic complex along the Ailao Shan-Red River belt, southwestern Yunnan, China: Evidence from $^{40}\text{Ar}/^{39}\text{Ar}$ geochronology. Journal of Asia Earth Science, doi:10.1016/j.jseaes.2011.04.01.

7 Exhumation of the Diancang Shan metamorphic complex along the Ailao Shan-Red River belt, southwestern Yunnan, China: evidence from $^{40}\text{Ar}/^{39}\text{Ar}$ thermochronology

Abstract

Exhumation of the high-grade metamorphic rocks from deep to shallow crustal levels in the Diancang Shan (DCS) massif is evident by the temporal transition from shearing and mylonitization at the amphibolite facies in the lower to middle crust, through retrograde ductile-brittle faulting at greenschist facies in the middle crust and brittle faulting near the surface. New $^{40}\text{Ar}/^{39}\text{Ar}$ ages of amphibole, muscovite, biotite and K-feldspar, mostly from mylonitic rocks, help constrain the thermal evolution of the massif during its exhumation. The thermochronologic studies have shown at least three stages of exhumation and cooling from late Oligocene to Pliocene, e.g., 28–13 Ma, 13–4 Ma and 4–0 Ma, respectively. The initiation of the unroofing history of the DCS massif resulted from ductile left-lateral shearing along the Ailao Shan-Red River shear zone (ASRR) since the late Oligocene. Diachronous onset and subsequent parallel cooling and exhumation characterize the early thermal history of the massif. The first stage of exhumation might have stopped due to the cessation of the left-lateral shearing at ca. 21 Ma, although cooling continued until 13 Ma ago to relatively low-temperature conditions. The second and third stages of cooling started from 13 Ma and lasted until the recent active faulting. The diversity of cooling rates during the second stage from 13 to 4 Ma suggests differences in exhumation rates at various localities. Ductile to brittle shearing along the eastern flank retrograde normal shear zone is the best explanation for the exhumation during this stage. The inhomogeneous cooling and exhumation of the lower plate of the normal fault zone possibly resulted from the tilting of the lower plate or differential exhumation of slabs in the lower plate. During the third stage, cooling and exhumation of the DCS massif since 4 Ma ago is recognized when higher temperature cooling paths are extended and plotted at a lower temperature of about 16°C, the present day average surface temperature. Therefore, the diachronous cooling and exhumation continuously spanned to the surface. The tectonic exhumation of the DCS massif

constitutes a part of the tectono-thermal evolution and diachronous exhumation of the metamorphic complexes in the fan-shaped area bounded broadly in SE Asia by the Red River fault zone and Sagaing fault zone since 36 Ma. Extrusion-induced strike-slip shearing and rotation and associated normal faulting, played important roles in the diachronous cooling and exhumation of the DCS massif and other metamorphic complexes in SE Asia.

7.1 Introduction

The most spectacular tectonic activity in Southeast Asia is widely cited as the consequence of Cenozoic continental collision between the Indian and Eurasian plates since the Eocene. Large-scale strike-slip faults extend well beyond the Himalaya and the Tibetan plateau, deep into the Southeast Asian continent (e.g., Molnar and Tapponnier, 1975; Tapponnier et al., 1982, 1986; Avouac and Tapponnier, 1993; Chung et al., 1997, 1998, 2005; Replumaz et al., 2004) (Fig. 7.1). High-grade metamorphic rocks are exposed within, or immediately adjacent to, the continental strike-slip fault systems in a fan-shaped area, which is bounded by the Ailao Shan-Red River (ASRR) fault zone to the east and the Sagaing fault zone to the west. Well-documented examples include the Bu Khang dome (e.g., Jolivet et al., 1999; Nagy et al., 2008) and the Day Nui Con Voi complex (e.g., Nam et al., 1998; Vuong 2007; Ye et al., 2008) in Vietnam, the Mogok metamorphic complex in Burma (e.g., Searle 2007), the Maoping metamorphic core complex in Thailand (e.g., Macdonald et al., 1993) and the Ailao Shan-Red River (ASRR) metamorphic complex belt in Yunnan, China (e.g., Tapponnier et al., 1990; Wang et al., 2000; Maluski et al., 2001) (Fig. 7.1).

The more than 1000 km NW-trending ASRR fault zone is suggested to be the most pronounced geological discontinuity in Southeast Asia (e.g., Tapponnier and Molnar, 1977; Bureau of Geology and Mineral Resources of Yunan, 1983; Allen et al., 1984; Tapponnier et al., 1986, 1990; Zhong et al., 1990; Leloup et al., 1995; Chung et al., 1997; Wang et al., 1997) (Fig. 7.1B). Four narrow NW–SE oriented high-grade metamorphic massifs, e.g., the Xuelong Shan (XLS), Diancang Shan (DCS), Ailao Shan (ALS) metamorphic complexes in China and the Day Nui Con Voi (DNCV) metamorphic complex in Vietnam, are exposed along the shear zone (Fig. 7.1). In many places, they are bounded by brittle faults in the Mesozoic or Cenozoic basins on both sides. For example, on the eastern and western sides of the ALS massif are the Mesozoic Chuxiong basin and the Lanping-Simao basin, respectively. To the eastern and western sides of the DCS massif, are the Cenozoic Erhai Lake basin and the Lanping Mesozoic basin, respectively (e.g., Bureau of Geology and Mineral Resources of Yunnan, 1983). Research spanning more than twenty years has provided a wealth of information on the geometry of the

ASRR shear zone and its structural, thermal and geomorphologic evolution (e.g., Harrison et al., 1992; Leloup and Kienast, 1993b; Schärer et al., 1990, 1994; Leloup et al., 1995, 2001a, b; Harrison et al., 1996; Chung et al., 1997; Wang et al., 1998a, b, 2000; Zhang and Schärer, 1999; Sun et al., 2003; Burchfiel et al., 2003; Gilley et al., 2003; Schoenbohm et al., 2004; Searle, 2006; Liu et al., 2006, 2007; Yeh et al., 2008; Cao et al., 2010a, b). Limited thermochronological studies conducted on the massifs, including the DCS of the ASRR shear zone, have focused on the tectono-magmatic evolution with the aim of constraining the timing and amount of displacement, the rate of movement along the shear zone, and the exhumation processes of the metamorphic massifs (e.g., Schärer et al., 1990, 1994; Harrison et al., 1992; Leloup and Kienast, 1993b; Zhang and Schärer, 1999; Gilley et al., 2003; Cao et al., 2010a, b).

Most early hypotheses assumed that the exhumation of the high-grade metamorphic complexes in SE Asia are related to the Cenozoic left-lateral strike-slip shearing during the extrusion of the Indochina block (e.g., Tapponnier et al., 1982, 1990; Leloup et al., 2001b). For example, most authors suggested that the ASRR left-lateral strike-slip shearing was a long-lasting event, which started at least ca. 35 Ma ago and lasted until ca. 17 Ma, and was accompanied by the exhumation of the metamorphic rocks along the shear zone (Schärer et al., 1990, 1994; Harrison et al., 1992; Leloup et al., 1993a, 1995; Zhang and Schärer, 1999; Gilley et al., 2003). Searle (2006) redated the metamorphism of the DNCV metamorphic rocks in Vietnam, and interpreted it to be unrelated to shearing along the ASRR shear zone. He then argued that shearing fabrics associated with the left-lateral slip post-dated peak metamorphism at relatively low-temperature conditions. The author, therefore, suggested that the left-lateral shearing along the ASRR shear zone initiated 21 Ma ago, rather than 35 Ma ago, and consequently questioned the role of the shear zone during post-collisional accommodation of shortening in eastern Tibet. The exhumation of the shear zone rocks has been variously explained by the transtension resulting in the opening of the South China Sea (e.g., Biais et al., 1993; Leloup et al., 1995; Harrison et al., 1996; Leloup et al., 2001b; ; Lee and Watkins, 1998; Zhu et al., 2009) and by the contemporaneous regional shortening and transpression (e.g., Wang and Burchfiel, 1997; Schoenbohm et al., 2004), or by both synchronous or non-synchronous transpression and transtension (e.g., Leloup and Kienast, 1993b; Leloup et al., 1995).

Although recent geodynamic models have highlighted the insights into the tectonic evolution and exhumation of deep crustal rocks along the ASRR shear zone under the framework of dynamic evolution of a continent-continent collisional orogen, controversy still exists in regard to the timing and mechanisms of exhumation of the high-grade metamorphic complexes along the ASRR zone. The thermochronologic study of the high-grade rocks is therefore critical in

deciphering the cooling history and processes of exhumation of the metamorphic complexes. Radiometric dating has assumed an increasingly pivotal role in unraveling the complicated tectonic histories of many metamorphic complexes. The $^{40}\text{Ar}/^{39}\text{Ar}$ isotope dating is a widely used, powerful technique to date metamorphism and related deformational events, and has become one of the most commonly used tools for assessing the tectonothermal evolution of orogenic belts. Various minerals (e.g., zircon, amphibole, muscovite, biotite, K-feldspar and apatite) with different closure temperatures are used as thermochronometers to help resolve polyphase deformation, cooling history and exhumation processes. This dating helps reconstruct the cooling path of a given area over temperature ranges from $> 700\text{ }^{\circ}\text{C}$ to ca. $150\text{ }^{\circ}\text{C}$ (e.g., McDougall and Harrison, 1988; Hurford et al., 1989).

In this paper, we present new $^{40}\text{Ar}/^{39}\text{Ar}$ age data of amphibole, muscovite, biotite and K-feldspar collected from granitic and amphibolitic rocks and mica schists from the DCS metamorphic massif. This data, coupled with our previously published U-Pb zircon ages from the pre-, syn- and post-kinematic granites and structural investigations, further constrain the timing of regional deformation as well as the cooling history and exhumation processes of the high-grade metamorphic complex in the DCS. As discussed below, the sequence of tectonic evolution spans from 34 Ma ago to the present, and so records the time through the initial stage of exhumation to the youngest rapid exhumation. We have recognized and considered distinct segments of the cooling paths in three main stages of cooling and exhumation across the metamorphic complex. They are applied to constrain the timing of the three main episodes of tectonic deformation in a framework of regional tectonic extrusion and block rotation.

7.2 Geological setting

The DCS metamorphic complex lies in the northwestern part of the ASRR shear zone (e.g., Wang et al., 1997). It is an elongated metamorphic massif (ca. 20 km wide and 80 km long) and is separated from the ALS massif to the south by the Midu gap (Leloup et al., 1995) which is an approximately 80 km long segment of brittlely deformed, essentially unmetamorphic Mesozoic sedimentary rocks (Fig. 7.1, Fig. 7.2A and C).

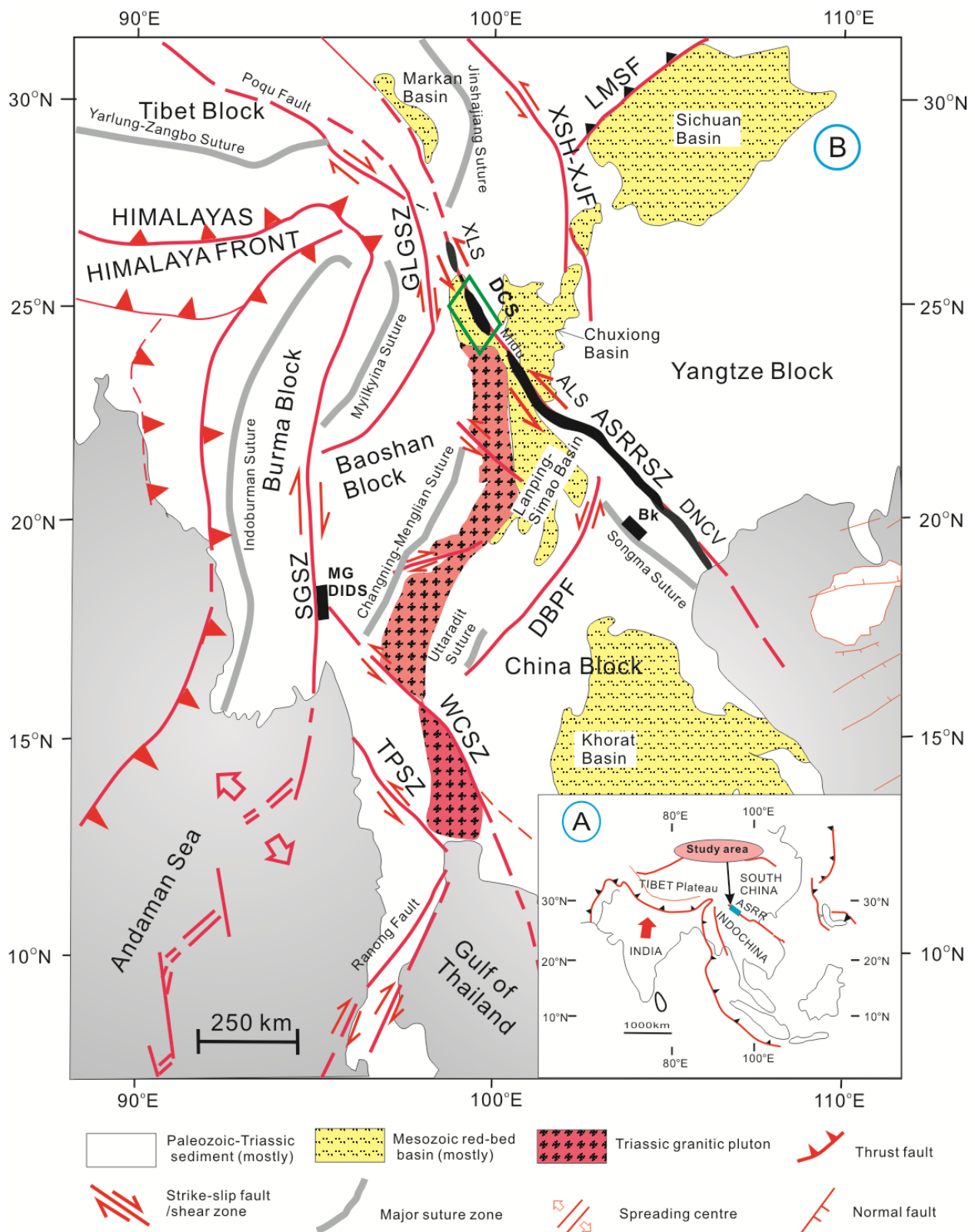


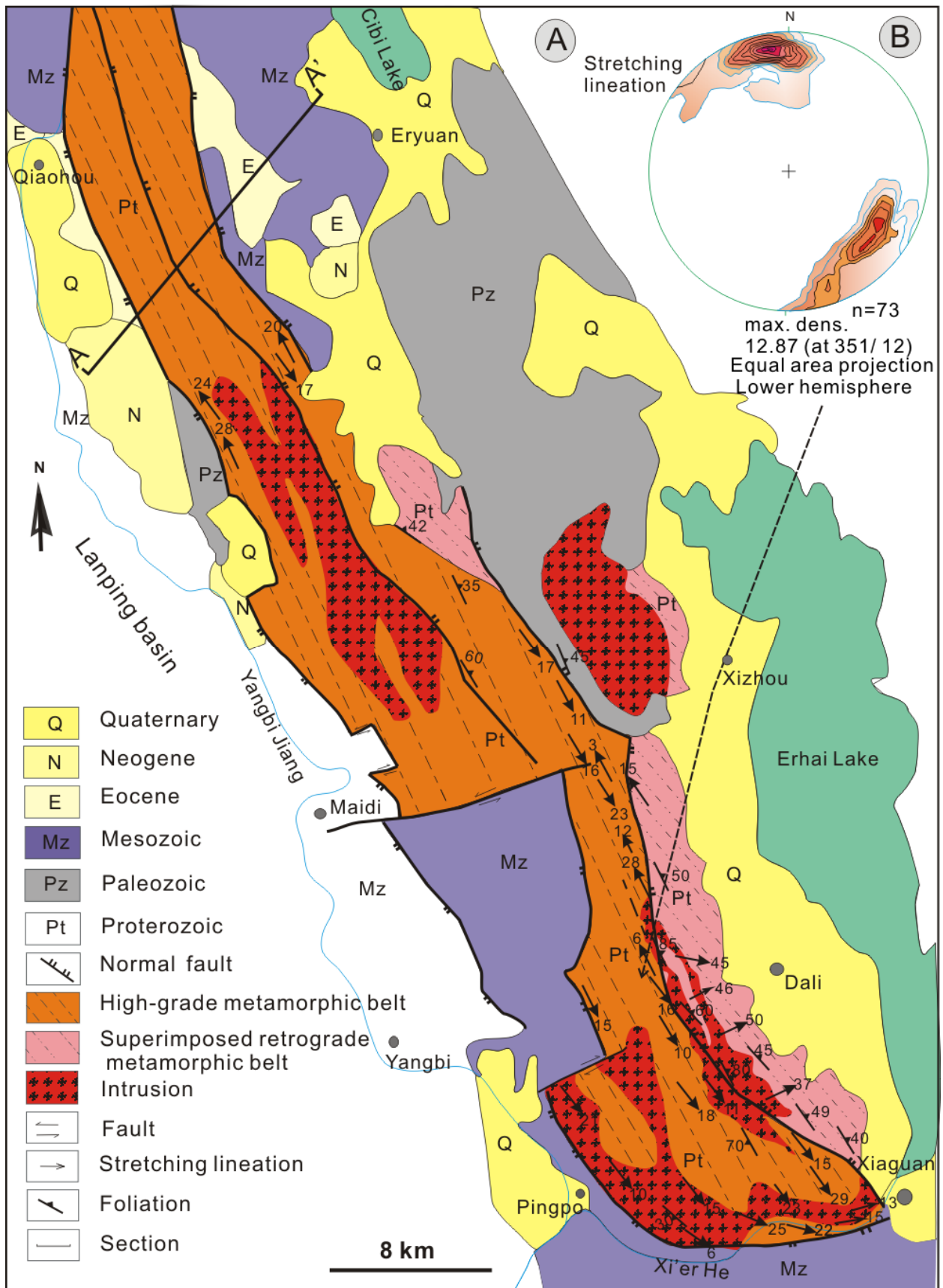
Fig. 7.1 Tectonic sketch map of Southeast Asia (modified after Tapponnier et al.,1986, Morley, 2000). A) Geological sketch of the extrusion of Indochina in response to northward penetration by India. B) Major sutures and shear zones/faults in Southeast Asia. GLGSZ = Gaoligong shear zone; SGSZ = Sagaing shear zone; TPSZ = Three Pagoda shear zone; WCSZ = Wang Chao shear zone; LMSF= Longmen Shan Fault;

XSH-XJF = Xianshuihe-Xiaojiang Faults; DBPF = Dien Bien Phu Fault; ASRRSZ = Ailao Shan-Red River shear zone; XLS = Xuelong Shan; DCS = Diancang Shan; ALS = Ailao Shan; DNCV = Day Nui Con Voi; BK=Bu Khang complex; MG=Mogok gneiss dome; DIDS= Doi-Inthanon-Doi-Suthep metamorphic complex

7.2.1 Deformation structures and microfabrics in sheared high-grade metamorphic rocks

The core of the DCS metamorphic complex is characterized by widespread exposures of Neoproterozoic amphibolites, schists, gneisses, marbles and granitic intrusions of various ages. The metamorphic rocks typically have high-temperature mineral assemblages up to amphibolite facies which contain sillimanite, garnet, staurolite and kyanite in metapelitic rocks, amphibole, plagioclase (+/- garnet) in metamafic volcanics, tremolite, diopside, olivine, calcite and dolomite in metacarbonates, two feldspars, quartz and micas in metamorphosed granitoids. Structures consistent with intense ductile to brittle shearing are widely distributed in the metamorphic unit across the mountain belt. Left-lateral shearing is characterized by strong mylonitization (Fig. 7.3a–d) generating sub-vertical foliations, subhorizontal stretching lineations (Fig. 7.3a and b), isoclinal A-type folds and sheath folds (Fig. 7.3c). In most areas of the metamorphic massif, stretching lineation predominates foliation in the fabric components of the high-temperature mylonites. The weakly developed mylonitic foliation, striking NW320° to SE140°, dips steeply westward and eastward along the western and central eastern flanks of the massif, respectively. In the central part of the DCS massif, however, the mylonitic foliation becomes obviously steep. On a Flinn diagram, the high-temperature mylonites plot near the prolate strain field (e.g., Liu et al., 2007). Mesoscopic structures and fabrics include shear bands (Fig. 7.3b and e), asymmetric folds, boudinage fabric in felsic veins, S-C fabrics in biotite-plagioclase gneiss (Fig. 7.3e), sillimanite-garnet-hornblende- plagioclase gneiss (Fig. 3f) and syn-kinematic porphyritic monzogranite. The asymmetric strain fringes of feldspar and amphibole porphyroclasts (e.g., sigmoidal and delta fabrics) consistently indicate a left-lateral shear sense in the high-grade massif.

In the sheared granitic rocks, feldspar grains are elongated, partially twinned or dynamically recrystallized, forming the foliation S in the S-C fabrics of the mylonites. The feldspar porphyroclastic cores show undulatory and inhomogeneous extinction and have core-mantle structures and subgrains (Fig. 7.3g). The deformation of K-feldspar was associated with metasomatism by relatively Na-rich plagioclase to form myrmekite structures, suggesting plastic deformation at feldspar recrystallization temperatures above 550°C (e.g., Vernon, 1991; Menegon et al., 2006). Most feldspar recrystallization was dominated by subgrain rotation. The recrystallization-accommodated dislocation creep in feldspar is generally completed at



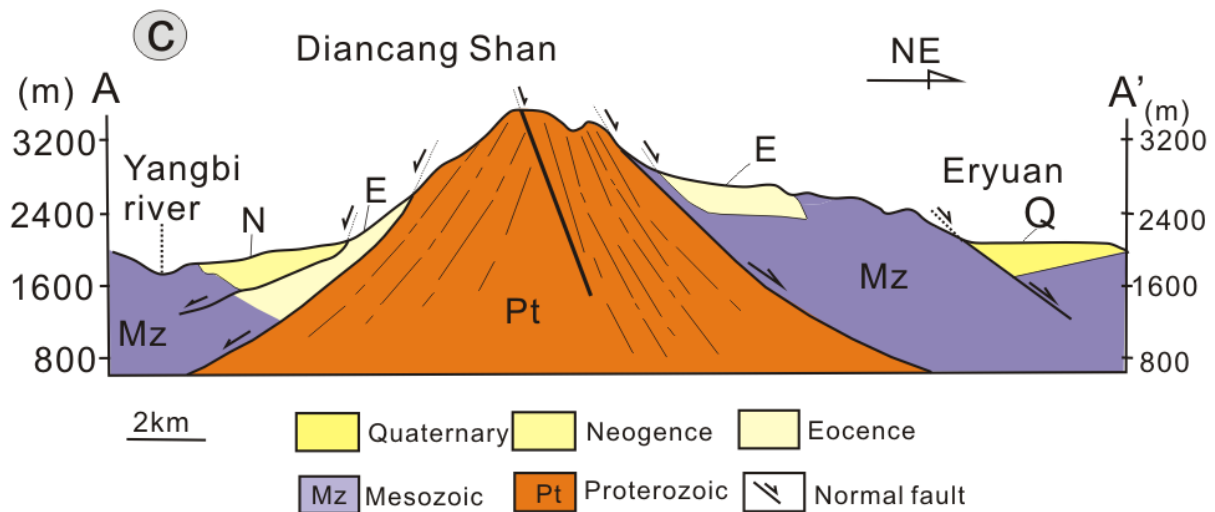


Fig. 7.2 Structural outline of the Diancang Shan metamorphic complex. A) Geological map of the Diancang Shan area (modified from Yunnan Bureau of Geology and Mineral Resources, 1994). B) Projection of stretching lineation from the central part of high-grade mylonites. C) Geological section across the Diancang Shan massif.

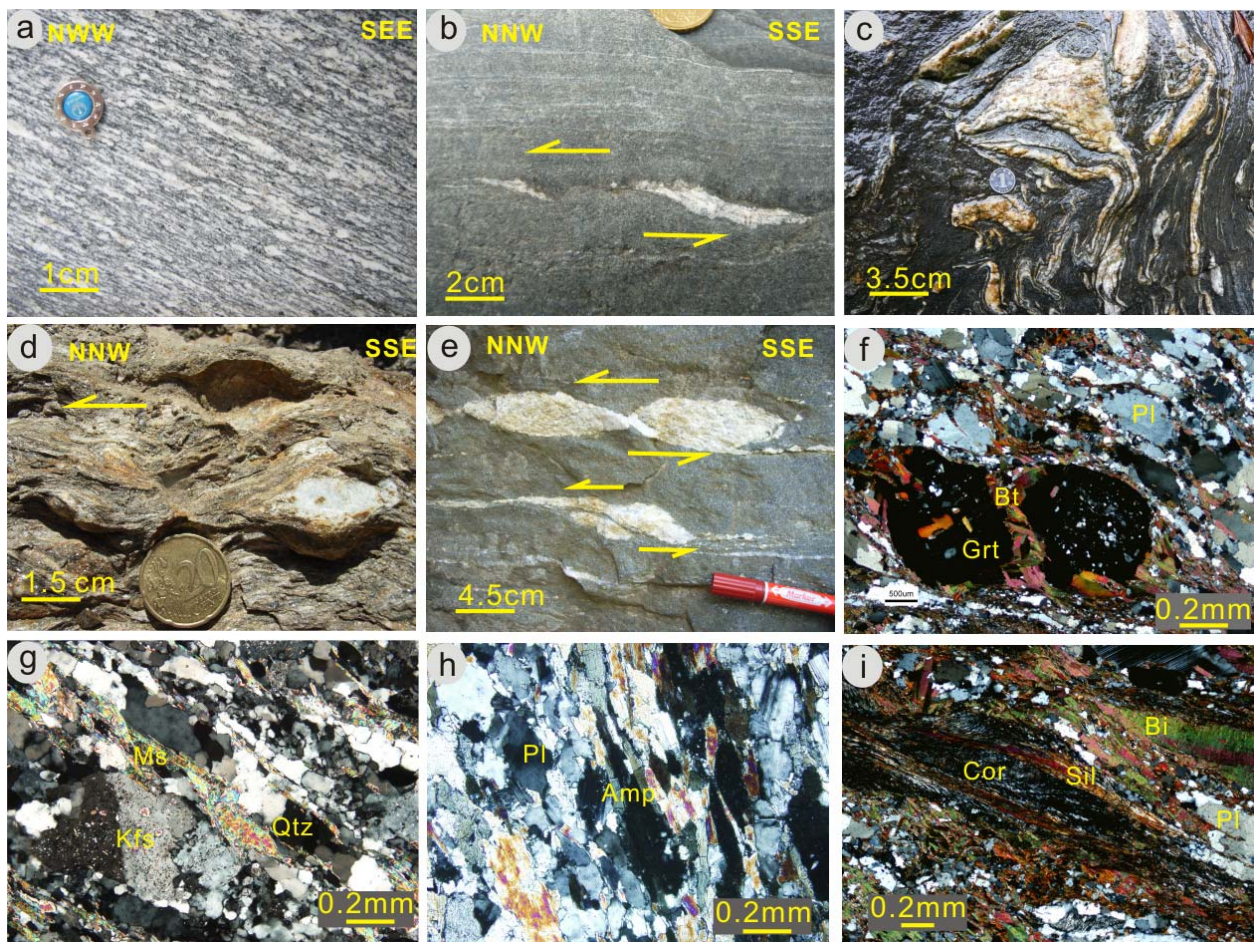


Fig. 7.3 Meso- and micro-structures of high-grade metamorphic rocks from the central part of the Diancang Shan metamorphic complex. a) highly deformed granite mylonite with a NNW trending stretching lineation; b)

mylonitic amphibolites with sheared felsic sigmoidal fabrics and left-lateral shear criteria; c) sheath fold with axes parallel to the NNW-SSE subhorizontal stretching lineation in the metamorphosed paragneisses; d) granitic mylonite with k-feldspar porphyroclasts; e) mylonitic amphibolites with sheared felsic dykes. The sheared felsic dykes exhibit boudinage, S-C and sigmoid fabrics and left lateral shear criteria; f) rotated garnet porphyroblasts in the paragneiss; g) core-mantle texture defined by K-feldspar cores surrounded by small subgrains and dynamically recrystallized new grains around their margins, quartz ribbons and muscovite in the granite mylonite; h) strongly deformed amphibole and plagioclase grains occur as extremely fine grains in ultramylonite. i) sillimanite, cordierite, biotite and plagioclase in the sheared paragneiss.

moderately high-temperature recrystallization, or within middle to upper amphibolite facies conditions (e.g., Tullis, 1983; Tullis and Yund, 1987; Mandal et al., 1997). The compositions of coexisting recrystallized plagioclase and K-feldspar give at least a general indication of high-temperature recrystallization (e.g., Vernon, 2000). Most quartz grains have typical polygonal grain shapes in aggregates and are parallel to the major foliation and stretching lineation of the rocks. Some quartz ribbons occur along a pervasive planar fabric. They are generally polycrystalline and the individual crystals do not show any intracrystalline strain under the optical microscope (Fig. 7.3g). The quartz ribbons and their serrated grain boundaries also suggest high-temperature deformation conditions (e.g., McLelland, 1984; Passchier and Trouw, 2005). The amphibole grains from amphibolite mylonites and ultramylonites in the DCS massif show distinct plastic deformation characteristics under amphibolite facies conditions (e.g., Cao et al., 2010a). Amphibole grains are intensely deformed with obvious grain size reduction (Fig. 7.3h). The oriented amphibole grains form the cores of the sigma or delta fabrics. Grains in other orientations constitute the tails of the fabrics, or S and C in high-temperature S-C fabrics, respectively. In addition, sillimanite and garnet porphyroblasts formed under amphibolite facies are commonly sheared during left-lateral shearing (Fig. 7.3f and i).

7.2.2 Low-grade retrograde zone

A tectonic zone along the eastern margin of the high-grade massif is composed of rocks which were sheared during retrograde metamorphism at lower greenschist facies. The retrograde zone overprinting the high-temperature metamorphic belt is more than 1500 m thick, and is truncated by a normal fault along the eastern edge of the DCS mountain range (Fig. 7.2A). The chloritic mylonites constitute the major part of the retrograde mylonite zone (Fig. 7.4a–c). They were formed at greenschist facies conditions and contain green biotite, chlorite, sericite, albite and quartz. Some granitic plutons were sheared into L-S fabrics with equal development of foliation and stretching lineation (Fig. 7.4c). The foliation is marked by the preferred orientation of planar

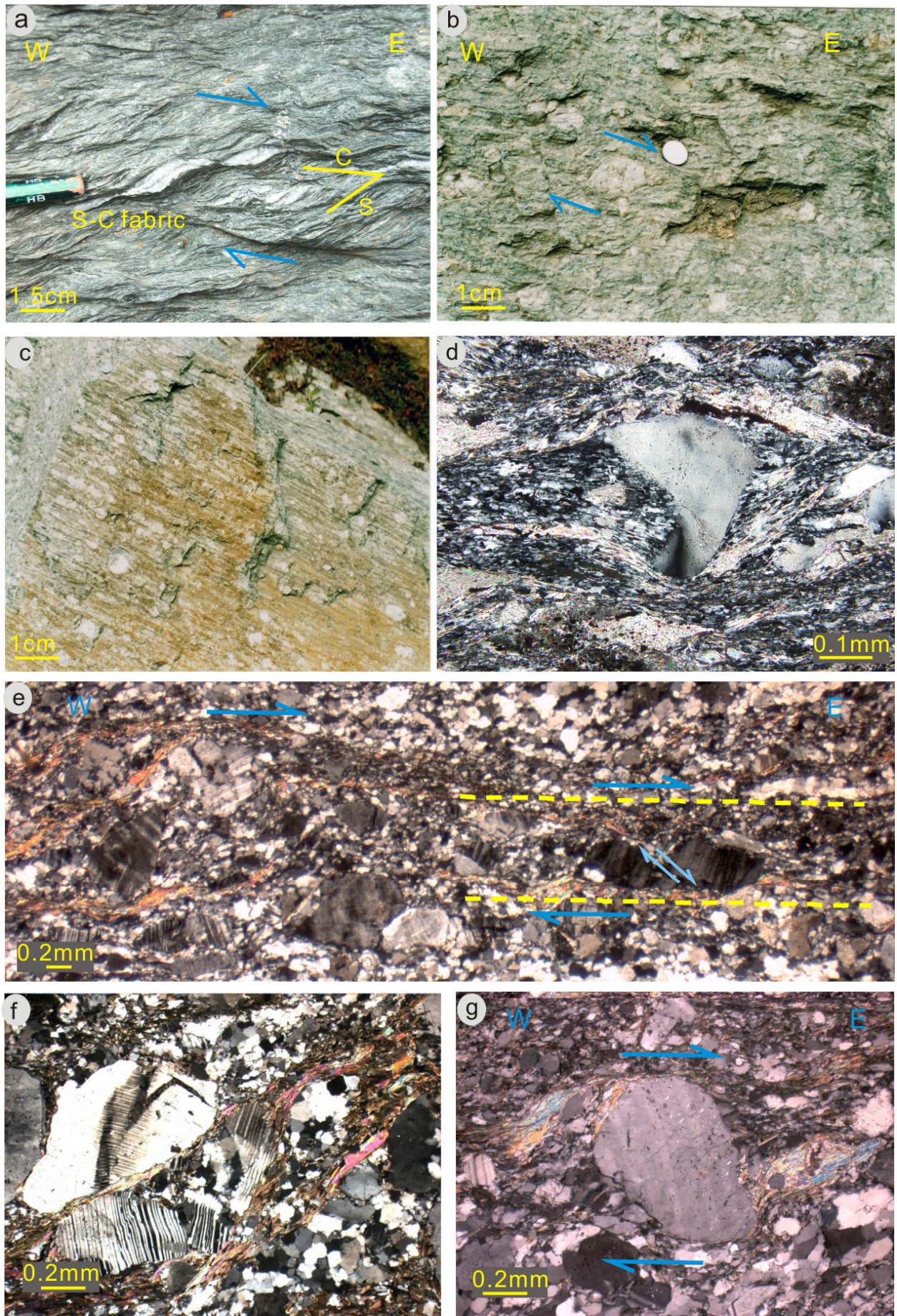


Fig. 7.4 Meso- and micro-structures from the retrograde metamorphic belt along the eastern flank of the Diancang Shan metamorphic complex. a) S-C fabrics in the chloritic mylonitic schists; b) chloritic mylonites with plagioclase porphyroclasts; c) granitic mylonites with equally developed foliation and lineation (L-S fabric); d) deformed quartz porphyroclase and sericite ; e) recrystallized and brittly deformed plagioclase aggregates in granite. Bookshelf fabrics, c-foliation planes and the stretching lineations with the shear sense of top-to-the-east or southeast directed movement; f) broken twinned plagioclase porphyroclasts in S-C fabrics; g) delta fabrics formed by rotation of rigid and deformed plagioclase grains with muscovite and sericite grains in the tails in the rigid plagioclase porphyroclasts.

minerals (e.g., chlorite and green biotite) and by flattened quartz. The foliation strikes NNW–SSE or N–S and dips to the E or SSE at a low angle. Striae, mostly defined by the growth of fibrous chlorite grains, are widely distributed at the easternmost, marginal part of this zone. Some weak stretching lineations show high dip angles of up to 70–90°. In the Flinn diagram, the mylonites plot, different from the high-temperature mylonites, near the plane strain area (Liu et al., 2007). S–C fabrics are formed with S-planes defined by grain aggregates of elongated quartz and fractured plagioclase and C-planes by chlorite and biotite grains. Shear sense indicators, e.g. S-C and bookshelf fabrics, show typical top-to-the-east or southeast shearing.

Under the microscope, quartz grains in all rock types within this zone show characteristics of dynamic recrystallization by subgrain rotation. Bulging recrystallization, however, dominates within the chlorite zone (Fig. 7.4d). Twinned feldspar grains are deformed mainly by fracturing forming domino/bookshelf microstructural patterns (Fig. 7.4e–f). In mylonitic granite, sigma or delta fabrics are developed with porphyroclastic feldspar grains forming the cores. Quartz and mica or chlorite grains constitute the tails (Fig. 7.4g). Coexistence of recrystallized polygonal quartz grains and irregular plagioclase grains induced by both recrystallization and brittle deformation, as well as local ultracataclasites, indicate deformation at the ductile-brittle transition along the eastern retrograde zone.

7.2.3 Cenozoic brittle faults, fault-bounded basin and sediments

Cenozoic active normal faults and basins bind the high-grade metamorphic complex on both sides of the DCS mountain range. To the eastern flank of the DCS Mountain, a half-graben related to active normal faults leads to the low relief forming the Erhai Lake basin in which a sequence of more than 800 m thick Pliocene to Holocene sedimentary package was deposited (Fig. 7.2A). To the northeast of the lake, the Eocene to Neogene sediments are exposed close to the Cibi Lake and Eryuan (Fig. 7.2A and C; Fan et al., 2006). To the northwest and west of the DCS massif, normal faults extend along the Heihuijiang River. The Eocene to the Neogene

sediments, resting unconformably on the Mesozoic sequence constitute the majority of the young terrace deposits in the Qiaohou Basin to the west of the DCS massif. The Eocene and the Neogene sediments dip towards the DCS massif, which argues for a rollover-type structure. These sedimentary features indicate that the Qiaohou Basin also formed as a half-graben (e.g., Wang et al., 1997; Fan et al., 2006). The development of the basin is probably coeval with the exhumation of the DCS massif.

Triangular shaped facets due to normal faulting, interpreted as fault scarps, are widespread along both the western and eastern flanks of the DCS range. They are especially obvious along the eastern flank of the DCS, at different elevations from about 1800 m to the peak (at ca. 4000 m) of the mountain range. The active faults along the eastern flank dip eastward at high angles (about 50–60°). The western to southwestern slopes are also westerly dipping normal faults, with dip angles of about 30–40°. The southeastern portion of the DCS is a horst bounded by two parallel normal faults, which are continuously exposed at a SSE-dipping surface. Triassic and Jurassic metasedimentary rocks occur west and southwest of the high-grade massif, grading from very-low grade metamorphic Triassic metasedimentary rocks to Cretaceous sedimentary rocks in the Lanping basin.

7.3. Analytical techniques and sample descriptions

7.3.1 Analytical techniques

$^{40}\text{Ar}/^{39}\text{Ar}$ analytical techniques largely follow descriptions given in Handler et al. (2004) and Rieser et al. (2006). Preparation of the samples before and after irradiation, $^{40}\text{Ar}/^{39}\text{Ar}$ analyses, and age calculations were carried out at the ARGONAUT Laboratory of the Institute for Geology and Palaeontology at the University of Salzburg. The mineral separates were obtained by crushing hand-sized samples and sieving through 200–355 μm fractions. They were further purified by washing with deionized water. Mineral concentrates were packed in aluminium-foil and placed in quartz vials. For calculation of the J-values, flux-monitors were placed between each 4–5 unknown samples. The sealed quartz vials were irradiated in the MTA KFKI reactor (Budapest, Hungary) for 16 hours. Correction factors for interfering isotopes were calculated from 10 analyses of two Ca-glass samples and 22 analyses of two pure K-glass samples, and are: $^{36}\text{Ar}/^{37}\text{Ar}_{(\text{Ca})} = 0.00022500$, $^{39}\text{Ar}/^{37}\text{Ar}_{(\text{Ca})} = 0.00061400$ and $^{40}\text{Ar}/^{39}\text{Ar}_{(\text{K})} = 0.026600$. Variation in the flux of neutrons was monitored with the DRA1 sanidine standard for which a $^{40}\text{Ar}/^{39}\text{Ar}$ plateau age of 25.03 ± 0.05 Ma was originally reported (Wijbrans et al., 1995). Here we use the

revised value of 25.26 ± 0.05 Ma (Van Hinsbergen et al., 2008). $^{40}\text{Ar}/^{39}\text{Ar}$ analyses were carried out using a UHV Ar-extraction line equipped with a combined MERCHANTEKTM UV/IR laser system, and a VG-ISOTECHTM NG3600 mass spectrometer.

Stepwise heating analyses of samples were performed using a defocused (~1.5 mm diameter) 25 W CO₂-IR laser operating in Tem₀₀ mode at wavelengths between 10.57 and 10.63 μm. Gas admittance and pumping of the mass spectrometer and the Ar-extraction line are computer controlled using pneumatic valves. The NG3600 is an 18 cm radius 60° extended geometry instrument, equipped with a bright Nier-type source operated at 4.5 kV. Measurements are performed on an axial electron multiplier in static mode, peak-jumping and stability of the magnet is controlled by a Hall-probe. For each increment the intensities of ^{36}Ar , ^{37}Ar , ^{38}Ar , ^{39}Ar and ^{40}Ar are measured, the baseline readings on mass 34.5 are automatically subtracted. Intensities of the peaks are back-extrapolated over 16 measured intensities to the time of gas admittance either by a straight line or a curved fit, depending on intensity and type of pattern of the evolving gas. Intensities are corrected for system blanks, background, post-irradiation decay of ^{37}Ar , and interfering isotopes. Isotopic ratios, ages and errors for individual steps are calculated following suggestions by McDougall and Harrison (1999) and Scaillet (2000) using decay factors reported by Steiger and Jäger (1977). Definition and calculation of plateau ages were carried out using ISOPLOT/EX (Ludwig, 2001).

7.3.2 *Sample descriptions*

Samples were collected mainly from two sections, i.e., the SS' section along the southern end of the massif and NN' section across the high-grade metamorphic rocks in the middle of the DCS complex (Fig. 7.5). All dated samples were examined in thin sections to exclude grains with possible inclusions in dated minerals, alteration along the grain boundaries and secondary thermal and/or tectonic overprint. The relationships between various dated minerals were carefully analyzed. In this section, we describe critical microscopic observations on samples with scattered age plots (see next section) using the above-mentioned criteria. The observations of each sample are described separately from east to west in each section.

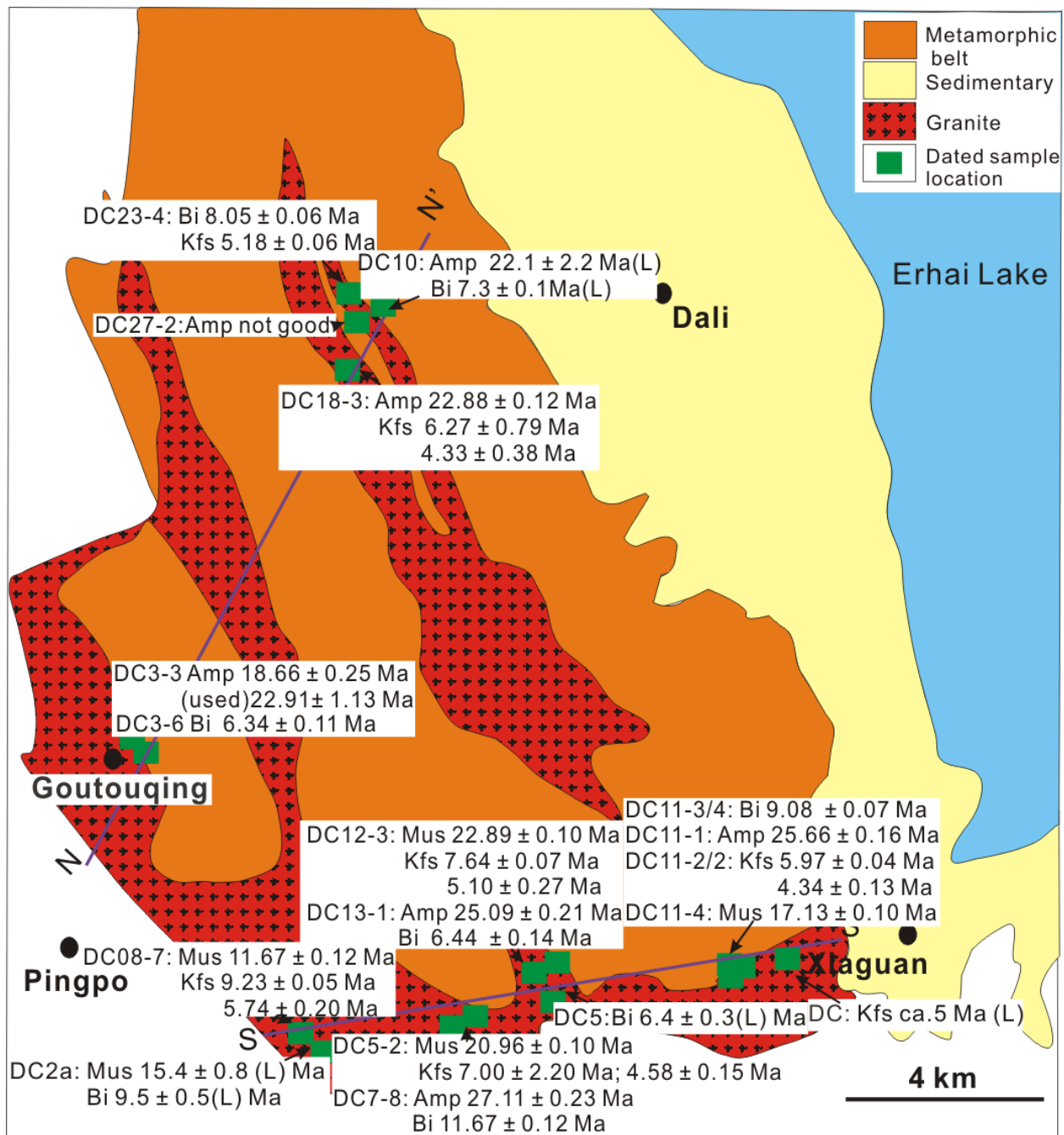


Fig. 7.5 Sample locations and Ar-Ar ages of this study and of Leloup et al., 1993 in the Diancang Shan metamorphic complex (L= Leloup et al., 1993).

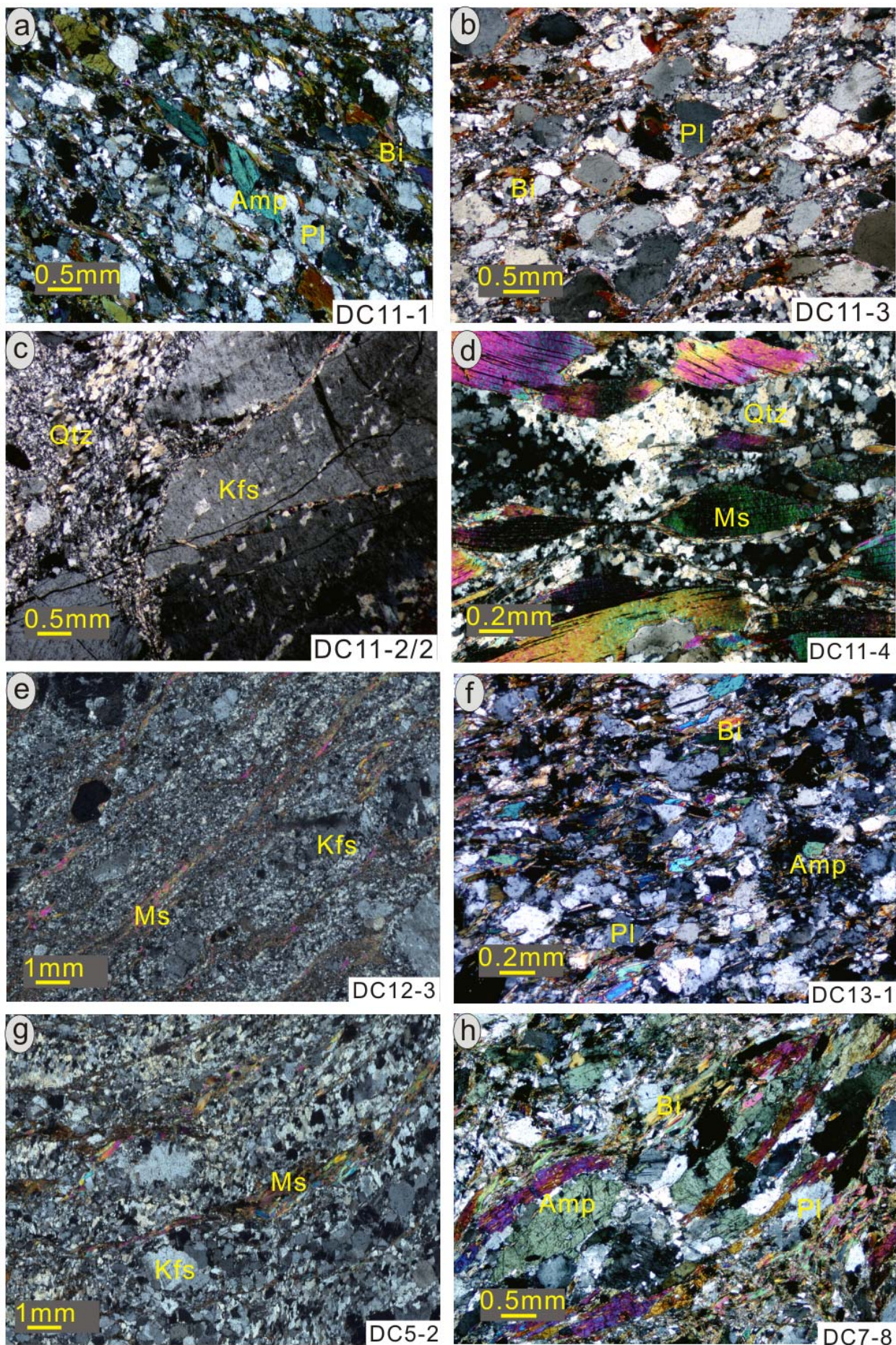
Samples from the SS' section

Samples DC11-1 (amphibolite) (Fig. 7.6a), DC11-3/4 (granodiorite) (Fig. 7.6b), DC11-2/2 (coarse-grained granitic pegmatite) (Fig. 7.6c) and DC11-4 (fine-grained muscovite leucogranite) (Fig. 7.6d) are collected from the south of Xiaguan (latitude and longitude: $25^{\circ}34'25.6''$, $100^{\circ}10'18.9''$). Sample DC11-1 is from an amphibolite boudinage. Elongated coarse amphibole, laminated biotite, lens-shaped plagioclase and quartz aggregates constitute the mylonitic foliation and the stretching lineation. Asymmetric tails of elongated amphibole grains show σ -

fabrics indicating left-lateral shear. Subgrains or recrystallized amphibole grains were not observed. Concentrates of amphibole minerals were separated from the sample. Sample DC11-3/4 is a coarse-grained mylonitic granodiorite and consists mainly of plagioclase, biotite and quartz. The mylonitic fabric is delineated by quartz aggregates and fine-grained mica surrounding feldspar porphyroclasts. Concentrates of biotite minerals were separated from the sample. Sample DC11-2/2 is a granitic pegmatite, containing K-feldspar, plagioclase and quartz. The pegmatite dyke cuts across the high-temperature mylonitic foliation. Macroscopically, the pegmatite is weakly deformed or nearly undeformed. Under the microscope, the feldspar grains often show microcracks, some of which are filled with fine-grained quartz. Quartz grains exhibit equant to slightly elliptical grains with undulose extinction indicating weak plastic deformation. Concentrates of K-feldspar minerals were separated from the sample. Sample DC11-4 is a deformed fine-grained muscovite leucogranite with an assemblage of feldspar, muscovite and biotite. It intruded the highly deformed amphibolite. There is a pronounced stretching lineation in the rock. Coarse muscovite grains present S-C fabrics or fish-shaped fabrics consistent with left-lateral shearing. Concentrates of muscovite porphyroclastic minerals were separated from the sample.

Samples DC12-3 (Fig. 7.6e) and DC13-1 (Fig. 7.6f) were collected from the Dapoqing at the southern end of the DCS massif (latitude and longitude: 25°34'19.7", 100°08'33.4"). Sample DC12-3 is a two-mica granitic mylonite with the mineral assemblages of K-feldspar, plagioclase, biotite, muscovite and quartz. A remarkable feature of the mylonites is their well-developed stretching lineation fabrics and an equally developed foliation defined by the feldspar, biotite and muscovite aggregates. The microstructures of the granitic mylonite reveal mostly high-temperature solid-state deformation features. The feldspar grains are characterized by plastic crystal deformation and strong dynamic recrystallization in the high strain zone. There are asymmetric tails of fine-grained quartz-feldspar grain aggregates around K-feldspar porphyroclasts. Muscovite grains are aligned in the shear planes. Concentrates of muscovite and K-feldspar minerals were separated from the sample. Sample DC13-1 is a garnet-hornblende biotite gneiss, which consist mainly of elongated amphibole grains, laminated biotite grains and lens-shaped plagioclase. The amphiboles are 100–200 μm in size and show a shape-preferred orientation. Concentrates of amphibole and biotite minerals were separated from the sample.

Samples DC5-2 (Fig. 7.6g) and DC7-8 (Fig. 7.6h) were collected from the southern end of the DCS massif (latitude and longitude: 25°33'50.4", 100°07'55.6"). Sample DC5-2 is a coarse- to medium-grained monzogranite, with mineral assemblages of K-feldspar, plagioclase, muscovite, biotite and quartz. The feldspar porphyroclasts show asymmetric fabrics in a very fine-grained



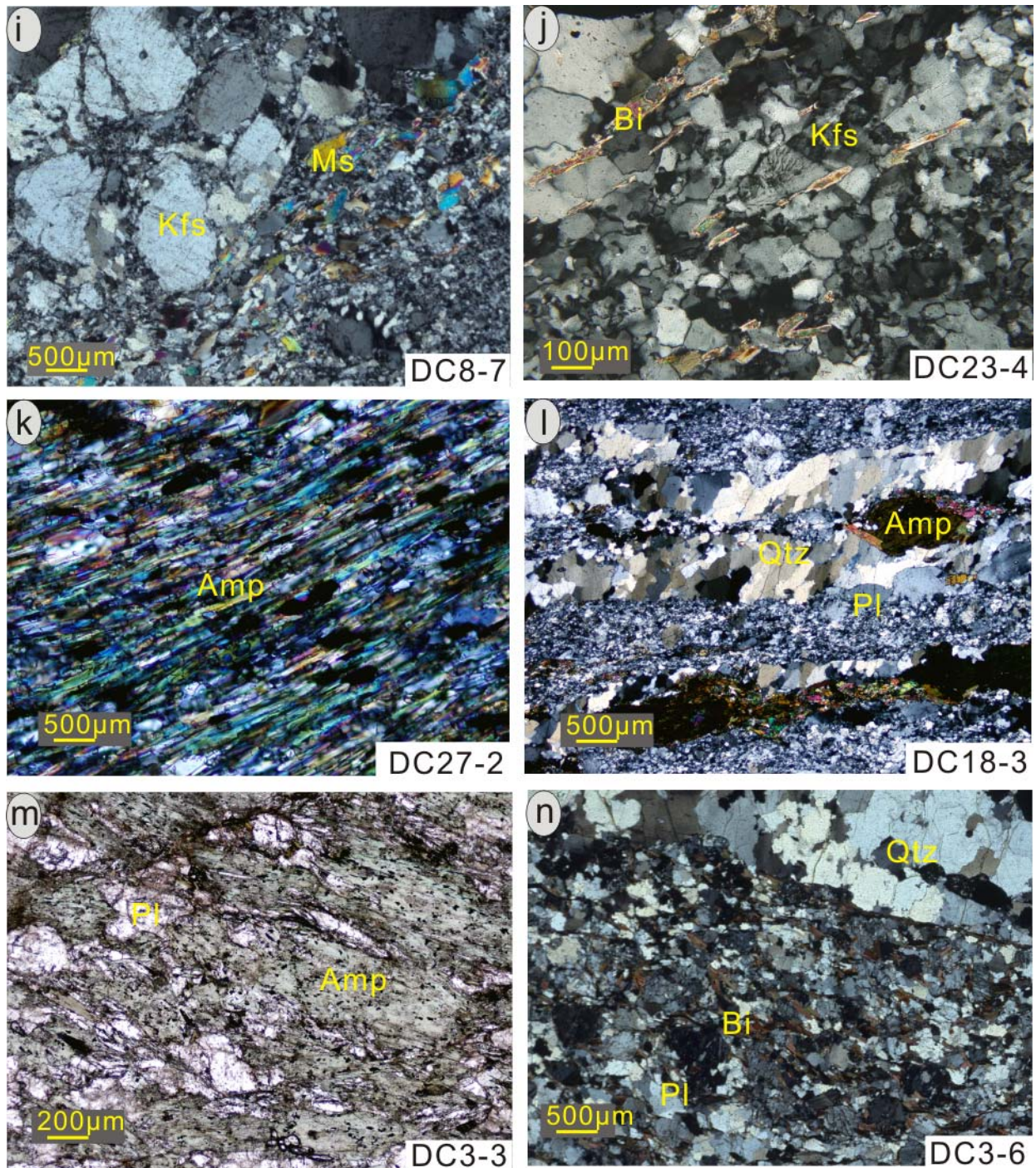


Fig. 7.6 Microstructures of the dated samples from the Diancang Shan metamorphic complex. a) Oriented amphibole, biotite and plagioclase in the amphibolite (sample DC11-1); b) deformed plagioclase surrounded by the fine-grained quartz and biotite in the granite gneiss (sample DC11-3/4); c) weakly deformed coarse-grained granitic pegmatite with quartz aggregates and coarse brittle-deformed K-feldspar and plagioclase (sample DC11-2-2); d) coarse fish-shaped muscovite grains with S-C fabrics in the white-mica leucogranite (sample DC11-4a); e) intense dynamic recrystallization of feldspar and oriented fine-grained muscovite in the two-mica granite mylonite (sample DC12-3); f) amphibole, biotite and plagioclase grains in the amphibole-biotite gneiss (sample DC13-1); g) recrystallized muscovite and feldspar porphyroclasts surrounded by the very fine-grained matrix in the two-mica porphyritic monzogranite (sample DC-5-2); h) strongly oriented and

elongated amphibole and mica grains in the amphibole-biotite gneiss (sample DC7-8); i) oriented coarse muscovite and fractured feldspar grains in the mica-pegmatite (sample DC8-7); j) complete recrystallization of feldspar in the porphyroclastic monzogranite mylonite (sample DC23-4); k) strongly shape preferred orientations of fine-grained amphibole in the ultramylonitic amphibolite (sample DC27-2); l) dynamic recrystallization of feldspar, quartz aggregates and amphibole porphyroclasts in the amphibole-bearing granitic mylonites (sample DC18-3); m) weakly deformed coarse-grained amphibole in the amphibolite (sample DC3-3), Note the dark inclusions and uneven extinction; n) strongly recrystallized feldspar, quartz ribbon aggregates and fine-grained biotite in the biotite schist (sample DC3-6).

matrix. Concentrates of muscovite and K-feldspar minerals were separated from the sample. Sample DC7-8 was collected from a mica-amphibolite layer ca. 200 m west to the porphyritic monzogranite (sample DC5-2). It consists mainly of plagioclase and biotite. Elongated micas and amphiboles exhibit a preferred orientation. The elongated augen-shaped, sigma- and delta-type porphyroclasts of amphibole indicate the shear sense. Subgrains or recrystallized grains of amphibole are not observed. Concentrates of amphibole and biotite minerals were separated from the sample.

Sample DC8-7 (Fig. 7.6i) is a muscovite pegmatite from the southwestern end of the DCS massif (latitude and longitude: 25° 34' 28.9", 100° 05' 02.9"). The pegmatite contains coarse feldspar, quartz and muscovite. The pegmatite dyke transects the high-temperature mylonitic foliation at a high angle. The feldspars are slightly recrystallized and show microcrack fabrics. Intragranular fractures within the grains are randomly oriented and some cracks are filled with fine-grained quartz. Concentrates of muscovite and K-feldspar minerals were separated from the sample.

Samples from the NN' section

Samples DC23-4 (Fig. 6j) and DC27-2 (Fig. 7.6k) were collected from the NN' part of the high-grade metamorphic rocks in DCS (25°42'03.1", 100°06'10.8"). Sample DC23-4 is a synkinematic porphyroclastic monzogranite, which mainly contains K-feldspar, plagioclase, quartz and biotite. It is a tabular and elongated body with concordant relationships to the wall rocks. The rocks have a medium- to fine-grained inequigranular fabric and show synkinematic magmatic deformation structures. The feldspar grains form augen-shaped, sigma- and delta-type porphyroclasts, which indicate a northwest sense of shear. Concentrates of biotite and K-feldspar minerals were separated from the sample. Sample DC27-2 is an ultramylonitic amphibolite. Amphibole, plagioclase and biotite grains occur as extremely fine grains. Quartz grains form ribbons with a thickness of 160–200 µm. The rocks are homogeneous in microstructures and grain size distribution throughout the sample and minerals have a strong shape preferred

orientation, forming the L-fabrics of the mylonites. Amphiboles of 50–150 μm in size show a shape preferred orientation. They, together with biotite and feldspar, define the stretching lineation and foliation. The occurrence of chlorite along the rims of amphibole and biotite grains indicates the retrograde metamorphism in a later event. Concentrates of amphibole minerals were separated from the sample.

Sample DC18-3 (Fig. 7.6l) is a mylonitized granodiorite from the central-eastern part of the DCS massif (latitude and longitude: 25°41'03.5", 100°06'05.00"). The granodiorite mainly contains K-feldspar, plagioclase, quartz, amphibole and biotite. The feldspar grains are characterized by plastic crystal deformation and strong dynamic recrystallization. Most quartz grains form polygonal aggregates that are parallel to the major foliation and lineation. Serrated grain boundaries are common. Some quartz grains show evidence of overprinted low-temperature deformation. Biotite occurs as a secondary phase forming rims or tails of amphibole grains. Concentrates of amphibole and K-feldspar minerals were separated from the sample.

Samples DC3-3 (Fig. 7.6j and m) and DC3-6 (Fig. 7.6n) were collected from the central-western part of the DCS massif (latitude and longitude: 25°36'01.4", 100°04'14.3"). Sample DC3-3 is a coarse-grained amphibolite mainly composed of amphibole and plagioclase. The amphibole has a preferred dimensional orientation parallel to the stretching lineation. Subgrains or newly recrystallized grains are not observed. Concentrates of amphibole minerals were separated from the sample. Sample DC3-6 is coarse-grained amphibole-biotite schist. The sample consists mainly of plagioclase, amphibole, biotite and quartz. Amphibole and biotite grains are well oriented, defining the lineation. Concentrates of biotite minerals were separated from the sample.

7.4. Results

$^{40}\text{Ar}/^{39}\text{Ar}$ mineral dating was performed on 21 mineral concentrates from the above-mentioned samples. The appropriate samples were selected according to their mineral composition in order to cover minerals with different Ar closure temperatures, which include amphibole at ca. 500–550 °C (Harrison, 1981), white mica at ca. 425 °C (Harrison et al., 2009) and biotite at ca. 275–300 °C (Harrison et al., 1985). Because the K-feldspar has a range of closure temperatures between ca. 160 and 250 °C or 200 to 250 °C (e.g., Lovera et al., 1989), we here use a closure temperature of 250 °C for plateau respected or mean ages and 160 °C for switched low-laser energy steps. $^{40}\text{Ar}/^{39}\text{Ar}$ age spectra for amphibole, muscovite, biotite and K-feldspar from the DCS massif are presented in Figures 7, 8, 9 and 10. The complete results of step-heating

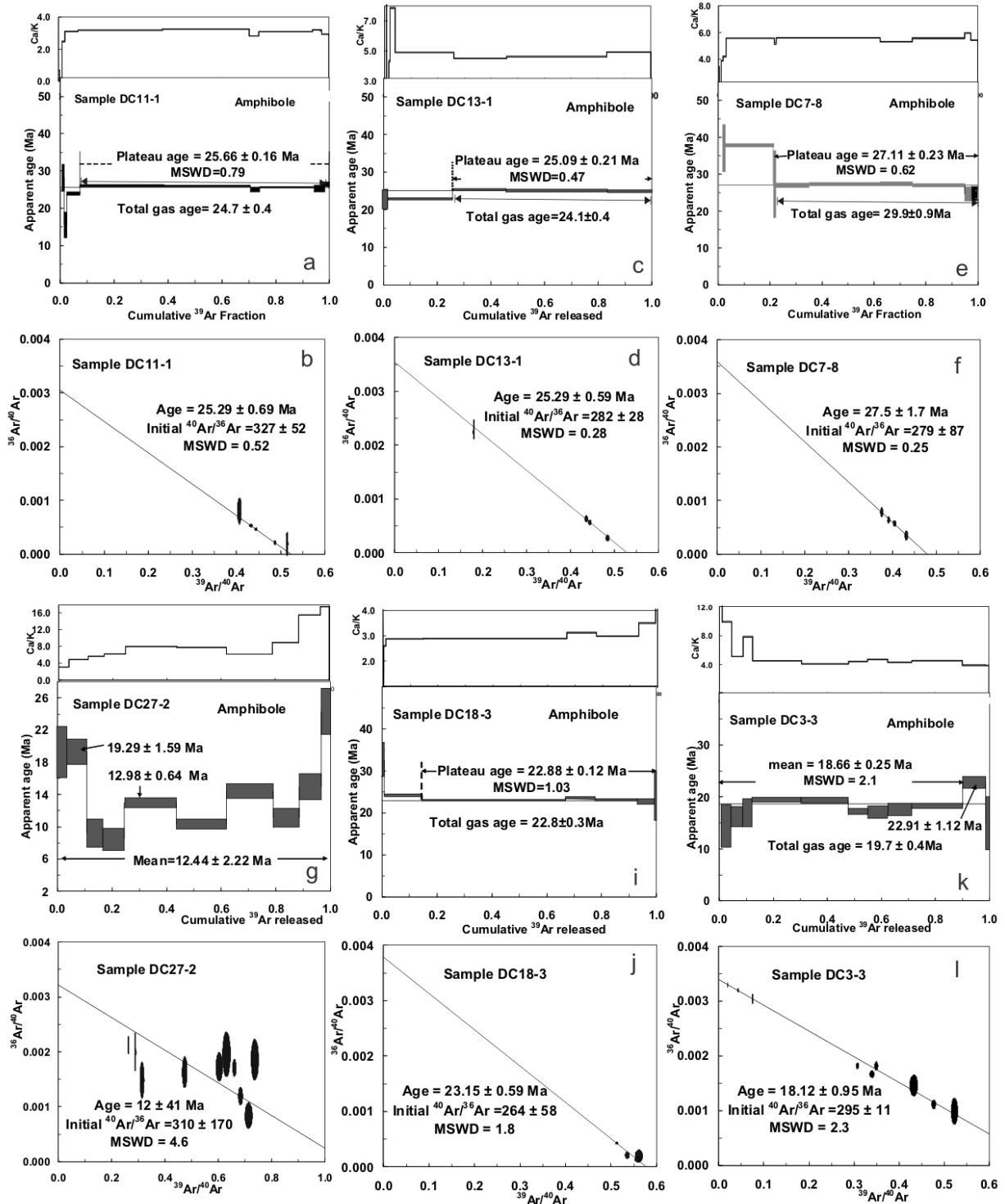


Fig. 7.7 ^{40}Ar - ^{39}Ar data for amphibole from various rocks of the DCS metamorphic complex. All samples with the release spectrum and inverse isotope correlation diagram analyzed by the laser-ablation step-heating method are presented. MSWD-mean square of weighted deviates.

experiments are provided in Table 7.1. Overall, the samples yield plateau ages with at least three consecutive heating steps that have acceptable mean square of weighted deviates (MSWD) values (see text). Anomalously young and old apparent ages from initial and final heating steps

were excluded. In the following, we discuss the results for each mineral separately, always in the same order from south to north and from east to west in each section. A summary of the samples analyzed and calculated ages are given in Table 7.2.

7.4.1 Amphibole (T_c ca. 550°C)

Six amphibole concentrates have been dated (Fig. 7.7).

Amphiboles from the samples DC11-1, DC13-1, DC7-8, DC18-3 have constant Ca/K ratio (Fig. 7.7a, c, e, i), suggesting that the amphiboles are not zoned and bear no inclusion of other mineral phases. The results give plateau ages of 25.66 ± 0.11 Ma (steps 4–9 including 90.1 percent of ^{39}Ar released, Fig. 7a), 25.09 ± 0.21 Ma (steps 3–5 including 75.5 percent of ^{39}Ar released, Fig. 7.7c), 27.11 ± 0.23 Ma (steps 1–5 including 78.5 percent of ^{39}Ar released, Fig. 7e) and 22.88 ± 0.12 Ma (steps 2–6 including 86.1 percent of ^{39}Ar released, Fig. 7.7i). Isotope inversion resulted in ages of 25.29 ± 0.69 Ma (with a $^{40}\text{Ar}/^{36}\text{Ar}$ initial value of 327 ± 52) (Fig. 7.7b), 25.29 ± 0.59 Ma (with a $^{40}\text{Ar}/^{36}\text{Ar}$ initial value of 282 ± 28) (Fig. 7.7d), 27.50 ± 1.70 Ma (with a $^{40}\text{Ar}/^{36}\text{Ar}$ initial value of 279 ± 87) (Fig. 7.7f) and 23.15 ± 0.59 Ma (with a $^{40}\text{Ar}/^{36}\text{Ar}$ initial value of 264 ± 58) (Fig. 7.7j). Both plateau and inversion ages for each sample are the same within the error. We consider the plateau ages of 25.66 ± 0.16 Ma (DC11-1), 25.09 ± 0.21 Ma (DC13-1), 27.11 ± 0.23 Ma (DC7-8), and 22.86 ± 0.14 (DC18-3) as geologically significant.

In contrast to the above mentioned amphibole concentrates, the amphibole from the sample DC27-2 is poor in potassium and the argon release pattern is highly scattered between 8.40 ± 1.37 Ma (step 4) and 19.29 ± 1.59 Ma (step 2), except at the last step with a maximum age of 19.29 ± 1.59 Ma. The mean age is 12.44 ± 2.22 Ma (Fig. 7.7g). The scattering of the data points suggests that the Ar was released from different reservoirs as illustrated by the Ca/K pattern (Fig. 7.7g). Isotope inversion resulted in a meaningless age of 12 ± 41 Ma (Fig. 7.7h). The age spectrum of the sample is highly discordant, which is presumably a consequence of chloritization and the low K content. Petrographically, most amphiboles are broken down during dynamic recrystallization and partly transformed into chlorite along the boundaries of the amphibole grains during retrograde metamorphism in the eastern retrograde shear zones.

Finally, the Ar release pattern of amphibole from the sample DC3-3 is slightly scattered, allowing calculation of a mean age of 18.66 ± 0.25 Ma (Fig. 7.7k) and the Ca/K ratios are constant throughout the experiment. Isotope inversion resulted in a well-constrained age of 18.12 ± 0.95 Ma (with an $^{40}\text{Ar}/^{36}\text{Ar}$ initial value of 295 ± 11) (Fig. 7.7l). The plateau age of 18.66 ± 0.25 Ma is considered to be geologically significant.

7.4.2 White mica (T_c ca. 425 °C)

The four white mica concentrates are from samples along the Xianguang-Pingpo section. They resulted in plateau ages of 17.13 ± 0.10 Ma (DC11-4, steps 1–10 including 97.3 percent of ^{39}Ar released, Fig. 7.8a), 22.89 ± 0.10 Ma (DC12-3, steps 5–8 including 79.1 percent of ^{39}Ar released, Fig. 8c), 20.96 ± 0.10 Ma (DC5-2, steps 1–5 including 88.1 percent of ^{39}Ar released, Fig. 7.8e) and 12.53 ± 0.07 Ma (DC8-7, steps 2–12 including 88.1 percent of ^{39}Ar released, Fig. 7.8g), respectively. Correspondingly, isotope inversion resulted in ages of 16.48 ± 0.67 Ma (with a $^{40}\text{Ar}/^{36}\text{Ar}$ initial value of 357 ± 75 , Fig. 8b), 23.60 ± 4.0 Ma (with a $^{40}\text{Ar}/^{36}\text{Ar}$ initial value of 312 ± 29 , Fig. 8d), 20.84 ± 0.28 Ma (with a $^{40}\text{Ar}/^{36}\text{Ar}$ initial value of 312 ± 29 , Fig. 7.8f) and 12.79 ± 0.46 Ma (with a $^{40}\text{Ar}/^{36}\text{Ar}$ initial value of 319 ± 23 , Fig. 7.8h). We consider the plateau ages of 17.13 ± 0.10 Ma, 22.89 ± 0.10 Ma, 20.96 ± 0.10 and 12.53 ± 0.07 Ma as geologically significant.

7.4.3 Biotite (T_c ca. 300 °C)

Among the five biotite concentrates, three (DC11-3/4, DC13-1, DC7-8) are from the south Xianguang-Pingpo (Xi'er He) section, and two (DC3-6 and DC23-4) from the north central section. The samples resulted in plateau ages of 9.08 ± 0.07 Ma (DC11-3, steps 4–11 including 84.6 percent of ^{39}Ar released) (Fig. 7.9a), 6.44 ± 0.14 Ma (DC13-1, steps 2–7 including 73.3 percent of ^{39}Ar released, Fig. 7.9c), 11.67 ± 0.12 Ma (DC7-8, steps 4–9 including 78.8 percent of ^{39}Ar released, Fig. 7.9e), 8.05 ± 0.06 Ma (DC23-4, steps 3–14 including 93.2 percent of ^{39}Ar released, Fig. 7.9g), and 6.34 ± 0.11 Ma (DC3-6, steps 4–7 including 71.8 percent of ^{39}Ar released) (Fig. 7.9i). For these samples, isotope inversion resulted in ages of 8.91 ± 0.21 Ma (with a $^{40}\text{Ar}/^{36}\text{Ar}$ initial value of 337 ± 28 , Fig. 7.9b), 5.75 ± 0.99 Ma (with a $^{40}\text{Ar}/^{36}\text{Ar}$ initial value of 341 ± 27 , Fig. 9d), 11.93 ± 0.59 Ma (with a $^{40}\text{Ar}/^{36}\text{Ar}$ initial value of 390 ± 24 , Fig. 7.9f), 6.4 ± 1.1 Ma (with a $^{40}\text{Ar}/^{36}\text{Ar}$ initial value of 301 ± 33 , Fig. 9h), and 7.40 ± 1.10 Ma (with a $^{40}\text{Ar}/^{36}\text{Ar}$ initial value of 211 ± 56 , Fig. 7.9j), respectively. We consider the plateau ages of 9.08 ± 0.07 Ma, 6.44 ± 0.14 Ma, 11.67 ± 0.12 Ma, 8.05 ± 0.06 Ma and 6.34 ± 0.11 Ma as geologically significant.

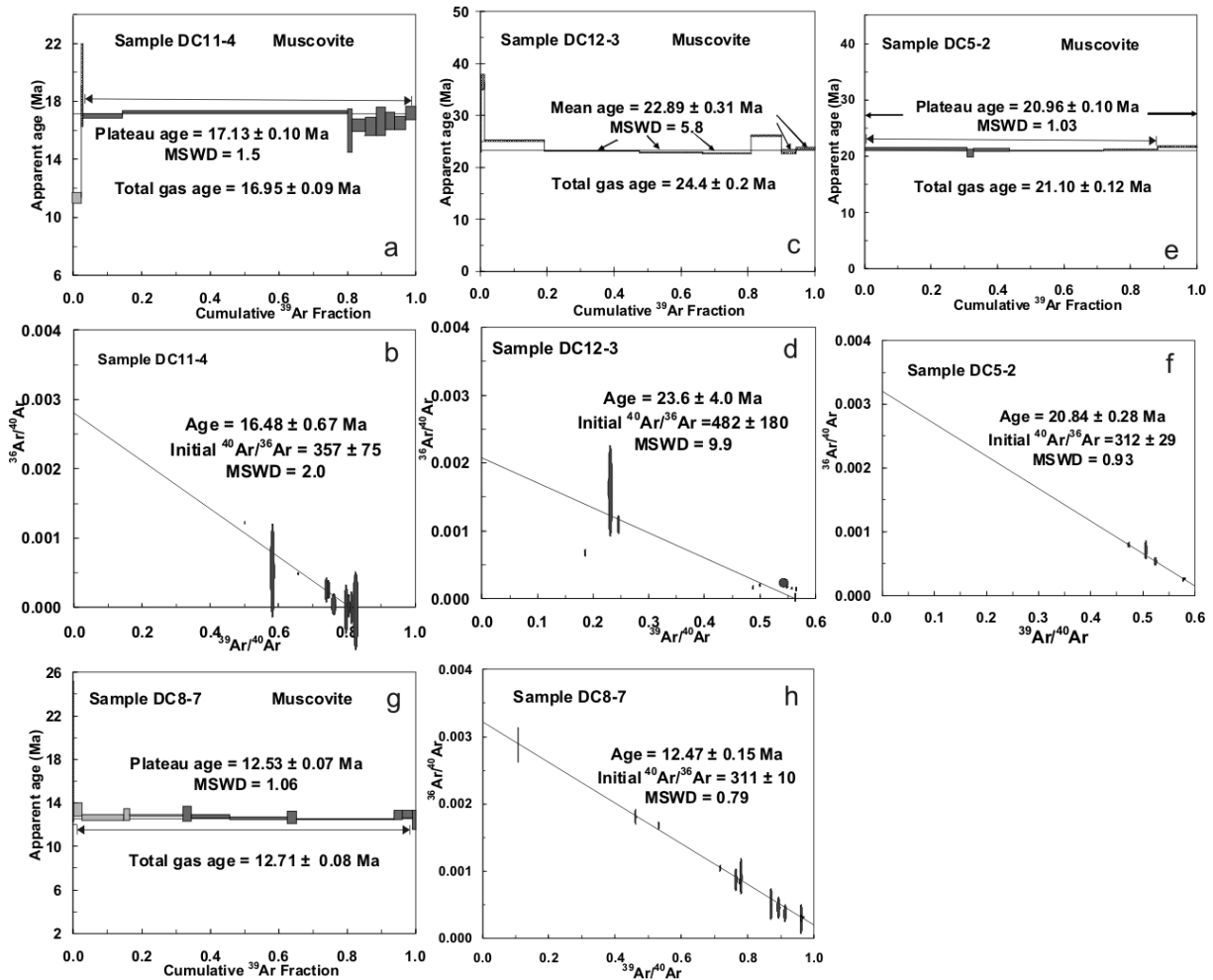


Fig. 7. ^{40}Ar - ^{39}Ar data for white mica from various rocks of the DCS metamorphic complex. All samples with the release spectrum and inverse isotope correlation diagram analyzed by the laser-ablation step-heating method and are presented. MSWD-mean square of weighted deviates.

7.4.4 K-feldspar (T_c ca. 250 °C)

Four K-feldspar samples were collected along the southern section and two from the north-central section. The sample DC11-2/2 is the easternmost one and the experiment resulted in a plateau age of 5.97 ± 0.03 Ma (steps 5–11 including 71 percent of ^{39}Ar released) (Fig. 7.10a). Isotope inversion resulted in an age of 5.56 ± 0.83 Ma (with a $^{40}\text{Ar}/^{36}\text{Ar}$ initial value of 336 ± 81) (Fig. 7.10b). We consider the plateau age of 5.97 ± 0.03 Ma as geologically significant. The sample DC12-3 was collected in the central part of the Xiaguan-Pingpo section. The argon release pattern yields a highly scattered pattern and is subdivided into two portions: the low-laser

energy release steps 1 to 6 yield a mean age of 7.5 ± 1.6 Ma and the high laser energy steps 8 to 17 again yield a mean with an age of 33.1 ± 1.6 Ma (Fig. 7.10c). Isotope inversion calculation of the two portions as mentioned above yield ages of 5.45 ± 0.44 Ma and 33.09 ± 0.80 Ma (Fig. 7.10d and e). We interpret the two ages (7.5 ± 1.6 Ma and 33.1 ± 1.6 Ma) as the result of compositionally distinct groups, which resulted in the two distinct ages and both ages are likely to be geologically significant. The westernmost sample (DC5-2) of the Xiaguan-Pingpo section also resulted in a scattered section. Low laser-energy steps 1 to 5 resulted in a U-shaped pattern with a minimum age of 4.38 ± 0.07 Ma (Fig. 7.10f). The high laser energy steps 6 to 14 yield a mean with an age of 13.45 ± 0.40 Ma (Fig. 10f). Isotope inversion resulted in an age of 12.9 ± 1.7 Ma (with a $^{40}\text{Ar}/^{36}\text{Ar}$ initial value of 387 ± 230) (Fig. 7.10g). We interpret the two ages to result from compositionally distinct groups leading to the two distinct ages. Both ages (4.38 ± 0.07 Ma and 12.9 ± 1.7 Ma) are likely to be geologically significant. The sample DC8-7 resulted in a plateau age of 9.23 ± 0.05 Ma (steps 4–6 including 76.9 percent of ^{39}Ar released (Fig. 7.10h). Isotope inversion resulted in an age of 8.50 ± 3.30 Ma (with a $^{40}\text{Ar}/^{36}\text{Ar}$ initial value of 312 ± 15) (Fig. 7.10i). The plateau age of 9.23 ± 0.05 Ma is here considered to be geologically significant.

The sample DC23-4 is the northernmost sample. The experiment resulted in a scattered argon release pattern with an age of the youngest step (step 3) at 5.18 ± 0.06 and the oldest step (step 6) at 8.88 ± 0.03 Ma (Fig. 7.10j). The mean age of the entire release spectrum is 7.45 ± 0.99 Ma (Fig. 10j). Isotope inversion resulted in an age of 6.4 ± 2.3 Ma (with a highly scattering initial $^{40}\text{Ar}/^{36}\text{Ar}$ value of 381 ± 400) (Fig. 7.10k). We interpret the mean age 7.45 ± 0.99 Ma as somehow significant. The sample DC18-3 is from the center of the metamorphic dome, collected in the northern part of the studied area. The experiment resulted in a scattered argon release pattern with an age of the youngest step (step 2) at 4.33 ± 0.38 and the oldest step (step 8) at 12.01 ± 0.09 Ma (Fig. 7.10l). The mean age of steps 1–7 is 6.27 ± 0.79 Ma (Fig. 7.10l). Isotope inversion of these steps 1–7 results in an age of 4.80 ± 0.79 Ma (with a highly scattering initial $^{40}\text{Ar}/^{36}\text{Ar}$ value of 1024 ± 210) (Fig. 7.10m). Because of the high variation of ages, we conclude that argon release occurred from compositionally non-uniform mineral grains. We interpret the mean age of 6.27 ± 0.79 Ma as geologically significant.

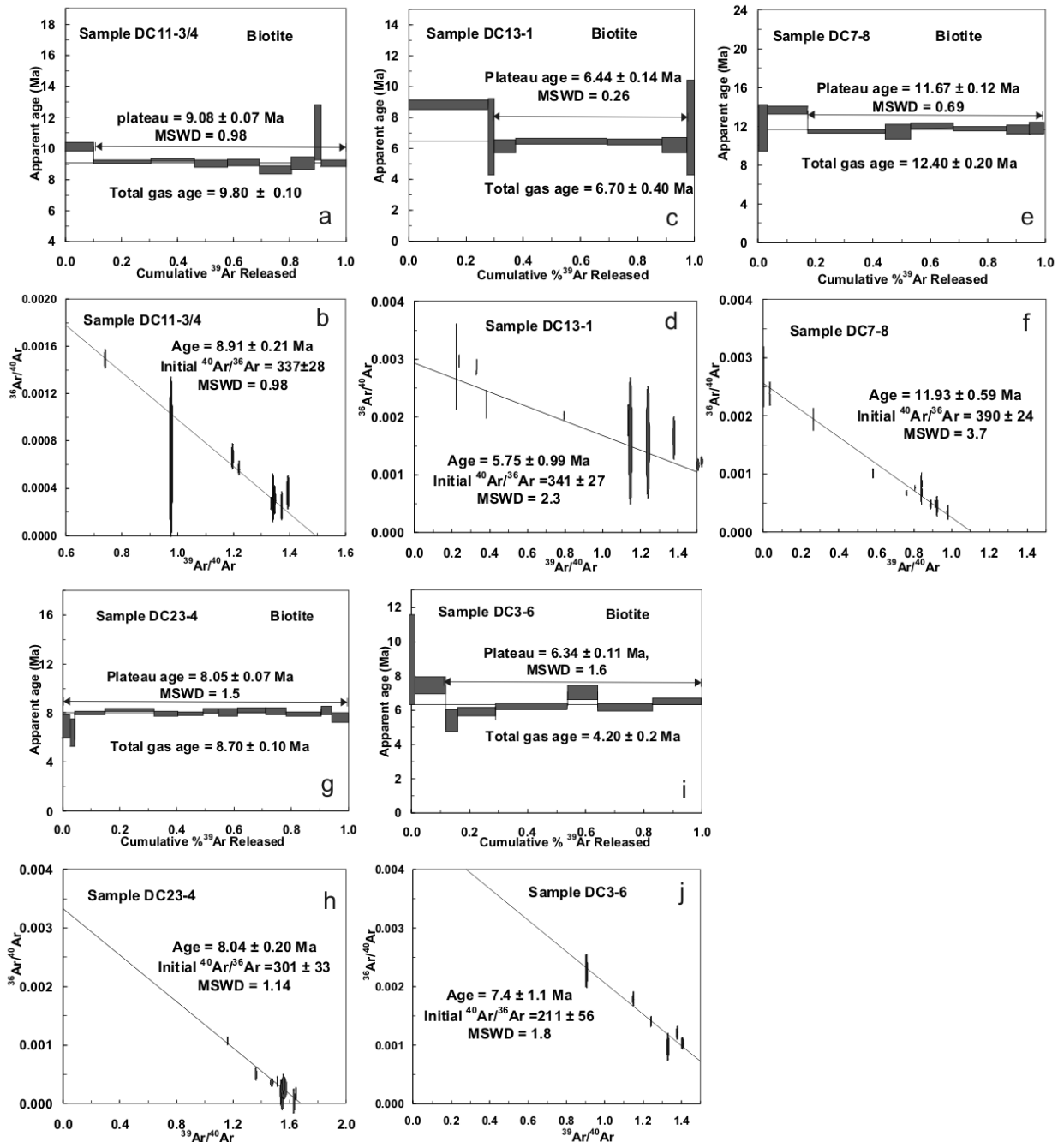


Fig. 7.9 $^{40}\text{Ar}/^{39}\text{Ar}$ data for biotite of the DCS metamorphic complex. All samples are shown with the release spectrum and inverse isotope correlation diagram analyzed by the laser-ablation step-heating method. MSWD-mean square of weighted deviates.

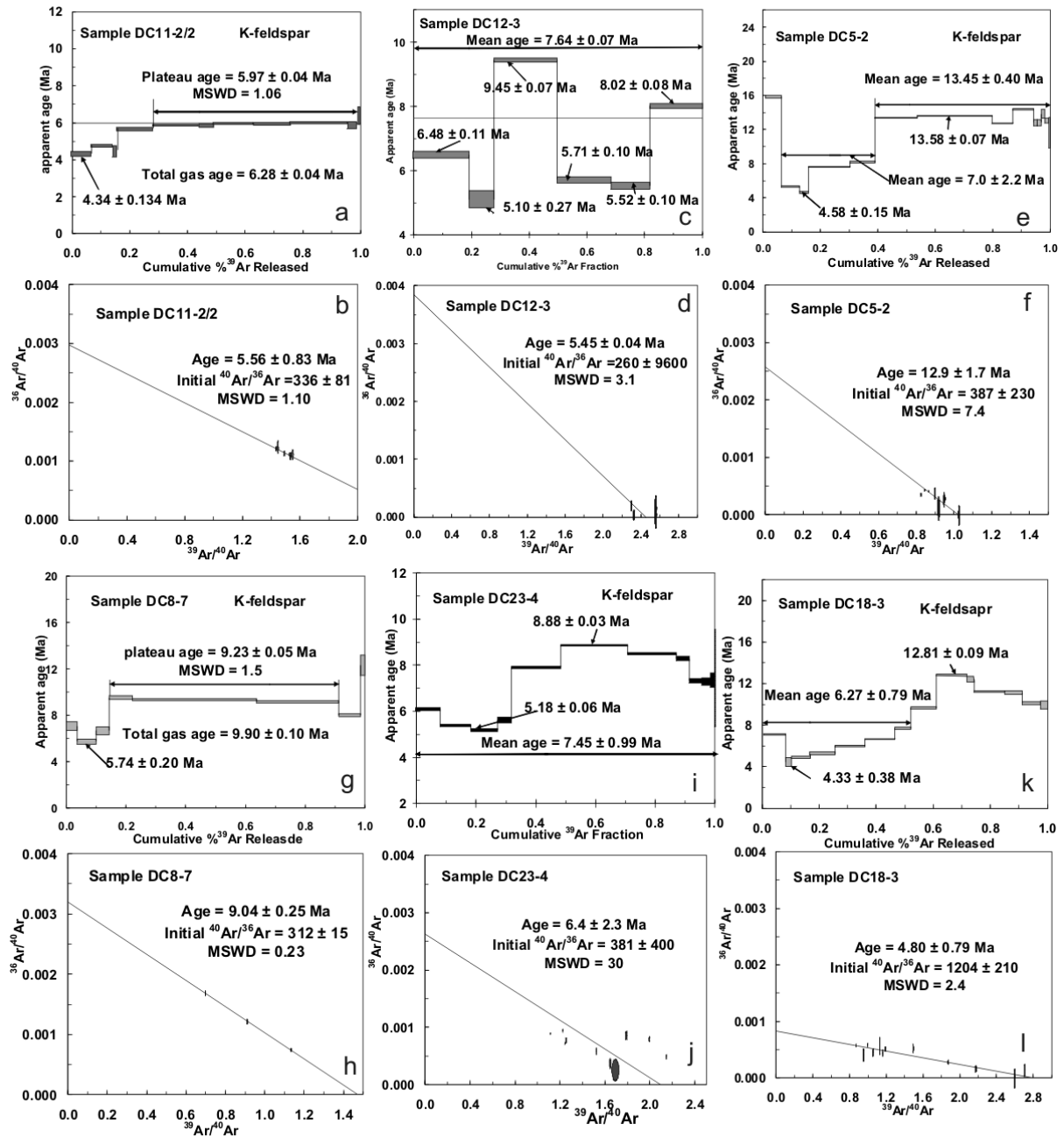


Fig. 7.10 ^{40}Ar - ^{39}Ar data for K-feldspar from various rocks of the DCS metamorphic complex. All samples are shown with the release spectrum and inverse isotope correlation diagram and are analyzed by the laser-ablation step-heating method and presented. MSWD-mean square of weighted deviates.

7.5 Discussion

7.5.1 Cooling paths and age compilations

The $^{40}\text{Ar}/^{39}\text{Ar}$ geochronological data of the amphibole, muscovite, biotite and K-feldspar in this study revealed ages ranging from 27 to 4 Ma (Table 7.2 and Fig. 7.5). This data, together with some of the U-Pb zircon ages (e.g. Cao et al. 2010b) (Fig. 7.11), shows a temperature-time-integrated cooling-deformation-exhumation history of the DCS metamorphic complex in the temperature range from ca. 700 to 160°C and ages from the Eocene (31 Ma) to the Pliocene (4 Ma) (Fig. 7.11). Although the dated samples are not always exactly from the same localities adjacent samples are treated as equivalents. Therefore, we have designated eight localities to show the cooling paths (paths A to H in Fig. 7.11).

Amphibole ages obtained from the mylonitic rocks suggest that the rocks experienced high-temperature left-lateral strike-slip deformation at ca. >550 °C (e.g. Harrison, 1981; Cao et al., 2010a) between ca. 27 and 23 Ma. The amphibole ages from the northern (path E) and southwestern (path F) (ca. 23 Ma) sectors are significantly younger than the three amphibole ages from the southern end (ca. 25 to 27 Ma, paths A, B, C) of the DCS massif. Consequently, the southern part cooled earlier than the northern and southwestern parts, revealing an early differential cooling and exhumation of the DCS metamorphic complex. Muscovites (closure temperature ca. 425 °C) were investigated only from samples of the southern section, and ages vary between 23 and 13 Ma. Thin section observations showed two groups of muscovite samples. The older muscovite grains (23 Ma and 21 Ma) are highly deformed and recrystallized. In samples DC12-3 and DC5-2, they are intensely deformed and constitute part of the L-mylonites. The age (ca. 17 Ma) of the deformed, but unrecrystallized muscovite grains in the leucogranite sample (DC11-4) is younger than the highly deformed and recrystallized samples. In addition, the youngest age (ca. 13 Ma) (sample DC8-7) is from the post-kinematic pegmatite sample, and the investigated muscovite grain is only weakly deformed.

In the DC11 sampling location (path B), the amphibole (sample DC11-1) yielded a plateau age of 26 Ma and muscovite from the unrecrystallized muscovite (sample DC11-4) a plateau age of 17 Ma, representing a cooling rate of 14 °C/Ma from 550 to 425 °C. The amphibole from the amphibolite (sample DC7-8) yielded a plateau age of 27 Ma and the muscovite from the deformed granite (sample DC5-2) a plateau age of 21 Ma. An assumed time-integrated cooling rate is ca. 21 °C/Ma from 550 °C to 425 °C (path A). The $^{40}\text{Ar}/^{39}\text{Ar}$ biotite ages record cooling through the Ar retention temperature of 300 °C. Ages in the southern section range between 11.67 and 6.44 Ma (samples DC11-3/4, DC13-1 and DC7-8). The youngest age (6.34 Ma) is

from the sample collected along the western part of the northern sector and the age of 8.05 Ma is from the sample in the middle part. A thermal gradient from 425 °C at ca. 23 Ma to 300 °C at ca. 6 Ma (sample DC12-3, muscovite and biotite), suggests a time-integrated cooling rate of about 11 °C/Ma (path G). At other locations, a cooling rate of about 14 °C/Ma (path A) was calculated from ca. 21 Ma (sample DC5-2, muscovite) to ca. 12 Ma (sample DC7-8, biotite) and a cooling rate of about 17 °C/Ma (path B) from ca. 17 Ma (sample DC11-4, muscovite) to ca. 9 Ma (sample DC11-3, biotite).

On the other hand, in locations where there are no muscovite samples, the amphibole ages and cooling ages of pre-shearing granites are applied to calculate the thermal gradients. Assuming a simple linear cooling in the northern section, cooling from 550 °C at ca. 23 Ma (sample DC3-3 and DC18-3, amphibole) to 300 °C at ca. 6 Ma (sample DC-3-6 and DC23-4, biotite) suggests time-integrated cooling rates of about 15°C /Ma (path F) and 17°C (path E), respectively. Similarly, a thermal gradient of 13°C (path C) is calculated for the cooling from 550 °C at ca. 25 Ma to 300 °C at ca. 6 Ma (biotite) for the sample DC13-1. For the sample DC23-4, a pre-shearing monzogranite, it is assumed that the rocks cooled down to the setting temperatures immediately after their crystallization. Subsequent cooling would have resulted from the exhumation. For this sample, a thermal gradient of 16°C/Ma is calculated from the peak temperature (625°C) of the metamorphic rocks to the biotite retention temperature 300 °C at ca. 8 Ma (sample DC23-4, biotite).

The K-feldspar (retention temperature: 250 °C for plateau or mean ages and 160 °C for the youngest significant low-laser energy step) ages mainly range between 4 and 9 Ma. Sample DC23-4, assuming a simple linear cooling from about 300 °C (biotite, 8 Ma) to 250 °C (K-feldspar, 7 Ma), yields a rate of about 50 °C/Ma. In the same sample (DC8-7), a time-integrated cooling rate of about 44 °C/Ma (path H) is calculated with a thermal gradient from 425 °C (Muscovite) at ca. 13 Ma to 250 °C (K-feldspar) at ca. 9 Ma. For the other samples, the time-integrated cooling rates are about 17 °C/Ma between ca. 9 Ma (sample DC11-3/4, biotite) and ca. 6 Ma (sample DC11-2/2, K-feldspar), about 10 °C/Ma from ca. 12 Ma (DC7-8, biotite) to ca. 7 Ma (DC5-2, K-feldspar), and about 140 °C/Ma from ca. 6 Ma (DC13-1, biotite) to ca. 5 Ma (DC12-3, K-feldspar). The biotite and K-feldspar cooling ages indicate differential cooling between 300 and 250 °C. Cooling rates vary from 10 °C/Ma to an extremely high value of ca. 140 °C/Ma (Fig. 11).

The youngest low-laser energy step ages of K-feldspars are 4.34 ± 0.13 Ma (DC11-2/2), 5.10 ± 0.27 Ma (DC12-3), 4.58 ± 0.15 Ma (DC5-2), 5.74 ± 0.20 Ma (DC8-7), 5.18 ± 0.06 Ma (DC23-4),

4.33 ± 0.39 Ma (DC18-3). Consequently, subsequent cooling from 160°C/Ma to surface temperatures and associated exhumation is a very young process which occurred during the Pliocene until the Holocene. For the samples DC23-4, DC11-2/2, DC3-6, DC5-2, DC8-7, cooling from 250 °C to 160 °C gives the cooling rates of about 30 °C/Ma, 45 °C/Ma, 41 °C/Ma, 30 °C/Ma and 33 °C/Ma, respectively (Fig. 11). The diverging cooling paths between 300 °C and 250 °C become subparallel and finally reach surface temperature.

The new $^{40}\text{Ar}/^{39}\text{Ar}$ ages and cooling paths obtained by the coexisting amphibole, muscovite, biotite and K-feldspar indicate an obvious correlation between sample location (Fig. 7.5) and cooling history (Fig. 7.11), suggesting that the thermal histories were synchronous or diachronous at different periods of tectonic deformation at the scale of our study. The analysis of time-integrated cooling rates reveals that the cooling history and tectono-thermal evolution within the DCS massif is far from a linear, simple history, although Leloup et al. (1993a) suggested that the thermal histories were nearly synchronous at the scale of the DCS massif by the $^{40}\text{Ar}/^{39}\text{Ar}$ analysis of K-feldspar. In fact, the $^{40}\text{Ar}/^{39}\text{Ar}$ ages and cooling rates within the DCS are variable. It is our opinion that the long-lasting ASRR tectonic activity in the DCS massif led to a very heterogeneous cooling history and pattern, with different portions of the DCS being exhumed (hence cooled) at various rates at different ages.

7.5.2 Cooling history of the metamorphic rocks and tectonic deformation

The structural geology of the DCS area is dominated by tectono-metamorphic zones, including the central high-grade complex of high-temperature mylonites and the eastern retrograde zone in which the high-grade complex was subjected to lower greenschist retrograde metamorphism. The different zones are bounded by the late Cenozoic faults that also separate the DCS complex and the Erhai lake to the east. As a result, four major Cenozoic tectonic events are recognized in the DCS area: an early post-collisional extension (e.g., Chung et al., 1997), a major left-lateral high-temperature strike-slip shearing (e.g., Leloup et al., 1993a; Liu et al. 2006; Cao et al., 2010b), a ductile to brittle normal faulting, and finally successive brittle faulting (e.g., Wang et al., 2006), which all played an important role in the tectonic evolution of the DCS massif and contributed to the exhumation of the high-grade metamorphic complex. However, the cooling history of the DCS metamorphic complex is still poorly constrained, although K-feldspar $^{40}\text{Ar}/^{39}\text{Ar}$ dating shows two stages of exhumation, e.g., the initial phase of slow cooling at around 22 Ma (e.g., Leloup et al., 1993a; Harrison et al., 1996) and the second stage rapid cooling

Table 7. 2 Summary of thermochronologic data of the samples from the DCS massif.

Sample			Plateau/Mean		Isotope correlation				Total gas	
Sample No.	Rock Type	Altitude (m)	Mineral Type	Age (Ma)	Steps ³⁹ Ar	MSWD	Age (Ma)	⁴⁰ Ar/ ³⁶ Ar	MSWD	age (Ma)
DC11-1	Amphibolite	1715 ± 16	Amphibole	25.66 ± 0.16	4-9 (90.1%)	0.79	25.29 ± 0.69	327 ± 52	0.52	24.7 ± 0.4
DC13-1	Gt-Hbl-Bi gneiss	1857 ± 10	Amphibole	25.09 ± 0.21	3-5 (75.5%)	0.47	25.29 ± 0.59	282 ± 28	0.28	24.1 ± 0.4
DC7-8	Gr-Bi-amphibolite	1801 ± 13	Amphibole	27.11 ± 0.23	1-5 (78.5%)	0.62	27.5 ± 1.70	279 ± 87	0.25	29.9 ± 0.9
DC18-3	Hbl-granite	3541 ± 29	Amphibole	22.88 ± 0.12	2-6 (86.1%)	1.03	23.15 ± 0.59	264 ± 58	1.80	22.8 ± 0.3
DC27-2	Amphibolite	3003 ± 10	Amphibole	19.29 ± 1.59	one step	8.20	12.00 ± 41.00	310 ± 170	4.60	13.4 ± 0.4
				12.44 ± 2.22*	1-10 steps					
DC3-3	Amphibolite	1649 ± 22	Amphibole	18.66 ± 0.25*	10 steps	2.10	18.12 ± 0.95	295 ± 11	2.30	19.7 ± 1.1
				22.91 ± 1.12	one step					
DC11-4	Leucogranite	1715 ± 16	Muscovite	17.13 ± 0.10	1-10 (97.3%)	1.50	16.48 ± 0.67	357 ± 75	2.00	17.0 ± 0.1
DC12-3	Granite	1857 ± 10	Muscovite	22.89 ± 0.10	5 steps (79.1%)	5.80	23.60 ± 4.0	421 ± 90	9.90	24.4 ± 0.2
DC5-2	Monzogranite	1801 ± 13	Muscovite	20.96 ± 0.10	1-5 (88.1%)	1.03	20.84 ± 0.28	312 ± 29	0.93	21.1 ± 0.12
DC8-7	Pegmatite	1735 ± 10	Muscovite	12.53 ± 0.07	2-12 (67.8%)	1.06	12.79 ± 0.46	319 ± 23	0.79	12.71 ± 0.1
DC11-3/4	Bi-Granite	1715 ± 16	Biotite	9.08 ± 0.07	4-11 (84.6%)	0.98	8.91 ± 0.21	337 ± 28	0.98	9.80 ± 0.1
DC13-1	Gt-Hbl-Bi gneiss	1857 ± 10	Biotite	6.44 ± 0.14	2-7 (73.3%)	0.26	5.75 ± 0.99	341 ± 27	2.30	6.7 ± 0.4
DC7-8	Gr-Bi-amphibolite	1801 ± 13	Biotite	11.67 ± 0.12	4-9 (78.8%)	0.69	11.93 ± 0.59	390 ± 24	3.70	12.4 ± 0.2
DC23-4	Monzogranite	3003 ± 10	Biotite	8.05 ± 0.06	3-14 (93.2%)	1.50	6.4 ± 1.1	301 ± 33	1.14	8.7 ± 0.1
DC3-6	Hbl-Bi schist	1649 ± 22	Biotite	6.34 ± 0.11	4-7 (71.8%)	1.60	7.4 ± 1.10	211 ± 56	1.80	4.2 ± 0.2
DC11-2/2	Pegmatite	1715 ± 16	K-feldspar	5.97 ± 0.04	5-11 (71%)	1.06	5.56 ± 0.83	336 ± 81	1.10	6.3 ± 0.0
				4.34 ± 0.13 "						
DC12-3	Granite	1857 ± 10	K-feldspar	7.64 ± 0.072 *	1-6 steps		5.45 ± 0.04	260 ± 9600	3.10	3.7 ± 0.0
				5.10 ± 0.27"						
DC5-2	Monzogranite	1801 ± 13	K-feldspar	7.00 ± 2.20*	1-5 steps					
				13.45 ± 0.40*	6-14 step		12.9 ± 1.70	387 ± 230	7.40	13.0 ± 0.1
				4.58 ± 0.15"						
DC8-7	Pegmatite	1735 ± 10	K-feldspar	9.23 ± 0.05	4-6 (76.9%)	1.50	9.04 ± 0.25	312 ± 15	0.23	9.9 ± 0.1
				5.74 ± 0.20"						
DC23-4	Monzogranite	3003 ± 10	K-feldspar	7.45 ± 0.99 *	1-12 steps		6.4 ± 2.30	381 ± 400	30.00	7.2 ± 0.1
				5.18 ± 0.06"						
DC18-3	Hbl-granite	3541 ± 29	K-feldspar	6.27 ± 0.79 *	1-7 steps		4.80 ± 0.79	1204 ± 210	2.40	8.4 ± 0.1
				12.81 ± 0.09	one step					
				4.33 ± 0.38						

Notes: *Age calculated from selected steps,"Age from youngest step. All errors are 1σ and do not include error in decay constants or fluence monitor age.

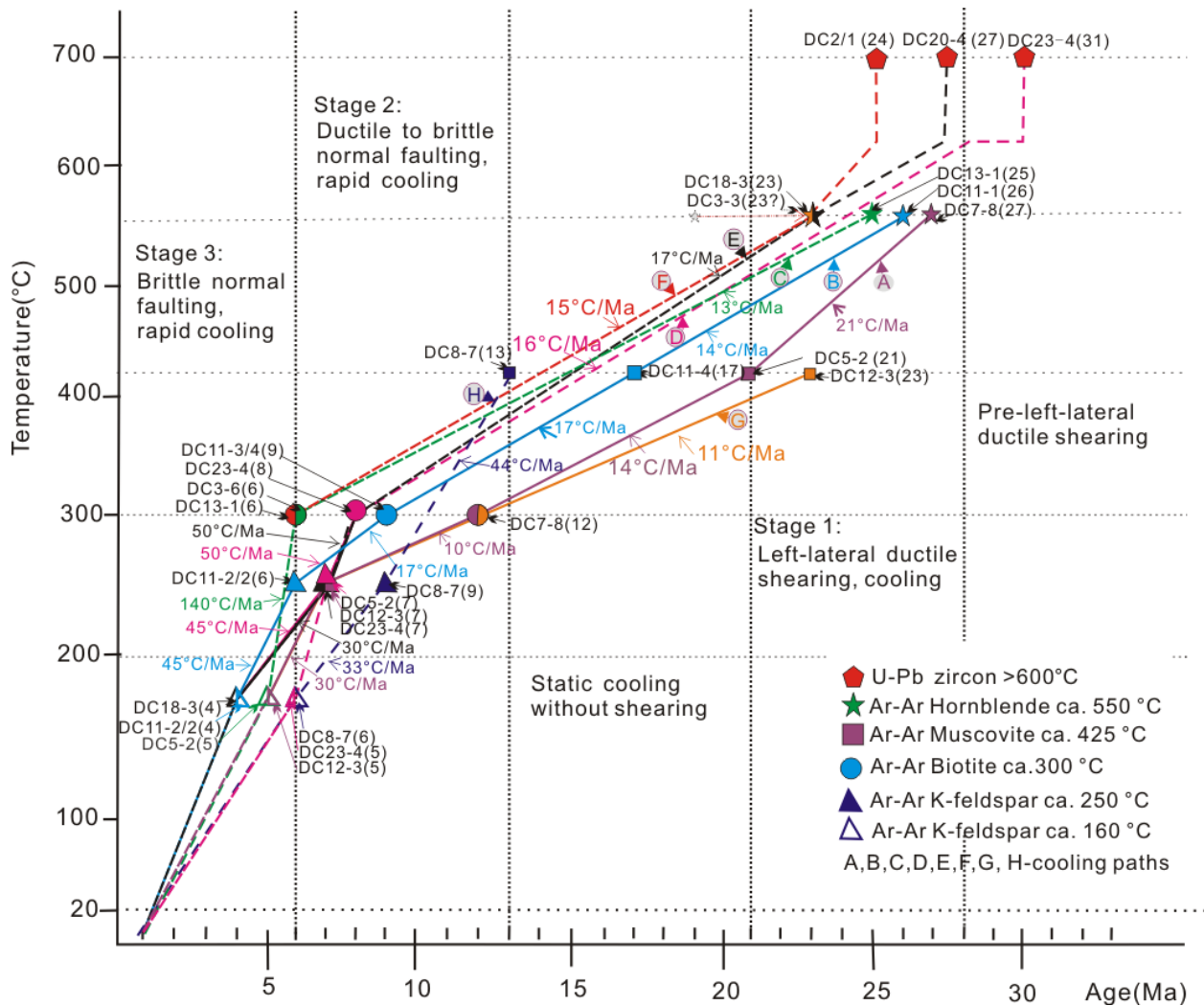


Fig. 7.11 Time-integrated cooling rates of the Diancang Shan metamorphic complex, combining the results of argon thermochronology (this study) and zircon U-Pb ages (from Cao et al., 2010). A, B, C, D, E, F, G and H present the cooling paths by the nearest or the same location samples to calculate. The number is the age with geological significance in the brackets behind every sample.

starting at ca. 4.7 Ma (Leloup et al., 1993a). Here, compilation of some of our previously published zircon U-Pb age data of leucogranitic intrusions (Cao et al., 2010b) and the new thermochronological results help to constrain the thermal evolution of the complex and provide clues to the understanding of the tectonic deformation. Three major stages of cooling and exhumation processes are demonstrated in the DCS metamorphic massif, e.g., an early relatively slow cooling and two later stages of rapid cooling. The cooling paths of various segments (Fig. 7.11) suggest diachronous and synchronous exhumation across the metamorphic complex.

It is noteworthy that the following data corrections were done during the correlation analysis. The sample DC3-3 gives a major plateau age of ca. 19 Ma, which is much younger than the other amphibole ages, making the cooling paths slightly different from those of the other

samples. When the thin sections and $^{40}\text{Ar}/^{39}\text{Ar}$ data of the sample were examined in detail, we found that the amphibole grains in the sample are full of opaque inclusions and the distinction of the amphibole grains are generally not homogeneous. Possibly due to the presence of excess non-radioactive argon, the age spectrum moves to the younger end. There is, however, one step of 20% argon release, which gives an age of ca. 23 Ma, which is similar to the other amphibole ages, and also results in a cooling path parallel to the other three major cooling paths at other localities.

On the other hand, the metamorphic and deformation temperatures of the high-grade metamorphic rocks range from 575 to 625°C (e.g., Leloup et al., 1993a; Cao et al., 2010a). After their intrusion into the metamorphic rocks, the pre- and syn-kinematic intrusions are assumed to cool down rather rapidly from the crystallization temperature at about 700°C to their equilibrium temperature at about 625°C. Thereafter, they experienced similar cooling as the metamorphic rocks. In the following, we discuss the results of cooling for the exhumation history. Tentative models for exhumation combining results of the cooling history with regional geology are shown in Figure 7.12 a–c.

Stage 1: Late Oligocene to middle Miocene relatively slow exhumation and left-lateral shearing

The first stage of cooling of the metamorphic rocks started > 27 (or 28) Ma ago, before the rocks of sample DC7-8 (locality A path) passed through the closure temperature of amphibole (Fig. 11). Most other parts of the area were still under the 575-625° metamorphic zone (e.g., Cao et al., 2010a). Cooling of the samples from other localities (B, C, D, E and F) occurred in a successive sequence with a relatively short time span (1 to 2 Ma), as the rocks at locality A continued cooling. Similar cooling rates from 13°C/Ma to 17°C/Ma give rise to the sub-parallel characteristics of the cooling paths. Such cooling events lasted until 9 Ma (path B, DC11-3), 8 Ma (paths, D and E, sample DC23-4) and 6 Ma (paths C and F, samples DC13-1 and DC3-6) respectively. The cooling path A and G are different from the others in that they have different cooling rates, although overall they are similar to each other.

The first stage of exhumation is a relatively slow and diachronous process related to left-lateral ductile shearing (Fig. 7.12a). It is obvious from the above data that the initiation of the first step exhumation of the massif started from path A of the southern section, where the cooling path passes through the amphibole closure temperature at the earliest age (>27 Ma). However, for other localities, the cooling paths pass through the amphibole closure temperature in a younging succession from paths B, C, D, E to F. Based on the mineral ages (amphibole,

muscovite or biotite) we infer the diachronous cooling of the massif to have occurred at the initial stage of exhumation. Subsequent cooling paths at different localities are parallel to each other. The parallelism of the cooling paths suggests, however, that the subsequent exhumation of the massif is a steady cooling process without any tilting. Therefore, cooling paths A and G reach the biotite closure temperature the earliest (12 Ma) and path E latest (6 Ma). Because of the remarkable consistency of the starting age of exhumation and the onset of left-lateral shearing from the zircon U-Pb ages of leucogranitic rocks (Cao et al., 2010b), the earliest exhumation of the massif is, therefore, ascribed to the ductile shearing along the ASRR belt. Although the exhumation may have stopped due to the cessation of the left-lateral shearing at ca. 21 Ma (Cao et al., 2010b), cooling continued to relatively low-temperature conditions. Continuous cooling with a constant slow cooling rate at the different localities reached the biotite closure temperature (300°C) at 9 Ma (B), 8 Ma (C and E), and 6 Ma (D and F), respectively. At path A such slow cooling continues and the K-feldspar closure temperature at about 260°C is reached at 7 Ma.

Stage 2: Late Miocene rapid cooling and exhumation and ductile-to-brittle normal faulting

The fast cooling of the second stage started at 12 Ma along the path H (DC7-8) (or 13 Ma at DC8-7) when continued slow cooling was still taking place at the other localities. There is a diversity of cooling rates in this stage, varying from 140°C/Ma to 17°C/Ma with the majority between 45 and 50°C/Ma, indicating differences in exhumation rates. Between the higher temperature range of the K-feldspar closure temperature (260°C) and the lower limit of the K-feldspar closure temperature (160°C), the cooling paths also change, but not to a large extent. In spite of the fact that the different localities reached the biotite closure temperature at various times between 12 and 6 Ma, the time differences of different cooling paths become small to 6 and 4 Ma, at the lower K-feldspar closure temperature (160 °C), respectively.

The normal faulting along the eastern and western flanks of the DCS mountain range is responsible for the second stage of fast cooling and diachronous exhumation of the DCS high-grade metamorphic massif (Fig. 7.12b). Faulting at the ductile to brittle transition was accompanied by infiltration of fluid phases into the shear zone resulting in low-grade chloritization along the kilometer-scale normal fault zone (see also Leloup et al., 1993, 1995). The inhomogeneous cooling and exhumation of the lower plate of the normal fault zone possibly resulted from the tilting of the lower plate block or differential exhumation of slabs in the lower plate. Differences in cooling rates may be attributed to the occurrences of many separate low-temperature shear zones in the lower plate.

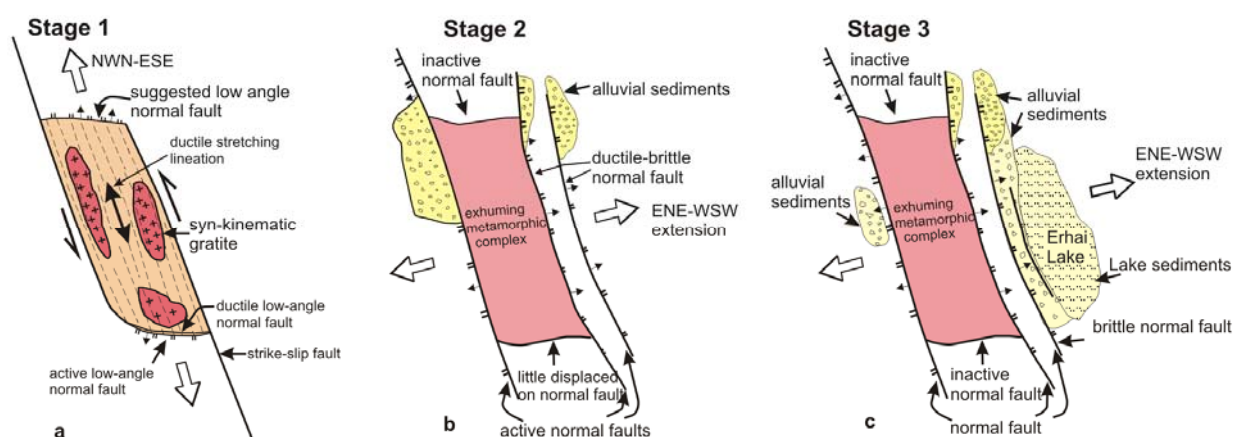


Fig. 7.12. Tentative models for three stages of exhumation of the Diancang Shan metamorphic complex. For explanation see text.

Stage 3: Early Pliocene to Holocene rapid cooling/exhumation and brittle faulting

The final stage of cooling and exhumation of the DCS massif is recognized when the higher temperature cooling paths are extended and plotted to a lower temperature at about 16°C for the present day average surface temperature from 4 to 0 Ma. The absence of low-temperature chronological data has led to two possibilities for the trend of the cooling paths. As a first approach, it is reasonable to extend the higher temperature cooling paths to the lower temperature domain. Therefore, diachronous cooling and exhumation continuously spans to the surface. Continuous tilting of the massif is inferred, therefore, from such a situation. However, there are possibly different rates of cooling and exhumation and different degrees of tilting, so that the cooling paths have a high convergence rate. The other possibility is that the different localities reached the surface at different times from ca. 4 to 1 Ma. In such a case, the massif is uplifted as a rigid block without tilting.

If the former case of the tectonics of the DCS massif is considered, i.e. continuous cooling and exhumation but with different rates and degrees of tilting, this tectonic model likely best explains the recent cooling of the massif near the surface. Brittle normal faults dipping at ca. 60° are widespread along the eastern and western flanks of the DCS (Fig. 7.12c). The most obvious dipping faults border Erhai Lake to the east and the DCS to the west. The west-bounding fault of the DCS is poorly known, but may have also accommodated a similar amount of vertical displacement. Both faults were formed due to Pliocene to Holocene regional extension (e.g., Wang et al., 1997), which may have partly contributed to the low-temperature cooling and exhumation of the DCS massif. Brittle normal faults are also observed inside the high-grade

massif. Rollover of the upper plate is rather obvious if the depths of the Quaternary sediments are examined and may also offer support to the tilting of the lower plate.

7.5.3 Regional tectonic implications

The above thermochronological results demonstrate that the DCS metamorphic massif underwent three stages of cooling/exhumation, e.g. a relatively slow cooling from 27-13 Ma and two rapid cooling phases between 13 and 0 Ma. They are correlated to the three stages of tectonic deformation during the exhumation of the DCS metamorphic massif. The left-lateral shearing was initiated shortly before path A passed through the amphibole closure temperature at about 28 Ma. The left-lateral shearing movement was accompanied by exhumation, and, therefore, cooling of the high-grade metamorphic rocks. The cooling and exhumation are diachronous at the onset of shearing but synchronous during subsequent evolution, and cooling continued to the biotite closure temperature at 12 to 6 Ma, respectively, although the high-temperature left-lateral shearing may have stopped at an early age (ca. 21 Ma). The second stage of deformation is a ductile to brittle extensional faulting at middle to upper crustal levels. From the cooling data it is also clear that the faulting may have occurred 13 or 12 Ma ago in some places, and dominant faulting started at ca. 9 Ma. The faulting induced tilting of the lower plate or differential exhumation within the lower plate, as shown by the diachronous cooling and exhumation until the different localities passed the lower closure temperature of K-feldspar between 6 and 4 Ma ago. The final stage of deformation is probably also accompanied by slightly diachronous cooling and exhumation of the DCS massif, which is attributed to the brittle faulting on both sides of the DCS range. The faulting is therefore constrained between 4 (locally 6) to 0 Ma.

The tectonic deformation that led to the cooling and exhumation of the DCS massif has its counterparts on a regional scale. There are several high-grade metamorphic massifs in SE Asia, e.g., the DCS, XLS, ALS and DNCV complexes, the Mogok (MG) gneiss belt, the Doi Inthanon-Doi Suthe (DIDS) metamorphic core, and Bu Khang (BK) complexes, the Wang Chapo (WC) - Three Pagodas (TP) metamorphic belt and the ASRR metamorphic belt (Fig. 1) (e.g., Nam et al., 1998; Jolivet et al., 1999; Maluski et al., 2001; Nagy et al., 2008). They occur in a fan-shaped area bounded by the ASRR fault to the east and the Sagaing fault to the west. The major NE-directed extension and exhumation of the entire BK complex in central Vietnam began at 36 Ma and culminated at 21 Ma (e.g., Lepvrier et al., 1997; Jolivet et al., 1999), which was accompanied by syn-kinematic granite emplacement and deformation (ca. 26–24 Ma) (e.g., Nagy et al., 2001, 2008). The left-lateral transtensional deformation and cooling of the DNCV

metamorphic complex in North Vietnam occurred between ca. 34 and 17 Ma (e.g., Nam et al., 1998, 2001; Wang et al., 1998b; Anczkiewicz et al., 2007). In the ALS, rapid cooling occurred diachronously along the strike from 25 Ma in the SE to 17 Ma in the NW end (e.g., Harrison et al., 1996) or 33–17 Ma (e.g. Tapponnier et al., 1990; Leloup et al., 2001b). Successively exhumed metamorphic massifs also include the MG gneiss dome (26–14 Ma), and the DIDS metamorphic complex (27–16 Ma) (e.g., Morley et al., 2002; Barr et al., 2002). The left-lateral shearing along the NW-striking TP in Thailand (ca. 36–33 Ma, biotite: $^{40}\text{Ar}/^{39}\text{Ar}$ and K-Ar) and WC faults (ca. 33–31 Ma; biotite ages) experienced subsequent rapid uplift during E-W extension at 25–23 Ma (e.g., Lacassin et al., 1997). The above thermochronological data from the metamorphic massifs suggests that their exhumation is diachronous, broadly in the range of 36 Ma to 4 Ma ago. Such a diachronous exhumation style may suggest that the extrusion of the Indochina block has not homogeneously affected the entire area. Instead, different parts in the extruding block responded to the extrusion in different ways at various times, so that the exhumation of the massifs is either strike-slip-related (e.g., ASRR massifs and TP massif) or extensional-related (e.g., the WC massif and BK complex) in a broad time span from 36 to 21 Ma.

On the other hand, a remarkable feature of the Cenozoic evolution of Southeast Asian tectonics is the rotation of crustal blocks. A large clockwise rotation of up to 90° of the Indochina block has been recognized due to paleomagnetic investigations (e.g., Funahara et al., 1993; Huang and Ophyke, 1993; Chen et al., 1995). From the paleomagnetic measurements it is clear that two stages of block rotation occurred: an early stage of fast rotation from the late Cretaceous through to the Eocene (3.33°/ma) and slow rotation since the Miocene (2.77°/Ma). These block rotations have been sporadic to the present day (e.g., Liu et al., 2006). The former may have triggered the extrusion at regional scale ductile strike-slip shearing, and therefore the early stage of exhumation of the DCS massif. The latter has contributed to the E-W directed regional tectonic extension and the last two stages of cooling and exhumation of the DCS massifs. Furthermore, the differential exhumation of the metamorphic massifs also implies that there is a differential block rotation within Indochina. The rotation of the different parts of the Indochina block may have led to the extension and loss of its tectonic continuity.

7.6. Conclusions

(1) New $^{40}\text{Ar}/^{39}\text{Ar}$ amphibole, muscovite, biotite and K-feldspar data shows that there are three stages of dominant cooling and exhumation of the DCS massif. The first stage of the

thermochronological evolution of the DCS massif started diachronously from >27 to 23 Ma, with subsequent homogeneous and relatively slow cooling and exhumation until 13 Ma ago. The last two stages are shown to be diachronous throughout the whole period of evolution from 13 to 0 Ma.

(2) The cooling and exhumation of the DCS metamorphic massif are attributed to the regional tectonics. Three stages of regional deformation are well constrained by thermochronology. The new data shows that ductile left-lateral shearing initiated ca. 28 Ma ago and underwent high-temperature deformation between 28 and 21 Ma, and that slow cooling continued to low-temperatures until 13 Ma ago. The second and third deformations are ductile to brittle, and normal faulting occurred from 4 to 0 Ma.

(3) On a regional scale, the tectonic exhumation of the DCS massif is a part of the tectono-thermal evolution and diachronous exhumation of the metamorphic complexes since 36 Ma in a fan-shaped area in SE Asia that is broadly bounded by the ASRR and Sagaing shear zones. Extrusion-induced strike-slip shearing and rotated normal faulting played important roles in the diachronous cooling and exhumation of the metamorphic complexes in SE Asia.

Table 7. 1 ^{40}Ar - ^{39}Ar step heating data for amphibole, muscovite, biotite and K-feldspar of the Diancang Shan massif

Amphibole														
$^{36}\text{Ar}/^{39}\text{Ar}$	\pm	$^{37}\text{Ar}/^{39}\text{Ar}$	\pm	$^{40}\text{Ar}/^{39}\text{Ar}$	\pm	$^{36}\text{Ar}/^{40}\text{Ar}$	\pm	$^{39}\text{Ar}^{\text{K}}/^{40}\text{Ar}^{\text{K}}$	\pm	$\%^{40}\text{Ar}^{\text{K}}$	$\%^{39}\text{Ar}$	age [Ma]	\pm [Ma]	
Sample: DC11-1-amphibole		Amphibolite		200-355 μm		12 grains		J-Value: 0.007402 \pm 0.000031						
1	0.05184	0.00155	0.6812	0.0212	19.3076	0.1500	0.00268	0.00008	4.011	0.450	20.8	0.5	52.78	5.85
2	0.02917	0.00096	0.0006	0.0076	10.7625	0.0663	0.00271	0.00009	2.116	0.284	19.7	0.9	28.04	3.74
3	0.00390	0.00089	2.4731	0.0314	2.1548	0.0189	0.00181	0.00041	1.143	0.264	53.6	1.0	15.21	3.50
4	0.00244	0.00011	3.1005	0.0188	2.3203	0.0109	0.00105	0.00005	1.783	0.033	77.6	4.9	23.66	0.44
5	0.00194	0.00004	3.1756	0.0188	2.3341	0.0125	0.00083	0.00002	1.949	0.017	84.3	31.2	25.84	0.25
6	0.00178	0.00004	3.2474	0.0166	2.2723	0.0081	0.00078	0.00002	1.939	0.013	86.2	32.0	25.71	0.20
7	0.00101	0.00028	2.8306	0.0125	1.9664	0.0053	0.00052	0.00014	1.832	0.082	94.3	3.5	24.30	1.08
8	0.00113	0.00005	3.0896	0.0072	2.0759	0.0051	0.00055	0.00002	1.924	0.014	93.7	19.9	25.51	0.22
9	0.00270	0.00039	3.2056	0.0268	2.4796	0.0165	0.00109	0.00016	1.873	0.116	76.2	2.7	24.85	1.54
10	0.00126	0.00137	3.1774	0.0448	2.7315	0.0261	0.00046	0.00050	2.548	0.407	94.0	0.7	33.71	5.33
11	0.00068	0.00030	2.9345	0.0286	2.2326	0.0080	0.00030	0.00014	2.205	0.091	99.8	2.6	29.21	1.20
Sample: DC13-1-amphibole		Amphibolite		200-355 μm		12 grains		J-Value: 0.007456 \pm 0.000029						
1	0.26282	0.00878	18.8619	0.4339	80.2529	1.5918	0.00327	0.00009	3.861	2.120	4.8	0.1	51.20	27.72
2	0.10153	0.00385	13.0789	0.1097	32.9777	0.1929	0.00308	0.00012	3.850	1.137	11.6	0.6	51.06	14.86
3	0.04413	0.00256	2.8955	0.0338	13.9496	0.0532	0.00316	0.00018	1.076	0.756	7.7	0.8	14.42	10.09
4	0.01781	0.00338	4.3180	0.0852	8.3939	0.1482	0.00212	0.00040	3.401	1.003	40.5	0.5	45.17	13.17
5	0.01441	0.00064	7.8633	0.0498	5.5285	0.0339	0.00261	0.00012	1.775	0.190	32.1	1.9	23.71	2.53
6	0.00315	0.00006	4.8847	0.0255	2.3470	0.0080	0.00134	0.00002	1.719	0.018	73.9	22.0	22.98	0.26
7	0.00158	0.00008	4.4929	0.0225	2.0873	0.0110	0.00076	0.00004	1.898	0.025	91.8	19.8	25.35	0.35
8	0.00231	0.00007	4.6150	0.0310	2.2733	0.0108	0.00102	0.00003	1.875	0.023	83.2	37.7	25.05	0.32
9	0.00256	0.00008	4.9198	0.0190	2.3117	0.0113	0.00111	0.00004	1.862	0.027	81.2	16.6	24.87	0.37
Sample: DC7-8-amphibole		Amphibolite		200-355 μm		12 grains		J-Value: 0.007364 \pm 0.000031						
1	0.15288	0.00578	3.4121	0.0800	46.4978	0.9072	0.00329	0.00011	1.524	1.512	3.3	0.3	20.14	19.87
2	0.10098	0.00240	1.9970	0.0421	36.7364	0.3482	0.00275	0.00006	7.013	0.665	19.1	0.7	90.85	8.40
3	0.01177	0.00204	3.8745	0.0454	9.1310	0.0964	0.00129	0.00022	5.899	0.610	64.6	0.8	76.72	7.78
4	0.01133	0.00163	4.2032	0.0658	5.9085	0.1294	0.00192	0.00028	2.819	0.492	47.8	1.2	37.07	6.41
5	0.00502	0.00011	5.5685	0.0364	4.0123	0.0142	0.00125	0.00003	2.883	0.035	72.1	18.5	37.90	0.48
6	0.00155	0.00230	5.1735	0.0985	2.2045	0.1201	0.00070	0.00105	2.070	0.693	94.7	0.7	27.30	9.07
7	0.00333	0.00016	5.5955	0.0373	2.6802	0.0130	0.00124	0.00006	2.047	0.048	76.9	13.0	27.00	0.64
8	0.00290	0.00010	5.5946	0.0370	2.5750	0.0131	0.00112	0.00004	2.072	0.033	81.0	27.2	27.32	0.45
9	0.00200	0.00013	5.3157	0.0194	2.3376	0.0111	0.00086	0.00006	2.080	0.041	89.7	12.4	27.43	0.54
10	0.00267	0.00009	5.5649	0.0500	2.4878	0.0150	0.00108	0.00003	2.048	0.029	82.9	20.2	27.01	0.40
11	0.00478	0.00048	5.9648	0.0437	2.9023	0.0370	0.00165	0.00017	1.868	0.147	64.7	2.4	24.65	1.94
12	0.00304	0.00051	5.4275	0.0395	2.4355	0.0180	0.00125	0.00021	1.878	0.152	77.7	2.6	24.78	1.99
Sample: DC27-2-amphibole		Amphibolite		200-355 μm		12 grains		J-Value: 0.007501 \pm 0.000026						
1	0.00755	0.00081	3.0811	0.0221	3.4824	0.0194	0.00217	0.00023	1.432	0.240	41.4	3.8	19.28	3.21
2	0.00907	0.00040	4.8613	0.0111	3.8111	0.0094	0.00238	0.00010	1.433	0.119	37.8	7.2	19.29	1.59
3	0.00432	0.00043	5.6245	0.0344	1.6060	0.0244	0.00269	0.00027	0.680	0.129	42.9	5.9	9.17	1.74
4	0.00387	0.00034	6.1743	0.0408	1.3795	0.0163	0.00281	0.00025	0.622	0.101	45.8	7.9	8.40	1.37
5	0.00347	0.00016	7.9337	0.0677	1.4833	0.0111	0.00234	0.00011	0.962	0.047	65.7	18.9	12.98	0.64
6	0.00427	0.00015	7.7266	0.0582	1.5328	0.0096	0.00279	0.00010	0.762	0.047	50.3	18.4	10.28	0.63
7	0.00250	0.00022	6.1322	0.0390	1.4233	0.0175	0.00176	0.00016	1.070	0.068	76.3	17.0	14.43	0.91
8	0.00480	0.00029	8.8922	0.0466	1.6734	0.0223	0.00287	0.00017	0.823	0.088	49.7	9.6	11.10	1.18
9	0.00682	0.00039	15.4000	0.0699	2.1152	0.0255	0.00322	0.00019	1.109	0.119	52.6	8.1	14.94	1.59
10	0.00850	0.00070	17.4220	0.1189	3.1713	0.0502	0.00268	0.00022	1.812	0.215	57.0	3.3	24.36	2.87
Sample: DC18-3-amphibole		Honblende-granite		200-355 μm		10 grains		J-Value: 0.007462 \pm 0.0000281						
1	1.88129	0.14949	3.7064	0.3808	800.1076	58.7164	0.00235	0.00007	244.964	24.780	30.5	0.0	1875.46	118.05
2	0.65291	0.04794	0.9890	0.1903	221.6063	10.3402	0.00295	0.00017	28.728	11.098	13.0	0.0	350.40	123.04
3	0.20807	0.01087	0.2262	0.3328	68.6821	0.8604	0.00303	0.00015	7.186	3.125	10.5	0.1	94.23	39.94
4	0.20758	0.01450	1.1254	0.3857	84.2645	2.5506	0.00246	0.00016	22.989	3.932	27.3	0.1	285.64	45.20
5	0.01536	0.00103	2.5948	0.0290	6.8339	0.0356	0.00225	0.00015	2.446	0.306	35.9	0.8	32.63	4.05
6	0.00247	0.00007	2.8730	0.0108	2.3590	0.0110	0.00105	0.00003	1.796	0.024	76.9	13.7	24.02	0.33
7	0.00149	0.00002	2.8916	0.0148	1.9742	0.0064	0.00076	0.00001	1.702	0.009	87.2	52.1	22.77	0.15
8	0.00110	0.00007	3.1207	0.0235	1.8911	0.0106	0.00058	0.00004	1.751	0.024	93.7	10.8	23.42	0.33
9	0.00092	0.00006	2.9853	0.0118	1.8162	0.0114	0.00051	0.00003	1.720	0.020	95.9	15.4	23.01	0.28
10	0.00114	0.00013	3.5054	0.0236	1.8050	0.0171	0.00063	0.00007	1.677	0.041	94.1	6.2	22.44	0.56
11	0.00129	0.00147	4.1608	0.0656	1.9145	0.0839	0.00068	0.00077	1.787	0.442	94.4	0.7	23.89	5.87
Sample: DC3-3-amphibole		Amphibolite		200-355 μm		12 grains		J-Value: 0.007286 \pm 0.000029						
1	0.48200	0.00577	15.2379	0.1521	151.0087	1.4875	0.00319	0.00003	9.656	1.199	6.3	1.0	122.65	14.73
2	0.14666	0.00131	9.8967	0.0758	43.8121	0.3125	0.00335	0.00002	1.114	0.312	2.5	3.5	14.58	4.07
3	0.07241	0.00060	5.1422	0.0325	22.3227	0.1305	0.00324	0.00002	1.243	0.152	5.6	4.3	16.27	1.98
4	0.04103	0.00071	7.8424	0.0675	12.9289	0.0913	0.00317	0.00005	1.306	0.210	10.1	3.5	17.09	2.73
5	0.00691	0.00011	4.5499	0.0319	3.2605	0.0152	0.00212	0.00003	1.498	0.034	46.2	18.1	19.58	0.44
6	0.00580	0.00012	4.1202	0.0424	2.9533	0.0291	0.00197	0.00004	1.489	0.041	50.8	17.5	19.47	0.54
7	0.00618	0.00015	4.4470	0.0514	2.8773	0.0201	0.00215	0.00005	1.323	0.046	46.3	7.0	17.31	0.61
8	0.00443	0.00029	4.7078	0.0525	2.3310	0.0303	0.00190	0.00013	1.313	0.089	56.8	7.4	17.18	1.17
9	0.00287	0.00030	4.3299	0.0445	1.9353	0.0173	0.00148	0.00016	1.354	0.091	70.7	8.9	17.70	1.19
10	0.00336	0.00011	4.5654	0.0350	2.1184	0.0130	0.00159	0.00005	1.407	0.036	67.1	18.9	18.40	0.47
11	0.00241	0.00025	3.9353	0.0589	2.2272	0.0486	0.00108	0.00011	1.754	0.087	79.5	8.4	22.91	1.13
12	0.00290	0.00129	3.8953	0.0481	1.7745	0.0831	0.00164	0.00073	1.152	0.390	65.7	1.4	15.07	5.08

Chapter 7: High-grade metamorphic complex, geochronology, cooling and exhumation

Muscovite

	$^{36}\text{Ar}/^{39}\text{Ar}$	\pm	$^{37}\text{Ar}/^{39}\text{Ar}$	\pm	$^{40}\text{Ar}/^{39}\text{Ar}$	\pm	$^{36}\text{Ar}/^{40}\text{Ar}$	\pm	$^{39}\text{Ar}^{\text{K}}/^{40}\text{Ar}^*$	\pm	$\%^{40}\text{Ar}^*$	$\%^{39}\text{Ar}$	age [Ma]	\pm [Ma]
Sample: DC11-4-Muscovite	Leucogranite		200-355 μm		10 grains	J-Value: 0.007419 \pm 0.000031								
1	0.00902	0.00010	0.0206	0.0349	3.5409	0.0111	0.00255	0.00003	0.849	0.029	24.2	2.7	11.33	0.39
2	0.00097	0.00073	0.1460	0.2420	1.7394	0.0105	0.00056	0.00042	1.436	0.217	83.8	0.4	19.12	2.88
3	0.00221	0.00003	0.0021	0.0348	2.0177	0.0024	0.00110	0.00001	1.337	0.009	67.2	11.5	17.81	0.14
4	0.00073	0.00001	0.0004	0.0061	1.5422	0.0025	0.00048	0.00001	1.299	0.004	85.7	65.6	17.30	0.09
5	0.00003	0.00038	0.0022	0.0196	1.2397	0.0068	0.00003	0.00031	1.204	0.113	99.2	1.3	16.04	1.51
6	0.00006	0.00011	0.0859	0.0250	1.2666	0.0029	0.00005	0.00009	1.227	0.034	99.0	3.8	16.35	0.45
7	0.00005	0.00016	0.0838	0.0310	1.2541	0.0037	0.00004	0.00013	1.219	0.048	99.3	3.3	16.24	0.63
8	0.00002	0.00025	0.0177	0.0915	1.2785	0.0046	0.00002	0.00020	1.246	0.075	99.6	2.7	16.61	0.99
9	0.00035	0.00015	0.0445	0.0416	1.3754	0.0051	0.00026	0.00011	1.248	0.046	92.5	2.6	16.63	0.61
10	0.00036	0.00012	0.0846	0.0322	1.3635	0.0043	0.00026	0.00008	1.236	0.034	92.5	3.3	16.47	0.46
11	0.00009	0.00012	0.1052	0.0268	1.3371	0.0074	0.00007	0.00009	1.291	0.035	98.5	2.9	17.19	0.47
Sample: DC12-3-Muscovite	Mylonitic granite		200-355 μm		12 grains	J-Value: 0.007427 \pm 0.000031								
1	0.00685	0.00187	0.0068	1.5386	4.3315	0.0447	0.00158	0.00043	2.281	0.562	53.0	0.2	30.31	7.40
2	0.00442	0.00035	0.0127	0.4106	4.0803	0.0162	0.00108	0.00009	2.748	0.108	67.8	0.8	36.45	1.43
3	0.00366	0.00018	0.1998	0.0538	5.3670	0.0088	0.00068	0.00003	4.272	0.055	80.0	2.0	56.35	0.75
4	0.00041	0.00003	0.0006	0.0192	2.0282	0.0029	0.00020	0.00001	1.882	0.009	94.0	17.6	25.04	0.15
5	0.00031	0.00001	0.0004	0.0120	1.8502	0.0035	0.00017	0.00001	1.732	0.005	95.0	28.0	23.07	0.12
6	0.00028	0.00002	0.0006	0.0183	1.8216	0.0026	0.00015	0.00001	1.713	0.006	95.4	18.4	22.81	0.12
7	0.00025	0.00002	0.0007	0.0238	1.7965	0.0021	0.00014	0.00001	1.696	0.008	95.8	14.2	22.58	0.14
8	0.00033	0.00004	0.0012	0.0376	2.0767	0.0027	0.00016	0.00002	1.953	0.011	95.3	9.0	25.98	0.18
9	0.00043	0.00007	0.0024	0.0768	1.8701	0.0185	0.00023	0.00004	1.717	0.028	93.1	4.4	22.86	0.38
10	0.00003	0.00006	0.0030	0.0188	1.8023	0.0032	0.00002	0.00003	1.766	0.018	99.4	5.5	23.51	0.26
Sample: DC5-2-Muscovite	Augen gneisses		200-355 μm		10 grains	J-Value: 0.0073211 \pm 0.000030								
1	0.14481	0.02843	0.1316	3.1469	36.0069	2.3389	0.00402	0.00075	-68.03	-7.96	-18.91	0.0	-92.17	110.64
2	0.00169	0.00006	0.0004	0.0067	2.1414	0.0059	0.00079	0.00003	1.617	0.018	76.4	30.6	21.23	0.25
3	0.00142	0.00019	0.0065	0.1052	2.0044	0.0048	0.00071	0.00009	1.558	0.055	78.8	2.0	20.46	0.73
4	0.00103	0.00008	0.0012	0.0188	1.9354	0.0056	0.00053	0.00004	1.606	0.023	84.1	10.9	21.09	0.32
5	0.00045	0.00002	0.0004	0.0108	1.7515	0.0020	0.00026	0.00001	1.591	0.005	92.3	28.3	20.90	0.11
6	0.00043	0.00003	0.0007	0.0187	1.7600	0.0030	0.00025	0.00002	1.606	0.009	92.6	16.4	21.08	0.14
7	0.00025	0.00003	0.0010	0.0258	1.7426	0.0027	0.00014	0.00002	1.642	0.010	95.7	11.9	21.56	0.16
Sample: DC8-7-Muscovite	Amphibolite		200-355 μm		10 grains	J-Value: 0.0073347 \pm 0.000031								
1	0.02732	0.00164	0.2904	1.1353	9.4995	0.0646	0.00288	0.00017	1.419	0.490	15.0	0.2	18.79	6.45
2	0.00393	0.00016	0.0020	0.0895	2.2007	0.0059	0.00178	0.00007	1.014	0.047	46.6	2.5	13.43	0.62
3	0.00251	0.00006	0.0024	0.0222	1.9148	0.0036	0.00131	0.00003	1.146	0.018	60.7	12.2	15.18	0.25
4	0.00115	0.00013	0.0175	0.1625	1.3381	0.0038	0.00086	0.00010	0.974	0.041	74.3	1.7	12.92	0.55
5	0.00078	0.00003	0.0019	0.0173	1.3345	0.0024	0.00058	0.00002	1.078	0.009	82.5	15.6	14.29	0.14
6	0.00057	0.00018	0.0117	0.1093	1.1781	0.0031	0.00049	0.00015	0.983	0.053	85.4	2.5	13.03	0.70
7	0.00129	0.00004	0.0026	0.0240	1.4243	0.0013	0.00091	0.00003	1.017	0.012	72.8	11.3	13.48	0.17
8	0.00031	0.00003	0.0018	0.0164	1.0689	0.0014	0.00029	0.00003	0.952	0.010	91.3	16.5	12.62	0.14
9	0.00029	0.00014	0.0107	0.1000	1.0690	0.0025	0.00027	0.00014	0.957	0.043	91.9	2.7	12.69	0.57
10	0.00031	0.00001	0.0014	0.0063	1.0613	0.0013	0.00030	0.00001	0.942	0.003	91.1	28.4	12.49	0.07
11	0.00051	0.00011	0.0167	0.0254	1.1485	0.0032	0.00045	0.00010	0.972	0.034	86.6	2.5	12.88	0.45
12	0.00041	0.00009	0.0469	0.0139	1.1242	0.0027	0.00037	0.00008	0.978	0.026	89.1	2.9	12.97	0.35
13	0.00118	0.00022	0.0236	0.0718	1.3125	0.0040	0.00090	0.00017	0.937	0.066	72.9	1.0	12.43	0.87

Biotite

	$^{36}\text{Ar}/^{39}\text{Ar}$	\pm	$^{37}\text{Ar}/^{39}\text{Ar}$	\pm	$^{40}\text{Ar}/^{39}\text{Ar}$	\pm	$^{36}\text{Ar}/^{40}\text{Ar}$	\pm	$^{39}\text{Ar}^{\text{K}}/^{40}\text{Ar}^*$	\pm	$\%^{40}\text{Ar}^*$	$\%^{39}\text{Ar}$	age [Ma]	\pm [Ma]
Sample: DC11-3/4-Biotite	Granodiorite		200-355 μm		10 grains	J-Value: 0.007402 \pm 0.000031								
1	0.67994	0.05037	0.1123	0.5381	181.9728	10.9314	0.00374	0.00016	-18.971	-8.806	-10.43	0.0	-273.00	136.82
2	0.00356	0.00011	0.0869	0.0029	2.5836	0.0050	0.00138	0.00004	1.511	0.033	59.1	4.5	20.06	0.44
3	0.00765	0.00049	0.1057	0.0069	4.0959	0.0092	0.00187	0.00012	1.816	0.146	44.6	1.6	24.10	1.93
4	0.00202	0.00007	0.0002	0.0012	1.3801	0.0025	0.00147	0.00005	0.756	0.022	55.9	9.3	10.07	0.29
5	0.00047	0.00003	0.0001	0.0010	0.8475	0.0014	0.00055	0.00004	0.683	0.009	83.2	19.3	9.09	0.13
6	0.00020	0.00003	0.0001	0.0014	0.7760	0.0011	0.00026	0.00003	0.690	0.008	92.0	14.6	9.19	0.11
7	0.00056	0.00006	0.0009	0.0063	0.8635	0.0016	0.00065	0.00007	0.672	0.018	80.3	10.9	8.95	0.24
8	0.00022	0.00006	0.0001	0.0154	0.7699	0.0016	0.00029	0.00008	0.678	0.017	91.2	10.8	9.03	0.23
9	0.00026	0.00007	0.0030	0.0010	0.7442	0.0017	0.00035	0.00009	0.641	0.020	89.3	10.7	8.54	0.27
10	0.00024	0.00010	0.0008	0.0011	0.7729	0.0014	0.00031	0.00013	0.676	0.030	90.6	7.7	9.01	0.41
11	0.00069	0.00046	0.0176	0.0052	1.0522	0.0039	0.00065	0.00044	0.824	0.136	80.4	2.2	10.97	1.80
12	0.00018	0.00006	0.0050	0.0008	0.7560	0.0012	0.00024	0.00008	0.676	0.017	92.6	8.3	9.00	0.24
Sample: DC13-1-Biotite	Lamprophyre		200-355 μm		12 grains	J-Value: 0.007449 \pm 0.000029								
1	0.33802	0.06277	0.4658	1.0043	115.1033	9.5424	0.00294	0.00049	15.228	16.698	13.2	0.0	193.85	201.54
2	0.11815	0.00292	0.0000	0.0570	39.0083	0.1187	0.00303	0.00007	4.068	0.856	10.4	0.9	53.85	11.17
3	0.02527	0.00076	0.0144	0.0008	8.6479	0.0182	0.00292	0.00009	1.154	0.226	13.4	2.9	15.45	3.01
4	0.01373	0.00098	0.2185	0.0073	6.0124	0.0194	0.00228	0.00016	1.944	0.289	32.5	1.5	25.93	3.83
5	0.00362	0.00008	0.0071	0.0014	1.7565	0.0031	0.00206	0.00004	0.661	0.023	38.2	25.3	8.86	0.31
6	0.00159	0.00063	0.0007	0.0086	1.0047	0.0055	0.00158	0.00062	0.508	0.185	51.9	2.1	6.81	2.48
7	0.00148	0.00022	0.0109	0.0037	0.8894	0.0023	0.00166	0.00024	0.427	0.064	49.5	7.0	5.73	0.85

Chapter 7: High-grade metamorphic complex, geochronology, cooling and exhumation

8	0.00102	0.00005	0.0000	0.0007	0.8099	0.0018	0.00125	0.00006	0.483	0.014	61.7	30.9	6.48	0.19
9	0.00095	0.00005	0.0189	0.0013	0.7880	0.0016	0.00121	0.00006	0.482	0.015	63.3	18.5	6.46	0.20
10	0.00220	0.00019	0.0283	0.0022	1.1170	0.0023	0.00197	0.00017	0.443	0.058	40.6	8.4	5.95	0.77
11	0.00178	0.00078	0.0269	0.0085	1.1033	0.0066	0.00161	0.00071	0.552	0.230	51.3	2.4	7.41	3.08

Sample: DC7-8-Biotite Amphibolite 200-355 μm 10 grains J-Value: 0.007354 \pm 0.000031

1	0.56286	0.11057	0.2101	1.5650	210.2093	31.3558	0.00268	0.00034	-9.316	-28.145	-4.43	0.0	-128.04	400.89
2	0.06002	0.00342	0.0012	0.0553	25.1212	0.2793	0.00239	0.00013	1.689	1.309	6.7	0.3	22.27	17.15
3	0.00722	0.00047	0.0007	0.0989	3.7397	0.0081	0.00193	0.00013	0.896	0.184	24.1	2.1	11.85	2.43
4	0.00173	0.00009	0.0000	0.0086	1.7374	0.0032	0.00100	0.00005	1.036	0.034	60.6	9.8	13.70	0.45
5	0.00089	0.00004	0.0001	0.0012	1.3415	0.0017	0.00067	0.00003	0.966	0.015	73.5	26.1	12.78	0.20
6	0.00095	0.00003	0.0000	0.0050	1.2679	0.0017	0.00075	0.00003	0.870	0.013	70.1	19.2	11.51	0.17
7	0.00090	0.00022	0.0044	0.0016	1.2166	0.0027	0.00074	0.00018	0.839	0.084	70.5	6.3	11.09	1.11
8	0.00054	0.00006	0.0040	0.0012	1.1520	0.0029	0.00047	0.00005	0.915	0.023	81.3	10.3	12.10	0.30
9	0.00053	0.00005	0.0001	0.0012	1.1228	0.0018	0.00048	0.00004	0.888	0.019	81.0	13.3	11.74	0.25
10	0.00035	0.00008	0.0085	0.0021	1.0479	0.0029	0.00034	0.00008	0.884	0.033	86.5	5.6	11.69	0.44
11	0.00049	0.00012	0.0034	0.0038	1.1111	0.0027	0.00044	0.00011	0.894	0.048	82.4	3.5	11.82	0.64
12	0.00000	0.00031	0.0006	0.0055	1.1605	0.0029	0.00000	0.00026	1.134	0.119	100.0	1.9	14.98	1.57
13	0.00006	0.00050	0.0002	0.0061	1.5245	0.0060	0.00004	0.00033	1.476	0.194	98.5	1.5	19.48	2.54

Sample: DC23-4-Biotite Porphyritic monzonite granite 200-355 μm 10 grains J-Value: 0.007497 \pm 0.000026

1	0.72379	0.01080	0.0061	0.1293	238.3230	1.7619	0.00304	0.00004	24.416	2.784	10.2	0.2	303.26	31.84
2	0.02334	0.00063	0.1113	0.0186	8.3607	0.0337	0.00279	0.00007	1.444	0.185	17.3	0.8	19.42	2.48
3	0.00566	0.00024	0.0005	0.0310	2.1814	0.0042	0.00259	0.00011	0.483	0.071	22.4	2.6	6.53	0.96
4	0.00334	0.00028	0.0008	0.0385	1.4432	0.0047	0.00232	0.00019	0.428	0.082	30.2	1.7	5.79	1.11
5	0.00092	0.00004	0.0043	0.0008	0.8885	0.0015	0.00103	0.00004	0.591	0.011	68.6	10.2	7.98	0.15
6	0.00024	0.00003	0.0033	0.0138	0.7052	0.0031	0.00034	0.00004	0.608	0.009	89.6	17.1	8.21	0.12
7	0.00021	0.00007	0.0068	0.0186	0.6695	0.0018	0.00032	0.00011	0.581	0.021	90.3	8.3	7.84	0.29
8	0.00025	0.00004	0.0001	0.0205	0.6868	0.0011	0.00036	0.00006	0.587	0.012	89.0	8.8	7.93	0.17
9	0.00012	0.00008	0.0038	0.0023	0.6761	0.0015	0.00018	0.00012	0.613	0.025	94.4	5.2	8.28	0.34
10	0.00016	0.00008	0.0006	0.0020	0.6678	0.0057	0.00024	0.00012	0.593	0.024	92.5	6.7	8.01	0.32
11	0.00037	0.00006	0.0002	0.0012	0.7603	0.0018	0.00049	0.00007	0.624	0.017	85.1	9.9	8.43	0.22
12	0.00004	0.00007	0.0152	0.0018	0.6397	0.0015	0.00006	0.00012	0.603	0.022	98.4	7.0	8.14	0.30
13	0.00012	0.00004	0.0993	0.0014	0.6344	0.0010	0.00019	0.00006	0.578	0.012	95.1	12.1	7.80	0.17
14	0.00014	0.00010	0.2274	0.0047	0.6726	0.0029	0.00021	0.00014	0.620	0.029	95.9	3.6	8.36	0.39
15	0.00034	0.00009	0.0620	0.0024	0.6627	0.0014	0.00052	0.00013	0.539	0.026	84.8	5.8	7.28	0.36

Sample: DC3-6-Biotite Mica-schist 200-355 μm 10 grains J-Value: 0.007310 \pm 0.000030

1	0.36454	0.01118	0.5399	0.1833	130.2969	2.3826	0.00280	0.00007	22.592	2.707	17.3	0.1	275.75	30.66
2	0.06695	0.00496	0.0130	0.0975	30.0289	0.2809	0.00223	0.00016	10.219	1.462	34.1	0.2	129.97	17.95
3	0.01476	0.00119	0.0089	0.0125	5.2254	0.0236	0.00282	0.00023	0.838	0.352	16.1	1.2	11.02	4.61
4	0.00437	0.00013	0.0033	0.0106	1.8844	0.0031	0.00232	0.00007	0.566	0.039	30.5	7.1	7.45	0.51
5	0.00252	0.00022	0.0016	0.0045	1.1370	0.0050	0.00221	0.00019	0.367	0.064	33.0	2.9	4.83	0.84
6	0.00157	0.00007	0.0000	0.0014	0.8996	0.0018	0.00174	0.00008	0.410	0.021	46.9	8.8	5.39	0.27
7	0.00114	0.00005	0.0001	0.0044	0.8343	0.0012	0.00136	0.00005	0.472	0.014	58.4	16.9	6.21	0.18
8	0.00074	0.00012	0.0066	0.0023	0.7809	0.0021	0.00094	0.00015	0.538	0.034	71.3	7.1	7.07	0.45
9	0.00088	0.00006	0.0074	0.0015	0.7540	0.0016	0.00117	0.00007	0.467	0.016	64.2	12.9	6.14	0.22
10	0.00074	0.00005	0.0126	0.0020	0.7398	0.0018	0.00100	0.00007	0.495	0.015	69.4	11.2	6.52	0.20
11	0.00121	0.00005	0.0651	0.0015	2.1214	0.0022	0.00057	0.00002	1.743	0.014	83.2	15.6	22.84	0.21
12	0.00075	0.00004	0.3968	0.0035	7.7575	0.0103	0.00010	0.00001	7.536	0.016	97.5	13.9	96.75	0.43
13	0.00448	0.00041	0.2327	0.0110	6.8003	0.0185	0.00066	0.00006	5.466	0.122	80.7	1.5	70.68	1.57
14	0.00439	0.00085	0.2043	0.0191	6.6296	0.0230	0.00066	0.00013	5.320	0.253	80.6	0.7	68.83	3.22

K-feldspar

	$^{36}\text{Ar}/^{39}\text{Ar}$	\pm	$^{37}\text{Ar}/^{39}\text{Ar}$	\pm	$^{40}\text{Ar}/^{39}\text{Ar}$	\pm	$^{36}\text{Ar}/^{40}\text{Ar}$	\pm	$^{39}\text{Ar}^{\text{K}/40}\text{Ar}^*$	\pm	$\%^{40}\text{Ar}^*$	$\%^{39}\text{Ar}$	age [Ma]	\pm [Ma]
Sample: DC11-2/2-K-feldspar	Pegmatite		200-355 μm		10 grains		J-Value: 0.007479 \pm 0.000027							
1	0.04264	0.00077	0.0004	0.0059	18.0414	0.0421	0.00236	0.00004	5.415	0.226	30.1	0.8	71.63	2.95
2	0.00076	0.00003	0.0026	0.0003	0.5733	0.0009	0.00133	0.00006	0.322	0.010	58.9	6.8	4.34	0.13
3	0.00084	0.00002	0.0019	0.0004	0.6288	0.0006	0.00133	0.00003	0.355	0.006	59.0	7.5	4.79	0.08
4	0.00010	0.00008	0.0005	0.0014	0.3884	0.0011	0.00025	0.00020	0.333	0.023	92.0	1.4	4.48	0.31
5	0.00120	0.00002	0.0014	0.0002	0.8022	0.0009	0.00149	0.00003	0.422	0.006	54.4	12.4	5.68	0.09
6	0.00073	0.00001	0.0012	0.0002	0.6796	0.0011	0.00108	0.00002	0.437	0.004	66.9	15.6	5.89	0.05
7	0.00072	0.00004	0.0002	0.0004	0.6722	0.0015	0.00107	0.00005	0.434	0.011	67.2	5.1	5.84	0.15
8	0.00069	0.00001	0.0011	0.0003	0.6780	0.0006	0.00102	0.00002	0.447	0.004	68.7	13.7	6.02	0.06
9	0.00076	0.00002	0.0016	0.0002	0.6965	0.0006	0.00109	0.00003	0.445	0.006	66.4	12.7	5.99	0.08
10	0.00085	0.00001	0.0004	0.0002	0.7238	0.0013	0.00117	0.00002	0.447	0.004	64.1	19.7	6.02	0.06
11	0.00086	0.00005	0.0012	0.0006	0.7175	0.0011	0.00120	0.00007	0.438	0.014	63.3	3.2	5.90	0.20
12	0.00204	0.00057	0.0008	0.0080	1.0262	0.0086	0.00198	0.00055	0.398	0.167	39.8	0.2	5.36	2.25
13	0.00120	0.00012	0.0005	0.0053	0.8726	0.0033	0.00137	0.00014	0.492	0.036	58.2	0.8	6.63	0.48

Sample: DC12-3-K-feldspar Mylonitic granite 200-355 μm 7 grains J-Value: 0.007435 \pm 0.000030

1	0.00361	0.00014	0.1030	0.0035	2.6517	0.0061	0.00136	0.00005	1.565	0.041	59.6	1.0	20.88	0.55
2	0.00856	0.00017	0.0212	0.0037	23.6295	0.0401	0.00036	0.00001	21.075	0.062	89.3	1.4	262.61	1.22
3	0.00054	0.00004	0.0016	0.0006	1.2284	0.0025	0.00044	0.00003	1.041	0.012	86.6	3.6	13.91	0.17
4	0.00019	0.00003	0.0013	0.0004	0.5673	0.0007	0.00034	0.00005	0.484	0.008	89.5	5.8	6.48	0.11
5	0.00004	0.00007	0.0015	0.0011	0.4186	0.0010	0.00009	0.00016	0.380	0.020	97.0	2.6	5.10	0.27

Chapter 7: High-grade metamorphic complex, geochronology, cooling and exhumation

6	0.00011	0.00002	0.0009	0.0005	0.7657	0.0006	0.00014	0.00002	0.707	0.005	95.6	6.5	9.45	0.07
7	0.00002	0.00002	0.0045	0.0005	0.4575	0.0011	0.00004	0.00005	0.426	0.007	98.9	5.7	5.71	0.10
8	0.00008	0.00003	0.0040	0.0006	0.4628	0.0007	0.00018	0.00005	0.412	0.008	94.5	4.0	5.52	0.10
9	0.00014	0.00002	0.0030	0.0005	0.6658	0.0007	0.00020	0.00003	0.599	0.005	93.7	5.5	8.02	0.08
10	0.00023	0.00002	0.0015	0.0004	1.4005	0.0024	0.00016	0.00002	1.307	0.007	95.2	6.4	17.45	0.11
11	0.00060	0.00002	0.0011	0.0003	2.9003	0.0039	0.00021	0.00001	2.696	0.006	93.8	13.8	35.80	0.16
12	0.00044	0.00001	0.0015	0.0002	2.6426	0.0041	0.00017	0.00000	2.485	0.005	95.0	13.9	33.03	0.15
13	0.00048	0.00002	0.0013	0.0003	2.4836	0.0013	0.00019	0.00001	2.316	0.006	94.2	9.2	30.79	0.15
14	0.00073	0.00003	0.0022	0.0007	2.7871	0.0028	0.00026	0.00001	2.544	0.009	92.2	5.8	33.80	0.18
15	0.00060	0.00004	0.0006	0.0006	2.8175	0.0030	0.00021	0.00001	2.612	0.011	93.6	4.0	34.70	0.20
16	0.00103	0.00005	0.0013	0.0006	2.8155	0.0064	0.00037	0.00002	2.485	0.015	89.1	3.1	33.03	0.24
17	0.00102	0.00006	0.0021	0.0010	2.3878	0.0028	0.00043	0.00002	2.060	0.017	87.2	2.2	27.42	0.25
18	0.00145	0.00022	0.0003	0.0034	2.8300	0.0081	0.00051	0.00008	2.374	0.065	84.7	0.8	31.57	0.86
19	0.00130	0.00007	0.0023	0.0011	2.8559	0.0045	0.00045	0.00003	2.445	0.023	86.4	1.8	32.51	0.32
20	0.00128	0.00006	0.0025	0.0009	2.5715	0.0026	0.00050	0.00002	2.168	0.017	85.2	2.7	28.85	0.26

Sample: DC5-2-K-feldspar	Augen-gneisses			200-355 μm	7 grains	J-Value: 0.007333 \pm 0.000031								
1	0.35760	0.03095	0.4790	0.4856	267.1777	13.5691	0.00134	0.00009	161.558	11.060	60.5	0.0	1409.86	67.10
2	0.02443	0.00048	0.0024	0.0049	28.6459	0.0476	0.00085	0.00002	21.400	0.145	74.8	0.6	262.97	1.95
3	0.00089	0.00004	0.0166	0.0010	1.4874	0.0017	0.00060	0.00002	1.199	0.011	82.1	5.6	15.80	0.16
4	0.00025	0.00002	0.0174	0.0006	0.4976	0.0007	0.00050	0.00004	0.398	0.005	84.6	6.2	5.26	0.07
5	0.00022	0.00004	0.0103	0.0013	0.4365	0.0010	0.00050	0.00009	0.346	0.011	84.5	3.3	4.58	0.15
6	0.00028	0.00001	0.0052	0.0004	0.6822	0.0006	0.00041	0.00002	0.573	0.003	87.4	14.5	7.57	0.06
7	0.00030	0.00002	0.0039	0.0003	0.7313	0.0009	0.00041	0.00003	0.616	0.006	87.4	8.7	8.13	0.09
8	0.00047	0.00002	0.0035	0.0003	1.1757	0.0007	0.00040	0.00001	1.012	0.005	88.0	14.7	13.34	0.08
9	0.00051	0.00001	0.0019	0.0001	1.2079	0.0007	0.00042	0.00001	1.030	0.003	87.2	26.2	13.58	0.07
10	0.00030	0.00002	0.0019	0.0004	1.0741	0.0012	0.00028	0.00002	0.960	0.005	91.7	7.2	12.66	0.08
11	0.00042	0.00002	0.0022	0.0004	1.2368	0.0010	0.00034	0.00002	1.085	0.006	89.7	7.2	14.30	0.10
12	0.00029	0.00009	0.0085	0.0023	1.0799	0.0019	0.00027	0.00009	0.969	0.027	92.0	1.3	12.78	0.36
13	0.00001	0.00009	0.0071	0.0021	0.9994	0.0020	0.00001	0.00009	0.969	0.028	99.7	1.3	12.78	0.37
14	0.00014	0.00014	0.0053	0.0027	1.1132	0.0046	0.00012	0.00013	1.046	0.042	96.3	1.3	13.79	0.55
15	0.00041	0.00007	0.0017	0.0026	1.1353	0.0023	0.00036	0.00006	0.987	0.022	89.0	1.6	13.01	0.29
16	0.00066	0.00045	0.0183	0.0136	1.0953	0.0094	0.00060	0.00041	0.876	0.134	82.0	0.3	11.55	1.76

Sample: DC8-7-K-feldspar	Pegmatite			200-355 μm	7 grains	J-Value: 0.007393 \pm 0.000031								
1	0.38774	0.00686	0.1442	0.0381	169.8893	1.6022	0.00228	0.00003	55.299	1.798	32.6	0.1	618.39	17.17
2	0.07032	0.00276	0.1952	0.0677	25.3382	0.2284	0.00278	0.00011	4.545	0.796	18.0	0.1	59.63	10.28
3	0.01218	0.00078	0.1584	0.0076	5.2150	0.0144	0.00233	0.00015	1.601	0.230	30.9	0.5	21.23	3.04
4	0.00350	0.00010	0.1246	0.0022	1.5827	0.0025	0.00221	0.00006	0.531	0.029	34.1	3.6	7.07	0.39
5	0.00185	0.00005	0.1535	0.0018	0.9933	0.0012	0.00186	0.00005	0.431	0.015	44.6	6.0	5.74	0.20
6	0.00146	0.00009	0.2024	0.0029	0.9451	0.0028	0.00154	0.00009	0.502	0.025	54.6	4.7	6.68	0.34
7	0.00234	0.00004	0.1660	0.0017	1.3945	0.0012	0.00168	0.00003	0.688	0.012	50.3	7.9	9.15	0.17
8	0.00133	0.00003	0.0532	0.0003	1.1226	0.0011	0.00119	0.00002	0.705	0.008	64.3	41.6	9.38	0.11
9	0.00066	0.00002	0.0495	0.0005	0.9085	0.0010	0.00073	0.00002	0.690	0.005	78.2	27.5	9.18	0.08
10	0.00085	0.00003	0.1283	0.0017	0.9360	0.0012	0.00091	0.00004	0.668	0.010	73.4	6.7	8.88	0.14
11	0.00001	0.00022	0.0337	0.0046	0.9500	0.0028	0.00001	0.00024	0.922	0.066	99.9	1.4	12.26	0.88

Sample: DC23-4-K-feldspar	Porphyritic monzonite granite				200-355 μm	7 grains	J-Value: 0.007493 \pm 0.000026								
1	1.56280	0.70141	5.7713	4.1177	1318.1425	551.3491	0.00119	0.00019	859.738	368.725	65.0	0.0	3621.15	669.81	
2	0.05423	0.00110	0.0000	0.0380	50.1420	0.1143	0.00108	0.00002	34.090	0.334	68.0	0.4	410.40	3.81	
3	0.00189	0.00005	0.0139	0.0010	1.6896	0.0035	0.00112	0.00003	1.106	0.016	66.5	2.7	14.89	0.22	
4	0.00045	0.00002	0.0112	0.0003	0.6119	0.0006	0.00074	0.00003	0.452	0.006	77.3	7.9	6.10	0.08	
5	0.00023	0.00001	0.0087	0.0003	0.4922	0.0004	0.00046	0.00002	0.400	0.003	85.8	9.8	5.39	0.05	
6	0.00040	0.00002	0.0053	0.0002	0.5268	0.0005	0.00075	0.00003	0.383	0.005	76.7	8.9	5.18	0.06	
7	0.00048	0.00003	0.0040	0.0006	0.5845	0.0016	0.00082	0.00005	0.417	0.009	74.7	4.5	5.63	0.12	
8	0.00077	0.00001	0.0029	0.0002	0.8394	0.0007	0.00091	0.00002	0.587	0.004	72.2	15.8	7.92	0.06	
9	0.00080	0.00001	0.0014	0.0001	0.9207	0.0005	0.00087	0.00001	0.659	0.003	73.7	21.8	8.88	0.05	
10	0.00057	0.00001	0.0012	0.0002	0.8268	0.0006	0.00069	0.00001	0.632	0.003	79.0	15.8	8.52	0.05	
11	0.00061	0.00002	0.0014	0.0006	0.8212	0.0014	0.00074	0.00003	0.615	0.007	77.4	4.1	8.30	0.10	
12	0.00038	0.00003	0.0018	0.0005	0.6807	0.0008	0.00055	0.00004	0.543	0.008	83.1	4.0	7.33	0.11	
13	0.00022	0.00004	0.0001	0.0009	0.6325	0.0010	0.00035	0.00006	0.541	0.012	89.2	2.9	7.29	0.16	
14	0.00015	0.00007	0.0020	0.0018	0.6158	0.0072	0.00024	0.00012	0.546	0.023	92.7	1.2	7.36	0.31	
15	0.00040	0.00053	0.0000	0.0000	0.6982	0.0078	0.00058	0.00076	0.552	0.156	82.2	0.2	7.45	2.11	

Sample: DC18-3-K-feldspar	Hbl-granite			200-355 μm	8 grains	J-Value: 0.007468 \pm 0.000028								
1	0.25223	0.02179	0.0001	0.5134	436.7809	15.8642	0.00058	0.00005	362.221	14.398	82.9	0.0	2362.86	52.58
2	0.04563	0.00195	0.0507	0.0422	94.2741	0.4763	0.00048	0.00002	80.769	0.703	85.7	0.1	851.53	6.42
3	0.00397	0.00017	0.0018	0.0041	3.0200	0.0063	0.00131	0.00006	1.820	0.050	60.8	1.3	24.36	0.67
4	0.00034	0.00002	0.0093	0.0007	0.6472	0.0008	0.00052	0.00003	0.522	0.007	84.1	7.6	7.01	0.09
5	0.00003	0.00010	0.0059	0.0030	0.3560	0.0014	0.00007	0.00027	0.322	0.029	97.8	1.9	4.33	0.39
6	0.00005	0.00003	0.0126	0.0008	0.3962	0.0006	0.00013	0.00007	0.356	0.008	96.2	6.4	4.79	0.11
7	0.00001	0.00004	0.0085	0.0007	0.4116	0.0007	0.00001	0.00009	0.384	0.011	99.7	8.5	5.16	0.14
8	0.00007	0.00002	0.0073	0.0006	0.4862	0.0008	0.00014	0.00004	0.440	0.006	95.7	10.0	5.91	0.08
9	0.00015	0.00001	0.0037	0.0004	0.5597	0.0006	0.00027	0.00002	0.489	0.004	91.7	10.5	6.57	0.06
10	0.00035	0.00003	0.0038	0.0007	0.6962	0.0015	0.00050	0.00005	0.566	0.010	84.5	5.3	7.61	0.14
11	0.00042	0.00002	0.0033	0.0006	0.8667	0.0014	0.00049	0.00003	0.715	0.007	85.1	9.0	9.61	0.10
12	0.00065	0.00002	0.0055	0.0005	1.1724	0.0013	0.00055	0.00002	0.954	0.007	83.3	10.3	12.81	0.10

13	0.00042	0.00008	0.0024	0.0020	1.0756	0.0024	0.00039	0.00007	0.925	0.023	88.1	2.4	12.41	0.31
14	0.00058	0.00002	0.0031	0.0004	1.0321	0.0008	0.00056	0.00002	0.834	0.007	83.0	10.6	11.20	0.10
15	0.00042	0.00004	0.0015	0.0008	0.9737	0.0014	0.00043	0.00004	0.825	0.012	87.1	5.9	11.08	0.16
16	0.00037	0.00004	0.0002	0.0013	0.8874	0.0010	0.00042	0.00004	0.751	0.011	87.3	6.2	10.09	0.15
17	0.00050	0.00009	0.0045	0.0019	0.9104	0.0018	0.00055	0.00010	0.736	0.027	83.3	2.3	9.90	0.36
18	0.00113	0.00025	0.0134	0.0047	1.3117	0.0053	0.00086	0.00019	0.951	0.074	74.0	1.1	12.77	0.99
19	0.00118	0.00039	0.0000	0.0000	1.5819	0.0066	0.00074	0.00025	1.207	0.116	77.6	0.6	16.19	1.55

Acknowledgements

This study has received financial support from the National Natural Science Foundation of China (40872139), the 111 Project (B07011) of the Ministry of Education, State Key Laboratory of Geological Processes and Mineral Resources (Grant No. GPMR200837) and the Fundamental Research Funds for the Central Universities (Grant No. GPMR2009PY01). Profs Michel Faure, John Craddock and Lorence G. Collins, an anonymous reviewer and the associate editor Prof. John G. Liou are appreciated for their thoughtful and constructive comments and reviews, which substantially improved this work. We acknowledge final polishing of the text by Isabella Merschorf.

References

- Allen, C.R., Gillespie, A.R., Han, Y., Sieh, K.E., Zhang, B., Zhu, C., 1984. Red River and associated faults, Yunnan province, China: Quaternary geology, slip rates, and seismic hazard. *Geological Society of American Bulletin* 95, 686–700.
- Anczkiewicz, R., Viola, G., Muntener, O., Thirlwall, M.F., Villa, I.M., Quong, N.Q., 2007. Structure and shearing conditions in the DayNuiCon Voi massif: Implications for the evolution of the Red River shear zone in northern Vietnam. *Tectonics* 26, TC2002, doi:10.1029/2006TC001972.
- Avouac, J.P., Tapponnier, P., 1993. Kinematic model of active deformation in central Asia. *Geophysical Research Letters* 20, 895–898.
- Barr, S.M., MacDonald, A.S., Miller, B.V., Reynolds, P.H., Rhodes, B.P., Yokart, B., 2002. New U–Pb and $^{40}\text{Ar}/^{39}\text{Ar}$ ages from the Doi Inthanon and Doi Suthep metamorphic core complexes, northwestern Thailand. In: Mantajit, N. (ed.), *Proceedings of the Symposium on Geology of Thailand*. Department of Mineral Resources, Bangkok, 284–294.
- Briaais, A., Patriat, P., Tapponnier, P., 1993. Updated interpretation of magnetic anomalies and seafloor spreading stages in the South China Sea: implications for the Tertiary tectonics of Southeast Asia. *Journal of Geophysical Research* 98, 6299–6328.

- Burchfiel, B.C., Wang, E.C., 2003. Northwest-trending, middle Cenozoic, left-lateral faults in southern Yunnan, China, and their tectonic significance. *Journal of Structural Geology* 25, 781–792.
- Bureau of Geology and Mineral Resources of Yunnan, 1983. Geological map of Yunnan, Kunming, China.
- Bureau of Geology and Mineral Resources of Yunan, 1991. Geological map of Yunnan, Kunming, China.
- Cao, S.Y., Liu, J.L., Leiss, B., 2010a. Orientation-related deformation mechanisms of naturally deformed amphibole in amphibolite mylonites from the Diancang Shan, SW Yunnan, China. *Journal of Structural Geology* 32, 606–622.
- Cao, S.Y., Liu, J.L., Leiss, B., Neubauer, F., Genser, J., Zhao, C.Q., 2010b. Oligo-Miocene shearing along the Ailao Shan-Red River shear zone: constraints from structural analysis and zircon U/Pb geochronology of magmatic rocks in the Diancang Shan massif, SE Tibet, China. *Gondwana Research*. GR549, 10.1016/j.gr.2010.10.006.
- Chen, H.H., Dobson, J., Heller, F., Hao, J., 1995. Paleomagnetic evidence for clockwise rotation of the Simao region since the Cretaceous: a consequence of India-Asia collision. *Earth and Planetary Science Letters* 134, 203–217.
- Chung, S.L., Lee, T.Y., Lo, C.H. Wang, P.L. Chen, C.Y., Yem, N.T., Hoa, T.T., Wu, G.Y., 1997. Intraplate extension prior to continental extrusion along the Ailao Shan Red River shear zone. *Geology* 25, 311–314.
- Chung, S.L., Lo, C.H., Lee, T.Y., Zhang, Y.Q., Xie, Y.W., Li, X.H., Wang, K.L., Wang, P.L., 1998. Diachronous uplift of the Tibetan plateau starting from 40 Myr age. *Nature* 394, 769–773.
- Chung, A.L., Chu, M.F., Zhang, Y.Q., Xie, Y.W., Lo, C.H., Lee, T.Y., Lan, C.Y., Zhang, X.H., Zhang, Q., Wang, Y.Z., 2005. Tibetan tectonic evolution inferred from spatial and temporal variations in post-collisional magmatism. *Earth-Science Reviews* 68, 173–196.
- Fan, C., Wang, G., Wang, S., Wang, E., 2006. Structural Interpretation of Extensional Deformation along the Dali Fault System, Southeastern Margin of the Tibetan Plateau. *International Geology Review* 48, 287–310.
- Funahara, S., Nishiwaki, N., Murata, F., Otofujii, Y., Wang, Y.Z., 1993. Clockwise rotation of the Red River fault inferred from paleomagnetic study of Cretaceous rocks in the Shan-Thai-Malay block of western Yunnan, China. *Earth and Planetary Science Letters* 117, 29–42.

- Gilley, L.D., Harrison, T.M., Leloup, P.H., Ryerson, F.J., Lovera, O.M., Wang, J.H., 2003. Direct dating of left-lateral deformation along the Red River shear zone, China and Vietnam. *Journal of Geophysical Research* 108, doi:10.1029/2001 JB001726.
- Handler, R., Neubauer, F., Velichkova, S.H., Ivanov, Z., 2004. $^{40}\text{Ar}/^{39}\text{Ar}$ age constraints on the timing of magmatism and cooling in the Panagyurishte region, Bulgaria. *Schweizerische Mineralogische und Petrographische Mitteilungen* 84, 119–132.
- Harrison, T. M., 1981. Diffusion of ^{40}Ar in hornblende. *Contributions to Mineralogy and Petrology* 78, 324–331.
- Harrison, T.M., Duncan, I., McDougall, I., 1985. Diffusion of ^{40}Ar in biotite: temperature, pressure, and compositional effects. *Geochimica Cosmochimica Acta* 49, 2461–2468.
- Harrison, T.M., Chen, W.J, Leloup, P.H., 1992. An early Miocene transition in deformation regime within the Red River fault zone, Yunnan, and its significance for Indo-Asian tectonics. *Journal of Geophysical Research* 97, 7159–7182.
- Harrison, T.M, Leloup, P.H., Ryerson, F.J., Tapponnier, P., Lacassin, R., Chen, W.J., 1996. Diachronous initiation of transtension along the Ailao Shan-Red River Shear zone, Yunnan and Vietnam. In: Harrison, T.M., Yin, A. (Eds.), *The Tectonics of Asian*. Cambridge University Press, New York, pp. 208–226.
- Harrison, T. M., Célérier, J., Aikman, A. B., Hermann, J., Heizler, M. T., 2009. Diffusion of ^{40}Ar in muscovite. *Geochimica et Cosmochimica Acta* 73, 1039–1051.
- Huang, K., Opdykea, N.D., 1993. Paleomagnetic results from Cretaceous and Jurassic rocks of South and Southwest Yunnan: evidence for large clockwise rotations in the Indochina and Shan-Thai-Malay terranes. *Earth and Planetary Science Letters* 117, 507–524.
- Hurford, A.J., Flisch, M., Jäger, E., 1989. Unravelling the thermo-tectonic evolution of the Alps: a contribution from fission track analysis and mica dating. In: Coward, M.P. Dietrich, D., Park, R.G. (Eds), *Alpine Tectonics*, *Journal of geology society London*, Geological Society Special Publication No. 45, pp. 369–398
- Jolivet, L., Maluski, H., Beyssac, O., Goffé, B., Lepvrier, C., Phan, T.T., Nguyen, V.V., 1999. Oligocene-Miocene Bu Khang extensional gneiss dome in Vietnam: Geodynamic implications. *Geology* 27, 67–70.
- Lacassin, R., Maluski, H., Leloup, P.H., Tapponnier, P., Hinthong, C., Siribhakdi, K., Chuaviroj, S., Charoenravat, A., 1997. Tertiary diachronic extrusion and deformation of western Indochina: structural and $^{40}\text{Ar}/^{39}\text{Ar}$ evidence. *Journal of Geophysical Research* 102 (B5), 10013–10037.

- Lee, G.H., Watkins, J.S., 1998. Seismic stratigraphy and hydrocarbon potential of the Phu Khan Basin, offshore Central Vietnam, South China Sea. *AAPG Bulletin* 82, 1711–1735.
- Leloup, P.H., Harrison, T.M., Ryerson, F.J., Chen, W.J., Li, Q., 1993a. Structural, petrological and thermal evolution of a Tertiary Ductile strike-slip shear zone, Diancang Shan, Yunnan. *Journal of Geophysical Research* 98, 6715–6743.
- Leloup, P.H., Kienast, J.R., 1993b. High-temperature metamorphism in a major strike-slip shear zone: the Ailao Shan–Red River, People’s Republic of China. *Earth and Planetary Science Letters* 118, 213–234.
- Leloup, P.H., Lacassin, R., Tapponnier, P., Schärer, U., Zhong, D.L., Liu, X.H., Zhang, L.S., Ji, S.C., Phan, T.T., 1995. The Ailao Shan-Red River shear zone (Yunnan, China), Tertiary transform boundary of Indochina. *Tectonophysics* 251, 3–84.
- Leloup, P.H., Lacassin, R., Tapponnier, P., Harrison, T.M., 2001a. Comment on “Onset timing of left-lateral movement along the Ailao Shan–Red River shear zone: $^{40}\text{Ar}/^{39}\text{Ar}$ dating constraint from the Nam Dinh area, northeastern Vietnam” by Wang et al., 2000, *Journal of Asian Earth Sciences* 18, 281–292. *Journal of Asian Earth Sciences* 20, 95–99.
- Leloup, P.H., Arnaud, N., Lacassin, R., Kienast, J.R., Harrison, T.M., Phan, T.T., Replumaz, A., Tapponnier, P., 2001b. New constraints on the structure, thermochronology, and timing of the Ailao Shan-Red River shear zone, SE Asia. *Journal of Geophysical Research* 106, 6683–6732.
- Lepvrier, C., Maluski, H., Vuong, N.V., Roques, D., Axent, V., Rangin, C., 1997. Indosinian NW-trending shear zones within the Truong Son belt (Vietnam) $^{40}\text{Ar}/^{39}\text{Ar}$ Triassic ages and Cretaceous to Cenozoic overprints. *Tectonophysics* 283, 105–127.
- Liu, J.L., Song, Z.J., Cao, S. Y., Zhai, Y.F., Wang A.J., Gao, L., Xiu, Q.Y., Cao, D.H., 2006. The dynamic setting and processes of tectonic and magmatic evolution of the oblique collision zone between Indian and Eurasian plates: exemplified by the tectonic evolution of the Three River region, eastern Tibet (in Chinese). *Acta Petrologica Sinica* 22, 775–786.
- Liu, J.L., Cao, S.Y., Zhai, Y.F., Song, Z.J. Wang, A.J., Xiu, Q.Y., Gao, L., Guan, Y., 2007. Rotation of Crustal Blocks as an Explanation of Oligo–Miocene Extension in Southeastern Tibet–Evidenced by the Diancangshan and Nearby Metamorphic Core Complexes. *Earth Science Frontiers* 14, 40–48.
- Lovera, O.M., Richter, F.M., Harrison, T.M., 1989. The $^{40}\text{Ar}/^{39}\text{Ar}$ thermochronometry for slowly cooled samples having a distribution of diffusion domain sizes. *Journal of Geophysical Research* 94, 17917–17935.

- Ludwig, K.R., 2001, Users Manual for Isoplot/Ex – A Geochronological Toolkit for Microsoft Excel, Berkeley Geochronological Center, Special Publication No. 1a.
- Mandal, N., Fujino, K., Samanta, S.K., 1997. Development of quartz ribbons in quartzofeldspathic granulites. *Journal of Earth System Science* 106, 225–236.
- Macdonald, A.S., Barr, S.M., Dunning, G.R., Yaowanoyothin, W.Y., 1993, The Doi Inthanon metamorphic core complex in NW Thailand: age and tectonic significance. *Journal of Southeast Asia Earth Sciences* 8, 117–125.
- Maluski, H., Lepvrier, C., Jolivet, L., Carter, A., Roques, D., Beyssac, O., Tang, T.T., Thang, N.D., Avigad, D., 2001. Ar-Ar and fission-track ages in the Song massif: Early Triassic and Cenozoic tectonics in northern Vietnam. *Journal of Asian Earth Science* 19, 233–248.
- McDougall, I., Harrison, M.T., 1988, *Geochronology and thermochronology by the $^{40}\text{Ar}/^{39}\text{Ar}$ method*. New York, Oxford University Press, 212.
- McDougall, I., Harrison, M.T., 1999, *Geochronology and Thermochronology by the $^{40}\text{Ar}/^{39}\text{Ar}$ Method*. second, Oxford Oxford, University Press, p. 269.
- McLelland, J., 1984. The origin of ribbon lineation within the southern Adirondacks. U.S.A.. *Journal of Structure Geology* 6, 147–157.
- Menegon, L., Pennacchioni, G., Stünitz, H., 2006. Nucleation and growth of myrmekite during ductile shear deformation in metagranites. *Journal of Metamorphic Geology* 24, 553–568.
- Molnar, P., Tapponnier, P., 1975. Cenozoic tectonics of Asia: Effects of a continental collision. *Science* 189, 419–426.
- Morley, C.K., 2002. A tectonic model for the Tertiary evolution of strike-slip faults and rift Basins in SE Asia. *Tectonophysics* 347, 189–215.
- Nagy, E.A., Maluski, H., Lepvrier, C., Schärer, U., Thi, P.T., Leyreloup, A., Thich, V.V., 2001. Geodynamic significance of the Kontum Massif in central Vietnam: composite $^{40}\text{Ar}/^{39}\text{Ar}$ and U–Pb ages from Paleozoic to Triassic. *Journal of Geology* 109, 755–770.
- Nagy, E.A., Schärer, U., Minh, N.T., 2008. Oligo-Miocene granitic magmatism in central vietnam and implications for continental deformation in Indochina. *Terra Nova* 12, 67–76.
- Nam, T.N, Toriumi M., Itaya, T., 1998. P-T-t paths and post-metamorphic exhumation of the Day Nui Con Voi shear zone in Vietnam. *Tectonophysics* 290, 299–318.
- Nam, T.N., Sano, Y., Terada, K., Toriumi, M., Quynh, P.V., Dung, L.T., 2001. First SHRIMP U–Pb zircon dating of granulites from the Kontum massif (Vietnam) and tectonothermal implications. *Journal of Asian Earth Sciences* 19, 77–84.
- Passchier, C.W., Trouw, R.A.J., 2005. *Microtectonics*. Springer-Verlag, Berlin.

- Replumaz, A., Karason, H., van der Hilst, R. D., Besse, J., Tapponnier, P., 2004. 4-D evolution of SE Asia's mantle from geological reconstructions and seismic tomography. *Earth and Planetary Science Letters* 221, 103–115.
- Rieser, A.B., Liu, Y.J., Genser, J., Neubauer, F., Handler, R., Friedl, G., Ge, X.H., 2006. $^{40}\text{Ar}/^{39}\text{Ar}$ ages of detrital white mica constrain the Cenozoic development of the intracontinental Qaidam Basin, China. *Geological Society of America Bulletin* 118, 1522–1534.
- Scaillet, S., 2000. Numerical error analysis in $^{40}\text{Ar}/^{39}\text{Ar}$ dating. *Earth and Planetary Science Letters* 162, 269–298.
- Schärer, U., Tapponnier, P., Lacassin, R., Leloup, P.H., Dalai, Z., Ji, S.C., 1990. Intraplate tectonics in Asia: a precise age for large-scale Miocene movement along the Ailao Shan-Red River shear zone, China. *Earth and Planetary Science Letters* 97, 65–77.
- Schärer, U., Zhang, L.S., Tapponnier, P., 1994. Duration of strike-slip movements in large shear zones: The Red River belt, China. *Earth and Planetary Science Letters* 126, 379–397.
- Schoenbohm, L.M., Whipple, K.X., Burchfiel, B.C., Chen, L., 2004. Geomorphic constraints on surface uplift, exhumation and plateau growth in the Red River region, Yunnan Province, China. *Geological Society of American Bulletin* 116, 895–909.
- Searle, M., 2006. Role of the Red River Shear zone, Yunnan and Vietnam, in the continental extrusion of SE Asia. *Journal of the Geological Society, London* 163, 1025–1036.
- Searle, M.P., Noble, S.R., Cottle, J.M., Waters, D.J., Mitchell, A.H.G., Hlaing, Tin., Horstwood, M.S.A. 2007. Tectonic evolution of the Mogok metamorphic belt, Burma (Myanmar) constrained by U-Th-Pb dating of metamorphic and magmatic rocks. *Tectonics*, 26, TC3014, doi: 10.1029/2006TC002083.
- Steiger, R.J., Jäger, E., 1977. Subcommittee on geochronology: convention on the use of decay constants in geo- and cosmochronology. *Earth Planetary Science Letters* 36, 359–362.
- Sun, Z., Zhong, Z.H., Zhou, D., Qiu, X.L., Wu, S.M., 2003. Deformation mechanism of Red River fault zone during Cenozoic and experimental evidences related to Yinggehai basin formation. *Journal of Tropical Oceanography* 22, 1–9.
- Tapponnier, P., Molnar, P., 1977. Active faulting and tectonics of China, *Journal of Geophysical Research* 82, 2905–2930.
- Tapponnier, P., Peltzer, G., Armijo, R., Le Dain, A.Y., Cobbold, P., 1982. Propagating extrusion tectonic in Asia: new insights from simple experiments with plasticine. *Geology* 10, 611–616.

- Tapponnier, P., Peltzer, G., Armijo, R., 1986. On the mechanics of the collision between India and Asia. In: Coward, M.P., Ries, A.C. (Eds.), *Collision Tectonics*. Geological Society of London Special Publication 19, 115–157.
- Tapponnier, P., Lacassin, R., Leloup, P.H., Schärer, U., Zhong, D.L., Liu, X.H., Ji, S.C., Zhang, L.S., Zhong, J.Y., 1990. The Ailao Shan/Red River metamorphic belt: Tertiary left-lateral shear between Indochina and South China. *Nature* 343, 431–437.
- Tullis, J., 1983. Deformation of feldspars. In: Ribbe, P.H. (Eds.), *Feldspar Mineralogy*, Mineralogical Society of America, pp. 297–323.
- Tullis, J., Yund, R.A., 1987. Transition from cataclastic flow to dislocation creep of feldspar: mechanisms and microstructures. *Geology* 15, 606–609.
- van Hinsbergen, D.J.J., Straathof, G.B., Kuiper, K.F., Cunningham, W.D., Wijbrans, J., 2008. No vertical axis rotations during transpressional orogeny in the NE Gobi Altai: coinciding Mongolian and Eurasian early Cretaceous apparent polar wander paths. *Geophysical Journal International* 173, 105–126.
- Vernon, R.H. 1991. Questions about myrmekite in deformed rocks. *Journal of Structural Geology* 13, 979–985.
- Vernon, R.H., 2000. Review of microstructural evidence of magmatic and solid-state flow. *Electronic Geosciences*. Springer, 2000.
- Vuong, N.V., 2007. Late Eocene metamorphism and ductile deformation age of Con Voi range, the Red River shear zone: evidence from the garnet Sm/Nd dating. *VNU Journal of Science, Earth Sciences* 23, 69–75.
- Wang, E., Burchfiel, B.C., 1997. Interpretation of Cenozoic tectonics in the right-lateral accommodation zone between the Ailao Shan shear zone and the eastern Himalayan syntaxis. *International Geology Review* 39, 191–219.
- Wang, E., Burchfiel, B.C., Royden, L.H., Chen, L.Z., Chen, J.S., Li, W.X., Chen, Z.L. (Eds.), 1998a, Late Cenozoic Xianshuihe-Xiaojiang, Red River, and Dali Fault Systems of Southwestern Sichuan and Central Yunnan, China. Special Paper, Geological Society of America, 327.
- Wang, E., Fan, C., Wang, G., Shi, X.H., Chen, L.Z., Chen, Z.L., 2006. Deformation and geomorphic processes in the formation of the Ailao Shan-Diancang range, west Yunnan. *Quaternary Sciences* 26, 220–227.
- Wang, P.L., Lan, C.Y., Yem, N.T., Lo, C.H., Lee, T.Y., Chung, S.L., 1998b. Thermochronological evidence for the movement of the Ailao Shan-Red River shear zone: a perspective from Vietnam. *Geology* 26, 887–890.

- Wang, P.L., Lo, C.H., Chung, S.L., Lee, T.Y., Lan, C.Y., Thang, T.V., 2000. Onset timing of left-lateral movement along the Ailao Shan–Red River shear zone: $^{40}\text{Ar}/^{39}\text{Ar}$ dating constraint from the Nam Dinh area, northeastern Vietnam. *Journal of Asian Earth Science* 18, 281–292.
- Wijbrans, J.R., Pringle, M.S., Koppers, A.A.P., Schveers, R., 1995. Argon geochronology of small samples using the Vulkaan argon laserprobe: *Proc. Koninklijke Academie Wetenschappen* 98, 185–218.
- Yeh, M.W., Lee, T.Y., Lo, C.H., Chung, S.L., Lan, C.Y., Anh, T.T., 2008. Structural evolution of the Day Nui Con Voi metamorphic complex: Implications on the development of the Red River Shear Zone, Northern Vietnam. *Journal of Structural Geology* 30, 1540–1553.
- Zhang, L.S., Schärer, U., 1999. Age and origin of magmatism along the Cenozoic Red River shear belt, China. *Contributions to Mineralogy and Petrology* 134, 67–85.
- Zhong, D.L., Tapponnier, P., Wu, H.W., Zhang, L.S., Ji, S.C., Zhong, J.Y., Liu, X.H., Schaerer, U., Lacassiu, R., Leloup, P., 1990. Large-Scale Strike-Slip-Fault-the Major Structure of Intracontinental Deformation after Collision. *Chinese Science Bulletin* 35, 304–309.
- Zhu, M.Z., Graham, S., McHargue, T., 2009. The Red River Fault zone in the Yinggehai Basin, South China Sea. *Tectonophysics* 476, 397–417.

8 Summary and outlook

The case studies included in this thesis (Chapters 1 to 7) aim to enhance the understanding of new evidences for the Cenozoic deformation, tectono-magmatic and thermochronological evolution of the ASRR shear zone in Southeast Asia, based on detailed and quantitative analysis of macro-, micro- and submicrostructure deformation, texture and isotopic dating. As such, the results presented in these chapters provided further insight into the main questions addressed in this thesis, namely 1) main deformation characteristics e.g. macro- and microstructures, texture developments, deformation mechanisms and deformation conditions (P-T) of the mylonitic high-grade metamorphic rocks along the ASRR shear zone; 2) Cenozoic tectonic and magmatic evolution; 3) onset timing and duration of the left-lateral movement along the ASRR shear zone; 4) cooling history, exhumation mechanisms (P-T-t-D paths) of the high-grade metamorphic complex.

8.1 Macro- and microstructures, textures and deformation mechanisms

Chapter 2 and 3 mainly describe the results about the high-temperature mylonites derived from either granitic rocks or amphibolitic rocks which constitute the main part of the shear zones in the high-grade metamorphic complex. Structural, microstructural, sub-microstructural and texture analysis and P/T estimation reveal that deformation of rocks occurred at high-temperature condition. Mesoscopic structures for high temperature shearing prevail in the central high strain shear zone of the DCS massif. Complex and sheath folds formed by ductile flow are frequently observed in sheared schists and granitic mylonites. A remarkable feature of the mylonites (both metamorphic and granitic-derived) is their extremely strong stretching lineation fabrics, in contrast to poorly developed mylonitic foliation, thus forming L and L-S tectonites. Intensive plastic deformation of feldspar, quartz and amphibole under amphibolite facies all consistently document a left-lateral shearing along the ASRR shear zone, which also helps to constrain the timing of initiation of left-lateral shearing.

Plagioclase grains in the mylonitic rocks are characterized by crystal plastic deformation and dynamic recrystallization. They are elongated or partly twinned, and some are dynamically recrystallized into fine grains in the matrix. Undulatory and inhomogeneous extinction, grain elongation, deformation twinning and subgrain formation are common in porphyroclastic plagioclase grains. Quartz grains may form monomineralic bands or constitute polymineralic bands with plagioclase grains. They are characterized by high temperature grain growth, forming

equant grains with straight boundaries and triple junctions, or rectangular quartz ribbons parallel to the dominant foliation in the mylonites. Sheared amphibolite mylonites are characterized by porphyroclastic microstructures and the ultramylonites are highly lineated with alternating amphibole- and quartzofeldspathic domains. Amphibole and plagioclase grains are intensively deformed with obvious grain size reduction, but quartz grains are recrystallized dominantly by grain growth. The amphibole grains in the mylonitic rocks are deformed and dynamically recrystallized at amphibolite facies. In the mylonitic amphibolites, there are two types of amphibole porphyroclasts, i.e. type I “hard” and type II “soft” porphyroclasts. Type I porphyroclasts are typical “hard” porphyroclasts during shearing without any evidence for dynamic recrystallization. Mechanical rotation is responsible for the deformation and orientation pattern of the type I porphyroclasts. Type II porphyroclasts are typical “soft” porphyroclasts and have mantled microstructures. Dynamic recrystallization by combined subgrain nucleation due to twinning and dislocation creep generates fine grains of amphibole in the matrix. Most fine grains in the matrix have close relationships with the type II porphyroclasts. During the deformation and recrystallization, the type II porphyroclasts have initial crystallographic orientations that are propitious for the (100) [001] slip system to be activated and therefore (100) micro-twinning becomes the most dominant deformation mechanism. It is therefore proposed that twinning nucleation recrystallization (TNR) is one of the most important processes that operate during dynamic recrystallization of amphibole. Initial crystallographic orientations of amphibole grains from the host rocks have strong effects on the rheological behavior of the grains during deformation.

Optical and TEM observations suggest that during deformation and dynamic recrystallization of amphibole grains in the mylonitic rocks high temperature ductile flow dominate the deformation of quartz and plagioclase grains. The existence of quartzofeldspathic components leads to strain localization and strain softening during mylonitization, which is possibly an important triggering for the deformation and dynamic recrystallization of amphibole grains.

8.2 Timing of left-lateral shearing along the Ailao Shan-Red River shear

There have been extensive discussions on the timing of left-lateral shearing along the ASRR and the mechanism of exhumation of the high-grade metamorphic rocks. Chapter 4 and 5 examines a detailed and integrated study on the timing of plutonic intrusion and shearing in the wall rocks using optical microscope (deformation microstructures), EBSD (textures of amphibolite, quartz and feldspar) and SHRIMP zircon U-Pb dating in the Diancang Shan massif

along Ailao Shan-Red River shear zone. Macro- and microstructural, and textural analysis reveal intensive plastic deformation of feldspar, quartz and amphibole under amphibolite facies. They all consistently document a left-lateral shearing. The porphyritic monzogranite mylonite along the shear zone possesses evidences where the granite experienced a sequential and progressive process from crystallization during magma emplacement, through submagmatic flow to solid-state plastic deformation. It is suggested that the early-kinematic pluton subsequently experienced strong left-lateral strike-slip shearing. The development of complex quartz c-axes pole figures in granitic mylonites may have recorded a successive variation of deformation conditions during progressive shearing. They are coherent with solid-state high-temperature ductile deformation during regional left-lateral shearing. Relatively low-temperature modification of the quartz c-axis fabrics can be related to an exhumation and cooling event of the Diancang Shan massif during a later event. All the magmatic zircons give U-Pb ages of ca. 31 Ma for the crystallization of the granite. This age provides therefore the lower time bracketing the left-lateral shearing along the ASRR shear zone at the Diancang Shan high-grade metamorphic massif. The ages of ca. 24 Ma from the post-kinematic granitic rocks should represent a young age for the termination of the ductile left-lateral strike-slip shearing, and the youngest age of ca. 21 Ma is inferred to date the final phase of regional ductile deformation and left lateral shearing at least in the DCS massif along the ASRR shear belt. From the analyses, we reasonably suggest that the ages of ca. 21 Ma should represent the timing of the termination of left-lateral strike-slip shearing.

8.3 Eocene-Miocene tectono-magmatic evolution in the Ailao Shan-Red River shear zone

The relation between magmatism and shearing has become the solely important way to provide a means of determination of the age of the deformational event. Chapter 6 further insights into the Eocene-Miocene tectonic-magmatic evolution of the DCS massif along the Ailao Shan-Red River shear zone mainly based on our structural analysis and new zircon U-Pb isotopic dating from the granitic rocks. The combined structural and geochronological results have revealed a successive magmatic intrusion and crystallization related to shearing in the DCS massif. Three main type intrusions, pre-kinematic, syn-kinematic and post-kinematic, were observed within the DCS massif, which show variable degrees of deformation ranging from undeformed pegmatitic dykes to strongly sheared layered granites with foliations and lineations. Field and microscopic observations reveal that pre-kinematic and syn-kinematic intrusions are coevally deformed with high-temperature mylonitization. All the samples record three stage

successive kinematic evolution of the shear zone from Eocene to Miocene ages between ca. 34 and 20 Ma.

The emplacement of the pre-kinematic alkaline magmas in the ASRR shear zone appears to have been accompanied by development of Eocene to Oligocene rifted sedimentary basins. We also propose that the short time span (ca. 34-31 Ma) emplacement of pre-kinematic plutons during late Eocene to Oligocene possibly can be directly related to the high-potassic alkaline magmatic activity as a response to the post-collisional extension. The recognition of magmatic and shearing microstructures in the syn-kinematic granitic intrusions in the DCS implies a transition from magmatic through submagmatic to solid-state plastic deformation during the emplacement of the plutons. To document this transition it is important to prove that the solid-state plastic deformation occurred at high-temperature conditions. The post-kinematic granitic intrusions are very weakly deformed or nearly undeformed, sharply cut the high-temperature mylonitic foliation. Development of solid-state brittle deformation fabrics document continued progressive deformation at relative low temperature during the latest stages of magma crystallization and cooling. From all these analyses, we reasonably suggest that the final stages of progressive shearing can be constrained by the youngest magmatic zircon crystallization age related to brittle shearing continued to ca. 21 Ma. The most straightforward interpretation of our data indicate that magmatism of the DCS shearing recorded a maximum age of the initiation at ca. 31 Ma, culminated during the main periods between 27 and 24 Ma at high temperature ductile deformation condition (amphibolite facies metamorphic conditions) and terminated at about 24 or 21 Ma at a low temperature related to rapid cooling. The emplacement of the three stages of granitic intrusions is spatially confined and temporally related to a continuum of ductile to brittle deformation, which may also indicate a change in the rheology of the crust evolving from ductile to brittle state.

8.4 Cooling history and exhumation of the high-grade metamorphic complexes

Deep-crustal level high-grade metamorphic rocks were exposed within or immediately adjacent to the continental strike-slip fault systems in SE Asia in a fan-shaped area, which is bounded by the ASRR fault to the east and the Sagaing fault to the west. Debate exists on the ages of exhumation of these high-grade metamorphic massifs, e.g. XLS, DCS, ALS and DNCV, along the ASRR shear zone. Chapter 7 presents the results of a series of geochronological data have shown a complicated cooling-exhumation history of these massifs. New $^{40}\text{Ar}/^{39}\text{Ar}$ amphibole, muscovite, biotite and K-feldspar data show that there are three stages of dominant

cooling and exhumation of the DCS massif. The early stage of the thermochronological evolution of the DCS massif started with an onset diachronous from >27 to 23 Ma, but subsequent homogeneous cooling and exhumation. The latter two stages are shown to be diachronous throughout the whole period of evolution from 13 to 0 Ma. The cooling and exhumation of the massif is attributed to regional tectonic deformation. Three stages of regional tectonic deformation is well constrained with thermochronological timing. The new data show that ductile left lateral shearing initiated at c.a. 28 Ma ago and slow cooling continued to low temperatures to 12 and 6 Ma. The second and third tectonic deformations are ductile to brittle and brittle normal faulting that operated mainly between 11 and 6 Ma, and 7 to 0 Ma. In a regional scale, the tectonic exhumation of the DCS massif consists a part of the tectono-thermal evolution and diachronous exhumation of the metamorphic complexes broadly since 36 Ma in a fan-shaped area bounded by the Red River fault zone and Sagaing fault zone in SE Asia. Extrusion-induced strike-slip shearing and rotation-resulted normal faulting played important roles in the diachronous cooling and exhumation of the metamorphic complexes in SE Asia.

8.5 Concluding remarks and future work

This thesis integrated results from basic geological field survey and mapping, microstructure analysis by OM (optical microscopy), sub-microstructure analysis by TEM (transmission electron microscope), texture analysis by EBSD (electron backscattered diffraction), mineral chemistry analysis by EPMA (electron probe microanalysis), U-Pb zircon dating by SHRIMP-II and LA-ICP-MS, Ar/Ar dating of amphibole, white mica, biotite and K-feldspar, to have a detailed discussion on the deformation, tectono-magmatism, timing of shearing, cooling history and exhumation mechanism of high-grade metamorphic rocks exposed in the Diancang Shan metamorphic massif along the ASRR shear zone. It is unified by the goal of understanding the deformation, tectonic and thermochronology evolution of the ASRR shear zone, by questions of fundamental crustal dynamics and tectonic processes.

The following aspects will be the major contents of further study:

- ◆ Field relationships north and west sections of the DCS complex.
- ◆ The relationship between extension, right-lateral displacement and timing on the ASRR fault still remains unclear, but could probably be resolved through more detailed field mapping and additional thermochronology studies.

- ◆ A combination of additional apatite and zircon fission-track and (U-Th)/He thermochronology could help to establish the lower temperature cooling history of the metamorphic complex, defining a minimum age for the last deformation event and exhumation processes.
- ◆ The structural relations of high-grade, low-grade metamorphic rocks and the sedimentary rocks to reveal the general structural framework of the complex that the constitution and structural styles, deformation and mechanism of exhumation.
- ◆ Further detailed analysis on metamorphic evolution and PTt-D path configuration to elucidate the thermal-dynamic processes before and during exhumation of the metamorphic complex.
- ◆ Further detailed tectono-metamorphic-magmatism and thermochronology evidences should be sought out in the ALS, XLS, and other metamorphic complexes in SE Asia.
- ◆ The real role of the tectonic deformation along the major shear zones in accommodating the Indian-Asian plate interactions.

Curriculum vitae

Name: Shuyun Cao

Date of birth: 03/23/1978

Nationality: Chinese

Educational background

- 10/2007-10/ 2010: Doctorate, Geoscience Centre, University of Göttingen, Germany.
- 09/2005-06/2007: Master, College of the Earth Sciences and Resources, China University of Geosciences (Beijing), China.
- 09/1998-07/2002: Bachelor, College of Resource and Environment Science, Hunan Normal University, China.

Work Experience

- 08/2002-2005/09: Geography Lecturer. No. 2 Middle School of Zhuzhou, Hunan Province.